MACROPOROUS HYDROGELS FOR TISSUE ENGINEERING AND WOUND CARE

MACROPOROUS HYDROGELS IN TISSUE ENGINEERING AND WOUND CARE

By SAMANEH TOUFANIAN, B.Sc.

A Thesis Submitted to the School of Graduate Studies in Partial Fulfilment of the Requirements for the Degree Doctor of Philosophy in Chemical Engineering

McMaster University

DOCTOR OF PHILOSOPHY (2023), Hamilton, Ontario (Chemical Engineering)

TITLE: Macroporous Hydrogels in Tissue Engineering and Wound Care

AUTHOR: Samaneh Toufanian, B.Sc. (Sharif University of Technology)

SUPERVISOR: Professor Todd R. Hoare

NUMBER OF PAGES xxiii, 207

Lay Abstract

Hydrogels have been studied in various applications like targeted drug delivery, tissue engineering, regenerative medicine, and medical devices due to their tunable nature and their capacity to retain water. In many of these applications the pore size and porosity are the key to the performance of a hydrogel in a given application. In particular, the rate at which nutrients or wastes can move through a hydrogel, the stiffness of a hydrogel, and the interactions of a hydrogel with cells are all strongly dependent on the porosity of a hydrogel. Therefore, many techniques have been developed to produce hydrogels with well-defined pore sizes, in particular "macroporous" hydrogels that have larger pores at or above the size of a cell. However, the typical techniques used to make such hydrogels often require additives or manufacturing steps that make them challenging to implement in different applications. This thesis addresses challenges in the fabrication of controllable porosity of hydrogels for applications in wound care (including the treatment of antibiotic-resistant infected wounds) and regenerative medicine, in the latter case enabling minimally invasive injection of a macroporous hydrogel as well as enhancing its mechanics to better mimic native tissues. Each of these solutions aims to bring effective novel treatments to patients, offering alternative therapies for existing challenges in healthcare.

Abstract

Hydrogels are three-dimension networks of water-soluble polymer chains and have attracted interest in biomedical engineering, targeted drug delivery, tissue engineering, and regenerative medicine due to their ability to retain water coupled with their highly tunable physicochemical and biological properties. In the specific context of wound care, hydrogels can both maintain high wound hydration as well as absorb and manage wound exudate, both of which are major challenges in wound care. Hydrogel wound dressings can simultaneously deliver medication directly to the wound to suppress or treat infections, including antibiotic-resistant strains such as Methicillin-resistant *S. aureus* (MRSA). This thesis develops two wound care products that can address challenges in the selection and delivery of drugs to treat antibiotic-resistant strain infections: (1) *in situ*-gelling poly(oligoethylene glycol methacrylate) (POEGMA) hydrogel wound dressings containing self-assembled nanoparticles encapsulated with fusidic acid; and (2) an *in situ* calcium-crosslinked alginate scaffold produced using pressurized gas expanded liquids (PGX) technology impregnated with fusidic acid or tigecycline using supercritical adsorptive precipitation (sc-AP). The POEGMA hydrogel wound dressings helped supress MRSA infection and prevent systemic infection during the course of treatment, facilitating a 1-2 fold decrease in bacterial load in the wound bed. The sc-AP technology was shown to be compatible with loading clinically-relevant doses of both antimicrobial compounds, while the resulting wound dressings were effective in treating MRSA wound infections. In case of tigecycline loaded alginate scaffolds, the infection was completely cleared.

In tissue engineering applications, injectable macroporous hydrogels are particularly limited by two factors: (1) their need for invasive administration, typically implantation; and (2) their generally weak mechanics. In the first case, reports of injectable hydrogels often involve toxic compounds or by-products that result in loss of cell viability. This thesis addresses this challenge by design and development of a POEGMA-based macroporous hydrogel scaffold based on a novel, non-cytotoxic pore forming emulsion based on perfluorocarbons. Use of the pore-forming emulsion significantly improved cell viability *in vitro* 14 days after injection and was well tolerated *in vivo* with minimal to no inflammatory response. In the second case, an interpenetrating “hard-soft” nanofibrous hydrogel network was fabricated by co-electrospinning POEGMA with poly(caprolactone) (PCL). The PCL phase significantly enhanced the mechanical properties of the electrospun POEGMA hydrogel scaffold making handling and manipulating the scaffolds possible, while the presence of the POEGMA phase significantly improved the biological properties of PCL scaffolds in terms of supporting significantly enhanced cell proliferation and delayed bacterial adhesion.

Collectively, the advances made in this work address key challenges in the application of hydrogels in tissue engineering and wound care, with future potential to be applied to solve practical clinical challenges.

Acknowledgements

I would like to dedicate this work to all those who have had limited access to education, and those who have not been able to dream. I have been extremely privileged to have been able to follow my dreams and have had the opportunity to experience joy in peeking into the wonders of the universe. I can only hope that I am able to pay this forward.

When I stuffed my entire life in two 23-kilogram suitcases, a 16-kilogram carry-on, and a backpack that I could barely carry, I naively thought I had packed everything I needed start my journey 10,000 kms away from home. As recommended by the internet I had packed photos of friends, family and memories and packed treats, spices, and herbs as reminders. Little did I know what I would miss, time spent with family and friends, and all the missed birthdays, new years and wedding celebrations could never fit into a vessel and be transported. What helped me be able to push through and sit where I am sitting today was the non-stop support of my family. So, I would like to take this opportunity to highlight their support and contribution to this work that has not otherwise been mentioned.

Special thanks to my Mother, Shani, you are the wind beneath my wings, the roots that keep me grounded and the rock I rely on. Looking back, I am amazed at all you did for my education and growth and how you made it all look so effortless. It is often said that a true leader is one that is invisible, and you are a true testament to that.

I would like to thank my father Saeid. You have raised me to be the ambitious dreamer I am today. You taught me to never take no for an answer and strive to be the best version of myself. You believed in me the most in moments when I least believed in myself.

You reminded me to stay true to my values and who I am even if I was swimming against the tide. You taught me to choose for myself before others had a chance to and for that, I am ever more grateful.

Reyhaneh, I would not have been here today if I did not have you as a role model. You are the scientist I aspire to be. You are always there when I need a push or a reality check. Walt Disney said: “If you can dream it, you can do it” and having you as sister helped me be able to dream of the life I have today.

I would like to thank my supervisor Professor Todd Hoare. Your patience and support have helped me understand the value of investing in people. Your guidance has changed my approach in striving to find great solutions in impossible situations. Being part of your team has been a great honor and I could not have asked for a better mentor on this journey.

Finally, I would like to thank everyone whose contributed to this work and their expertise is woven into this work: The Ceapro Inc. research and development department including Dr. Paul Moquin, Dr. Bernhard Seifried, Dr. Byron Yepez, Emily Wong and Dr. Ricardo Couto, the Coombes Lab including Professor Brian Coombes and Jody Mohammed, Center for Advanced Light Microscopy, especially Dr. João Pedro Bronze de Firmino, the Hoare Lab including Nate Dowdall, Andrew Lofts, Christina McCabe, Meghan Kostashuk, Evelyn Cudmore, Alex Caschera, Seamus Adams, Ridhdhi Dave and the rest of the Hoare Lab.

Table of Contents

List of Figures

List of Tables

List of Abbreviations and Symbols

^{1}H NMR	Proton nuclear magnetic resonance
AA	Acrylic Acid
ADH	Adipic acid dihydrazide
AIBME	2,2-azobisisobutyric acid dimethyl ester
Alg	Alginate
ARGET-ATRP	Activators regenerated by electron transfer atom transfer radical polymerization
ASES	Aerosol Antisolvent Extraction System
ATPS	Aqueous two-phase systems
ATRP	Atom-transfer radical polymerization
BET	Brunauer, Emmett and Teller
BSA	Bovine Serum Albumin
CFU	Colony forming units
Đ	Dispersity
DCM	Dichloromethane
DIW	Deionized Water
DLS	Dynamic Light Scattering
DMAEMA	2-(dimethylamino)ethyl methacrylate
DMEM	Dulbecco’s Modified Eagle’s Medium-high glucose
DMF	Dimethylformamide
DN	Double Network
ECM	Extra Cellular Matrix
EDC	N’-ethyl-N-(3-dimethylaminopropyl)-carbodiimide
EDTA	Ethylenediaminetetraacetic acid
ESI	Electrospray ionization
FA	Fusidic acid
GAS	Gas antisolvent process
GelMA	Gelatin methacryloyl
HPLC	High Performance Liquid Chromatography
LB	Lysogeny broth
LC/MS	Liquid chromatography–mass spectrometry
M_n	Number average molecular weight

MRM	Multiple reaction monitoring
MRSA	Methicillin-resistant Staphylococcus aureus
MSC	Mesenchymal stem cells
MTS	[3-(4,5-dimethylthiazol-2-yl)-5-(3-carboxymethoxyphenyl)-2-(4-sulfophenyl)-2H-tetrazolium
M_w	Weight average molecular weight
PALS	Phase aligned light scattering
PBS	Phosphate buffered saline
PCA	Precipitation with a compressed antisolvent
PCL	Poly(caprolactone)
PDI	Poly Dispersity Index
PEG	Polyethylene glycol
PEO	Polyethylene oxide
PES	Polyethersulfone
PFA	Pore forming Agent
PFC	Perfluorocarbon
PFE	Pore forming emulsion
PFnP	Perfluoro-n-pentane
PGX	Pressurized Gas eXpanded
PLA	Poly (lactic acid)
PLGA	poly D,L-lactic-co-glycolic acid
PNIPAM	Poly(N-isopropylacrylamide)
POEGMA	Poly(oligo ethylene glycol methacrylate)
POEGMA-Ald	Aldehyde functionalized POEGMA
POEGMA-Hzd	Hydrazide functionalized POEGMA
RESS	Rapid expansion of supercritical solution
SAP	Self-assembled Nanoparticles
SAS	Supercritical antisolvent process
sc-CO_2	Supercritical Carbon Dioxide
SEDS	Solution enhanced dispersion by supercritical fluids
SWF	Simulated Wound Fluid
TGA	Thioglycolic acid
THF	Tetrahydrofuran
Tris	Tris(hydroxymethyl)aminomethane

Declaration of Academic Achievement

The majority of the work presented in this thesis was designed, executed, analyzed and interpreted by the author, in consultation with Dr. Todd Hoare with the exception of the following:

Chapter 2: Pressurized Gas eXpanded Liquids (PGX) processing and supercritical adsorptive precipitation was led on site by the Ceapro Inc. research and development team at their facility in Edmonton, Alberta.. Helium ion microscopy was performed by Ricardo Couto and nitrogen adsorption and Brunauer–Emmett–Teller analysis was performed by Emily Wong. All antimicrobial evaluations including *in vitro* and *in vivo* experiments were performed by Jody Mohammed. Liquid chromatography mass spectrometry analyses to determine drug concentrations were performed by the technical staff at the Centre for Microbial Chemical Biology.

Chapter 3: PLA-POEGMA brush co-polymer was synthesized and characterized by Ridhdhi Dave. Jody Mohammed performed flash nanoprecipitation to produce self-assembled nanoparticles and performed all antimicrobial assays including in vitro and in vivo experiments. Liquid chromatography mass spectrometry analyses to determine drug concentrations and drug loading was performed by the technical staff at the Centre for Microbial Chemical Biology.

Chapter 4: João Pedro Bronze de Firmino assisted with developing the ImageJ macro for Live/Dead image analysis. Seamus Adams assisted with in vitro mammalian cell culture and performed temperature response experiments. Andrew Lofts and Meghan

Kostashuk assisted with in vivo subcutaneous injections. Amanda Hopp and Michael Lowlar consulted with regards to pathology and level of inflammatory response.

Chapter 5: Evelyn Cudmore and Alexander Caschera assisted with bacterial adhesion experiments. Mya Sharma performed contact angle measurements. Rodrigue Caron performed mechanical studies at the Biomomentum Inc., Laval, Quebec.

Chapter 1- Introduction

1.1. Hydrogels

Hydrogels are three dimensional, water insoluble networks of polymer chains capable of retaining large amounts of water [1]. The capacity of hydrogels to retain water, coupled with their highly tunable nature, has made them popular in an array of applications including biomedical engineering [2], and environmental applications such as heavy-metal adsorption [3], water treatment [4], and water desalination. Innovative fabrication processes have made hydrogels suitable for an array of therapeutic and healthcare applications such as wound care [5], targeted drug delivery [6], tissue engineering and regenerative medicine [7], materials to regulate biological adhesion [8], ophthalmic and ocular therapies [9, 10], medical devices [11], and personal care products [12]. More specifically, in wound care, the capacity of hydrogels to bind water can help manage exudate effectively, accelerate wound healing, and provide a physical barrier against debris and bacteria [13]. In tissue engineering, hydrogels can mimic extracellular matrices (ECMs) that can control tissue structure, signal cell function, and regulate diffusion of chemicals such as nutrients, growth factors, oxygen, and waste in and out of the tissue [14].

1.1.1. Porosity in hydrogels

Among the multiple properties of hydrogels, controlling the porosity of a hydrogel is typically key to the success of a hydrogel in biomedical applications. Porosity in hydrogels can be defined on two different length scales: (1) inherent porosity, sometimes referred to as mesh size [15], which is present in all hydrogels, typically has dimensions on the nanoscale, and can be controlled by the molecular weight of the polymer chains between the physical or chemical crosslinks comprising the hydrogel (i.e. the crosslinking density [15, 16]); and (2) macroporosity, which is typically on the microscale and may or may not exist depending on the fabrication/manufacturing processing involved in making the hydrogel.

1.1.2. Mesh size

Mesh size is the key parameters that controls diffusion through bulk hydrogels and is critical in the design of hydrogels for biomedical applications since their utility critically depends on the diffusion of solutes (bioactive compounds, waste, oxygen, etc.) in and out of the gel phase [17]. In general, the diffusion rate is positively correlated with the mesh size and negatively correlated with hydrogel-solute interactions, with the hydrodynamic radius and the stiffness of the molecule diffusing through the gel also critical to determining local diffusability [16, 18, 19]. Hydrogels with limited diffusion of locally secreted molecules (signalling molecules or growth factors) can promote local accumulation of such factors; in contrast, when diffusion rates are higher, these molecules spread over larger volumes around the secreting cell [19] (Figure 1-1).

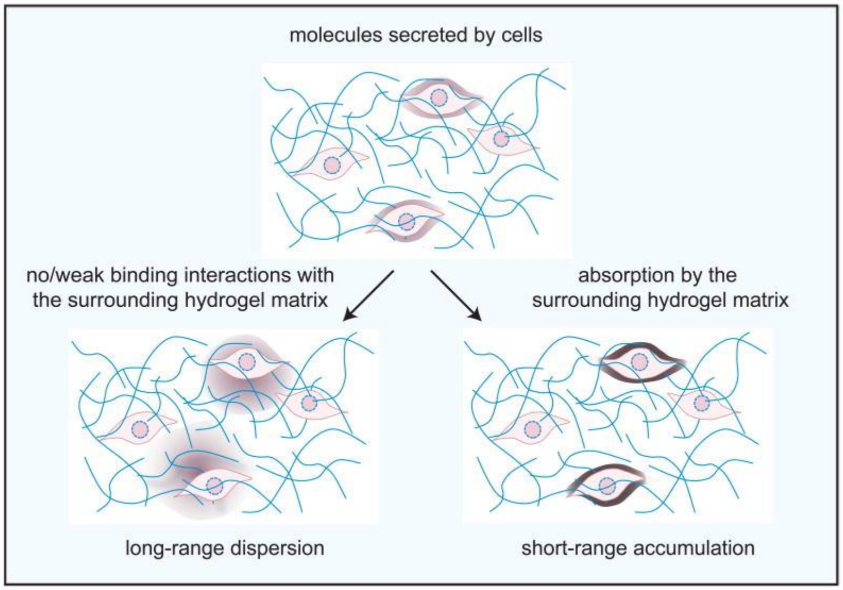

Figure 1-1- Impact of solute-hydrogel interactions and mesh size in regulating local diffusion rates in hydrogels. Reproduced with permission from Elsevier [19].

1.1.3. Macroporosity

Since the typically nanoscale mesh size is often insufficient to sustain cell proliferation [20] or nutrient/waste transport within larger hydrogel scaffolds [21], hydrogels designed for tissue engineering applications benefit from having larger pores to accommodate cell proliferation [22] and/or reduce the effective diffusion path (i.e. tortuosity) for nutrient/waste diffusion to improve cell viability [22, 23]. The diversity of polymers available, coupled with the diversity of processing methods available to fabricate those polymers into scaffolds with different internal and external dimensions and porosities [2], enables the customization of a specific scaffold for a desired application. More specifically, both the cell line to be delivered by/recruited into the scaffold as well as the chemistry, architecture, and geometry of the scaffold itself must be considered to ensure that the scaffold is providing the optimal physical, mechanical, chemical, and/or biological cues for regenerating the targeted tissue type(s) [24]. However, given the correlations between many of the key properties of a polymeric scaffold (i.e. mechanics and porosity), the rational design of a specific scaffold for a particular application can be challenging. For example, a number of studies have explored how the local mechanics of the scaffold can impact cell responses such as attachment, type and the extent of ECM production, differentiation, migration, and proliferation [25, 26]; however, other studies have suggested that cell motility is instead more strongly correlated to subtle changes in the pore size, porosity, pore connectivity, and/or strut flexural rigidity (which takes into account subtle changes in the length and thickness of the materials connecting the pores) of the scaffold architecture, all of which are directly or indirectly correlated with the scaffold mechanics [25]. Similarly, it is well understood that different cell lines interact differently with the surrounding structures depending on the geometry and size of the pores in the scaffold [24]. The pore size distribution can also play a critical role in the cell response to macroporous hydrogel scaffolds, with non-uniform pore sizes potentially leading to localized mechanical stress concentration as a result of inhomogeneous mechanical properties as well as non-uniform tissue regeneration related to differential diffusion in different parts of the scaffold [27]. As such, to efficiently regenerate tissues through the rational design of tissue scaffolds, it is critical to comprehensively understand and decouple the effects of scaffold microarchitecture and the macroscopic properties of tissue scaffolds.

1.2. Techniques to Generate Macroporosity in Hydrogels

A variety of different techniques has been used to create macroporous hydrogel scaffolds. In the following section, some of the most used techniques, factors which could influence scaffold microarchitecture, as well as benefits and limitations of each technique are discussed.

1.2.1. Gas-in-liquid foam templating

Gas-in-liquid foam templating involves creating porous foams by blowing gas into the structure to create gas bubbles. Inert gases like carbon dioxide and nitrogen are most commonly used in this technique. In some cases, dissolution of the gas into the matrix followed by rapid depressurization is instead used, with the rapid depressurization reducing the solubility of the foaming gas and leading to formation of bubbles that leave behind pores [28]. Processing parameters can significantly influence the architecture of the resulting scaffolds if the solubility of some templating gases (such as carbon dioxide) in the polymer matrix is significantly impacted by pressure and temperature. Decreasing the saturation pressure typically leads to pore size increases and overall porosity decreases based on the reduced solubility of the gas [29]; conversely, by increasing foaming pressure, porosity increases and pore size decreases [29]. The rate of depressurization is essential to controlling the resulting structure, as too-rapid depressurization can lead to a non-uniform structure.

The viscosity of the polymer solution, and by extension the degree of crosslinking (which increases the solution viscosity), can also have drastic implications on the pore architecture achieved using gas-in-liquid foaming [30]. For example, Ji et al. observed a significant decrease in porosity (from 60% to 33%) when two different crosslinkers (genipin and glutaraldehyde) were used to prepare macroporous chitosan hydrogels, with the differences in porosity attributed to different crosslinking rates (and thus precursor viscosities) resulting from the different genipin and glutaraldehyde crosslink densities [28]. The crosslinking kinetics (i.e. the rate of viscosity increase of the crosslinking reaction) are also essential to consider, although the effects on pore generation are more challenging to generalize as the resulting morphology is a function of both the phase separation/pore generation kinetics as well as the crosslinking kinetics. For instance, Ji et al. demonstrated that when glutaraldehyde (fast kinetics) was used, both the average pore size and the percentage of macropores (pores larger than 50 µm in diameter) were significantly smaller than when genipin (slower kinetics) was used as the crosslinker to form chitosan-based macroporous hydrogels [28]. In a separate study, Ji et al. studied the importance of crosslinking kinetics and depressurization time and rate on pore size and porosity in glutaraldehyde-crosslinked chitosan scaffolds. By timing the depressurization to match the gelation time, glutaraldehyde-crosslinked chitosan scaffolds with 59% porosity could be fabricated, representing an almost two-fold increase in porosity compared to previous studies [28, 31].

A key benefit of the gas-in-liquid foam templating technique is that it is highly adaptable to different materials and can be implemented without introducing any organic solvents that might induce cytotoxicity. On the other hand, using surfactants or foam stabilizers is common in this technique and, if not removed properly, may result in cytotoxicity. Controlling pore distribution and connectivity is also a challenge with this approach. Uneven pore structures may be formed due to the accumulation of gas at the top of the sample, although for samples with targeted gradient porosities this may be an advantage in some circumstances [32]. Pore interconnectivity is also not inherently achieved with this technique, although increasing the gas content does increase the probability of interconnectivity. Vacuum-assisted treatments, heat treatments, or freeze drying post-treatments have been explored to improve the interconnectivity of the pores generated [33]. It is also common to observe a non-porous skin layer on the surface of scaffolds produced using this technique, a layer that can simply be removed or be cut off prior to use as a scaffold to improve nutrient/oxygen transfer and/or cell infiltration [34].

1.2.2. Gas foaming using effervescent salts

The incorporation of other solid/liquid components into the precursor gel solution that can generate gas (most commonly H_2 or CO_2) as a result of thermal dissociation or by exposing the pore generating component to acidic conditions can also lead to macroporous hydrogels using a gas foaming approach. In this technique, the degree of porosity is mainly a function of the effervescent salt content and processing conditions used. Increasing the amount of effervescent salt is a reliable solution to increasing porosity [35], as with conventional gas foaming. However, the advantage of the effervescent salt approach is that different average pore sizes may be created by controlling the pore generating compound particle size. For example, Fernández-Colino et al. demonstrated the fabrication of elastin-like hydrogels with three different pore sizes ranging between 24.3 and 58.6 µm using sieved $NaHCO_3$ fractions with different particle sizes [36]. Porosity may also be controlled by controlling the rate of dissolution/degradation of the effervescent salt additive by modifying the processing parameters such as pH (for effervescent salts activated in acidic conditions) and temperature (for effervescent salts are activated by heat); for example, Yoon and Park reported the fabrication of PLGA-based porous scaffold with porosities ranging between 86-96% by modifying the concentration of citric acid to generate pores from ammonium carbonate salt particles [37] while Lim et al. reported similar results with poly(caprolactone) based scaffolds [35]. There are also reports of porous polyethylene glycol-lysine dendrimer hydrogels in which the macroporosity is generated by reacting potassium carbonate with acetic acid, resulting in CO_2 release and pore formation that is stabilized via the inclusion of Pluronic F-68 surfactant [38].

Gas foaming using effervescent salts, as with gas-in-liquid foaming techniques, provides less control over pore size distribution and often leads to structures with a broad pore size distribution. Although pore sizes under 100 μm have been reported [36], pore sizes ranging between a few hundred μm to 1000 μm in the same scaffold are more commonly reported for this technique [39, 40]. An additional downside of the effervescent salt technique is the potential for residual salts inside the scaffold after the foaming process is complete, particularly inside pores that did not interconnect such that washing steps are unlikely to fully remove the residue. Such residues may cause local osmotic gradients and/or inherent cytotoxicity (depending on the salt used) that can impact cell viability.

1.2.3. Technologies based on supercritical fluids

Supercritical carbon dioxide (sc-CO_2) based technologies for fabricating aerogel-based scaffolds typically involve using a supercritical fluid (sc-CO_2, in some cases combined with organic solvents such as ethanol, methanol, isopropanol or acetone [41]) and subsequent phase separation induced through the introduction of an antisolvent or rapid depressurization [42]. Several supercritical fluids-based techniques have been developed for creating macroporous aerogel materials. In the rapid expansion of supercritical solutions (RESS) and gas antisolvent process (GAS) approaches, an aqueous or organic polymer solution respectively is mixed with supercritical fluid or gas phase to induce phase separation. RESS can be used in cases in which the polymer solution has some level of solubility in the supercritical fluid, while GAS is suitable for polymer solutions that are not soluble in the supercritical fluid. In the supercritical antisolvent process (SAS), also known as aerosol antisolvent extraction system (ASES) or precipitation with a compressed antisolvent (PCA), the polymer solution is sprayed in a chamber which already contains the antisolvent (supercritical fluid). These techniques offer a unique advantage over GAS and RESS in that it allows for continuous operations; however, SAS has not been implemented on a commercial scale due to challenges with operating whole systems at supercritical conditions and is still in its early stages in the pharmaceutical industry [43]. Solution-enhanced dispersion by supercritical fluids (SEDS) is a modified version of SAS that involves simultaneous spraying of the liquid polymer solution and the supercritical fluid; as the polymer solution makes contact with the supercritical fluid at high speed, the polymer solution is dispersed in the supercritical fluid which induces particle precipitation. Although SEDS offers flexibility of using aqueous or organic polymer solutions, there are still challenges associated with limited production scale and easy nozzle blockage, which if it occurs can pose significant costs as well as health and safety risks [44].

In contrast to these other techniques, the Pressurized Gas eXpanded liquids (PGX) technology is unique in that the supercritical fluid is modified with ethanol to increase water solubility in the supercritical fluid [45-47]. This process involves co-injecting an aqueous solution (or suspension) and the PGX fluid (consisting of sc-CO_2 and ethanol) into a pressurized chamber filled with PGX fluid, resulting in the fabrication of either high surface area particles or interconnected fibrous structures depending on the type of polymer processed and the processing conditions used. By avoiding the generation of liquid-vapor interfaces and capillary forces, the PGX process promotes supercritical fluid drying and thus the fabrication of highly porous aerogels that can be formed into hydrogels upon rehydration [48, 49]. While PGX products have been used in numerous applications including tissue engineering [50] and drug delivery [48], supercritical-dried aerogels are particularly attractive in wound healing applications given that the exudate allows for rehydration of the aerogel, providing a solution to exudate management while also facilitating the dressing removal process with minimal trauma to the sensitive wound bed [50]. The PGX process is also highly suitable for scale-up under good manufacturing practices [41, 48] and can enable simultaneous purification and extraction of hydrophobic contaminants from the material [45]. Although acquiring and maintaining high pressure equipment can increase processing costs, the large amounts of ethanol and CO_2 required for this technique can be collected and recycled on an industrial scale, mitigating both the economic costs and environmental impacts of the technology. Avoiding nozzle clogging, which poses significant safety concerns due to the pressures at which the system is operated, is also critical. The risks can be mitigated by using lower viscosity polymer solutions and homogenization of the polymer solution, in addition to using electronic control systems, automated shut-down systems, and appropriate safety valves in place in addition to having trained and informed operators on-site.

Given that PGX technology relies on rapid drying of the aqueous polymer jet using the supercritical fluid, the supercritical flow rate ratio (θ_{PGX}, defined in equation (1-1)) typically plays a critical role in determining the properties of the PGX processed materials [45]; for example, PGX processing gum arabic at higher θ_{PGX} resulted in significantly smaller and more spherical particles, increased specific surface area, and lower bulk density [46]. However, work on PGX processing of sodium alginate has shown that neither θ_{PGX} nor the ethanol flow rate have a significant impact on the macroporous structure as visualized using helium ion microscopy [45]. Therefore, while general trends in controlling product properties do exist, translating suitable processing parameters to different polymers should be done with caution. Equation (1-1) depicts a ternary phase diagram of water, ethanol, and CO_2 at 100 bar and 40°C, with the typical θ_{PGX} values of 4, 5, and 8 highlighted on the diagram to identify the typical PGX operating window.

$$\boldsymbol{\theta_{PGX}} = \frac{\textbf{Flow rate of (ethanol + carbon dioxide)}}{\textbf{Flow rate of aqueous solution}} \tag{1-1}$$

The aqueous solution viscosity can also significantly impact the surface area and pore structure of the resulting aerogel. At lower viscosities the PGX liquid and the aqueous solution can undergo more efficient mixing, resulting in the production of a higher surface area structure. It is worth mentioning that there is a minimum polymer concentration (reported as 0.5 wt% for sodium alginate) below which the PGX liquid cannot effectively remove all the water present in the aqueous solution [45], placing a practical restriction on the void volume of the resulting aerogel.

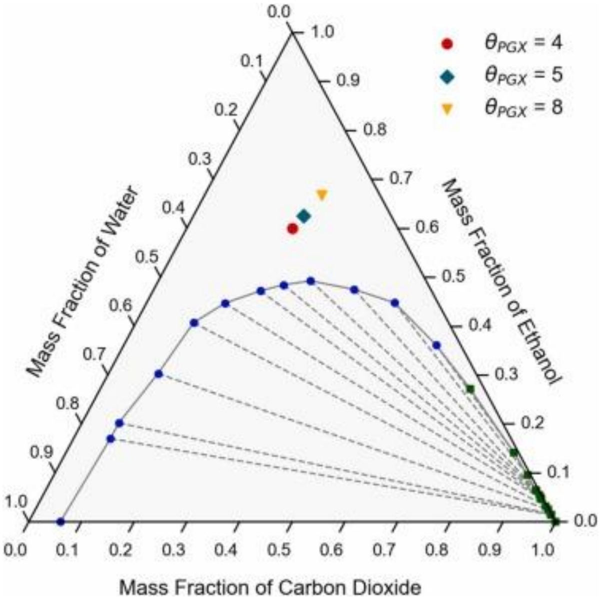

Figure 1-2- Ternary diagram of water, ethanol, and CO_2 at 100 bar and 40 °C. Reproduced with permission from Elsevier [45].

1.2.4. 3D printing

3D printing techniques can be used to create porous 3D constructs by printing hydrogels into filaments and subsequently assembling them layer-by-layer in a defined geometry. Macroporosity of 3D printed hydrogels is typically determined by the infill density and the infill pattern. The infill density refers to the “fullness” of a 3D printed construct; a 100% infill describes a bulk solid structure (in the case of a hydrogel, a material with only inherent porosity) while a 0% infill describes a structure printed with a hollow core (Figure 1-3-a). The infill pattern refers to the type of geometric patterns printed as the infill. Grid, triangular, and honeycomb structures are some of the more popular infill patterns commonly used in 3D printing (Figure 1-3-b), each of which enables the fabrication of specific pore shapes, transport pathways, and pore interconnections otherwise challenging to incorporate using many other macroporosity fabrication techniques. However, it should be noted that the softness and swelling capacity of hydrogels can result in the infill densities (and, to a lesser extent, infill geometries) after printing substantially deviating from the designed slicing infill density [51], posing a potential challenge in the design of highly controlled internal macroporosity in such printed structures.

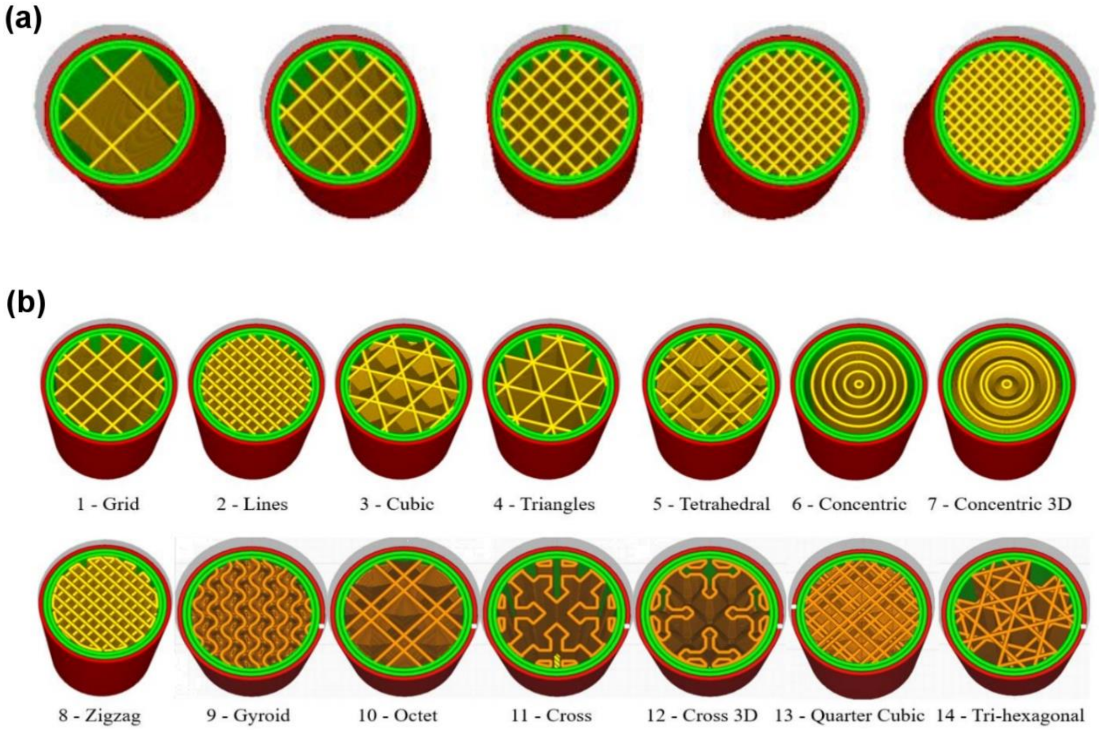

Figure 1-3- Schematic showing control over the internal macroporosity of a 3D printed construct by (a) changing the infill density (fixed grid pattern) or (b) changing the grid pattern. Reproduced with permission from Elsevier [52].

Relative to other methods for macropore generation, 3D printing enables the fabrication of porous hydrogel scaffolds with pre-designed and exceptionally well-controlled internal pore shapes and sizes [53]. An added benefit of using 3D printing in tissue engineering is the ability to fabricate co-cultures of two or more types of cells (e.g. fibroblasts and hepatocytes [54], keratinocytes and fibroblasts [55], bone marrow-derived mesenchymal stem cells and human umbilical artery smooth muscle cells [56]), which can be challenging to introduce using other fabrication strategies.

Hydrogel 3D printing can be achieved using different strategies including extrusion bioprinting [57], microfluidic bioprinting [20], embedded bioprinting [58], laser-assisted bioprinting [59], stereolithography bioprinting [60], and digital light processing bioprinting [61] each or which have their specific advantages and challenges [62]. For example a major challenge in extrusion bioprinting is the potential loss of cell viability during dispensing or printing when cells are exposed to mechanical shear stress when passing through the printing nozzle [63]. Furthermore, the low resolution of extrusion bioprinting (on the tens to hundreds of micron length scale) can affect regulation of cell responses which is predominantly regulated by nanoscale features [62, 64]. Microfluidics bioprinting uniquely allows for switching between materials [65] but requires expensive and specialized equipment to produce the microfluidic chips used as print heads and is therefore considered one of the more expensive 3D printing strategies [62]. Stereolithography bioprinting and digital light processing bioprinting mitigate resolution challenges by reducing the special resolutions and can produce large constructs quickly [66], with stereolithography bioprinting also useful for creating complex resolutions such as structures with a hollow core or perfusable structures [67]. This technique, however, can only be used with limited hydrogel types that are compatible with photopolymerization [62]; furthermore, the photoabsorbers and photoinitiators required to initiate the polymerization need to be chosen with care to avoid toxicity [68].

1.2.5. Electrospinning

Electrospun mats and tissue patches have been widely studied in a variety of applications such as wound dressings, skin grafts, vascular grafts, cardiac tissue patches, and others. Electrospinning involves producing fibres from a solution (or in some cases suspension) by pulling a charged droplet of electrospinning medium in an electric field while the medium is being injected through a capillary needle. The produced fibres are usually collected on an electrically conductive and grounded collector (Figure 1-4). The key advantage of electrospinning is the potential to access nanoscale dimensions, enabling better biomimicry of the native nanofibrous structure of native ECM. However, the technique is also limited by the challenges inherent in implementing hydrogel crosslinking in the context of the fabrication process (particularly if cells are co-electrospun with the scaffold precursor components) and the scaling challenges of fabricating large area/thickness electrospun mats given the low volume throughputs of the technique. Many modifications have been made to circumvent these limitations, as extensively reviewed by Xue et al. [69]; however, the incorporation of viable cells at scale remains a challenge.

Hydrogel electrospinning requires meticulous optimization of the electrospinning parameters around the crosslinking chemistry and gelation kinetics since crosslinking and gelation can significantly alter viscosity of the electrospinning solution and thus the type of electrospun product generated. When parameters are optimized, the electrospinning solution can still flow through the dispensing needle while also being viscous enough to generate a stable jet and maintain fiber morphology until it is collected on the grounded collector [70, 71]. High molecular weight polymers like polyethylene oxide are often used in this context to assist in fiber formation and stabilization [72, 73]. Alternately, to avoid the need to optimize processing times with gelation kinetics, post-crosslinking the nanofibrous scaffolds can be conducted by chemical crosslinking [74], ionic crosslinking [75], and/or photo crosslinking [76, 77]. However, immersing electrospun scaffolds in crosslinking solutions can lead to loss of fiber structure unless solvents in which the fibers are insoluble are used [75], a choice that can restrict the maximum crosslink density of the scaffold; photocrosslinking is limited to photocurable materials [78] and requires the use of photoinitiators that may induce cell toxicity [79].

The dual nature of the geometry of an electrospun scaffold (i.e. the dimensions of the fiber itself and the packing geometry/direction between the fibers) offers significant control over the pore size/structure of and thus cell responses to an electrospun scaffold. Cells can interact with pores in two ways based on the relative size of fibers and the cell line in question. For instance Rnjak-Kovacina et al. showed that human dermal fibroblasts wrap around individual fibers when the average fiber diameter is 6.5 µm and bridge between fibers when the average fiber diameter was >20 µm, suggesting that there is a critical pore size at which cells start changing their adhesion mode [80]. The fiber diameter can be increased by increasing flow rate, reducing voltage, and/or increasing the concentration of the electrospinning media [81], although a defined range of each of these variables specific to a given polymer limits the range of accessible fiber dimensions without compromising fiber quality. Porosity and pore size may be tuned indirectly through modifying processing parameters which influence fiber diameter (i.e. flow rate [82]) or the use of sacrificial fibers or particles that are electrospun in alternating layers or co-electrospun and removed during post processing [83].

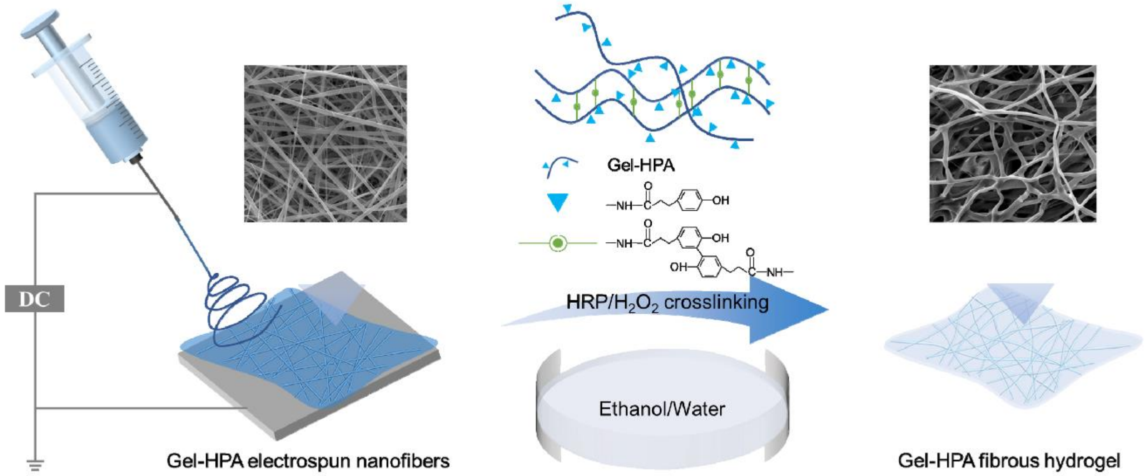

Figure 1-4- Schematic showing preparation of gelatin-hydroxyphenylpropionic acid (Gel-HPA) electrospun fibrous hydrogel scaffolds. Reproduced with permission from MDPI [84].

Electrospinning may also be combined with other techniques such as salt leaching [85], gas foaming [86], and emulsion templating [87] to form pores on different length scales and increase the overall porosity of the scaffold, techniques that are summarized in a recent review by Rnjak-Kovacina and Weiss [88]. Fiber alignment in a particular direction is also possible using specially designed collectors such as rotating drums, disks, cylindrically aligned wires, or the incorporation of a non-conductive gap in the collection drum [89-91]; magnetic fibers can also be directed using external magnetic fields to influence fiber morphology and enhance fiber alignment [92, 93]. Fiber alignment in tissue engineering scaffolds can significantly impact scaffold performance, cell proliferation, cell elongation, and cell viability, with particular benefits for mimicking tissues that are inherently anisotropic (e.g. muscle or nerve fibers) [94]. However, any alignment technique typically produces small scaffolds (~3 cm in width to reach maximum of 20% alignment), limiting the scale of the application of this particular approach for aligned fiber production [95].

While electrospun hydrogel scaffolds have been shown to effectively support cell viability and proliferation, they often lack in the mechanical strength required for some target applications such as vascular tissue grafts [96], and musculoskeletal tissue grafts (tendons and ligaments) [97]. The incorporation of hydrogel phases within stronger existing scaffolds based on poly(caprolactone), polyvinyl alcohol, or PLGA is highly attractive in this context. However, such reports rarely demonstrate both improved biological responses and suitable mechanical strength simultaneously [98]. Several approaches have been reported to address this challenge, including the use of nanofillers, blend electrospinning, and co-electrospinning. Nanoparticles can be effective for mechanical enhancement but (depending on their composition) can be associated with off-target side effects, posing potential safety concerns. Nanoparticles also have a high tendency to interact with plasma proteins [99] and often require complex multi-step surface modifications [100] to enable sufficient dispersion [101, 102] to ensure sufficient improvement in mechanical properties [103]. Blend electrospinning (electrospinning a blend of polymers) is restricted by phase separation upon drying, often leading to only a slight improvement in mechanical properties [98]. Co-electrospinning two or more streams of electrospun fibers can improve mechanical properties [104] but requires access to additional resources and equipment which can be expensive.

1.2.6. Emulsion templating and PolyHIPEs

Emulsion templating is a well-studied technique for forming porous scaffolds in diverse fields including not only tissue engineering but also gas adsorption and separation, as summarized well in a review by Claeyssens [105]. One of the biggest advantages of this technique is the ease to which porosity may be tuned simply by changing the volume ratio of the organic phase to aqueous phase and the nature of the interface between the two phases, typically through the introduction of one or more surfactant [106]. For biomedical applications, this surfactant use as well as the need to use an organic phase is often unfavorable for cell viability; however the use of a removable (e.g. volatile) organic phase and/or block copolymers or reactive block copolymers as surfactants [107, 108] has been shown to improve the cytocompatibility of the resulting scaffold.

Scaffolds based on polyHIPEs, freestanding structures made based on the emulsion templating technique of HIPEs (high internal phase emulsions), have attracted particular interest given that very high porosities ranging between 74-99% can be achieved [109]. While emulsion templating does not necessarily lead to an interconnected pore structure, maintaining such high porosities typically leads to good interconnection which is desirable for tissue engineering applications [110]. Despite the challenges associated with removing surfactants, surfactant-stabilized polyHIPEs are typically more favourable for tissue engineering applications [111] given that they usually have higher interconnectivity compared to particle stabilized polyHIPEs (i.e. Pickering polyHIPEs); pores with sizes in the 1-20 μm (or larger) size range with interconnected pore throats (diameter of connections between adjacent pores) ranging between 20-50% of pore diameter have been reported with surfactant-stabilized polyHIPEs [112] while Pickering polyHIPEs stabilized with particles such as functionalized carbon nanotubes or graphene oxide yield more closed pore sizes ranging between 200-700 µm [112]. Surfactants typically used to stabilize HIPEs include Tween-80, Span-80 and polyglycerol polyricinoleate (PGPR), with typically a large amount of surfactant (20-30% and in some cases up to 50% of the continuous phase) being required to stabilize the emulsion. [113]. Increasing surfactant concentration leads to a smaller average pore size and a narrower pore size distribution [114]. The addition of a small amount of surfactant in addition to the Pickering stabilizer can significantly improve interconnection, with laser scanning confocal microscopy indicating that the added surfactant can promote movement of the particles away from the contact point of adjacent droplets and open windows between pores after polymerization (Figure 1-5) [115]. Alternatively, amphiphilic block co-polymers such as gelatin-graft-poly(N-isopropylacrylamide) [107, 116], poly(4-vinylpyridine)-block-poly(ethylene glycol)-block-poly(4-vinylpyridine), Pluronic F-127 (poly(ethylene oxide-block-poly(propylene oxide)-block-poly(ethylene oxide) [108] can be used to stabilize HIPEs. The type of surfactant and combination of surfactants can impact pore size and pore interconnectivity, with two or three surfactant systems having been shown to improve the stability of HIPEs leading to smaller and more uniform droplets and therefore pores. [117].

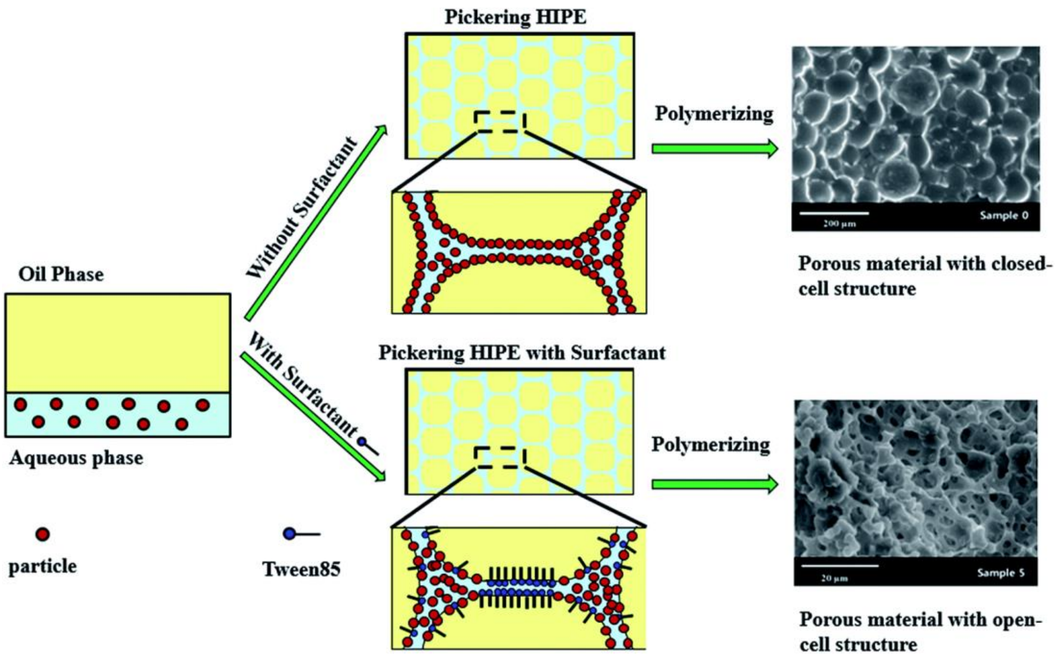

Figure 1-5- Schematic depicting how the interconnectivity of pores can be impacted by addition of surfactants in scaffolds produced through polyHIPE technology. Reproduced with permission from the Royal Society of Chemistry [115].

Porosity can be increased in polyHIPE hydrogel systems by simply increasing the volume ratio of the organic phase, although the volume percentage of the organic to aqueous phases does not necessarily predict the final porosity as the polymer phase may shrink during the crosslinking/polymerization process used for gel formation and/or expand under physiological conditions [113]. Changing the volume ratio of the organic and aqueous phases can also impact the interconnectivity of the resulting polyHIPE; for example, in an 2-ethylhexylacrylate system stabilized by isobornyl acrylate-trimethylolpropane triacrylate particles, increasing the volume ratio of the organic phase from 75% to 85% results in open cell (interconnected) structures [106].

Interconnections or pore windows (sometimes called pore throats) can form after thinned regions of the pore wall are ruptured (often during post processing) or as a result of partial but arrested coalescence of organic phase droplets [106]. Multiple synthetic strategies can be applied to control pore interconnectivity. For example, Robinson et al. investigated the fabrication of polyHIPE scaffolds based on propylene fumarate dimethacrylate (PFDMA) macromers in which the internal phase (droplets) consists of an aqueous phase and the external phase (continuous) consists of an organic phase. The type of polymerization initiator used (water soluble vs. non-water soluble), and therefore the locus of polymerization initiation, was observed to have a significant impact on the interconnectivity of the pores, with the use of a monomer soluble in the continuous phase being more likely to promote interconnected pore structures while the use of an initiator soluble in the internal phase the polymerization of the polyHIPE mainly resulting in closed pores (Figure 1-6) [118, 119]. Similar observations were also made by Gurevitch et al. for the fabrication of Pickering HIPEs based on polyacrylate [120].

The intensity or technique of mixing (e.g. overhead mixing versus vortex mixing versus magnetic stirring versus homogenization/sonication), the batch size, the temperature, and/or the duration/power of the mixing process can all significantly impact droplet size and subsequently the scaffold pore size, offering the potential for high tunability but also potential challenges with the reproducibility and scalability [121, 122].

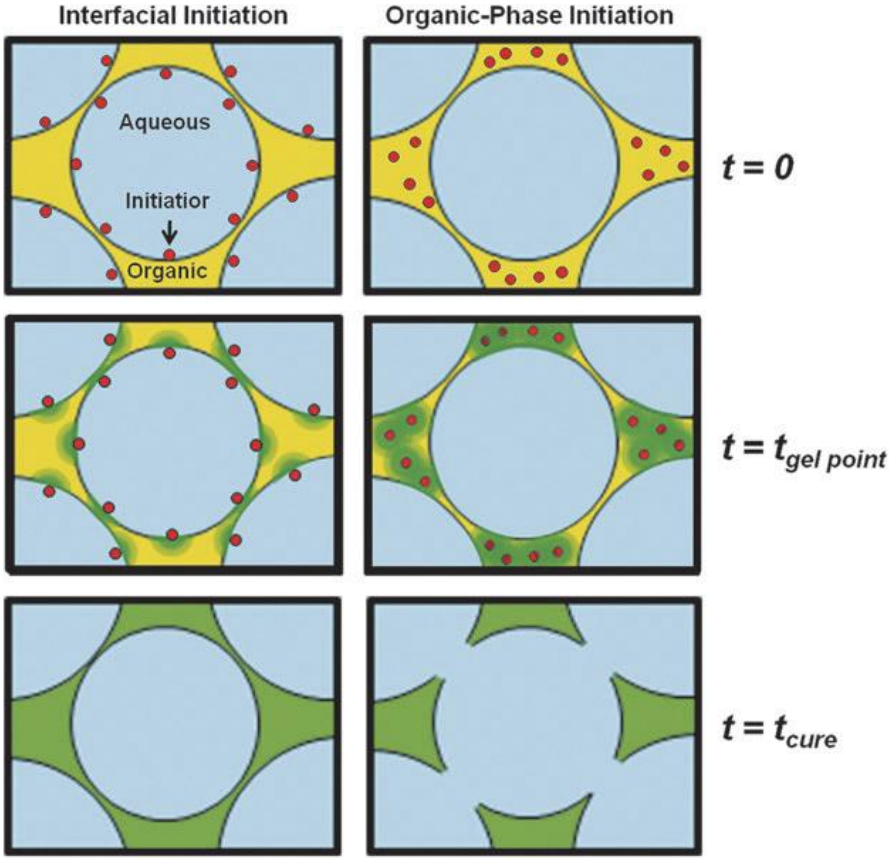

Figure 1-6- Schematic depicting how the choice of initiator (water soluble vs. water insoluble) can impact pore interconnectivity in polyHIPE fabrication. Reproduced with permission from Mary Ann Liebert [123].

Aqueous two-phase systems (ATPSs), which are formed by phase separation of an aqueous mixture containing two incompatible polymers at high concentration into two phases, are also attractive for biomedical applications since they avoid the need for organic solvents [124]. In ATPSs, phase separation is driven by differences in the hydrophobicity of the two solutes, with larger differences in hydrophobicity between the two ATPS-forming polymers being linked to a higher tendency for phase separation. For example, in a polyethylene glycol-dextran ATPS, increasing the hydrophobicity of the dextran component increases the difference between the hydrophobicity of the two components and thus increases the driving force for aqueous two-phase separation [125]. Many factors including the viscosity of the two phases, osmolarity, pH, or temperature can accelerate or trigger phase separation in ATPSs [126], with the equilibrium volume ratio of the two phases (and as a result the porosity of the hydrogel scaffold) determined by the phase diagram (Figure 1-7) associated with system. Many researchers have leveraged the kinetics of phase separation to produce macroporous hydrogels with designed pore architectures. Lui et al. successfully encapsulated human liver cancer cells (HepG2 and HeLa) cells in porous PEG-Alg (polyethylene glycol-alginate) beads by leveraging the aqueous two-phase separation of dextran-cell suspension and PEG-Alg followed by ionic crosslinking of the PEG-Alg phase using calcium. Cells encapsulated in the porous beads showed excellent viability, proliferation, and metabolic activity; furthermore, pore size can be controlled by changing the energy input associated with emulsification and/or the volume ratio of the PEG-Alg phase to the dextran phase [127]. Alternately, Ying et al. used a cell/gelatin methacryloyl (GelMA) mixture with poly(ethylene oxide) to form an APTS emulsion, with subsequent photocrosslinking of the GelMA phase used to produce porous cell-laden 3D-bioprinted hydrogels that were compatible with human hepatocellular carcinoma cells, human umbilical endothelial cells, and NIH/3T3 mouse fibroblasts [128]. While the potential to leverage the ease of emulsion fabrication while avoiding the use of organic solvents is an attractive feature of the APTS approach, predicting the volume fraction of each phase in ATPSs is generally challenging [129] and only limited polymer combinations can be used, significantly restricting the scope of accessible scaffold chemistries.

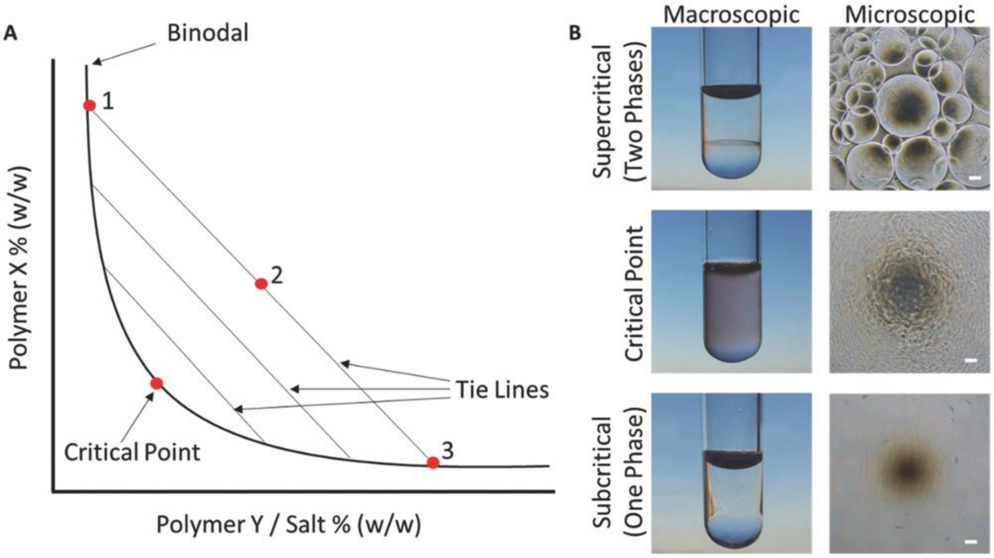

Figure 1-7- A mock binodal phase diagram on the left and corresponding images depicting phase separation expected in a dextran-polyethylene oxide APTS system; scale bar = 100 µm. Reproduced with permission from Wiley [124].

1.2.7. Salt leaching

Salt leaching, in which salt crystals are used as a sacrificial component that upon removal leave behind a porous polymeric structure, is one the most commonly used techniques for creating macroporous hydrogels [130]. The porosity of the resulting scaffold is directly correlated to the size and total volume of salt added, with most macroporous scaffolds prepared using 65-90 wt% salt to ensure pore interconnectivity and easy removal of salt after the gel has been templated [131, 132]. Porous scaffolds with a range of pore sizes may be created by templating against salt granules of different sizes [133], with salt crystal size control achievable by grinding or inducing precipitation in a supersaturated salt solution [130]. Particular pore size distributions may be achieved by passing the salt granules through multiple meshes to isolate particle size fractions to design the macroporous scaffold pore structure [134]. More recent work has particularly used salt leaching in the context of 3D printing to create macroporous 3D printed structures [135]. Alternately, to ensure interconnectivity, additional sacrificial components (such as polyethylene oxide) may be added to the polymer solution and removed in subsequent steps [132].

Salt leaching has the key advantages of being inexpensive and effective control of the overall porosity of the macroporous hydrogel [136]. However, uneven pore distributions coupled with often slow and/or ineffective porogen removal processes can lead to challenges with maintaining cell compatibility if cells are added prior to leaching [137]. Furthermore, although some degree of control can be exacted over the shape of the salt crystal used as the template, meticulous design of pore shape is challenging using this technique given the limited control possible over the shape of the templating salt crystals [138].

1.2.8. Inverse opal templating

Inverse opal scaffolds, like salt leaching, rely on the extraction of a template from a hydrogel matrix to leave behind macropores; however, in the inverse opal technique, the pore network is created by templating against a closed pack array of microspheres that are selectively degradable under a targeted condition [139]. Given the close-packed nature of the template, the resulting pore architecture can be directly determined by the dimension of the templating spheres in a way that is not possible using conventional salt leaching [140]. Templating spheres can be made of an array of materials, with poly(methyl methacrylate) (removed using tetrahydrofuran) [140], silica (removed using hydrofluoric acid) [141], alginate-calcium (removed using chelating agents) [142], and gelatin (removed through thermal treatment) [143] being most commonly used for hydrogel fabrication. Templating spheres may be commercially available or be created in-house through microfluidics techniques [144], atom transfer radical polymerization (ATRP) [145], emulsion polymerization [146] or other techniques that yield beads with a relatively uniform size. To improve interconnection, an annealing step is often used to fuses the spheres together to form an interconnected template, with the size of the opening between the pores or the window size controllable by the annealing conditions and durations used; in most cases, increasing the annealing time or temperature will result in a larger window size (the diameter of the openings between pores) [147]. However, due to the direct correlation between porosity and sphere packing, the accessible porosities using this technique are limited; for single-sized pores, porosity is approximately 74% irrespective of pore size [148], although higher porosities may be achieved if a broader size distribution of templating spheres is used [105].

The inverse opal technique can also be used to generate scaffolds with enhanced diffusion and interconnectivity [149], with the capacity of the inverse opal technique particularly enabling the generation of single pore size scaffolds that can yield improved fundamental insight into the effects of pore size distribution on biological responses such as proliferation, migration, and angiogenesis [150]. Anisotropic scaffolds could also be fabricated using the inverse opal templating technique by stretching the scaffold in a specific direction to create channels and promote cell alignment [151, 152]. Like with salt leaching, complete removal of the template can also be slow, require harsh conditions (e.g. hydrofluoric acid for silica removal), and/or be incomplete to leave template residue in the final hydrogel, with potential ramifications for both scaffold properties as well as cell viability over time.

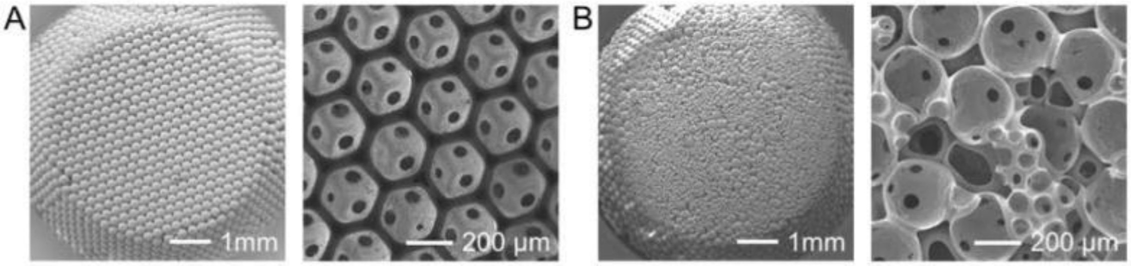

Figure 1-8- Scanning electron microscopy images showing (a) monodispersed gelatin beads and a PLGA inverse opal scaffolds with single-sized pores based on PLGA and (b) showing polydispersed gelatin beads and a PLGA based scaffold with non-uniform pore sizes. Reproduced with permission from Wiley [139].

1.2.9. Microgel assembly

Instead of assembling a sacrificial template to form a hydrogel around the template, macroporous hydrogels can also be prepared by directly assembling microgels into free-standing structures [153]. This technique could be considered parallel to the inverse opal technique in that both involve fusing, curing, and/or annealing microspheres into larger continuous structures; in this case, the microsphere is a microgel and the porous network is formed directly upon microgel assembly without the need for template removal. The microgels used for this technique can be prepared using an array of techniques such as microfluidics, emulsions, lithography, electrospraying, or the fragmentation of bulk hydrogels [154]. Each of these techniques offers unique design potential coupled with specific limitations. Microfluidics can create particles with an extremely narrow particle size distribution (<1-2%) but at relatively low yields [155]; alternatively, emulsion-based techniques can manufacture spherical microgels on a much larger production scale at the expense of much broader size distribution [156]. Tailored particle geometries (and thus customized packing densities) can be achieved using lithography-based techniques [157], but the lithographic technique requires advanced equipment. Mechanical fragmentation (typically achieved by forcing a bulk hydrogel through a mesh or fine screen [158]) rapidly creates irregular particles but with minimal control over particle size or geometry [159]. The ultimate choice of microgel building block should be made based on how precise the pore size/shape should be in the resulting macroporous hydrogel.

Microgel assembly could be achieved through covalent crosslinking (e.g. photo-initiated radical polymerization [160], click chemistry [161], enzymatic catalysis [162] etc.), physical interactions (host-guest interactions [163], electrostatic interactions [164], hydrogen bonding [165], etc.), cell-cell interactions (leveraging cell adhesion, migration, and proliferation between microgels [166]), or external driving forces (e.g. surface tension driven assembly [167], magnetic forces [168], acoustic vibrations [169], fluidic forces [170], etc.). Among the described methods, assembly of microgels using external driving forces requires a subsequent crosslinking step to obtain freestanding hydrogel structures.

Despite the obvious advantages of this method in terms of directly forming a macroporous hydrogel network without the need for templating or advanced processing, microgel-assembled hydrogels can be relatively weak due to limited crosslinking between microgels that may make such structures susceptible to failure (especially when exposed to shear stress) [171]. Additionally, manufacturing (particularly monodisperse) microgels can be challenging, replacing complexity in macroporous scaffold fabrication with complexity in the fabrication of the building blocks of the hydrogels [172].

1.2.10. Cryogenic techniques

Cryogenic-based techniques such as freeze-drying and cryogelation are also very common strategies for fabricating macroporous hydrogels [173]. Upon rapid freezing, an interpenetrating network of ice crystals is formed within the aqueous hydrogel scaffold, with subsequent sublimation of these crystals leaving behind a continuous network of pores. The shape of the ice crystals is determined by the kinetics of ice crystal nucleation and growth as well as heat transfer principles [174]. Due to the uncontrolled and often quenching freezing processes typically used in cryogelation techniques, scaffolds with non-uniform pore size and porosity are typically produced. By exploiting the inherent temperature gradients in such systems, it is common to observe directional ice crystal formation that can result in columnar ice crystal formation aligned in the same direction as the temperature gradient; relative to other techniques, this represents a facile method to template anisotropic tissue scaffolds for applications such as neural regeneration or guided angiogenesis [173, 174]. However, equiaxed ice crystals will form if a predominant direction of heat transfer is removed or mitigated [173]. For example Zhang et al. implemented different freezing rates in freeze dried scaffolds to create porous structures with different degrees of homogeneity, observing higher HUVEC cell count in scaffolds with narrower pore size distributions [175].

The pore size in scaffolds created using cryogenic techniques is primarily determined by the interplay between heat transfer and solidification kinetics. A larger undercooling (i.e. the difference between the actual temperature of the material and equilibrium freezing temperature) can lead to an increase in the nucleation rate and a decrease in the diffusion rate, resulting in the formation of smaller ice crystals and thus a scaffold with a smaller average pore size. For example, Hwang et al. observed closed or somewhat disconnected pores in cryogels prepared at -14°C while samples prepared at -20°C with a similar composition and cooling rate showed a continuous and interconnected pore structure [176]. The cooling rate can also influence scaffold structure, with scaffolds produced with constant cooling rates generating equiaxed pores (with uniformity optimized at a cooling rate of 0.9 °C/min) while scaffolds produced using the quenching technique with rapid cooling resulted in columnar pores [177]. Hwang et al. observed similar effects in cryogels in which samples prepared at fast cooling rates showed non-uniform pore structures compared to when slower cooling rates were utilized [176]. Alternately, the influence of the container used to form the cryogel can significantly alter heat transfer and thus the structure of the resulting macroporous hydrogel. For example, O'Brien et al. showed that using larger more compliant pans to form the hydrogels resulted in the formation of larger pores with a broader size distribution relative to when the samples were prepared using smaller less compliant pans, an effect attributed to different pan-shelf discontinuities resulting from different warping of the two pans. Dissolved salts can also impact pore size and porosity by reducing the amount of freezable water due to salt-water interactions, resulting in hydrogels with a smaller pore size and thicker walls [178].

Given that the gel phase forms in the unfrozen liquid phase in which the solutes are concentrated as ice crystals form [179], the pore architecture can also be modified by tuning the gelation kinetics relative to the nucleation and growth kinetics of the ice crystals [176, 180]. The amount of freezable water can be influenced by both the molecular weight and the chemistry of the precursor polymers. At the same freezing temperature, the amount of freezable water is higher in a system containing a lower molecular weight polymer precursor, resulting in higher porosity and larger ice crystals [181]. Higher concentrations of precursor polymers, a higher degree of functionalization in the precursor polymers, and/or increased concentrations of initiator and/or crosslinker can all accelerate the gelation kinetics, increasing the matrix viscosity and thus limiting the growth of the ice crystals to lead to smaller pores and thicker pore walls [176, 182, 183]. Since viscosity is inversely correlated with ice crystal growth and size, desired pore architectures could also be obtained by modifying the polymer precursor viscosity using thickening agents [184].

Manipulating the solubility of the polymer precursors during the cryogelation process can also alter pore size. For example, adding methanol or acetone (which are poor solvents for polyacrylamide gels) has been observed to lead to phase separation and the creation of pores smaller than 1 μm in the resulting cryogel in addition to the pores resulting from water crystallization which ranged between 10-80 μm in diameter [178]. Perez et al. prepared cryogels in water and a water-dioxane mixture using both a water soluble crosslinker (MBAAm) and a water insoluble crosslinker (d-DMTLT), with the sample prepared using MBAAm showing an open pore structure while the sample prepared with DMTLT showed a closed pore structure with thick pore walls [185].

The high sensitivity of the gel structure to the method used for cryogenic treatment represents both an opportunity to create diverse pore structures with similar materials but also a drawback in terms of the reproducibility challenges inherent in cryogenic fabrication strategies [177]. Another drawback of this technique is that freezing is not compatible with the direct inclusion of cells during the fabrication process, requiring post-loading for cell seeding.

1.2.11. Combination and special techniques

The techniques mentioned above can be combined to obtain porous 3D constructs to obtain multiple levels of porosity, for specific therapeutic goals, or to ensure pore interconnectivity. Given the relatively low resolution of most 3D printing techniques, 3D printing is most commonly used in combination with other pore generating technologies to obtain 3D printed structures with multiple levels of porosity: large pores between deposited strands of hydrogel, microporosity within the deposited strands, and the inherent porosity of the hydrogel (mesh size). For example, Sears et al. used a combination of emulsion templating and 3D printing and create 3D printed hydrogels with pores on three different length scales using an array of synthetic and natural polymers [186], Moazzam et al. reported the combination of 3D printing and cryogelation to create multi-scale porosity [187], while Armstrong et al. took advantage of thermally induced phase separation in alginate-Pluronic F127 mixtures in combination with 3D printing to form defined microporosity [188]. Cryogelation has been the most commonly used strategy for secondary pore generation given that it can easily be applied to any type of pre-formed scaffold and the ice crystals generated can pierce through existing pore walls to leave behind an interconnected macroporous structure [107, 189, 190]. However, if cells are incorporated directly into the initially formed scaffold, the number of secondary techniques that can be applied is subsequently limited, with the use of organic solvents (emulsion templating) or low temperatures (cryogelation) both posing cytocompatibility challenges.

However, there have been reports of successful 3D bioprinting using two immiscible aqueous phases using gelatin methacryloyl (GelMA) and PEO [128], with the use of this and other aqueous two-phase systems offering particular promise for creating cell laden microstructured macroporous gels.

1.2.12. Injectable porous hydrogels

While hydrogels are most typically surgically implanted given their high yield stresses that limit injectability, injectable hydrogels have more recently been developed to offer a less invasive route for clinicians to perform cell transplantation [14, 191]. For effective design of injectable macroporous hydrogels, all the precursor components of the hydrogel as well as any side products of the *in situ*-gelation process that facilitates injectability need to be non-cytotoxic and cytocompatible. Given the lack of cytocompatibility of most pore-forming additives (e.g. salts, organic solvents, cryoprocessing), few methods can easily be adapted to fabricate injectable macroporous hydrogels. As one example that was successful, Long et al. reported the use of magnesium particles for gas foaming and solid templating, leveraged *in situ* magnesium oxidation in the body to generate hydrogen gas (facilitating *in situ* foaming) while improving osteogenesis due to the presence of magnesium ion by products [192]. However, for soft tissues, there are few successful examples to report. As such, the design of a safe *in situ* technique for creating macroporous hydrogels following a simple injection remains a key technical challenge to effectively leveraging injectable hydrogels for tissue engineering applications.

1.3. Pore Architecture and its Impact on Cellular Response

The architecture of the porosity generated by the various fabrication techniques has significant impacts on the biological responses to the resulting macroporous materials. In this section, the major complex biological responses to scaffold architecture are explored with a specific emphasis on highlighting why simply reporting a single optimal pore size for engineered tissue scaffolds is typically insufficient for understanding the biological responses to such a scaffold.

1.3.1. Diffusion of nutrients and waste

Hindered diffusion of nutrients, oxygen, and metabolic waste can significantly impact scaffold performance in terms of inhibiting uniform tissue regeneration and hindering cell-cell communication through the retardation of soluble signalling molecule transport [150]. Pore architecture can significantly impact the diffusion rate. Falk et al. demonstrated how the diffusion paracetamol is reduced with decreasing average pore size of lyophilized chitosan scaffolds [193]. Choi et al. observed significantly higher diffusion rates in PLGA scaffolds prepared using the inverse opal technique with homogeneous 200 μm pores compared to scaffolds prepared with the same average pore size and the same technique but using a heterogeneous particle template; the resulting non-uniform pores in the heterogeneous template case resulted in reduced pore interconnectivity and thus hindered diffusion of nutrients and oxygen, resulting in lower levels of preosteoblast differentiation and a less uniform spatial distribution of fibroblasts [150].

1.3.2. Adhesion

Adhesion is the initial cellular response when adherent cells come into contact with scaffolds. Cells must first adhere to the scaffold by forming focal points (typically via integrin binding) before they engage in other functions such as migration, proliferation, and the deposition of extracellular matrix [194]. Hydrogel pore size strongly influences this initial adhesion response. In a study on cell-scaffold interactions between freeze dried collagen-GAG and MC-3T3-E1 cells by O'Brien et al., scaffolds with pore sizes ranging between 90-120 µm exhibited cell adhesion responses that were linearly proportional to the specific surface area of the scaffold, most likely attributable to the increased number of adhesion-promoting ligands accessible on the collagen that comprised the interface of the scaffold [195]. Pore structure can also influence how cells adhere. In electrospun scaffolds with large pores (20 µm), human dermal fibroblasts wrapped around and aligned with individual fibers; in contrast, in scaffolds with smaller pores (6.5 µm), cells bridged between multiple fibers and across pores [80], with each type of adhesion observed demonstrated to impact the resulting cell response.

1.3.3. Cell migration

Harley et al. reported an extensive study of how cell migration and infiltration is influenced by pore size (96 – 151 µm) in freeze-dried scaffolds by tracking and characterizing the migratory behaviour of individual mouse fibroblasts in three categories; locomotion persistence time (i.e. the degree of productive directional movement of cells), motile fraction (i.e. the percentage of time devoted to directional movement versus turning), and cell speed (i.e. the rate of directional movement) [25]. Cells in scaffolds with larger pore sizes tend to migrate through the scaffold slower than in scaffolds with smaller pore sizes; however, along the struts cells traveled faster through the junctions between pores that are more prevalent in small-pore scaffolds, highlighting the importance of junction architecture as well as the presence of more densely clustered binding ligands that could explain the increase in cell speed at junctions (Figure 1-9) [25]. It should however be noted that the authors tracked single cells as opposed to studying migratory behaviour of a population of cells and thus disregarded cells that were immobile, underwent division, or migrated out of the field of view, with no mention of what percentage of the cell population fell under these categories; this may account for the discrepancies between this study and other studies focusing on the behaviour of a population of cells and cell proliferation *in vivo* which report much faster overall cell migration (i.e. rates of of up to 3 µm/min in metastatic tumors [196]).

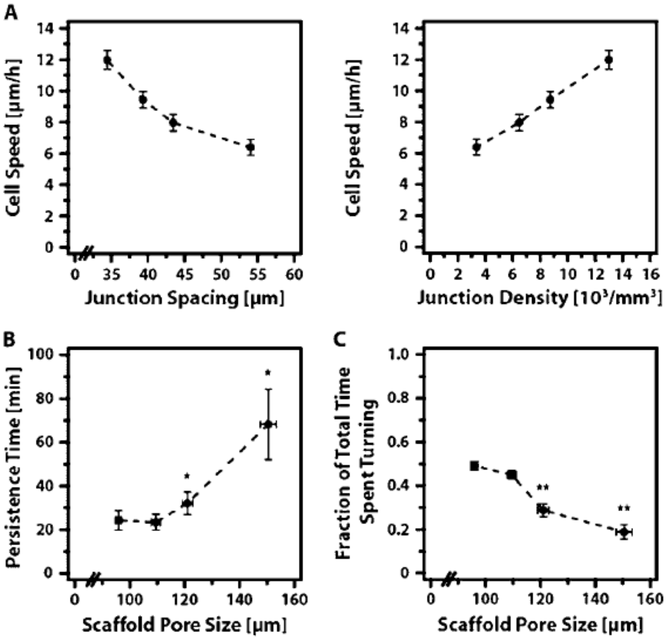

Figure 1-9- Effects of pore size and junction spacing/density on single cell migration and motility through macroporous scaffolds. Reproduced with permission from CellPress [25].

1.3.4. Proliferation and regenerative capacity

In general, the use of pores with sizes similar to or slightly larger than the target cell size can enhance the potential regenerative capacity of a scaffold. Specifically, there is a balance between the enhanced accessibility of binding sites in smaller pores with the steric limitations of cells moving between (or, at some point, fitting inside) the pores, with cells eventually aggregating at a high cell density on the outer surface of tissue engineered scaffolds if the pore size is too small for infiltration [82, 197]. The lower limit of pore size at which cell infiltration restrictions overshadow the benefits of increased surface area depends on the type of cell (Figure 1-10) and the therapeutic objectives of the scaffold [24]. For example, von Heimburg et al. showed that the growth and differentiation of preadipocytes into mature adipocytes (40-150 μm [198]) appeared to be restricted in directionally frozen and lyophilized scaffolds due to the small pore size of the scaffold, with a minimum of 45 μm diameter pores recommended to mediate adipogenic progenitors [199]. Similar studies on other cells are required to identify a specific range in which small pore sizes enhance regeneration [195, 197, 200].

Pore size uniformity also has a significant role in ensuring even migration and proliferation of cells throughout the implanted scaffolds [150]. Fibroblasts were shown to grow and proliferate unevenly in scaffolds with non-uniform pore sizes, with the proliferation pattern attributed both to steric limitations on cell diffusion as well as hindered nutrient diffusion in specific areas [148]. We would suggest that many previous reports in literature have failed to consider pore size uniformity as a key variable in regulating cell responses [150], making distinctions between the effects of mean pore size, pore size distribution and interconnectivity and their impact on cell proliferation challenging based on the existing literature.

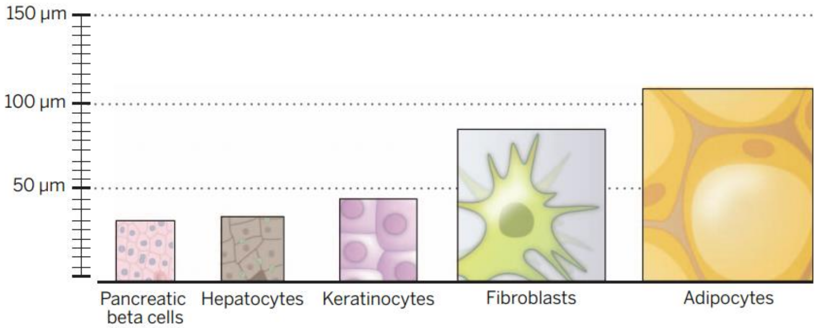

Figure 1-10- The sizes of various human cell types illustrated to scale. Reproduced with permission from Science. [24]

1.3.5. ECM production

The effects of pore architecture on cell adhesion are directly reflected in differences in the ECM production enabled by different scaffolds. For example, in a study by Kuboki et al. two distinct osteogenesis mechanisms were observed depending on the size of channels created in hydroxyapatite blocks, highlighting the importance of microarchitecture design in tissue scaffolds [201]. Complementary observations were made by Choi et al., who demonstrated that both organic and inorganic ECM secretion by pre-osteoblasts can be supported in apatite-coated PLGA scaffolds with small pore sizes (200 µm in diameter) while inorganic ECM is more favourably produced in scaffolds with large pore sizes (300 µm in diameter) [150]. Lowery et al. showed that human dermal fibroblasts started producing more ECM faster when added to electrospun scaffolds with smaller pores (6-15 µm), although the total number of cells in scaffolds with large diameters (21 µm) was ultimately higher given the lower restriction on cell transport into such scaffolds [80].

1.3.6. Differentiation

Differences in both cell adhesion and migration are also reflected in differences in cell differentiation. Choi et al. demonstrated that pre-osteoblast differentiation from mesenchymal stem cells (MSCs) was impacted by pore size in apatite-coated PLGA scaffolds, with significantly higher ALP activity (a biomarker indicative of osteogenic differentiation) observed on day 14 and 28 of an *in vitro* test with single-sized pores created using the inverse opal technique compared to scaffolds with a non-uniform pore size distribution (202 ± 94 µm) generated using the same technique (Figure 1-11) [150]. However, in 5-ethyl-5-(hydroxymethyl)-β,β-dimethyl-1,3-dioxane-2-ethanol diacrylate and poly(ethylene glycol) diacrylate hydrogel scaffolds fabricated using salt leaching, ALP activity was neither impacted by porosity (modified by pyrogen content) nor average pore size (modified by passing salt particles through a series of sieves). This contradictory result is speculated to relate to a particular feature of the material used to prepare the scaffolds or the pore size distributions chosen being either too wide or not different enough to enable the detection of significant differences, with the latter in our opinion being more likely given that control of pore size distribution can be difficult to achieve using salt leaching techniques in contrast to the inverse opal technique [131].

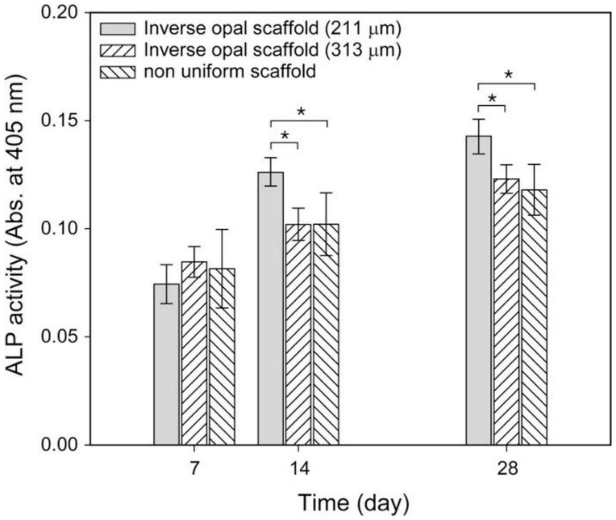

Figure 1-11- The effects of the pore size and the uniformity of the pore size distribution on the expression of biomarkers associated with preosteoblast differentiation. Reproduced with permission from the American Chemical Society [150]

1.3.7. Vascularization and angiogenesis

Effective vascularization of tissue scaffolds is also highly dependent on pore architecture, although the ideal pore size for *in vitro* cell responses can significantly differ from what is observed to work best *in vivo*. For example, Choi et al. showed that pore size could influence *in vivo* vascularization in poly(D,L-lactide-co-glycolide) (PLGA) scaffolds produced using the inverse opal technique containing single sized pores ranging from 79-312 µm in diameter, with smaller yet denser superficial blood vessels observed to form in scaffolds with smaller pore sizes but larger vessels with deeply penetrating interconnected structures and much lower densities observed to form in scaffolds with larger pore sizes (Figure 1-12) [26]. This result was attributed to small openings between small pores limiting or even blocking the penetration of blood vessels throughout the depth of the scaffolds. Increased migration of non-vascular cells through scaffolds with large pores followed by secretion of angiogenic factors (e.g., vascular endothelial growth factor, VEGF) could also improve the development of neovasculature in these structures. However, Choi et al. have not challenged this hypothesis with measuring the extent of hypoxia in the different scaffolds (a potentially significant confounding effect) as well as exploring how scaffold degradation may alter the results. In another study, Yin et al. showed increased secretion of VEGF when initially non-polarized macrophages were seeded onto scaffolds with a larger pore size (360 µm) compared to scaffolds with a smaller pore size (160 µm), a result corresponding to a facilitated M1 to M2 transition within the scaffold that leads to more effective healing [202].

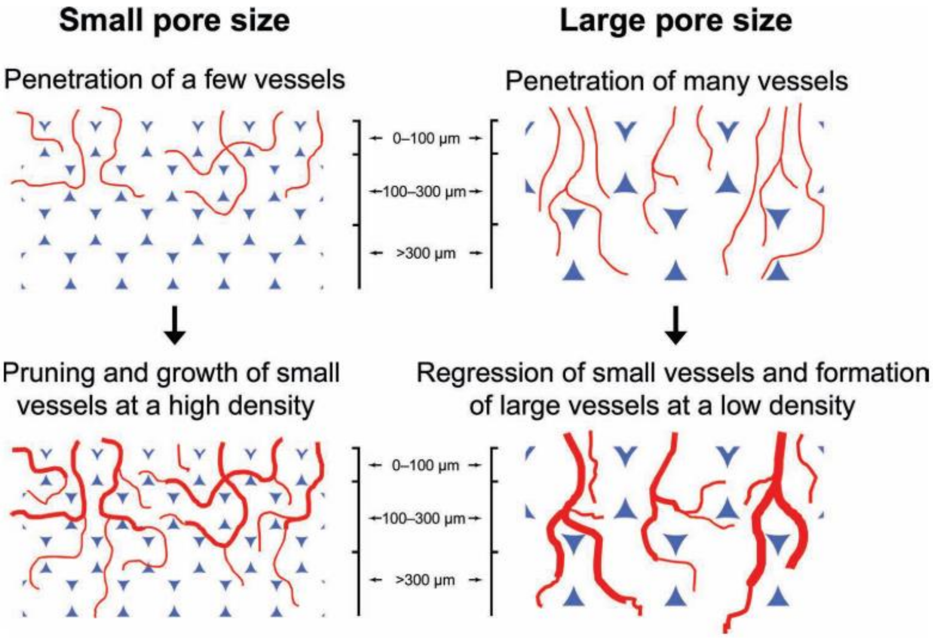

Figure 1-12 -Schematic of how blood vessels can penetrate differently in scaffolds with smaller and larger pore sizes. Reproduced with permission from Wiley [26].

1.4. Applications of Macroporous Hydrogels

The intentional design of pore architecture is significant in many applications of macroporous hydrogels. Average pore size, pore size distribution, interconnected pore structure, porosity, specific surface area, and pore shape can all impact the performance of macroporous hydrogels in different applications and contexts. In environmental applications, increased specific surface area can significantly enhance the effectiveness and scavenging capacity of hydrogels in wastewater treatment [203] and increase the absorption capacity of sodium alginate-polyacrylamide/graphene oxide composites toward copper and lead ions [204]. In personal care applications, the role of macroporosity in regulating the swelling capacity of a hydrogel is often the key advantage; for example, the pore architecture of porous bacterial cellulose and polyvinyl-alcohol hydrogels has been linked to changes in swelling properties advantageous in absorbent personal care products [205]. In solar water evaporation and desalination, the presence of interconnected channels is critical to ensuring proper water transport to the air-water interface [206]. However, the benefits of macroporous hydrogels have been leveraged most commonly in tissue engineering and wound care applications.

1.4.1. Macroporous hydrogels in tissue engineering

The diversity of polymers available, coupled with the diversity of processing methods available to fabricate those polymers into scaffolds with different internal and external dimensions [2], enables the customization of a specific scaffold to a specific tissue engineering context. More specifically, both the cells to be delivered by/recruited into the scaffold as well as the chemistry, architecture, and geometry of the scaffold itself must be considered to ensure that the scaffold is providing the optimal physical, mechanical, chemical, and/or biological cues for regenerating the targeted tissue type(s). However, given the correlations between many of the key properties of a polymeric scaffold (i.e. mechanics and porosity), the rational design of a specific scaffold for a particular application can be challenging. For example, a number of studies have explored how the local mechanics of the scaffold can impact cell responses such as attachment, type and the extent of extracellular matrix (ECM) production, cell differentiation, migration, and proliferation [25, 26]; however, other studies have suggested that cell motility is instead more strongly correlated to subtle changes in the architecture of porous scaffolds such as pore size [207], pore size distribution [150], porosity [208], pore connectivity [209], and/or strut flexural rigidity [210, 211]. The mechanics and pore structure of a hydrogel are intimately linked, such that differentiating effects of the two in tissue engineering is inherently challenging. For example, non-uniform pore sizes can lead to localized mechanical stress concentration as a result of inhomogeneous mechanical properties as well as non-uniform tissue regeneration related to differential diffusion in different parts of the scaffold [27]. Methods that can create directional pores are particularly relevant to the fabrication of tissues that have inherent alignment, with both cell migration and infiltration shown to improve in presence of fiber alignment and thus aligned channels in scaffolds [212, 213]. Rational design of pore architecture is thus critical to avoiding structural or mechanical mismatch between the implanted scaffold and ensuring that the morphology of the target tissue is adequately mimicked [214].

1.4.2. Macroporous hydrogels in wound care

An ideal wound dressing would be able to (1) absorb exudate, (2) maintain a hydrated interface, (3) be permeable to gases, (4) provide a physical barrier to protect the wound against bacteria and debris, (5) provide thermal insulation to the wound, (6) be cytocompatible, (7) be easily removed with limited adhesion to the wound, (8) be easily handled, (9) be consistently sterilizable, and (10) provide good geometric conformability to the wound site [13, 215]. Hydrogels address a number of these goals; coupling hydrogels with bioactive compounds such as nonsteroidal anti-inflammatory drugs, antimicrobial compounds, or growth factors can further address specific clinical challenges in treating various types of wounds (chronic vs. acute, infected wounds, etc.). Macroporosity has shown to improve hydrogel wound dressing performance by modulating inflammation, facilitating or accelerating cell migration and proliferation, and/or enhancing angiogenesis [153, 216, 217], with effective wound repair and successful regeneration of hair follicles commonly reported in wounds treated with macroporous hydrogels [218-220].

Despite the beneficial properties of hydrogels as a physical barrier to protect wounds, infections can still occur, particularly in chronic wounds that do not heal and are thus continuously susceptible to often antibiotic-resistant infections. In this context, combining macroporous hydrogels with controlled release vehicles that can enable the prolonged release of antimicrobial compounds could improve treatment of wound infections. However, the inherent hydrophilicity of hydrogels makes loading hydrophobic bioactive compounds (like many emerging antibiotics/antibiotic adjuvants) challenging, leading to numerous approaches aiming to encapsulate the drug in a particle (e.g.

nanoparticles [221], microparticles [222], or micelles [223]) that can be encapsulated into the hydrogel, using adsorptive precipitation to deposit drug on the scaffold (taking advantage of the high specific surface area of the macroporous scaffold) [224], or covalent tethering bioactive compounds to the scaffold [225] to effectively incorporate anti-infective properties into the macroporous scaffolds. For example, Chen et al. treated infected wounds with poly(N-isopropylacrylamide) porous beads loaded with vancomycin, enabling the rapid release of vancomycin from the porous beads triggered by increasing temperature (indicative of local inflammation) to effectively control infection while also promoting angiogenesis and collagen deposition [226]. Alternatively, Yang et al. fabricated an antimicrobial macroporous 3D printed wound dressing by combining N-halamine/TiO_2 with GelMA and xanthan gum to achieve 100% sterilization of high load *S. aureus* or *E. coli* bacterial suspensions (10^6-10^7 CFU/mL) over a 1 hour contact time while also significantly accelerating wound closure [227] while Priya et al. developed a bilayer cryogel with a top antiseptic polyvinylpyrrolidone-iodine layer and a bottom regenerative layer made of gelatin in which sustained iodine release and diffusion could be achieved through the gelatin layer to prevent infection while accelerating wound healing in rabbits [228]. However, the compositional complexity of many of these potential solutions limits their scalability and thus ultimate clinical application potential, suggesting the need for improved formulations particularly for treating the growing number of antibiotic-resistant bacteria.

1.5. Thesis Objectives

This thesis focuses on addressing some of the limitations in designing hydrogels as cell scaffolds for tissue engineering and/or wound dressings for effective wound regeneration. Each chapter aims to address a specific need or gap in tissue engineering and/or drug delivery associated with the use of hydrogels, with most chapters focused on addressing key challenges around the design and application of macroporous scaffolds (i.e. injectability, mechanics, drug impregnation) as identified in the literature review.

Chapter 2 explores the nanoencapsulation of antimicrobial compounds inside a hydrogel scaffold to produce an antimicrobial hydrogel treatment for methicillin-resistant *Staphylococcus aureus* (MRSA). Poly(lactic acid)-*block*-poly(oligoethylene glycol methacrylate) (PLA-POEGMA) self-assembled nanoparticles were loaded with fusidic acid using flash nanoprecipitation and physically embedded in a dynamically-crosslinked POEGMA hydrogel matrix. The antimicrobial performance of POEGMA hydrogel wound dressings was evaluated *in vitro* and *in vivo* using MRSA as an infection model. The *in vitro* drug release profile in simulated wound fluid showed a two-stage drug release profile with two different diffusion rates, with *in vivo* studies on MRSA-infected wounds showing effective 1-2 order of magnitude inhibition of bacterial growth using a 100,000 times lower antibiotic dose compared to the animal equivalent oral dose. These findings highlight the importance of local delivery of antibiotic to the wound to treat drug-resistant infections and could revive numerous antibiotic compounds that are eliminated during the early stages of drug discovery due to low water solubility. Additionally, this technology can be adapted to different antimicrobial compound suitable for combination therapy.

Chapter 3 focuses on the development of *in situ*-crosslinked pressurized gas expanded liquids (PGX) technology to address the scalability of macroporous hydrogel fabrication. Combined with sc-CO_2 impregnation to take advantage of the high porosity of the resulting scaffold to deposit poorly soluble antibiotics (fusidic acid and tigecycline) into the scaffold, PGX technology is shown to provide a scalable technique to deliver antimicrobial compounds that are otherwise difficult to administer due to their high hydrophobicity and/or low bioavailability. *In vitro* drug release studies and antimicrobial assays confirm successful impregnation of the chosen bioactive compounds, while an *in vivo* full thickness MRSA infected wound model shows a significant reduction or complete clearance of infection 48 hours post-treatment.

Chapter 4 describes the design and development a novel injectable macroporous hydrogel using a perfluorocarbon emulsion based on combining a low boiling point perfluorocarbon emulsion with an *in situ*-gelling POEGMA hydrogel based on hydrazone crosslinking. The resulting hydrogel is non-cytotoxic and well tolerated *in vivo* while improving long-term C2C12 mouse myoblast cell viability *in vitro*. In particular, controlling the rate of perfluorocarbon evaporation relative to the rate of gelation enables the formation and capture of a macroporous morphology both *in vitro* and *in vivo*, with the resulting porosity directly dependent on the amount of perfluorocarbon emulsion incorporated into the precursor materials. This chapter represents one of very few reports of injectable macroporous hydrogels using precursor materials that are much more tissue compatible than previous examples.

Chapter 5 explores how performing dual electrospinning of “hard” poly(caprolactone) (PCL) and POEGMA nanofibers can create an interpenetrating hard/soft nanofiber network with directionality that has significantly higher mechanical strength than a hydrogel-only scaffold while maintaining many of the benefits of hydrogel scaffolds (i.e. improved water uptake, tunable contact angles). Of particular note, the dual PCL-POEGMA scaffolds can both delay bacterial adhesion and support significantly higher cell proliferation relative to PCL-only scaffolds, a result we attribute to the role of the POEGMA interpenetrating phase in both increasing total interfacial surface area as well as diluting the high hydrophobicity of the PCL interface that can limit cell spreading and proliferation. This chapter represents to our knowledge the first example of creating electrospun scaffolds containing both hard (PCL) and soft (POEMGA) hydrogel nanofibers in a single fabrication step, suggesting potential future implications in tissue engineering of stiffer tissues.

Chapter 6 provides an overview of the contributions made to macroporous hydrogels in tissue engineering and wound care and provides an outline of future work that could conducted to extend and apply the results discussed.

Overall, this thesis provides potential solutions to many of the key limitations of particularly macroporous hydrogel use in biomedical applications, with future implications in improving wound care and effective regeneration of a tissues with a range of different mechanics.

1.6. References

[1] L.V. Korah, G. Anilkumar, S. Thomas, 5 - Hydrogels, DNA, and RNA polypeptides for the preparation of biomaterials, in: S. Thomas, P. Balakrishnan, M.S. Sreekala (Eds.), Fundamental Biomaterials: Polymers, Woodhead Publishing2018, pp. 85-104.
[2] K.J. De France, F. Xu, T. Hoare, Structured macroporous hydrogels: progress, challenges, and opportunities, Adv. Healthc. Mater. 7(1) (2018) 1700927.
[3] K. Zhang, X. Luo, L. Yang, Z. Chang, S. Luo, Progress toward Hydrogels in removing heavy metals from water: problems and solutions: a review, ACS ES&T Water 1(5) (2021) 1098-1116.
[4] V. Sinha, S. Chakma, Advances in the preparation of hydrogel for wastewater treatment: A concise review, J. Environ. Chem. Eng. 7(5) (2019) 103295.
[5] A. Francesko, P. Petkova, T. Tzanov, Hydrogel dressings for advanced wound management, Curr. Med. Chem. 25(41) (2019) 5782-5797.
[6] T. Hoare, D. Kohane, Hydrogels in drug delivery: progress and challenges, Polymer 49 (2008) 1993-2007.
[7] J.A. Hunt, R. Chen, T. van Veen, N. Bryan, Hydrogels for tissue engineering and regenerative medicine, J. Mater. Chem. B 2(33) (2014) 5319-5338.
[8] G. Bovone, O.Y. Dudaryeva, B. Marco-Dufort, M.W. Tibbitt, Engineering hydrogel adhesion for biomedical applications via chemical design of the junction, ACS Biomater. Sci. Eng. 7(9) (2021) 4048-4076.
[9] S. Kirchhof, A.M. Goepferich, F.P. Brandl, Hydrogels in ophthalmic applications, Eur J Pharm Biopharm 95 (2015) 227-238.
[10] R.C. Cooper, H. Yang, Hydrogel-based ocular drug delivery systems: emerging fabrication strategies, applications, and bench-to-bedside manufacturing considerations, J Control Release 306 (2019) 29-39.
[11] C.M. Kirschner, K.S. Anseth, Hydrogels in healthcare: from static to dynamic material microenvironments, Acta Biomater. 61(3) (2013) 931-944.
[12] A. Bashari, A. Rouhani Shirvan, M. Shakeri, Cellulose-based hydrogels for personal care products, Polym Adv Technol 29(12) (2018) 2853-2867.
[13] R.C. Op 't Veld, X.F. Walboomers, J.A. Jansen, F.A.D.T.G. Wagener, Design considerations for hydrogel wound dressings: strategic and molecular advances, Tissue Eng. Part B Rev. 26(3) (2020) 230-248.
[14] K.Y. Lee, D.J. Mooney, Hydrogels for tissue engineering, Chem. Rev. 101(7) (2001) 1869-1880.
[15] D. Al Sulaiman, P. Cadinu, A.P. Ivanov, J.B. Edel, S. Ladame, Chemically modified hydrogel-filled nanopores: a tunable platform for single-molecule sensing, Nano Lett. 18(9) (2018) 6084-6093.
[16] Y. Wu, S. Joseph, N.R. Aluru, Effect of cross-linking on the diffusion of water, ions, and small molecules in hydrogels, J. Mater. Chem. B 113(11) (2009) 3512-3520.
[17] E. Axpe, D. Chan, G.S. Offeddu, Y. Chang, D. Merida, H.L. Hernandez, E.A. Appel, A Multiscale model for solute diffusion in hydrogels, Macromolecules 52(18) (2019) 6889-6897.
[18] J.L. Stringer, N.A. Peppas, Diffusion of small molecular weight drugs in radiation-crosslinked poly(ethylene oxide) hydrogels, J Control Release 42(2) (1996) 195-202.
[19] O. Lieleg, K. Ribbeck, Biological hydrogels as selective diffusion barriers, Trends Cell Biol 21(9) (2011) 543-51.
[20] X. Ding, J. Gao, X. Yu, J. Shi, J. Chen, L. Yu, S. Chen, J. Ding, 3D-printed porous scaffolds of hydrogels modified with TGF-β1 binding peptides to promote in vivo cartilage regeneration and animal gait restoration, ACS Appl. Mater. Interfaces 14(14) (2022) 15982-15995.
[21] Q.L. Loh, C. Choong, Three-dimensional scaffolds for tissue engineering applications: role of porosity and rore size, Tissue Eng. Part B Rev. 19(6) (2013) 485-502.
[22] A.S. Hoffman, Hydrogels for biomedical applications, Adv. Drug Deliv. Rev. 64 (2012) 18-23.
[23] R. Gaetani, P.A. Doevendans, C.H.G. Metz, J. Alblas, E. Messina, A. Giacomello, J.P.G. Sluijter, Cardiac tissue engineering using tissue printing technology and human cardiac progenitor cells, Biomater. 33(6) (2012) 1782-1790.
[24] M.B. Ginzberg, R. Kafri, M. Kirschner, On being the right (cell) size, Science 348(6236) (2015) 1245075.
[25] B.A.C. Harley, H.-D. Kim, M.H. Zaman, I.V. Yannas, D.A. Lauffenburger, L.J. Gibson, Microarchitecture of Three-Dimensional Scaffolds Influences Cell Migration Behavior via Junction Interactions, Biophysical Journal 95(8) (2008) 4013-4024.
[26] S.W. Choi, Y. Zhang, M.R. Macewan, Y. Xia, Neovascularization in biodegradable inverse opal scaffolds with uniform and precisely controlled pore sizes, Adv Healthc Mater 2(1) (2013) 145-54.
[27] Y.S. Zhang, C. Zhu, Y. Xia, Inverse Opal Scaffolds and Their Biomedical Applications, Adv Mater 29(33) (2017) 10.1002/adma.201701115.
[28] C. Ji, N. Annabi, A. Khademhosseini, F. Dehghani, Fabrication of porous chitosan scaffolds for soft tissue engineering using dense gas CO2, Acta Biomater. 7(4) (2011) 1653-1664.
[29] P.A.M. Lips, I.W. Velthoen, P.J. Dijkstra, M. Wessling, J. Feijen, Gas foaming of segmented poly(ester amide) films, Polymer 46(22) (2005) 9396-9403.

[30] A. Sannino, P.A. Netti, M. Madaghiele, V. Coccoli, A. Luciani, A. Maffezzoli, L. Nicolais, Synthesis and characterization of macroporous poly(ethylene glycol)-based hydrogels for tissue engineering application, J Biomed Mater Res A 79A(2) (2006) 229-236.
[31] C. Ji, A. Khademhosseini, F. Dehghani, Enhancing cell penetration and proliferation in chitosan hydrogels for tissue engineering applications, Biomater. 32(36) (2011) 9719-9729.
[32] R. Luo, J. Wu, N.-D. Dinh, C.-H. Chen, Gradient porous elastic hydrogels with shape-memory property and anisotropic responses for programmable locomotion, Adv. Funct. Mater. 25(47) (2015) 7272-7279.
[33] I.B. Djemaa, S. Auguste, W. Drenckhan-Andreatta, S. Andrieux, Hydrogel foams from liquid foam templates: properties and optimisation, Adv. Colloid Interface Sci. 294 (2021) 102478.
[34] C. Ji, N. Annabi, M. Hosseinkhani, S. Sivaloganathan, F. Dehghani, Fabrication of poly-DL-lactide/polyethylene glycol scaffolds using the gas foaming technique, Acta Biomater. 8(2) (2012) 570-578.
[35] Y.-M. Lim, H.-J. Gwon, J. Shin, J.P. Jeun, Y.C. Nho, Preparation of porous poly(ε-caprolactone) scaffolds by gas foaming process and in vitro/in vivo degradation behavior using γ-ray irradiation, J Ind Eng Chem 14(4) (2008) 436-441.
[36] A. Fernández-Colino, F. Wolf, H. Keijdener, S. Rütten, T. Schmitz-Rode, S. Jockenhoevel, J.C. Rodríguez-Cabello, P. Mela, Macroporous click-elastin-like hydrogels for tissue engineering applications, Mater. Sci. Eng. C 88 (2018) 140-147.
[37] J.J. Yoon, T.G. Park, Degradation behaviors of biodegradable macroporous scaffolds prepared by gas foaming of effervescent salts, J. Biomed. Mater. Res. 55(3) (2001) 401-408.
[38] L. Griveau, M. Lafont, H. le Goff, C. Drouglazet, B. Robbiani, A. Berthier, D. Sigaudo-Roussel, N. Latif, C.L. Visage, V. Gache, R. Debret, P. Weiss, J. Sohier, Design and characterization of an in vivo injectable hydrogel with effervescently generated porosity for regenerative medicine applications, Acta Biomater. 140 (2022) 324-337.
[39] N.M. Kenna, A. Morrin, Inducing macroporosity in hydrogels using hydrogen peroxide as a blowing agent, Materials Chemistry Frontiers 1(2) (2017) 394-401.
[40] J.J. Yoon, T.G. Park, Degradation behaviors of biodegradable macroporous scaffolds prepared by gas foaming of effervescent salts, Journal of Biomedical Materials Research 55(3) (2001) 401-408.
[41] A. Bouchard, N. Jovanović, Á. Martín, G.W. Hofland, D.J.A. Crommelin, W. Jiskoot, G.-J. Witkamp, Effect of the modifier on the particle formation and crystallisation behaviour during precipitation from aqueous solutions, J. Supercrit. Fluids. 44(3) (2008) 409-421.
[42] S.-D. Yeo, E. Kiran, Formation of polymer particles with supercritical fluids: A review, J. Supercrit. Fluids. 34(3) (2005) 287-308.
[43] G. Liu, J. Li, S. Deng, Applications of supercritical anti-solvent Process in preparation of solid multicomponent systems, Pharmaceutics 13(4) (2021).
[44] R.K. Kankala, B.Q. Chen, C.G. Liu, H.X. Tang, S.B. Wang, A.Z. Chen, Solution-enhanced dispersion by supercritical fluids: an ecofriendly nanonization approach for processing biomaterials and pharmaceutical compounds, Int J Nanomedicine 13 (2018) 4227-4245.
[45] Z. Liu, R. Couto, B. Seifried, B. Yépez, P. Moquin, F. Temelli, Drying of sodium alginate using Pressurized Gas eXpanded (PGX) liquid technology, J. CO2 Util. 61 (2022) 102006.
[46] R. Couto, E. Wong, B. Seifried, B. Yépez, P. Moquin, F. Temelli, Preparation of PGX-dried gum arabic and its loading with coQ10 by adsorptive precipitation, J. Supercrit. Fluids. 156 (2020) 104662.
[47] N. Liu, R. Couto, B. Seifried, P. Moquin, L. Delgado, F. Temelli, Characterization of oat beta-glucan and coenzyme Q10-loaded beta-glucan powders generated by the pressurized gas-expanded liquid (PGX) technology, Food Res. Int. 106 (2018) 354-362.
[48] C.A. García-González, A. Sosnik, J. Kalmár, I. De Marco, C. Erkey, A. Concheiro, C. Alvarez-Lorenzo, Aerogels in drug delivery: from design to application, J Control Release 332 (2021) 40-63.
[49] L. Manzocco, K.S. Mikkonen, C.A. García-González, Aerogels as porous structures for food applications: Smart ingredients and novel packaging materials, Food Structure. 28 (2021) 100188.
[50] C.A. García-González, T. Budtova, L. Durães, C. Erkey, P. Del Gaudio, P. Gurikov, M. Koebel, F. Liebner, M. Neagu, I. Smirnova, An opinion paper on aerogels for biomedical and environmental applications, Molecules, 2019.
[51] P. Ravi, Understanding the relationship between slicing and measured fill density in material extrusion 3D printing towards precision porosity constructs for biomedical and pharmaceutical applications, 3D Printing in Medicine 6(1) (2020) 10.
[52] B. Pernet, J.K. Nagel, H. Zhang, Compressive strength assessment of 3D printing infill patterns, Procedia CIRP 105 (2022) 682-687.
[53] T. Billiet, M. Vandenhaute, J. Schelfhout, S. Van Vlierberghe, P. Dubruel, A review of trends and limitations in hydrogel-rapid prototyping for tissue engineering, Biomater. 33(26) (2012) 6020-6041.
[54] R. Taymour, D. Kilian, T. Ahlfeld, M. Gelinsky, A. Lode, 3D bioprinting of hepatocytes: core–shell structured co-cultures with fibroblasts for enhanced functionality, Sci. Rep 11(1) (2021) 5130.
[55] V. Lee, G. Singh, J.P. Trasatti, C. Bjornsson, X. Xu, T.N. Tran, S.-S. Yoo, G. Dai, P. Karande, Design and fabrication of human skin by three-dimensional bioprinting, Tissue Eng. Part C Methods 20(6) (2013) 473-484.

[56] X. Wang, M. Zhang, J. Ma, M. Xu, J. Chang, M. Gelinsky, C. Wu, 3D Printing of cell-container-like scaffolds for multicell tissue engineering, Engineering 6(11) (2020) 1276-1284.

[57] S. Ramesh, O.L.A. Harrysson, P.K. Rao, A. Tamayol, D.R. Cormier, Y. Zhang, I.V. Rivero, Extrusion bioprinting: Recent progress, challenges, and future opportunities, Bioprinting 21 (2021) e00116.

[58] X. Zeng, Z. Meng, J. He, M. Mao, X. Li, P. Chen, J. Fan, D. Li, Embedded bioprinting for designer 3D tissue constructs with complex structural organization, Acta Biomater. 140 (2022) 1-22.

[59] B. Guillotin, A. Souquet, S. Catros, M. Duocastella, B. Pippenger, S. Bellance, R. Bareille, M. Rémy, L. Bordenave, J. Amédée, F. Guillemot, Laser assisted bioprinting of engineered tissue with high cell density and microscale organization, Biomater. 31(28) (2010) 7250-7256.

[60] P.R. Martinez, A. Goyanes, A.W. Basit, S. Gaisford, Fabrication of drug-loaded hydrogels with stereolithographic 3D printing, Int. J. Pharm. 532(1) (2017) 313-317.

[61] H. Goodarzi Hosseinabadi, E. Dogan, A.K. Miri, L. Ionov, Digital light processing bioprinting advances for microtissue models, ACS Biomater. Sci. Eng. 8(4) (2022) 1381-1395.

[62] F. Xu, C. Dawson, M. Lamb, E. Mueller, E. Stefanek, M. Akbari, T. Hoare, Hydrogels for tissue engineering: addressing key design needs toward clinical translation, Front Bioeng Biotechnol 10 (2022) 849831.

[63] F. You, X. Wu, N. Zhu, M. Lei, B.F. Eames, X. Chen, 3D Printing of porous cell-laden hydrogel constructs for potential applications in cartilage tissue engineering, ACS Biomater. Sci. Eng. 2(7) (2016) 1200-1210.

[64] A.K. Miri, I. Mirzaee, S. Hassan, S. Mesbah Oskui, D. Nieto, A. Khademhosseini, Y.S. Zhang, Effective bioprinting resolution in tissue model fabrication, Lab Chip 19(11) (2019) 2019-2037.

[65] F. Feng, J. He, J. Li, M. Mao, D. Li, Multicomponent bioprinting of heterogeneous hydrogel constructs based on microfluidic printheads, Int J Bioprint 5(2) (2019) 202.

[66] M. Wang, W. Li, L.S. Mille, T. Ching, Z. Luo, G. Tang, C.E. Garciamendez, A. Lesha, M. Hashimoto, Y.S. Zhang, Digital light processing based bioprinting with composable gradients, Adv. Mater. 34(1) (2022) 2107038.

[67] B. Grigoryan, S.J. Paulsen, D.C. Corbett, D.W. Sazer, C.L. Fortin, A.J. Zaita, P.T. Greenfield, N.J. Calafat, J.P. Gounley, A.H. Ta, F. Johansson, A. Randles, J.E. Rosenkrantz, J.D. Louis-Rosenberg, P.A. Galie, K.R. Stevens, J.S. Miller, Multivascular networks and functional intravascular topologies within biocompatible hydrogels, Science 364(6439) (2019) 458-464.

[68] F.L.C. Morgan, L. Moroni, M.B. Baker, Dynamic bioinks to advance bioprinting, Adv. Healthc. Mater. 9(15) (2020) 1901798.

[69] J. Xue, T. Wu, Y. Dai, Y. Xia, Electrospinning and Electrospun Nanofibers: Methods, Materials, and Applications, Chem Rev 119(8) (2019) 5298-5415.

[70] D. Au - Sivakumaran, E. Au - Bakaic, S.B. Au - Campbell, F. Au - Xu, E. Au - Mueller, T. Au - Hoare, Fabricating Degradable Thermoresponsive Hydrogels on Multiple Length Scales via Reactive Extrusion, Microfluidics, Self-assembly, and Electrospinning, JoVE (134) (2018) e54502.

[71] F. Xu, H. Sheardown, T. Hoare, Reactive electrospinning of degradable poly(oligoethylene glycol methacrylate)-based nanofibrous hydrogel networks, ChemComm 52(7) (2016) 1451-1454.

[72] N.J. Pinto, A.T. Johnson, A.G. MacDiarmid, C.H. Mueller, N. Theofylaktos, D.C. Robinson, F.A. Miranda, Electrospun polyaniline/polyethylene oxide nanofiber field-effect transistor, Appl. Phys. Lett. 83(20) (2003) 4244-4246.

[73] A.R. Gonçalves de Pinho, I. Odila, A. Leferink, C. van Blitterswijk, S. Camarero-Espinosa, L. Moroni, Hybrid polyester-hydrogel electrospun scaffolds for tissue rngineering applications, Front Bioeng Biotechnol 7 (2019).

[74] Z. Cui, Z. Zheng, L. Lin, J. Si, Q. Wang, X. Peng, W. Chen, Electrospinning and crosslinking of polyvinyl alcohol/chitosan composite nanofiber for transdermal drug delivery, Adv. Polym. Technol. 37(6) (2018) 1917-1928.

[75] C.A. Bonino, M.D. Krebs, C.D. Saquing, S.I. Jeong, K.L. Shearer, E. Alsberg, S.A. Khan, Electrospinning alginate-based nanofibers: from blends to crosslinked low molecular weight alginate-only systems, Carbohydr. Polym. 85(1) (2011) 111-119.

[76] Y. Li, M. Vergaelen, E. Schoolaert, R. Hoogenboom, K. De Clerck, Effect of crosslinking stage on photocrosslinking of benzophenone functionalized poly(2-ethyl-2-oxazoline) nanofibers obtained by aqueous electrospinning, Eur. Polym. J. 112 (2019) 24-30.

[77] A. Deng, Y. Yang, S. Du, S. Yang, Electrospinning of in situ crosslinked recombinant human collagen peptide/chitosan nanofibers for wound healing, Biomater. Sci. 6(8) (2018) 2197-2208.

[78] C. Tang, C.D. Saquing, J.R. Harding, S.A. Khan, In situ cross-linking of electrospun poly(vinyl alcohol) nanofibers, Macromolecules 43(2) (2010) 630-637.

[79] A. Ovsianikov, M. Malinauskas, S. Schlie, B. Chichkov, S. Gittard, R. Narayan, M. Löbler, K. Sternberg, K.P. Schmitz, A. Haverich, Three-dimensional laser micro- and nano-structuring of acrylated poly(ethylene glycol) materials and evaluation of their cytoxicity for tissue engineering applications, Acta Biomater. 7(3) (2011) 967-974.

[80] J.L. Lowery, N. Datta, G.C. Rutledge, Effect of fiber diameter, pore size and seeding method on growth of human dermal fibroblasts in electrospun poly(ε-caprolactone) fibrous mats, Biomaterials 31(3) (2010) 491-504.

[81] A. Balguid, A. Mol, M.H. van Marion, R.A. Bank, C.V.C. Bouten, F.P.T. Baaijens, Tailoring fiber diameter in electrospun poly(ε-caprolactone) scaffolds for optimal cellular infiltration in cardiovascular tissue engineering, Tissue Eng. Part A 15(2) (2008) 437-444.

[82] J. Rnjak-Kovacina, S.G. Wise, Z. Li, P.K.M. Maitz, C.J. Young, Y. Wang, A.S. Weiss, Tailoring the porosity and pore size of electrospun synthetic human elastin scaffolds for dermal tissue engineering, Biomaterials 32(28) (2011) 6729-6736.

[83] A.K. Ekaputra, G.D. Prestwich, S.M. Cool, D.W. Hutmacher, Combining electrospun scaffolds with electrosprayed hydrogels leads to three-dimensional cellularization of hybrid constructs, Biomacromolecules 9(8) (2008) 2097-2103.

[84] K. Nie, S. Han, J. Yang, Q. Sun, X. Wang, X. Li, Q. Li, Enzyme-crosslinked electrospun fibrous gelatin hydrogel for potential soft tissue engineering, Polymers, 2020.

[85] T.G. Kim, H.J. Chung, T.G. Park, Macroporous and nanofibrous hyaluronic acid/collagen hybrid scaffold fabricated by concurrent electrospinning and deposition/leaching of salt particles, Acta Biomater. 4(6) (2008) 1611-1619.

[86] J. Jiang, M.A. Carlson, M.J. Teusink, H. Wang, M.R. MacEwan, J. Xie, Expanding two-dimensional electrospun nanofiber membranes in the third dimension by a modified gas-foaming technique, ACS Biomater. Sci. Eng. 1(10) (2015) 991-1001.

[87] A. Samanta, B. Nandan, R.K. Srivastava, Morphology of electrospun fibers derived from High Internal Phase Emulsions, J. Colloid Interface Sci. 471 (2016) 29-36.

[88] J. Rnjak-Kovacina, A.S. Weiss, Increasing the pore size of electrospun scaffolds, Tissue Eng. Part B Rev. 17(5) (2011) 365-372.

[89] P. Katta, M. Alessandro, R.D. Ramsier, G.G. Chase, Continuous electrospinning of aligned polymer nanofibers onto a wire drum collector, Nano Letters 4(11) (2004) 2215-2218.

[90] X. Li, M. Li, J. Sun, Y. Zhuang, J. Shi, D. Guan, Y. Chen, J. Dai, Radially aligned electrospun fibers with continuous gradient of SDF1α for the guidance of neural stem cells, Small 12(36) (2016) 5009-5018.

[91] P. Kiselev, J. Rosell-Llompart, Highly aligned electrospun nanofibers by elimination of the whipping motion, J. Appl. Polym. Sci. 125(3) (2012) 2433-2441.

[92] S. Rahmani, M. Rafizadeh, F. Afshar Taromi, Statistical analysis of nanofibers alignment in magnetic-field-assisted electrospinning including an alignment percentage formula, J. Appl. Polym. Sci. 131(23) (2014).

[93] Y. Liu, X. Zhang, Y. Xia, H. Yang, Magnetic-Field-Assisted Electrospinning of Aligned Straight and Wavy Polymeric Nanofibers, Advanced Materials 22(22) (2010) 2454-2457.

[94] I. Stefani, J.J. Cooper-White, Development of an in-process UV-crosslinked, electrospun PCL/aPLA-co-TMC composite polymer for tubular tissue engineering applications, Acta Biomater. 36 (2016) 231-240.

[95] R. Jalili, M. Morshed, S.A.H. Ravandi, Fundamental parameters affecting electrospinning of PAN nanofibers as uniaxially aligned fibers, J. Appl. Polym. Sci. 101(6) (2006) 4350-4357.

[96] A.P. Rickel, X. Deng, D. Engebretson, Z. Hong, Electrospun nanofiber scaffold for vascular tissue engineering, Mater Sci Eng C Mater Biol Appl 129 (2021) 112373.

[97] A. Sensini, G. Massafra, C. Gotti, A. Zucchelli, L. Cristofolini, Tissue engineering for the insertions of tendons and ligaments: An overview of electrospun biomaterials and structures, Front Bioeng Biotechnol 9 (2021).

[98] A.O. Lobo, S. Afewerki, M.M.M. de Paula, P. Ghannadian, F.R. Marciano, Y.S. Zhang, T.J. Webster, A. Khademhosseini, Electrospun nanofiber blend with improved mechanical and biological performance, Int J Nanomedicine 13 (2018) 7891-7903.

[99] K.J. De France, F. Xu, S. Toufanian, K.J.W. Chan, S. Said, T.C. Stimpson, E. González-Martínez, J.M. Moran-Mirabal, E.D. Cranston, T. Hoare, Multi-scale structuring of cell-instructive cellulose nanocrystal composite hydrogel sheets via sequential electrospinning and thermal wrinkling, Acta Biomater. 128 (2021) 250-261.

[100] D. Yang, X. Peng, L. Zhong, X. Cao, W. Chen, S. Wang, C. Liu, R. Sun, Fabrication of a highly elastic nanocomposite hydrogel by surface modification of cellulose nanocrystals, RSC Adv. 5(18) (2015) 13878-13885.

[101] A. Hivechi, S. Hajir Bahrami, R.A. Siegel, Investigation of morphological, mechanical and biological properties of cellulose nanocrystal reinforced electrospun gelatin nanofibers, Int. J. Biol. Macromol. 124 (2019) 411-417.

[102] J. Yang, J.-J. Zhao, C.-R. Han, J.-F. Duan, Keys to enhancing mechanical properties of silica nanoparticle composites hydrogels: The role of network structure and interfacial interactions, Compos. Sci. Technol. 95 (2014) 1-7.

[103] Z. Emami, M. Ehsani, M. Zandi, H. Daemi, M.-H. Ghanian, R. Foudazi, Modified hydroxyapatite nanoparticles reinforced nanocomposite hydrogels based on gelatin/oxidized alginate via schiff base reaction, Carbohydr. Polym. Technol. and Appl. 2 (2021) 100056.

[104] M.A. Al-Baadani, K. Hii Ru Yie, A.M. Al-Bishari, B.A. Alshobi, Z. Zhou, K. Fang, B. Dai, Y. Shen, J. Ma, J. Liu, X. Shen, Co-electrospinning polycaprolactone/gelatin membrane as a tunable drug delivery system for bone tissue regeneration, Mater. Des. 209 (2021) 109962.

[105] B. Aldemir Dikici, F. Claeyssens, Basic principles of emulsion templating and its use as an emerging manufacturing method of tissue engineering scaffolds, Front Bioeng Biotechnol 8 (2020) 875-875.

[106] E. Durgut, C. Sherborne, B. Aldemir Dikici, G.C. Reilly, F. Claeyssens, Preparation of interconnected pickering polymerized high internal phase emulsions by arrested coalescence, Langmuir 38(36) (2022) 10953-10962.

[107] B.H.L. Oh, A. Bismarck, M.B. Chan-Park, Injectable, interconnected, high-porosity macroporous biocompatible gelatin scaffolds made by surfactant-free emulsion templating, Macromol. Rapid Commun. 36(4) (2015) 364-372.

[108] T. Zhang, M.S. Silverstein, Robust, highly porous hydrogels templated within emulsions stabilized using a reactive, crosslinking triblock copolymer, Polymer 168 (2019) 146-154.

[109] S. Rahmani, M. Rafizadeh, F. Afshar Taromi, Statistical analysis of nanofibers alignment in magnetic-field-assisted electrospinning including an alignment percentage formula, J. Appl. Polym. Sci. 131(23) (2014).

[110] H.H. Mert, M.S. Mert, E.H. Mert, A statistical approach for tailoring the morphological and mechanical properties of polystyrene PolyHIPEs: looking through experimental design, Mater. Res. Express. 6(11) (2019) 115306.

[111] S. Kramer, N.R. Cameron, P. Krajnc, Porous polymers from high internal phase emulsions as scaffolds for biological applications, Polymers, 2021.

[112] L.L.C. Wong, V.O. Ikem, A. Menner, A. Bismarck, Macroporous polymers with hierarchical pore structure from emulsion templates stabilised by both particles and surfactants, Macromol. Rapid Commun. 32(19) (2011) 1563-1568.

[113] T. Zhang, R.A. Sanguramath, S. Israel, M.S. Silverstein, Emulsion templating: porous polymers and beyond, Macromolecules 52(15) (2019) 5445-5479.

[114] R. Moglia, M. Whitely, M. Brooks, J. Robinson, M. Pishko, E. Cosgriff-Hernandez, Solvent-free fabrication of polyHIPE microspheres for controlled release of growth factors, Macromol. Rapid Commun. 35(14) (2014) 1301-1305.

[115] W. Zhu, Y. Zhu, C. Zhou, S. Zhang, Pickering emulsion-templated polymers: insights into the relationship between surfactant and interconnecting pores, RSC Advances 9(33) (2019) 18909-18916.

[116] X. Huang, Y. Yang, J. Shi, H.T. Ngo, C. Shen, W. Du, Y. Wang, High-Internal-Phase Emulsion Tailoring Polymer Amphiphilicity towards an Efficient NIR-Sensitive Bacteria Filter, Small (Weinheim an der Bergstrasse, Germany) 11(37) (2015) 4876-4883.

[117] K. Rohm, I. Manas-Zloczower, D. Feke, Poly(HIPE) morphology, crosslink density, and mechanical properties influenced by surfactant concentration and composition, Colloids Surf. A: Physicochem. Eng. Asp. 583 (2019) 123913.

[118] R. Wu, A. Menner, A. Bismarck, Macroporous polymers made from medium internal phase emulsion templates: Effect of emulsion formulation on the pore structure of polyMIPEs, Polymer 54(21) (2013) 5511-5517.

[119] J.L. Robinson, R.S. Moglia, M.C. Stuebben, M.A.P. McEnery, E. Cosgriff-Hernandez, Achieving interconnected pore architecture in injectable PolyHIPEs for bone tissue engineering, Tissue Eng Part A 20(5-6) (2014) 1103-1112.

[120] I. Gurevitch, M.S. Silverstein, Nanoparticle-based and organic-phase-based AGET ATRP PolyHIPE synthesis within pickering HIPEs and surfactant-stabilized HIPEs, Macromolecules 44(9) (2011) 3398-3409.

[121] M.V. Kempin, M. Kraume, A. Drews, W/O Pickering emulsion preparation using a batch rotor-stator mixer – Influence on rheology, drop size distribution and filtration behavior, J. Colloid Interface Sci. 573 (2020) 135-149.

[122] I. Gurevitch, M.S. Silverstein, Polymerized pickering HIPEs: effects of synthesis parameters on porous structure, J. Polym. Sci., Part A: Polym. Chem. 48(7) (2010) 1516-1525.

[123] J.L. Robinson, R.S. Moglia, M.C. Stuebben, M.A.P. McEnery, E. Cosgriff-Hernandez, Achieving interconnected pore architecture in injectable PolyHIPEs for bone tissue engineering, Tissue Eng. Part A 20(5-6) (2014) 1103-1112.

[124] A.G. Teixeira, R. Agarwal, K.R. Ko, J. Grant-Burt, B.M. Leung, J.P. Frampton, Emerging biotechnology applications of aqueous two-phase systems, Adv. Healthc. Mater. 7(6) (2018) 1701036.

[125] K. Berggren, A. Wolf, J.A. Asenjo, B.A. Andrews, F. Tjerneld, The surface exposed amino acid residues of monomeric proteins determine the partitioning in aqueous two-phase systems, Biochim Biophys Acta Protein Struct Molec Enzym 1596(2) (2002) 253-268.

[126] M. Andes-Koback, C.D. Keating, Complete Budding and Asymmetric Division of Primitive Model Cells To Produce Daughter Vesicles with Different Interior and Membrane Compositions, J. Am. Chem. Soc. 133(24) (2011) 9545-9555.

[127] T. Liu, S. Yi, G. Liu, X. Hao, T. Du, J. Chen, T. Meng, P. Li, Y. Wang, Aqueous two-phase emulsions-templated tailorable porous alginate beads for 3D cell culture, Carbohydr. Polym. 258 (2021) 117702.

[128] G.-L. Ying, N. Jiang, S. Maharjan, Y.-X. Yin, R.-R. Chai, X. Cao, J.-Z. Yang, A.K. Miri, S. Hassan, Y.S. Zhang, Aqueous two-phase emulsion bioink-enabled 3D bioprinting of porous hydrogels, Adv. Mater. 30(50) (2018) 1805460.

[129] D.F.C. Silva, A.M. Azevedo, P. Fernandes, V. Chu, J.P. Conde, M.R. Aires-Barros, Determination of aqueous two phase system binodal curves using a microfluidic device, J. Chromatogr. A 1370 (2014) 115-120.

[130] Y.-C. Chiu, J.C. Larson, A. Isom, E.M. Brey, Generation of porous poly(ethylene glycol) hydrogels by salt leaching, Tissue Eng. Part C Methods 16(5) (2009) 905-912.

[131] M.W. Betz, A.B. Yeatts, W.J. Richbourg, J.F. Caccamese, D.P. Coletti, E.E. Falco, J.P. Fisher, Macroporous hydrogels upregulate osteogenic signal expression and promote bone regeneration, Biomacromolecules 11(5) (2010) 1160-1168.

[132] J. Reignier, M.A. Huneault, Preparation of interconnected poly(ε-caprolactone) porous scaffolds by a combination of polymer and salt particulate leaching, Polymer 47(13) (2006) 4703-4717.

[133] K.R. Coogan, P.T. Stone, N.D. Sempertegui, S.S. Rao, Fabrication of micro-porous hyaluronic acid hydrogels through salt leaching, European Polymer Journal 135 (2020) 109870.

[134] D. Shahriari, G. Loke, I. Tafel, S. Park, P.-H. Chiang, Y. Fink, P. Anikeeva, Scalable fabrication of porous microchannel nerve guidance scaffolds with complex geometries, Adv Mater 31(30) (2019) 1902021.

[135] S. Mohanty, K. Sanger, A. Heiskanen, J. Trifol, P. Szabo, M. Dufva, J. Emnéus, A. Wolff, Fabrication of scalable tissue engineering scaffolds with dual-pore microarchitecture by combining 3D printing and particle leaching, Mater. Sci. Eng. C 61 (2016) 180-189.

[136] M. Dušková-Smrčková, J. Zavřel, M. Bartoš, Z. Kaberova, E. Filová, J. Zárubová, M. Šlouf, J. Michálek, T. Vampola, D. Kubies, Communicating macropores in PHEMA-based hydrogels for cell seeding: probabilistic open pore simulation and direct micro-CT proof, Mater. Des. 198 (2021) 109312.

[137] R. Foudazi, R. Zowada, I. Manas-Zloczower, D.L. Feke, Porous hydrogels: present challenges and future opportunities, Langmuir 39(6) (2023) 2092-2111.

[138] E.S. Dragan, M.V. Dinu, Advances in porous chitosan-based composite hydrogels: synthesis and applications, React Funct Polym 146 (2020) 104372.

[139] Y.S. Zhang, C. Zhu, Y. Xia, Inverse opal scaffolds and their biomedical applications, Adv. Mater. 29(33) (2017) 1701115.

[140] Y. Zhang, S. Wang, M. Eghtedari, M. Motamedi, N.A. Kotov, Inverted-colloidal-crystal hydrogel matrices as three-dimensional cell scaffolds, Adv. Funct. Mater. 15(5) (2005) 725-731.

[141] B. Zhang, Y. Cai, L. Shang, H. Wang, Y. Cheng, F. Rong, Z. Gu, Y. Zhao, A photonic crystal hydrogel suspension array for the capture of blood cells from whole blood, Nanoscale 8(6) (2016) 3841-3847.

[142] P. Im, D.H. Ji, M.K. Kim, J. Kim, Fabrication of cell-benign inverse opal hydrogels for three-dimensional cell culture, J. Colloid Interface Sci. 494 (2017) 389-396.

[143] S.-W. Choi, Y. Zhang, S. Thomopoulos, Y. Xia, In vitro mineralization by preosteoblasts in poly(dl-lactide-co-glycolide) inverse opal scaffolds reinforced with hydroxyapatite nanoparticles, Langmuir 26(14) (2010) 12126-12131.

[144] S.-W. Choi, I.W. Cheong, J.-H. Kim, Y. Xia, Preparation of uniform microspheres using a simple fluidic device and their crystallization into close-packed lattices, Small 5(4) (2009) 454-459.

[145] J. Tan, G. Zhao, Y. Lu, Z. Zeng, M.A. Winnik, Synthesis of PMMA microparticles with a narrow size distribution by photoinitiated RAFT dispersion polymerization with a macromonomer as the stabilizer, Macromolecules 47(19) (2014) 6856-6866.

[146] A.M. Telford, B.T.T. Pham, C. Neto, B.S. Hawkett, Micron-sized polystyrene particles by surfactant-free emulsion polymerization in air: Synthesis and mechanism, J. Polym. Sci., Part A: Polym. Chem. 51(19) (2013) 3997-4002.

[147] Y.S. Zhang, K.P. Regan, Y. Xia, Controlling the pore sizes and related properties of inverse opal Scaffolds for tissue engineering applications, Macromol. Rapid Commun. 34(6) (2013) 485-491.

[148] Y.S. Zhang, S.-W. Choi, Y. Xia, Inverse opal scaffolds for applications in regenerative medicine, Soft Matter 9(41) (2013) 9747-9754.

[149] P.X. Ma, J.-W. Choi, Biodegradable polymer scaffolds with well-defined interconnected spherical pore network, Tissue Eng. 7(1) (2001) 23-33.

[150] S.-W. Choi, Y. Zhang, Y. Xia, Three-dimensional scaffolds for tissue engineering: the importance of uniformity in pore size and structure, Langmuir 26(24) (2010) 19001-19006.

[151] L. Xia, Y. Shang, X. Chen, H. Li, X. Xu, W. Liu, G. Yang, T. Wang, X. Gao, R. Chai, Oriented Neural Spheroid Formation and Differentiation of Neural Stem Cells Guided by Anisotropic Inverse Opals, Front Bioeng Biotechnol 8(848) (2020).

[152] J. Lu, F. Zheng, Y. Cheng, H. Ding, Y. Zhao, Z. Gu, Hybrid inverse opals for regulating cell adhesion and orientation, Nanoscale 6(18) (2014) 10650-10656.

[153] X. Zhang, Y. Li, D. He, Z. Ma, K. Liu, K. Xue, H. Li, An effective strategy for preparing macroporous and self-healing bioactive hydrogels for cell delivery and wound healing, Chem. Eng. J. 425 (2021) 130677.

[154] D. Zaeim, M. Sarabi-Jamab, B. Ghorani, R. Kadkhodaee, R.H. Tromp, Electrospray assisted fabrication of hydrogel microcapsules by single- and double-stage procedures for encapsulation of probiotics, Food Bioprod. Process. 102 (2017) 250-259.

[155] G.F. Christopher, S.L. Anna, Microfluidic methods for generating continuous droplet streams, J. Phys. D Appl Phys 40(19) (2007) R319.

[156] J. Cui, Y. Wang, A. Postma, J. Hao, L. Hosta-Rigau, F. Caruso, Monodisperse polymer capsules: tailoring size, shell thickness, and hydrophobic cargo loading via emulsion templating, Adv. Funct. Mater. 20(10) (2010) 1625-1631.

[157] M.E. Helgeson, S.C. Chapin, P.S. Doyle, Hydrogel microparticles from lithographic processes: novel materials for fundamental and applied colloid science, Curr. Opin. Colloid. Interface. Sci. 16(2) (2011) 106-117.

[158] T.J. Hinton, Q. Jallerat, R.N. Palchesko, J.H. Park, M.S. Grodzicki, H.J. Shue, M.H. Ramadan, A.R. Hudson, A.W. Feinberg, Three-dimensional printing of complex biological structures by freeform reversible embedding of suspended hydrogels, Sci Adv 1(9) (2015) e1500758.

[159] A.C. Daly, L. Riley, T. Segura, J.A. Burdick, Hydrogel microparticles for biomedical applications, Nat. Rev. Mater. 5(1) (2020) 20-43.

[160] S. Liang, Y. Guan, Y. Zhang, Layer-by-layer assembly of microgel colloidal crystals via photoinitiated alkyne–azide click reaction, ACS Omega 4(3) (2019) 5650-5660.
[161] S. Xin, O.M. Wyman, D.L. Alge, Assembly of PEG microgels into porous cell-Instructive 3D scaffolds via thiol-ene click chemistry, Adv. Healthc. Mater. 7(11) (2018) e1800160.
[162] R.A. Herman, X. Zhu, E. Ayepa, S. You, J. Wang, Advances in the one-step approach of polymeric materials using enzymatic techniques, Polymers, 2023.
[163] Z. Yu, J. Liu, C.S.Y. Tan, O.A. Scherman, C. Abell, Supramolecular nested microbeads as building blocks for macroscopic self-healing scaffolds, Angew. Chem., Int. Ed. 57(12) (2018) 3079-3083.
[164] Y.L. Han, Y. Yang, S. Liu, J. Wu, Y. Chen, T.J. Lu, F. Xu, Directed self-assembly of microscale hydrogels by electrostatic interaction, Biofabrication 5(3) (2013) 035004.
[165] Y.K. Jo, D. Lee, Biopolymer microparticles prepared by microfluidics for biomedical applications, Small 16(9) (2020) 1903736.
[166] Y.T. Matsunaga, Y. Morimoto, S. Takeuchi, Molding cell beads for rapid construction of macroscopic 3D tissue architecture, Adv. Mater. 23(12) (2011) H90-H94.
[167] Y. Du, M. Ghodousi, E. Lo, M.K. Vidula, O. Emiroglu, A. Khademhosseini, Surface-directed assembly of cell-laden microgels, Biotechnol. Bioeng. 105(3) (2010) 655-62.
[168] F. Xu, C.A. Wu, V. Rengarajan, T.D. Finley, H.O. Keles, Y. Sung, B. Li, U.A. Gurkan, U. Demirci, Three-dimensional magnetic assembly of microscale hydrogels, Adv Mater 23(37) (2011) 4254-60.
[169] F. Xu, T.D. Finley, M. Turkaydin, Y. Sung, U.A. Gurkan, A.S. Yavuz, R.O. Guldiken, U. Demirci, The assembly of cell-encapsulating microscale hydrogels using acoustic waves, Biomater. 32(31) (2011) 7847-7855.
[170] S.E. Chung, W. Park, S. Shin, S.A. Lee, S. Kwon, Guided and fluidic self-assembly of microstructures using railed microfluidic channels, Nat. Mater. 7(7) (2008) 581-587.
[171] H. Zhang, Y. Cong, A.R. Osi, Y. Zhou, F. Huang, R.P. Zaccaria, J. Chen, R. Wang, J. Fu, Direct 3D printed biomimetic scaffolds based on hydrogel microparticles for cell spheroid growth, Adv. Funct. Mater. 30(13) (2020) 1910573.
[172] Q. Feng, D. Li, Q. Li, X. Cao, H. Dong, Microgel assembly: fabrication, characteristics and application in tissue engineering and regenerative medicine, Bioact. Mater. 9 (2022) 105-119.
[173] B.B. Mandal, S.C. Kundu, Cell proliferation and migration in silk fibroin 3D scaffolds, Biomaterials 30(15) (2009) 2956-2965.
[174] A.J. Hibbitts, Z. Kočí, S. Kneafsey, A. Matsiko, L. Žilić, A. Dervan, P. Hinton, G. Chen, B. Cavanagh, J.K. Dowling, C.E. McCoy, C.T. Buckley, S.J. Archibald, F.J. O'Brien, Multi-factorial nerve guidance conduit engineering improves outcomes in inflammation, angiogenesis and large defect nerve repair, Matrix Biol. 106 (2022) 34-57.
[175] J. Zhang, A. Zhou, A. Deng, Y. Yang, L. Gao, Z. Zhong, S. Yang, Pore architecture and cell viability on freeze dried 3D recombinant human collagen-peptide (RHC)–chitosan scaffolds, Mater. Sci. Eng. C 49 (2015) 174-182.
[176] Y.S. Hwang, C. Zhang, S. Varghese, Poly(ethylene glycol) cryogels as potential cell scaffolds: effect of polymerization conditions on cryogel microstructure and properties, J. Mater. Chem. 20(2) (2010) 345-351.
[177] F.J. O'Brien, B.A. Harley, I.V. Yannas, L. Gibson, Influence of freezing rate on pore structure in freeze-dried collagen-GAG scaffolds, Biomaterials 25(6) (2004) 1077-1086.
[178] H. Kirsebom, D. Topgaard, I.Y. Galaev, B. Mattiasson, Modulating the Porosity of Cryogels by Influencing the Nonfrozen Liquid Phase through the Addition of Inert Solutes, Langmuir 26(20) (2010) 16129-16133.
[179] R.V. Ivanov, V.I. Lozinsky, S.K. Noh, S.S. Han, W.S. Lyoo, Preparation and characterization of polyacrylamide cryogels produced from a high-molecular-weight precursor. I. Influence of the reaction temperature and concentration of the crosslinking agent, J. Appl. Polym. Sci. 106(3) (2007) 1470-1475.
[180] X.P. Su, Q. Zhang, Q.W. Zhong, L. Liu, H.Y. Gao, R.J. Meng, J.M. Yao, Macroporous Cellulose-based Cryogels with Tunable Porous Structure and Surface Functional Groups, Fibers and Polymers 17(5) (2016) 712-720.
[181] R.V. Ivanov, V.I. Lozinsky, S.K. Noh, Y.R. Lee, S.S. Han, W.S. Lyoo, Preparation and characterization of polyacrylamide cryogels produced from a high-molecular-weight precursor. II. The influence of the molecular weight of the polymeric precursor, J. Appl. Polym. Sci. 107(1) (2008) 382-390.
[182] M. Zhai, F. Ma, J. Li, B. Wan, N. Yu, Preparation and properties of cryogel based on poly(hydroxypropyl methacrylate), J. Biomater. Sci. Polym. Ed. 29(12) (2018) 1401-1425.
[183] S. Mane, S. Ponrathnam, N. Chavan, Synthesis and characterization of hypercrosslinked hydroxyl functionalized co-polymer beads, Eur. Polym. J. 59 (2014) 46-58.
[184] J. Wei, C. Yin, H. Wang, Q. Wang, Polyampholyte-doped aligned polymer hydrogels as anisotropic electrolytes for ultrahigh-capacity supercapacitors, J. Mater. Chem. A 6(1) (2018) 58-64.
[185] P. Perez, F. Plieva, A. Gallardo, J. San Roman, M.R. Aguilar, I. Morfin, F. Ehrburger-Dolle, F. Bley, S. Mikhalovsky, I.Y. Galaev, B. Mattiasson, Bioresorbable and nonresorbable macroporous thermosensitive hydrogels prepared by cryopolymerization. role of the cross-linking agent, Biomacromolecules 9(1) (2008) 66-74.
[186] N.A. Sears, T.S. Wilems, K.A. Gold, Z. Lan, S.N. Cereceres, P.S. Dhavalikar, R. Foudazi, E.M. Cosgriff-Hernandez, Hydrocolloid inks for 3D printing of porous hydrogels, Adv. Mater. Technol. 4(2) (2019) 1800343.

[187] M. Moazzam, A. Shehzad, D. Sultanova, F. Mukasheva, A. Trifonov, D. Berillo, D. Akilbekova, Macroporous 3D printed structures for regenerative medicine applications, Bioprinting 28 (2022) e00254.

[188] J.P.K. Armstrong, M. Burke, B.M. Carter, S.A. Davis, A.W. Perriman, 3D bioprinting using a templated porous bioink, Adv. Healthc. Mater. 5(14) (2016) 1724-1730.

[189] Z. Yue, F. Wen, S. Gao, M.Y. Ang, P.K. Pallathadka, L. Liu, H. Yu, Preparation of three-dimensional interconnected macroporous cellulosic hydrogels for soft tissue engineering, Biomater. 31(32) (2010) 8141-8152.

[190] S. Zhou, A. Bismarck, J.H.G. Steinke, Interconnected macroporous glycidyl methacrylate-grafted dextran hydrogels synthesised from hydroxyapatite nanoparticle stabilised high internal phase emulsion templates, J. Mater. Chem. 22(36) (2012) 18824-18829.

[191] J.H. Lee, Injectable hydrogels delivering therapeutic agents for disease treatment and tissue engineering, Biomater. Res. 22(1) (2018) 27.

[192] Y. Tang, S. Lin, S. Yin, F. Jiang, M. Zhou, G. Yang, N. Sun, W. Zhang, X. Jiang, In situ gas foaming based on magnesium particle degradation: A novel approach to fabricate injectable macroporous hydrogels, Biomater. 232 (2020) 119727.

[193] B. Falk, S. Garramone, S. Shivkumar, Diffusion coefficient of paracetamol in a chitosan hydrogel, Mater. Lett. 58(26) (2004) 3261-3265.

[194] N.D. Gallant, K.E. Michael, A.J. García, Cell adhesion strengthening: contributions of adhesive area, integrin binding, and focal adhesion assembly, Mol. Biol. Cell. 16(9) (2005) 4329-4340.

[195] F.J. O'Brien, B.A. Harley, I.V. Yannas, L.J. Gibson, The effect of pore size on cell adhesion in collagen-GAG scaffolds, Biomaterials 26(4) (2005) 433-441.

[196] M. Sidani, J. Wyckoff, C. Xue, J.E. Segall, J. Condeelis, Probing the microenvironment of mammary tumors using multiphoton microscopy, J Mammary Gland Biol Neoplasia 11(2) (2006) 151-163.

[197] C.M. Murphy, M.G. Haugh, F.J. O'Brien, The effect of mean pore size on cell attachment, proliferation and migration in collagen–glycosaminoglycan scaffolds for bone tissue engineering, Biomaterials 31(3) (2010) 461-466.

[198] K.G. Stenkula, C. Erlanson-Albertsson, Adipose cell size: importance in health and disease, Am. J. Physiol. Regul. Integr. Comp. Physiol. 315(2) (2018) R284-R295.

[199] D. Von Heimburg, M. Kuberka, R. Rendchen, K. Hemmrich, G. Rau, N. Pallua, Preadipocyte-loaded collagen scaffolds with enlarged pore size for improved soft tissue engineering, Int J Artif Organs 26(12) (2003) 1064-1076.

[200] F.J. O'Briena;, B.A. Harley;, M.A. Wallerb;, Ioannis V. Yannasc, L.J. Gibsond;, P.J. Prendergast, The effect of pore size on permeability and cell attachement in collagen scaffolds for tissue engineering, Technol Health Care (2007).

[201] Y. Kuboki, Q. Jin, H. Takita, Geometry of Carriers Controlling Phenotypic Expression in BMP-Induced Osteogenesis and Chondrogenesis, J. Bone Jt. Surg. 83(1_suppl_2) (2001).

[202] Y. Yin, X.-T. He, J. Wang, R.-X. Wu, X.-Y. Xu, Y.-L. Hong, B.-M. Tian, F.-M. Chen, Pore size-mediated macrophage M1-to-M2 transition influences new vessel formation within the compartment of a scaffold, Appl. Mater. Today 18 (2020) 100466.

[203] S. Panja, S. Hanson, C. Wang, EDTA-Inspired polydentate hydrogels with exceptionally high heavy metal adsorption capacity as reusable adsorbents for wastewater purification, ACS Appl. Mater. Interfaces 12(22) (2020) 25276-25285.

[204] H. Jiang, Y. Yang, Z. Lin, B. Zhao, J. Wang, J. Xie, A. Zhang, Preparation of a novel bio-adsorbent of sodium alginate grafted polyacrylamide/graphene oxide Hydrogel for the adsorption of heavy metal ion, Sci. Total Environ. 744 (2020) 140653.

[205] N. Chunshom, P. Chuysinuan, S. Techasakul, S. Ummartyotin, Dried-state bacterial cellulose (acetobacter xylinum) and polyvinyl-alcohol-based hydrogel: an approach to a personal care material, J Sci.: Adv. Mater. Devices 3(3) (2018) 296-302.

[206] S.W. Sharshir, A.M. Algazzar, K.A. Elmaadawy, A.W. Kandeal, M.R. Elkadeem, T. Arunkumar, J. Zang, N. Yang, New hydrogel materials for improving solar water evaporation, desalination and wastewater treatment: A review, Desalination 491 (2020) 114564.

[207] M.C. Wake, C.W. Patrick Jr, A.G. Mikos, Pore morphology effects on the fibrovascular tissue growth in porous polymer substrates, Cell transplantation 3(4) (1994) 339-343.

[208] M.C. Wake, C.W. Patrick, A.G. Mikos, Pore Morphology Effects on the Fibrovascular Tissue Growth in Porous Polymer Substrates, Cell Transplantation 3(4) (1994) 339-343.

[209] A.R. Calore, V. Srinivas, L. Groenendijk, A. Serafim, I.C. Stancu, A. Wilbers, N. Leoné, A.A. Sanchez, D. Auhl, C. Mota, K. Bernaerts, J.A.W. Harings, L. Moroni, Manufacturing of scaffolds with interconnected internal open porosity and surface roughness, Acta Biomaterialia 156 (2023) 158-176.

[210] B.A.C. Harley, H.-D. Kim, M.H. Zaman, I.V. Yannas, D.A. Lauffenburger, L.J. Gibson, Microarchitecture of three-dimensional scaffolds influences cell migration behavior via junction interactions, Biophys. J. 95(8) (2008) 4013-4024.

[211] S.R. Peyton, A.J. Putnam, Extracellular matrix rigidity governs smooth muscle cell motility in a biphasic fashion, Journal of cellular physiology 204(1) (2005) 198-209.

[212] T.L. Jenkins, D. Little, Synthetic scaffolds for musculoskeletal tissue engineering: cellular responses to fiber parameters, NPJ Regen. Med. 4(1) (2019) 15.

[213] M.M.C.G. Silva, L.A. Cyster, J.J.A. Barry, X.B. Yang, R.O.C. Oreffo, D.M. Grant, C.A. Scotchford, S.M. Howdle, K.M. Shakesheff, F.R.A.J. Rose, The effect of anisotropic architecture on cell and tissue infiltration into tissue engineering scaffolds, Biomater. 27(35) (2006) 5909-5917.

[214] J. Xing, N. Liu, N. Xu, W. Chen, D. Xing, Engineering complex anisotropic scaffolds beyond simply uniaxial alignment for tissue engineering, Adv. Funct. Mater. 32(15) (2022) 2110676.

[215] T.S. Stashak, E. Farstvedt, A. Othic, Update on wound dressings: Indications and best use, Clin. Techniques in Equine Pract. 3(2) (2004) 148-163.

[216] J. Zeng, X. Chen, J. Zhang, Y. Qin, K. Zhang, X. Li, H. Cui, Stem cell spheroids production for wound healing with a reversible porous hydrogel, Mater. Today Adv. 15 (2022) 100269.

[217] T. Tokatlian, C. Cam, T. Segura, Porous hyaluronic acid hydrogels for localized nonviral DNA delivery in a diabetic wound healing model, Adv. Healthc. Mater. 4(7) (2015) 1084-1091.

[218] X. Long, X. Xu, D. Sun, Y. Hong, C. Wen, Y. Xie, B. Yan, H. Zhang, Q. Ge, W. Li, L. Duan, H. Ouyang, D. Wang, Biomimetic macroporous hydrogel with a triple-network structure for full-thickness skin regeneration, Appl. Mater. Today 27 (2022) 101442.

[219] R. Wei, T. Chen, Y. Wang, Q. Xu, B. Feng, J. Weng, W. Peng, J. Wang, By endowing polyglutamic acid/polylysine composite hydrogel with super intrinsic characteristics to enhance its wound repair potential, Macromol Biosci 21(5) (2021) 2000367.

[220] M. Xu, Q. Li, Z. Fang, M. Jin, Q. Zeng, G. Huang, Y.-G. Jia, L. Wang, Y. Chen, Conductive and antimicrobial macroporous nanocomposite hydrogels generated from air-in-water Pickering emulsions for neural stem cell differentiation and skin wound healing, Biomater. Sci. 8(24) (2020) 6957-6968.

[221] M. Hamidi, A. Azadi, P. Rafiei, Hydrogel nanoparticles in drug delivery, Adv. Drug Deliv. Rev. 60(15) (2008) 1638-1649.

[222] J.K. Oh, R. Drumright, D.J. Siegwart, K. Matyjaszewski, The development of microgels/nanogels for drug delivery applications, Prog. Polym. Sci. 33(4) (2008) 448-477.

[223] X. Yang, H. Ren, H. Zhang, G. Liu, Z. Jiang, Q. Qiu, C. Yu, N. Murthy, K. Zhao, J.F. Lovell, Y. Zhang, Antibiotic cross-linked micelles with reduced toxicity for multidrug-resistant bacterial sepsis treatment, ACS Appl. Mater. Interfaces 13(8) (2021) 9630-9642.

[224] K.-a. Johnson, N. Muzzin, S. Toufanian, R.A. Slick, M.W. Lawlor, B. Seifried, P. Moquin, D. Latulippe, T. Hoare, Drug-impregnated, pressurized gas expanded liquid-processed alginate hydrogel scaffolds for accelerated burn wound healing, Acta Biomater. 112 (2020) 101-111.

[225] N. Bhattarai, J. Gunn, M. Zhang, Chitosan-based hydrogels for controlled, localized drug delivery, Adv. Drug Deliv. Rev. 62(1) (2010) 83-99.

[226] C. Chen, Y. Liu, L. Sun, G. Chen, X. Wu, J. Ren, Y. Zhao, Antibacterial porous microcarriers with a pathological state responsive switch for wound healing, ACS Appl. Bio Mater. 2(5) (2019) 2155-2161.

[227] Z. Yang, X. Ren, Y. Liu, Multifunctional 3D printed porous GelMA/xanthan gum based dressing with biofilm control and wound healing activity, Mater. Sci. Eng. C 131 (2021) 112493.

[228] S.G. Priya, A. Gupta, E. Jain, J. Sarkar, A. Damania, P.R. Jagdale, B.P. Chaudhari, K.C. Gupta, A. Kumar, Bilayer cryogel wound dressing and skin regeneration grafts for the treatment of acute skin wounds, ACS Appl. Mater. Interfaces 8(24) (2016) 15145-15159.

Chapter 2- A Nanocomposite Dynamic Covalent Crosslinked Hydrogel Loaded with Fusidic Acid for Treating Antibiotic-Resistant Infected Wounds

Samaneh Toufanian[a,1], Jody Mohammed[b,1], Ridhdhi Dave[a], Brian K. Coombes[b, c], and Todd Hoare[a *]

[a] Department of Chemical Engineering, McMaster University, 1280 Main St. W., Hamilton, ON, Canada
[b] Department of Biochemistry and Biomedical Sciences, McMaster University, 1280 Main St. W. Hamilton, ON, Canada
[c] Michael G. DeGroote Institute for Infectious Disease Research, McMaster University, Canada

[1] These authors contributed equally to this work
* To whom correspondence should be addressed: hoaretr@mcmaster.ca

Abstract

Methicillin-resistant *Staphylococcus aureus* (MRSA) is associated with high levels of morbidity and is considered a difficult-to-treat infection, often requiring non-standard treatment regimens and antibiotics. Herein, we report an antimicrobial poly(oligoethylene glycol methacrylate) (POEGMA)-based composite hydrogel loaded with fusidic acid-encapsulating self-assembled poly lactic acid-*b*-poly(oligo(ethylene glycol) methyl ether methacrylate) (PLA-POEGMA) nanoparticles for the treatment of MRSA-infected skin wounds. The inclusion of the self-assembled nanoparticles (380 nm diameter when loaded with fusidic acid) does not alter the favorable mechanical properties and stability of the hydrogel in the context of its use as a wound dressing, while fusidic acid (FA) can be released from the hydrogel over ~10 hours via a diffusion-controlled mechanism. The antimicrobial studies demonstrate a clear zone of inhibition *in vitro* and a 1-2 order of magnitude inhibition of bacterial growth *in vivo* in an MRSA-infected full-thickness excisional murine wound model even at very low antibiotic doses. Our approach thus can both circumvent challenges in the local delivery of hydrophobic antimicrobial compounds as well as directly deliver antimicrobials into the wound to effectively combat methicillin-resistant infections using a fraction of the drug dose required using other clinically relevant strategies

Graphical Abstract

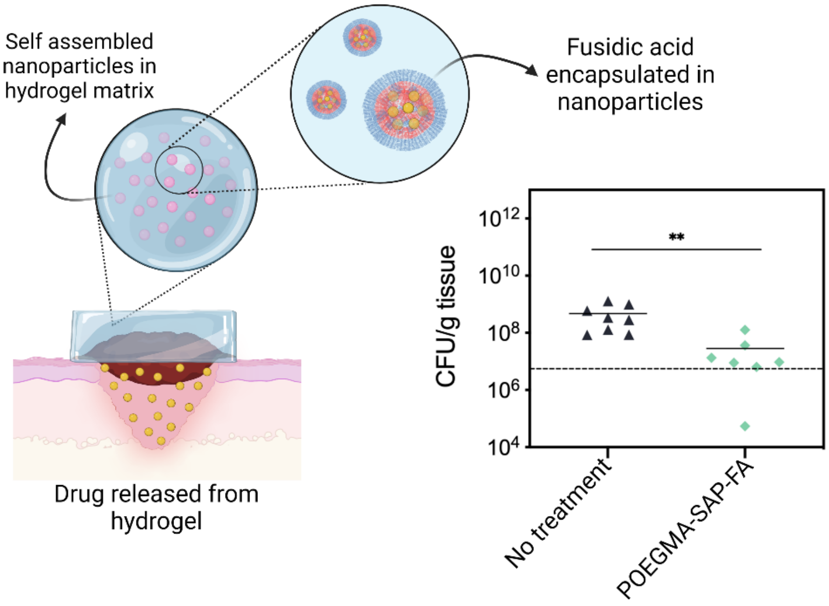

2.1. Introduction

Complications arising from skin wounds and abrasions of varying sizes, shapes, and causes represent one of the most commonly treated medical conditions worldwide [1, 2]. While the body's innate immune response and the natural wound healing process are in most cases effective in dealing with wounds, many pathogens can compromise the natural wound healing process. Such pathogens can lead to severe systemic complications and/or incomplete wound closure [3-5], issues that are occurring with increasing incidence worldwide [6]. While recent advancements in engineered wound dressings have aimed to address these complications via the incorporation of nanomaterials, plant-derived products, negative pressure therapies, or other strategies [7-9], challenges remain in treating compromised wounds infected with one or more of the *ESKAPE* pathogens that show antibiotic resistance [10-12]. Methicillin-resistant *S. aureus* (MRSA) has in particular demonstrated notably decreasing levels of susceptibility to several classes of antibiotics that have been used for *S. aureus* treatment since 1961 [13], leading to MRSA being identified as a key public health concern given the dwindling options available to treat community or hospital-acquired infections.

Among leading potential treatments for MRSA infections is fusidic acid (FA), a small molecule produced by a strain of *Fusidium* fungus [14]. FA is an ideal candidate for treating MRSA and other Gram-positive pathogens due to its low toxicity, minimal resistance levels, and lack of identified cross-resistance with other available antibiotics [15]. However, the low water solubility of FA is a major challenge in formulating this drug in clinical applications [14]. While FA can be formulated in aqueous solutions using its salt (sodium fusidate), solubility is maintained only under certain pH ranges that do not necessarily reflect the pH of some wounds [16]; furthermore, retention of the highly water soluble salt form in the wound tends to be short-lived, requiring larger administered doses and/or more frequent administration to successfully treat the infection [17]. As such, current approaches have aimed to formulate FA primarily in its poorly soluble free base form as either a topical application (cream or ointment) or as an oral dosage tablet [18, 19]. However, either formulation approach typically requires the use of high drug dosages to ensure that sufficient drug reaches the infection site to effectively treat the infection while minimizing the potential for the development of further drug resistance [20], leading to unwanted, systemic side-effects that can otherwise impact the rate or success of the intended therapy [21]. As such, there is a significant need to develop improved delivery approaches for localized wound therapy using fusidic acid. Developing such an approach is even more critical for enabling the effective delivery of many other emerging antibiotics that have efficacy in treating resistant bacterial strains but do not have a comparable stable or effective soluble form to sodium fusidate [16, 22, 23]; indeed, over 40% of newly discovered pharmaceutical compounds are removed from the product development pipeline due to their insufficient solubility and thus low bioavailability [24].

Hydrogel-based wound dressings offer a potential solution to the combination of existing challenges in infected wound management in that: (1) hydrogels can both absorb and retain water, meeting the requirements for exudate removal/wound hydration and leading to an easier removal from the wounds following treatment [25]; (2) hydrogels can provide a physical barrier to protect the healing tissue [26]; (3) the pore size and chemistry of a hydrogel can be controlled to meter the rate of local drug delivery via a combination of diffusion and affinity-based mechanisms [17, 27]; (4) hydrogels can locally deliver the drug to the wound, avoiding (or at least minimizing) systemic side-effects while in principle requiring less overall drug to achieve the desired clinical effect; and (5) hydrogels can be used to physically entrap or chemically tether a variety of other types of controlled drug delivery vehicles, allowing for the incorporation of a hydrophobic drug delivery vehicle within the otherwise hydrophilic gel network [28]. An array of methods has been developed to produce drug-eluting hydrogels in this context, including leveraging ionic interactions between the hydrogel matrix and bioactive compounds [29], covalent tethering of antibiotics to hydrogel matrices [30], or incorporating nanoparticles [31], microparticles [32, 33], microgels [34, 35], liposomes [36, 37], or micelles [38] loaded with (typically poorly water soluble) bioactive compounds into the hydrogel matrix. Block copolymer-based nanoparticles created via the self-assembly of amphiphilic block copolymers in water have attracted particular interest in this context given their capacity to load high quantities of poorly water-soluble drugs while also enabling control over the hydrogel-nanoparticle interface [39, 40], leading to the fabrication of mechanically strong nanocomposite hydrogels that can enable sustained drug release while still maintaining the bulk materials properties essential for use as functional wound dressings [41]. However, relatively few examples of hydrogel nanocomposite-based wound dressings for treating antibiotic-resistant infections have been reported, with the majority of the reported strategies aiming to treat infections using antimicrobial polypeptides that have limited shelf life and are expensive to produce. Herein, we report a nanocomposite hydrogel that enables effective loading and extended release of fusidic acid to treat MRSA-based wound infections. A poly(lactic acid)-block-poly(oligoethylene glycol methacrylate) (PLA-POEGMA) amphiphilic brush co-polymer is used to fabricate FA-loaded self-assembled nanoparticles (SAPs) that are subsequently encapsulated into a dynamic covalent POEGMA-based hydrogel. The hydrogel-based wound dressings, fabricated based on in situ-gelling hydrazide and aldehyde-functionalized POEGMA precursor polymers (Figure 2-1), retain strong mechanics due to the high interfacial stability between the nanoparticle and the hydrogel phase (both of which are based on the same POEGMA polymer). The nanoparticle phase enables FA loading into the hydrogel while the surrounding hydrogel enables localized and sustained antibiotic delivery. We demonstrate effective drug loading as well as effective suppression of MRSA both *in vitro* as well as in an *in vivo* murine infected wound model.

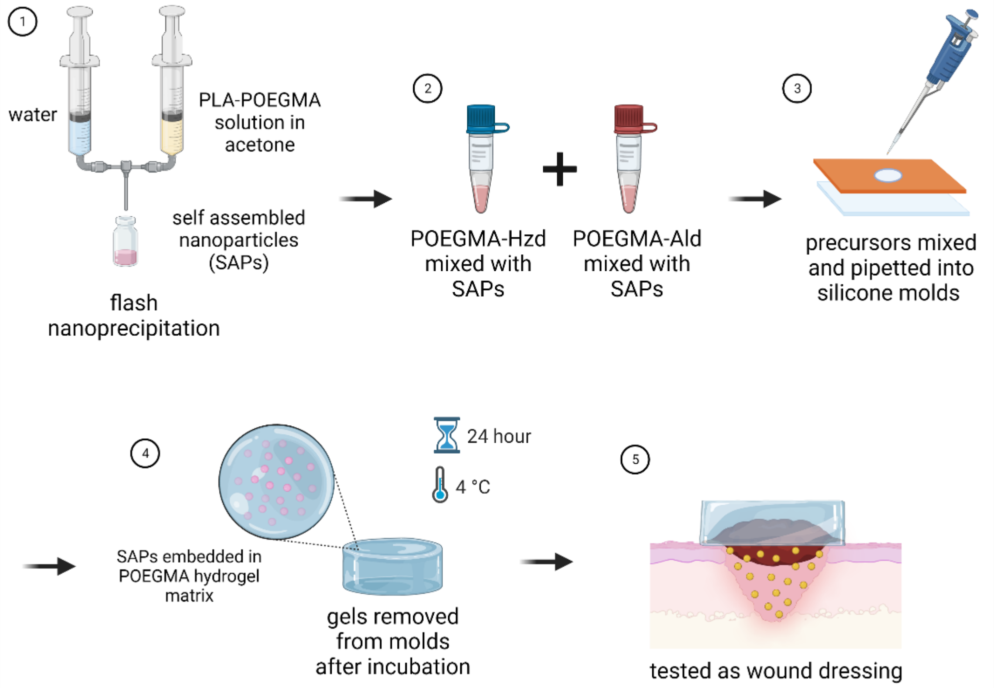

Figure 2-1- Schematic diagram depicting the fabrication of POEGMA/self-assembled nanoparticles (SAP) nanocomposite hydrogel wound dressings containing FA.

2.2. Materials and Methods

2.2.1. Materials

For hydrogel fabrication, oligo(ethylene glycol) methyl ether methacrylate with a number average molecular weight of 475 g/mol (Sigma-Aldrich, 95%) was purified using a basic aluminum-packed column to remove the inhibitors methyl ether hydroquinone and butylated hydroxytoluene prior to use. The chain transfer agent thioglycolic acid (TGA Sigma-Aldrich, 95%), the initiator 2,2'-azobis(2-methylpropionate) (AIBME, 98.5%, Wako Chemicals, Shanghai, China), acrylic acid (AA, 99% Sigma-Aldrich), 1,4-dioxane (anhydrous, Caledon Laboratory Chemicals, Georgetown, ON), adipic acid dihydrazide (ADH, 98%, Alfa Aesar), N′-ethyl-N-(3-(dimethylamino)propyl)-carbodiimide (EDC, Carbosynth, Compton CA, commercial grade), tris(hydroxymethyl)methylamine (Tris, Bio-Rad, Mississauga, ON), 6 N or 1 N hydrochloric acid (HCl, Fisher-Scientific Company, Saint-Laurent, QC), sodium chloride (NaCl, 99.0%, Sigma-Aldrich, Oakville, ON), calcium chloride ($CaCl_2$, 93%, Fisher-Scientific Company, Saint-Laurent, QC), sodium hydroxide (NaOH, Sigma-Aldrich, Oakville, ON), bovine serum albumin (BSA, lyophilized powder, ≥96%, Sigma-Aldrich, Oakville, ON), fusidic acid (FA, >98% purity, Ambeed, Arlington Heights, IL), and N,N-dimethylformamide (DMF, Caledon Laboratory Chemicals, Georgetown, ON) were all used as received. N,N-dimethylaminoethyl methacrylate (DMAEMA) was synthesized in-house as reported previously [42]. For nanoparticle synthesis, anisole (99.7%, anhydrous), poly(L-lactide), 2-bromoisobutyry-terminated (PLA-Br, 10 kDa), copper (II) bromide ($CuBr_2$, for synthesis), tris(2-dimethylaminoethyl)amine (Me_6TREN), tin(II) 2-ethylhexanoate ($Sn(Oct)_2$, 92.2-100%), methanol (anhydrous, ≥99.9%), tetrahydrofuran (THF, anhydrous, ≥99.9% inhibitor-free), dichloromethane (DCM, ≥99.8%), and lithium bromide (ReagentPlus, >99%) (all from Sigma-Aldrich) were used as received. For mass spectrometry analysis, acetonitrile (HPLC grade, Caledon Laboratories, Georgetown, ON), ethylenediaminetetraacetic acid (EDTA, ≥99, EMD Millipore, Oakville, ON), and formic acid (for mass spectrometry, Honeywell Fluka) were used as received. Double distilled reverse osmosis water (MilliQ) was used for all experiments except for mass spectrometry, for which HPLC grade water (Sigma-Aldrich, Oakville, ON) was used.

2.2.2. POEGMA precursor polymer synthesis and characterization

Hydrazide-functionalized POEGMA (POEGMA-Hzd) was synthesized using a modified protocol based on previously established methods [43]. Briefly, purified oligo(ethylene glycol) methyl ether methacrylate (8 g), TGA (0.002 g), AIBME (0.074 g), AA (0.6 g), and 1,4-dioxane (40 mL) were added to a 500 mL round bottom flask and purged with nitrogen for at least 30 minutes under magnetic mixing (250 rpm) at room temperature. The reaction was initiated by placing the round bottom flask in a preheated oil bath (85°C) under nitrogen. After 4 hours, the reaction was stopped by purging the reaction medium with air for at least 30 minutes. The dioxane solvent was then removed using a rotary evaporator (30 minutes, 37 °C, maximum vacuum), after which a 50 mg sample of the polymer was collected for base into acid titration. The remaining polymer (~8.7 g) was dissolved in 300 mL of MilliQ water to which ADH (6.94 g) and EDC (4.58 g) were added. The pH of the solution was maintained between 4.6-4.8 by adding 1 M HCl dropwise as needed over at least 6 hours. The polymer solution was stirred overnight followed by 6 cycles of dialysis (cellulose acetate membrane, 12.5 kDa molecular weight cut-off) for at least 6 hours each against 5 L of MilliQ water. The dialyzed solution was filtered using a 0.2 µm polyethersulfone (PES) filter to remove any insoluble fraction, after which the soluble polymer solution was freeze dried. The resulting polymer was dissolved at 20 wt% in MilliQ water and stored at 4 °C until use.

Aldehyde-functionalized POEGMA (POEGMA-Ald) was synthesized using a similar protocol. In a round bottom flask, a solution of purified $OEGMA_{475}$ (8 g), TGA (0.002 g), AIBME (0.05 g), DMAEMA (0.6 g), and 1,4-dioxane (40 mL) was purged with nitrogen for at least 30 minutes under magnetic mixing (250 rpm) at room temperature. The round bottom flask was placed in a preheated oil bath (85 °C) to initiate the reaction. After 4 hours, the reaction was stopped by purging the reaction medium with air for at least 30 minutes. After the dioxane was removed using a rotary evaporator (30 minutes, 37 °C, maximum vacuum). the synthesized polymer product (~9.4 g) was dissolved in 100 mL of MilliQ water to which 100 mL of 1 M HCl was added and the resulting solution was stirred overnight to hydrolyze the acetal groups on the DMAEMA monomer. The resulting aldehyde-functionalized polymer was dialyzed for 6 cycles of 6 hours each (cellulose acetate membrane, 12.5 kDa molecular weight cut-off), filtered using a 0.2 μm PES filter, and freeze dried. Polymer precursor solution (20 wt%) was prepared in MilliQ water and stored at 4 °C until use.

The degree of functionalization of POEGMA-Hzd was determined using base-into-acid conductometric titration using 0.1 M NaOH as the titrant by comparing the carboxylic acid content of the polymer before and after the carbodiimide-mediated hydrazide functionalization step using EDC and ADH. The degree of functionalization of POEGMA-Ald was determined via nuclear magnetic resonance (^{1}H NMR) using d6-DMSO as the solvent by comparing the aldehyde peak intensity at 9.5-9.8 ppm to that of the methoxy peak at 3.35-3.45 ppm. Polymer molecular weight and dispersity were evaluated using aqueous gel permeation chromatography (GPC, Agilent 1260 infinity II, Agilent Technologies, Santa Clara, California, USA) equipped with a Superose 6 Increase 10/300 GL column (Cytiva, Toronto, ON) maintained at 30 °C for separation and using PBS with 0.05 wt% sodium azide as the solvent (solvent flow rate = 0.5 mL/min).

2.2.3. PLA-POEGMA block copolymer synthesis and characterization

Activators regenerated by electron transfer atom transfer radical polymerization (ARGET ATRP) was used to synthesize the PLA-POEGMA$_n$ block copolymers. To prepare amphiphilic block copolymer, 0.02 mmol (0.2g) of the 2-bromoisobutyryl-terminated poly(L-lactide) macroinitiator (10 kDa molecular weight) was dissolved in 6 mL anisole together with 2.02 mmol (0.96 g) of OEMGA$_{475}$, 0.0089 mmol (2 mg) of $CuBr_2$ catalyst, and 0.0156 mmol (4 µL) of the ligand Me_6TREN. The mixture was degassed with nitrogen gas for 45 minutes, after which $Sn(Oct)_2$ (0.21 mmol) was added to the reaction mixture and the polymerization was continued for 45 minutes at 70 °C under constant stirring. To terminate polymerization, the reaction mixture was exposed to oxygen and subsequently filtered through a basic alumina column to remove $CuBr_2$ and $Sn(Oct)_2$. The resulting product was purified via 6 × 6 hours dialysis cycles against methanol and then dried using a rotary evaporator and under high vacuum (40 °C, 100 rpm, 50 mbar). The molecular weight of the polymer was determined via gel permeation chromatography using an Agilent 1260 Infinity II GPC (column: PLgel 5 um MIXED-D 300x7.5 mm, Agilent Technologies, flowrate: 0.5 mL/min, temperature: 60 °C) using DMF with 50 mL LiBr as the eluent and PEG standards (Polymer Laboratories) for calibration.

2.2.4. Preparation of self-assembled nanoparticles (SAPs)

PLA-POEGMA block copolymer (30 mg) was dissolved in 3 mL acetone via a bath sonicator-assisted process over ~2 hours, after which 2.4 mg of FA was added to reach an overall FA concentration of 0.8 mg/mL. The resulting solution was loaded into a 5 mL syringe, while a second 5 mL syringe was loaded with 3 mL MilliQ water. The particles were then generated using a gas-pressurized flash nanoprecipitation mechanism in which the two syringes were attached to a 3D-printed confined impinging jet mixer fitted with a release tube leading into a collection vial containing 3 mL of MilliQ water [44]. Following collection, the acetone solvent was removed overnight via evaporation and the drug-loaded particles were centrifuged for 30 min at 50,000 × g and 15°C. The supernatant was collected to quantify the amount non-encapsulated drug, with the collected pellet resuspended in 2 mL MilliQ water (resulting in a 1.5 wt% nanoparticle suspension) for further use. Control (carrier-only) SAPs were prepared using the same procedure but omitting the FA addition step.

2.2.5. Nanoparticle characterization

The intensity-weighted hydrodynamic diameter of SAPs was quantified using dynamic light scattering. The SAP suspension was diluted in a 1:10 volume in MilliQ water prior to analysis. The average hydrodynamic diameter of the SAPs was measured using a NanoBrook 90Plus Zeta Particle Size Analyzer (Brookhaven Instruments, Holtsville, NY), with the polydispersity index (PDI) and average hydrodynamic diameter (based on six independent measurements on two samples prepared independently) calculated using the accompanying analysis software; reported error bars represent the standard error. Electrophoretic mobility measurements were performed by diluting the sample at a 1:10 volume ratio in 5.6 mM NaCl and performing a measurement using the NanoBrook 90Plus Zeta Particle Size Analyzer (Brookhaven Instruments, Holtsville, NY).

2.2.6. Gel preparation

POEGMA-SAP hydrogels were prepared by diluting the stock 20 wt% POEGMA-Hzd and POEGMA-Ald polymer precursor solutions to 15 wt% using a suspension of either the FA-loaded SAP (treatment) or the control carrier-only SAP (control) suspension prepared as described in section 2.2.4 The two precursors were pre-mixed in equal volumes and then pipetted into silicone molds of the desired size specified in each subsequent assay. Gels were allowed to reach equilibrium crosslinking in the molds (covered to avoid water evaporation) and incubated at 4°C overnight, after which they were removed from the molds using a pre-wetted spatula.

2.2.7. Swelling studies

Simulated wound fluid (SWF) containing 2% bovine serum albumin, 0.02 M calcium chloride, 0.40 M sodium chloride, and 0.08 M Tris Buffer in MilliQ water was prepared, heated to 37°C, and adjusted to pH 8.4 (the measured wound pH in the animal model used for this study as determined using pH strips) using 6 M HCl and 1 M NaOH. Gels (9.52 mm in diameter and 3.2 mm thick, n=3 per formulation) were prepared at least 18 hours prior to the experiment according to gel preparation protocol described in section 2.2.6, placed in cell culture strainers, weighed (gel + strainer mass), fully immersed in a well of a 6-well plate containing SWF preheated to 37 °C, and incubated at 37 °C under light shaking (100 rpm). At each pre-determined timepoint, gels and strainers were removed from the SWF, wicked dry using a Kimwipe, and weighed. The swelling ratio was then calculated based on equation (2-1), in which W_t is the weight of the gel and strainer combined and W_s and W_0 are the weights of the strainer and the gel respectively at the beginning of the experiment. SWF was replenished as required within the first 8 hours and fully replaced with fresh prewarmed SWF every 24 hours thereafter. Plates were sealed with parafilm to minimize evaporation of water.

$$\boldsymbol{swelling\,ratio} = \frac{\boldsymbol{W_t - W_s}}{\boldsymbol{W_0}} \tag{2-1}$$

2.2.8. Hydrogel mechanics

Hydrogel mechanics were evaluated using the Mach-1 micromechanical analyzer (Biomomentum, Montreal, PQ). POEGMA control hydrogels (excluding SAPs) and POEGMA-SAP hydrogels (without added FA) were prepared as described in section 2.2.6 by pipetting 450 μL of an equal volume mixed precursor polymer solution (with or without SAPs) into silicone molds (12.7 mm in diameter and 3.2 mm thickness) and ensuring any bubbles were removed before gelation was completed. Samples were left to crosslink (covered to avoid water evaporation) at 4°C overnight, after which a stainless steel spatula pre-wetted in MilliQ water was used to remove the crosslinked gels from the molds. To assess the compressive modulus of the hydrogels, each gel was compressed by 15% of its original thickness at a 1% strain rate to obtain the stress-strain curve, with the resulting uniaxial stress (in the direction of compression) recorded. The compressive elastic modulus was calculated using the accompanying analysis software. To assess the shear storage and loss moduli of the hydrogels, a strain sweep was first performed on both types of gels to determine the linear viscoelastic region, after which a frequency sweep was performed on each gel at 0.0175 radians of strain (equivalent to 1 degree). The shear moduli were calculated using the accompanying analysis software using the sinusoid analysis option.

2.2.9. In vitro drug release kinetics

Gels containing with FA were prepared as described in section 2.2.6 by pipetting 35 µL of premixed hydrogel precursor solutions into silicone molds (5.2 mm in diameter, 3.2 mm thickness), allowing the materials to gel, removing the gels from the silicone molds, and then immersing the resulting disks in SWF (5 mL) preheated to 37 °C. For the duration of the experiment, samples were stored in a shaking incubator (37 °C, 100 rpm) protected from light. At each pre-determined timepoint, 500 µL of the release medium was collected and replaced with fresh SWF. The samples collected were stored at –10 °C until analysis using liquid chromatography/mass spectrometry (LC/MS). For LC/MS analysis, 50 µL of each collected drug release sample was placed into a microcentrifuge tube to which 200 µL of ice-cold acetonitrile containing 0.1% formic acid and 56 ng/mL of fusidic acid-d6 (used as the internal standard) was added to precipitate out the BSA. The tubes were vortexed for 1 minute and then centrifuged at 18,000 × g for 15 minutes to pellet out the precipitate. A volume of 100 µL was removed from the top and diluted 10× with acetonitrile containing 0.1% formic acid and 45 ng/mL of fusidic acid-d6 to ensure the measured FA concentration falls within the established standard curve. A 5 µL aliquot of this resulting solution was then injected into an Agilent 1290 Infinity II high performance liquid chromatograph equipped with an Agilent 6495C iFunnel QQQ mass spectrometer for detection (Agilent, Santa Clara, CA, USA). Each sample was prepared once and injected in duplicate. The autosampler was maintained at 10˚C throughout the analysis, while the analytical column was maintained at 30 ˚C. Separation of the analytes was achieved on an Agilent RRHD Eclipse Plus C18 analytical column (100 mm × 2.1 mm, i.d., 1.8 µm) using mobile phases consisting of (A) 0.1% (v/v) formic acid in water and (B) 0.1% (v/v) formic acid in acetonitrile using a constant flow of 0.3 mL/min. The separation of analytes was achieved by a linear solvent gradient ramping from 5% B to 97% B over seven minutes, holding at 97% B for 30 s (for analyte elution), ramping back down to 5% B over 30 s, and re-equilibrating the column at 97% B for an additional 2 minutes prior to the next sample addition (10 minute total run time). Electrospray ionization (ESI) in negative mode was used for multiple reaction monitoring and quantification of analytes, with full details of the mass spectrometry measurement and data analysis summarized in the supporting information section 2.7.1. Calibration was performed based on FA stocks prepared in blank solvent at low, mid, and high concentrations (6.25, 125 and 250 µg/mL). The cumulative drug release profile was determined using equation (2-2)), in which *C(t)* is sample concentration at time t (as determined via mass spectrometry) and *P(t-1)* is percentage cumulative drug release before time *t* [45].

$$\boldsymbol{Cumulative\ release\ P(t) = Release\ bath\ volume\ (V) \times C(t) + P(t-1)} \qquad \textbf{2-2)}$$

2.2.10. *In vitro bacterial growth inhibition assay*

An overnight culture of *Staphylococcus aureus* Rosenbach strain USA 300 was grown in LB broth (37 ˚C, 230 rpm shaking), after which a sterile inoculum loop was used to transfer and spread ~10 µL of bacterial culture onto prepared LB agar plates. Treatment disks (POEGMA-SAP-FA hydrogels prepared in silicone molds of 5.2 mm diameter and 3.2 mm thickness) were immediately placed in triplicate on the plates, with control disks (POEGMA-SAP without loaded FA) also added to the same plate to confirm typical bacteria growth in the absence of the loaded drug. Plates were inoculated at 37°C for 16 to 18 h. Zones of inhibition were measured physically with a ruler to 0.1 cm accuracy to assess the effective release of drug from the hydrogel disks.

2.2.11. In vivo skin wound studies

Animal experiments were conducted according to the guidelines set by the Canadian Council on Animal Care and the Province of Ontario using protocols approved by the Animal Review Ethics Board and McMaster University under Animal Use Protocol #20-12-41. Six to eight week old female BALB/c mice (Charles River Laboratories) were anesthetized using inhalant isoflurane. Buprenorphine (0.1 mg/kg) was administered intraperitoneally and eye gel was applied pre-procedure. A 2 cm^2 patch of hair was clipped from the dorsal surface, which was subsequently sterilized using a povidone-iodine wash. A plastic washer (6 mm inner diameter) was sutured in place and furthered glued down (Vetbond, 3M) for reinforcement. A 5 mm diameter full-thickness excisional wound was then created inside the inner washer opening using a biopsy punch. Wounds were immediately infected with a bacterial inoculum of 5×10^6 CFU of *Staphylococcus aureus* USA 300 suspended in PBS, after which the opening was covered with a layer of adhesive film (Opsite, Smith&Nephew) to ensure proper wound bed moisture. The infection was left to establish for one hour prior to the placement of treatment gel (POEGMA-SAP-FA hydrogel or POEGMA-SAP control hydrogel) inside the excised wound area. Mice were monitored for weight change and body condition scoring for 48 h at 24 h intervals, with replacement of the adhesive film layer to retain wound moisture performed whenever necessary. Following, the mice were euthanized and infected wound tissue and spleen samples were collected post-mortem, homogenized in phosphate buffered saline (PBS) (Retsch Mixer Mill 400, 30/s, 10 min), and plated on LB plates supplemented with oxacillin to quantify residual bacterial loads. Each reported data point represents one independent experiment for each treatment group, with n=8 independent experiments performed for each group. Statistical significance was determined using a non-parametric Kruskal-Wallis test (ns-no significance, $*p<0.05$, $**p<0.01$, $***p<0.001$).

2.3. Results and discussion

2.3.1. Polymer synthesis and characterization

The *in situ*-gelling POEGMA polymer precursors POEMGA-Hzd and POEGMA-Ald were prepared by chain transfer radical polymerization as per previous reports [43], with the key properties of the reactive precursor polymers used to prepare the hydrogels summarized in Table 2-1. All molecular weights were well below the renal cut-off, suggesting the potential to clear any polymer that may degrade from the hydrogel dressing over the time period of the experiment [42]. Furthermore, the experimentally measured degrees of functionalization of the aldehyde and hydrazide groups matched well with the target values, confirming reproducible synthesis of the gel precursor polymers.

Table 2-1-Molecular weight and degree of functionalization of hydrazide and aldehyde-functionalized POEGMA precursor polymers and self-assembled nanoparticle precursor PLA-POEGMA block copolymer

	M_n (kDa)	Dispersity Đ	Target Degree of Functionalization	Actual Degree of Functionalization
POEGMA-Hzd	10.0	4.3	30%	34%[a]
POEGMA-Ald	12.6	4.5	30%	32%[b]
PLA-POEGMA	17.5	1.4	N/A	N/A

[a] from conductometric titration; [b] from ^1H NMR

2.3.2. Self-assembled particle characterization

The PLA-POEGMA amphiphilic block copolymer precursor was synthesized via activators regenerated by electron transfer (ARGET) ATRP to perform chain extension on a brominated PLA macroinitiator. GPC analysis indicates an overall number average molecular weight of 17.5 kDa (Table 2-1). The resulting polymers were then processed using flash nanoprecipitation to create self-assembled nanoparticles (SAPs), with FA drug-loaded SAPs fabricated by co-dissolving (and subsequently co-precipitating) FA in the PLA-POEGMA polymer precursor solution. A comparison of the average hydrodynamic diameter values for carrier-only SAP (no drug) and FA-loaded SAP shows an approximate 1.4-fold increase in the average hydrodynamic diameter of the nanoparticles when FA was incorporated(Table 2-2), suggestive of successful encapsulation of FA; a non-paired two-tailed t-test highlighted that this size difference was statistically significant ($n=12$, $p<0.05$).

Table 2-2- Average hydrodynamic diameter and polydispersity index of self-assembled nanoparticles without added FA (Carrier-Only SAP) and with 0.8 mg/mL FA in the precursor solution (FA-Loaded SAP)

	Carrier-Only SAP	FA-Loaded SAP
Hydrodynamic diameter (nm)	285 ± 1	385 ± 12
Polydispersity Index (PDI)	0.26 ± 0.01	0.32 ± 0.01

Particle size distribution analysis indicates that while nanoparticles prepared with or without drug have a bimodal size distribution, those prepared with FA exhibit a significantly broader distribution (Figure 2-2). This result, consistent with other studies (including our own with similar block copolymers [44]), is attributed to the co-precipitation of the hydrophobic drug altering the aggregation kinetics of the block copolymers and shifting the overall hydrophobic-hydrophilic balance of the system such that less surface area can be effectively stabilized. Note that the presence of the small aggregate fraction (which is disproportionately accentuated in intensity-weighted distribution analysis) is not necessarily problematic in this application given that the aggregate fraction is still colloidally stable and the nanoparticles will be fully encapsulated inside the gel throughout the duration of their practical use in the wound dressing.

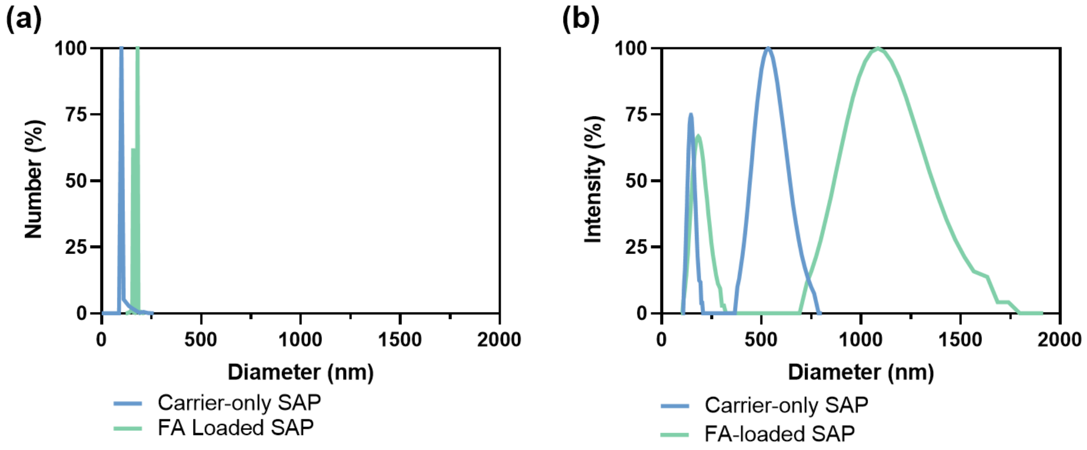

Figure 2-2- Representative DLS results showing the particle size distribution by (a) number averaging and (b) intensity averaging for carrier-only SAP and FA-loaded SAP

2.3.3. Hydrogel fabrication and characterization

Hydrogels were formed by pre-mixing equal volumes of the hydrazide and aldehyde-functionalized precursor polymer solutions POEGMA-Hzd and POEGMA-Ald (15 wt%) with 0.37 wt% of SAPs (carrier-only or FA-loaded). Bulk gelation, assessed by inverting a vial containing the same precursor solution every 5 seconds to observe if the solution flows, was achieved after 80 ± 5 sec, such that the overnight gelation period allowed in this work will provide ample time to achieve an equilibrium crosslinking density. Swelling studies in SWF (Figure 2-3-a) showed no significant difference between the swelling responses of a POEGMA prepared without SAPs and POEGMA-SAP gels, indicating that neither the swelling kinetics nor swelling equilibrium of the samples is impacted by the presence of SAPs. Both samples undergo rapid swelling over the first 8 hours followed by slower continuous swelling over the subsequent 7 day observation period, with no sign of degradation or dissolution over this time. Based on the lower expected degree of hydration of the hydrogel on a wound relative to this *in vitro* experiment (in which the hydrogel was fully immersed in buffer) coupled with the typical period of changing a hydrogel based wound dressing (typically every ~3 days) [46], this result suggests that the hydrogel would not degrade on the timescale of a practical wound dressing. The observed capacity for rapid hydrogel swelling is also relevant for facilitating effective absorption of wound exudate that is generated in many types of wounds [47].

Mechanical studies show that there is no significant difference between uniaxial compressive modulus or the shear storage modulus of POEGMA hydrogels and POEGMA-SAP hydrogels ($p > 0.05$ as per an unpaired two-tailed t-test). While the inclusion of nanoparticles inside hydrogels can negatively influence the overall hydrogel mechanics [48], the high compatibility between the POEGMA outer shell on the SAPs and the POEGMA-based bulk hydrogel minimizes any potential negative interfacial SAP-hydrogel effects on mechanics. The absolute values of the moduli (shear storage modulus ~3 kPa and compressive modulus ~12 kPa) are sufficiently high that the gel is expected to withstand any mechanical stresses applied during placement on and removal from a wound; furthermore, no observable flaking or gel fracture was observed during the mechanics test. The shear storage modulus of the hydrogels also falls within the typical human skin shear storage modulus range (2-8 kPa [49]), key to reducing the discomfort patients could experience as a result of incompatible mechanics between the dressing and the surrounding skin tissue; such mechanical mismatch can also result in additional stress being placed on the sensitive healing tissue, particularly problematic for dressings that are stiffer than skin. It is worth noting that, in contrast to skin grafts, using a dressing softer than skin is not likely to significantly reduce effectiveness while perhaps increasing patient comfort.

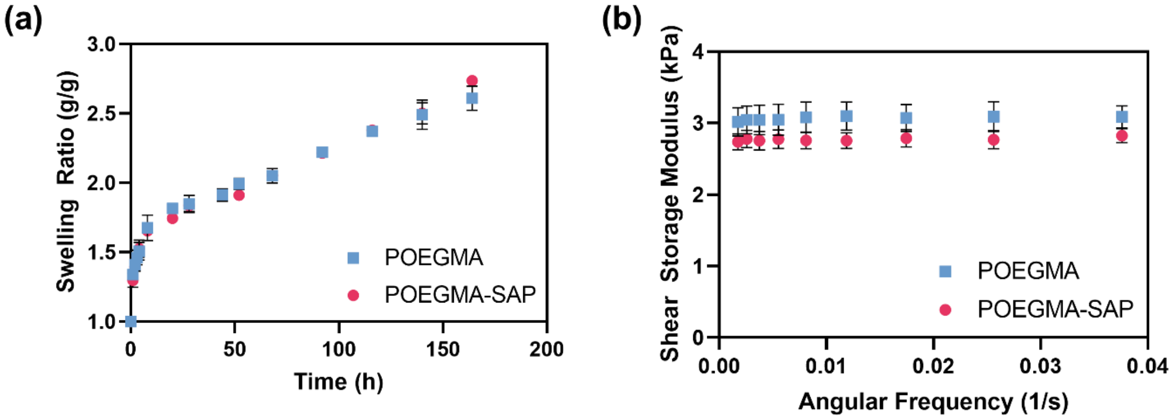

Figure 2-3- Physical properties of POEGMA hydrogel-based wound dressings: (a) swelling responses of POEGMA hydrogels with or without encapsulated SAPs in SWF (pH=8.4); (b) shear storage modulus vs. angular frequency within the linear viscoelastic regime for POEGMA hydrogels with and without encapsulated SAPs.

2.3.4. Drug Release Kinetics

Figure 2-4-a shows the cumulative drug release from the FA-loaded POEGMA-SAP-FA gels; results were normalized to the total drug encapsulated in each hydrogel as calculated based on the measured drug concentration in the supernatant from the drug loading experiment described in section 2.2.4 (8.7 ± 0.2 µg for each hydrogel). A significant burst of FA release was observed within the first 4 hours, a similar timescale to the rapid initial swelling observed (Figure 2-1-a); following, significantly slower but nonzero drug release was observed over the subsequent 120 hours, leading to a cumulative total of 4.8 ± 0.1 μg of FA (corresponding to 55.7 ± 1.4 % of the encapsulated FA) being released over the course of the experiment. To assess the mechanism of drug release, various types of drug release kinetic models were fit to the release profile. None of the zero-order or first-order models showed adequate fits (see Supporting Information 0); however, the log-log curve of the cumulative drug release normalized by the total amount of encapsulated FA shows two distinct linear sections (Figure 2-4-b), suggesting two different diffusion-controlled release steps that can each be fit well with the Korsmeyer-Peppas drug release model that is relevant for fitting diffusion-controlled drug release kinetics [50] (see Supporting Information 0 for the fits of various drug release kinetics models to this data). Equations *2-3*) and 2-4) show the best fit equation for the cumulative drug release profile. We anticipate these two steps correspond to: (1) release of drug from SAPs into the POEGMA gel phase and (2) subsequent release of drug from the POEGMA gel into the surrounding buffer. The minimum 16 hours of time between hydrogel fabrication and testing (used to ensure equilibrium crosslinking in the hydrogel) would allow for FA release from the SAPs to the hydrated POEGMA gel phase but would not allow release from the gel phase as no sink is present; as such, when the hydrogel is exposed to an external buffer at the start of the release experiment, this “pre-released” drug accounts for the rapid initial release, with the slower subsequent release corresponding to the sequential diffusion of drug from the encapsulated nanoparticles into the gel phase and finally out into the buffer. This type of release profile is beneficial in the context of antibiotic delivery, with the rapid initial release driving rapid bacterial killing (minimizing the opportunity for bacteria to develop resistance) while the slow continuous release observed in the later stages helps maintain the local drug concentration at the treatment site at a sufficient level to fully treat the infection.

$$\boldsymbol{Log}\ (\mathbf{Time}) \le \mathbf{0.493}:\ \mathbf{Log}\ (\mathbf{Drug\ Released}\ (\%) = \mathbf{0.47} \times \mathbf{Log}\ (\mathbf{Time}) + \mathbf{1.73} \qquad \mathbf{2\text{-}3)}$$

$$\boldsymbol{Log}\ (\mathbf{Time}) > \mathbf{0.493}:\ \mathbf{Log}\ (\mathbf{Drug\ Released}\ (\%) = \mathbf{0.02} \times \mathbf{Log}\ (\mathbf{Time}) + \mathbf{1.97} \qquad \mathbf{2\text{-}4)}$$

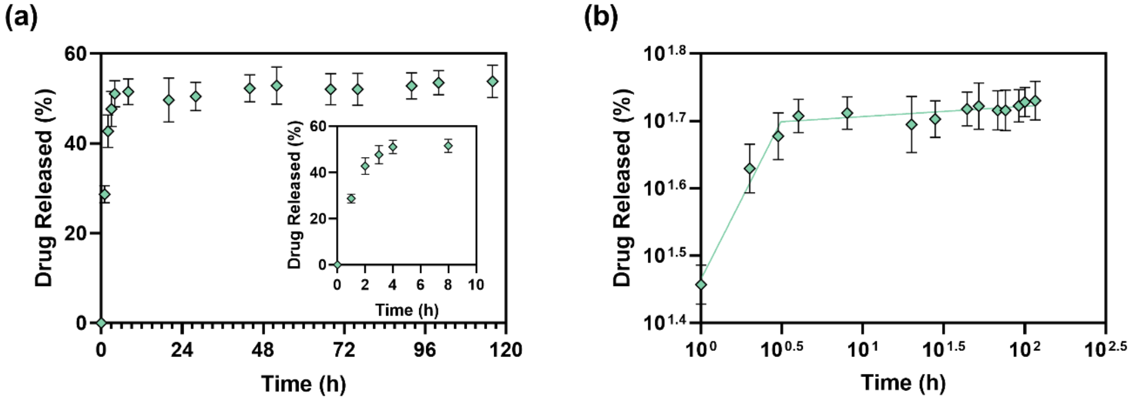

Figure 2-4- Cumulative drug release kinetics of FA from POEGMA-SAP-FA gels: (a) the cumulative mass release profile as a function of time (the inset graph shows a zoomed-in view of release over the first 10 hours) and (b) the normalized log-log transformation of the cumulative release profile (lines represent the best fit lines for the Korsmeyer-Peppas.equation for each step of the release profile). The values reported are normalized based on the total amount of encapsulated FA as measured based on a supernatant analysis of unencapsulated drug.

2.3.5. Antimicrobial Activity

Disk diffusion assays (Kirby-Bauer) were used to assess the bioactivity of FA released from POEGMA-SAP hydrogels *in vitro*. POEGMA-SAP-FA gels showed an average diameter of inhibition of 30.3 ± 0.5 mm while the control POEGMA-SAP gels showed no measurable zone of inhibition (Figure 2-5-a) confirming the capacity of the FA-loaded hydrogels to release an inhibitory concentration of FA.

Based on this result, a full-thickness excisional murine wound model was used to assess the therapeutic efficacy of the drug-loaded POEGMA-SAP-FA hydrogel compared to a carrier only POEGMA-SAP control hydrogel (FA free). Both infected wounds treated with the carrier-only POEGMA-SAP hydrogel (no FA) and the untreated control wounds showed 1-2 orders of magnitude increases in the bacterial load in the wound over the test period, with no significant difference observed between the material-only and untreated control result (Figure 2-5-b). In contrast, wounds treated with POEGMA-SAP-FA gels showed no increase in bacterial load between the time of infection and sacrifice, consistent with the bacteriostatic mode of action of FA; furthermore, the bacterial load in the wound bed was significantly lower with the POEGMA-SAP-FA hydrogel compared to either the unloaded hydrogel control or untreated control ($p<0.01$ via a two-tailed t-test). Since MRSA can cause disseminated systemic infections, we also measured the bacterial load in the spleen as a secondary measure of treatment efficacy. Application of POEGMA-SAP-FA hydrogels to MRSA-infected wounds eliminated systemic dissemination of MRSA in 5/8 mice, whereas 7/8 untreated mice and 8/8 mice treated with unloaded hydrogel had MRSA dissemination to the spleen (Figure 2-5-b). As such, POEGMA-SAP hydrogels can effectively deliver FA to treat wounds infected with MRSA and significantly reduce the risk of systemic dissemination. The presence of the hydrogel had no impact on the weight of the mice (Figure 2-5-c), suggesting the dressing itself did not induce any negative biological effects and confirming preliminary safety-of-use consistent with similar hydrogels used in other *in vivo* contexts [43].

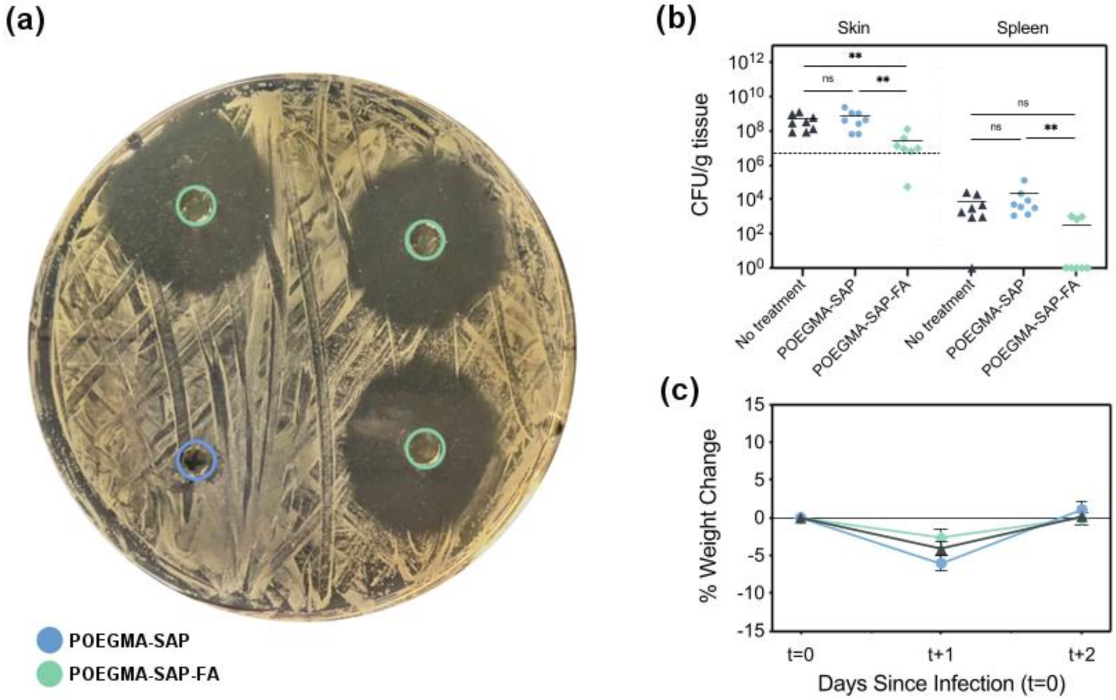

Figure 2-5- Antimicrobial activity of POEGMA-SAP hydrogels prepared with or without loaded FA: (a) *in vitro* disk diffusion assays on LB agar against MSRA show large zones of inhibition for POEGMA-SAP-FA hydrogels but no zone of inhibition for POEGMA-SAP hydrogels (bottom left corner gel). (b) *in vivo* CFU counts at the wound site (local infection) and in the spleen (systemic infection) following treatment of full thickness murine excise wounds inoculated topically with 5x10^6 CFU MRSA over a 2-day treatment period. The dashed horizontal line represents the inoculum dose, while each point represents one mouse (n=8 per group tested). (c) average % body weight change relative to the initial weight for mice with MRSA-infected wounds treated with POEGMA-SAP-FA or POEGMA-SAP relative to untreated mice (n=8, error bars represent standard error). Statistical significance was determined using a non-parametric Kruskal-Wallis test (ns-no significance, *$p<0.05$, **$p<0.01$, ***$p<0.001$).

Of note, based on the measured *in vitro* drug elution over the treatment period of our experiments, effective therapy is achieved at least 100,000 times lower antibiotic dose than is required for the currently clinically-relevant oral treatment [51] according to animal equivalent dose estimations suggested by A. B. Nair and Sherry Jacob [52]. While these values are estimations, this outcome highlights a key benefit of local delivery of antibiotics to wounds in contrast to oral treatments in terms of minimizing the total required dose and thus reducing the probability of systemic side-effects. A higher dose of drug could be delivered by simply replacing the hydrogel dressing more frequently (every 6-8 hours suggested by the *in vitro* drug release kinetics Figure 2-4). Furthermore, by combining a hydrophobic drug carrier (PLA-POEGMA self-assembled nanoparticles) with a hydrophilic bulk hydrogel (hydrazone-crosslinked POEGMA), the POEGMA-SAP gels can overcome the challenges posed by the low solubility of FA while also preserving the key benefits of hydrogels in wound healing. While FA is used as the target drug in this case, the technique described could be applied to deliver other hydrophobic antimicrobial compounds, anti-inflammatory compounds, and/or antioxidants (co-loaded in the same SAPs or loaded in separate SAPs and then mixed during the hydrogel fabrication step) to develop an array of functional wound dressings for delivering poorly water soluble drugs. In particular, this platform can be tuned to be effective against an array of bacterial strains requiring different therapeutic doses or combinations without limiting the options to charged antibiotics or requiring multi-step covalent tethering as with other common methods of creating drug-eluting hydrogels. Furthermore, although out of the scope of the current study given the animal model tested, the *in-situ* gelation capacity of the hydrazone-crosslinked POEGMA hydrogels offers potential to apply the wound dressing as a liquid on the wound that can quickly set, allowing the hydrogel to adapt to the wound area and ensure full coverage of the treatment area.

2.4. Conclusion

Nanocomposite hydrogels consisting of self-assembled FA-loaded PLA-POEGMA nanoparticles and *in situ*-gelling hydrazone-crosslinked POEGMA hydrogels can successfully treat MRSA-infected wounds. Hydrogel treatment could reduce MRSA loadings in the wound by 1-2 orders of magnitude while significantly reducing the probability of a systemic infection. The hydrogels also retain desirable physical properties (e.g. skin-mimetic mechanics and a high degree of swelling for exudate absorption) for supporting wound healing processes. The use of the described nanocomposite hydrogel thus represents an attractive approach for delivering hydrophobic antimicrobial compounds to treat MRSA infections~~,~~ particularly when compared to the currently used oral therapies. We anticipate a similar strategy could be used to encapsulate and deliver other antimicrobial agents that are currently of minimal practical use due to poor water solubility.

2.5. Acknowledgements

This work was supported by a grant to B.K.C. and T.H. from the Collaborative Health Research Projects (CHRP) program from the Canadian Institutes of Health Research and the Natural Sciences Engineering Research Council of Canada.

2.6. References

[1] R.G. Sawyer, T.L. Pruett, Wound infections, The Surgical clinics of North America 74(3) (1994) 519-536.
[2] M. Falcone, B. De Angelis, F. Pea, A. Scalise, S. Stefani, R. Tasinato, O. Zanetti, L. Dalla Paola, Challenges in the management of chronic wound infections, Journal of Global Antimicrobial Resistance 26 (2021) 140-147.
[3] S. Guo, L.A. DiPietro, Factors Affecting Wound Healing, Journal of Dental Research 89(3) (2010) 219-229.
[4] N.B. Menke, K.R. Ward, T.M. Witten, D.G. Bonchev, R.F. Diegelmann, Impaired wound healing, Clinics in Dermatology 25(1) (2007) 19-25.
[5] M.C. Robson, B.D. Stenberg, J.P. Heggers, Wound Healing Alterations Caused by Infection, Clinics in Plastic Surgery 17(3) (1990) 485-492.
[6] C.K. Sen, Human Wounds and Its Burden: An Updated Compendium of Estimates, Advances in Wound Care 8(2) (2019) 39-48.
[7] A. Naskar, K.-s. Kim, Recent Advances in Nanomaterial-Based Wound-Healing Therapeutics, Pharmaceutics 12(6) (2020) 499.
[8] K. De Brabandere, D. Jacobs-Tulleneers-Thevissen, J. Czapla, M. La Meir, G. Delvaux, F. Wellens, Negative-Pressure Wound Therapy and Laparoscopic Omentoplasty for Deep Sternal Wound Infections after Median Sternotomy, Texas Heart Institute Journal 39(3) (2012) 367-371.
[9] S. El-Ashram, L.M. El-Samad, A.A. Basha, A. El Wakil, Naturally-derived targeted therapy for wound healing: Beyond classical strategies, Pharmacological Research 170 (2021) 105749.
[10] M.S. Mulani, E.E. Kamble, S.N. Kumkar, M.S. Tawre, K.R. Pardesi, Emerging Strategies to Combat ESKAPE Pathogens in the Era of Antimicrobial Resistance: A Review, Frontiers in Microbiology 10 (2019) 539.
[11] H.D. Marston, D.M. Dixon, J.M. Knisely, T.N. Palmore, A.S. Fauci, Antimicrobial resistance, JAMA 316(11) (2016) 1193-1204.
[12] M.C. Enright, D.A. Robinson, G. Randle, E.J. Feil, H. Grundmann, B.G. Spratt, The evolutionary history of methicillin-resistant Staphylococcus aureus (MRSA), Proceedings of the National Academy of Sciences 99(11) (2002) 7687-7692.
[13] D.C. Kaur, S.S. Chate, Study of Antibiotic Resistance Pattern in Methicillin Resistant Staphylococcus Aureus with Special Reference to Newer Antibiotic, Journal of Global Infectious Diseases 7(2) (2015) 78-84.
[14] W.O. Godtfredsen, S. Jahnsen, H. Lorck, K. Roholt, L. Tybring, Fusidic Acid: a New Antibiotic., Nature 193 (1962).
[15] M.M. Curbete, H.R.N. Salgado, A Critical Review of the Properties of Fusidic Acid and Analytical Methods for Its Determination, Critical Reviews in Analytical Chemistry 46(4) (2016) 352-360.
[16] R.J. Bastin, M.J. Bowker, B.J. Slater, Salt selection and optimisation procedures for pharmaceutical new chemical entities, Organic Process Research & Development 4(5) (2000) 427-435.
[17] T. Hoare, D. Kohane, Hydrogels in drug delivery: progress and challenges, Polymer 49 (2008) 1993-2007.
[18] J. Trubiano, M.L. Grayson, 24 - Fusidic Acid, in: J.E. Bennett, R. Dolin, M.J. Blaser (Eds.), Mandell, Douglas, and Bennett's Principles and Practice of Infectious Diseases (Eighth Edition), W.B. Saunders, Philadelphia, 2015, pp. 304-309.e2.
[19] P.S. Nigam, A. Singh, METABOLIC PATHWAYS | Production of Secondary Metabolites – Fungi, in: C.A. Batt, M.L. Tortorello (Eds.), Encyclopedia of Food Microbiology (Second Edition), Academic Press, Oxford, 2014, pp. 570-578.
[20] D.Y.M. Leung, Assessing the Value of Fusidic Acid in Dermatology: Proceedings from the LEO Pharma Satellite Symposium, European Academy of Dermatology and Venerology (EADV), Vienna, 18 May 2007, Almqvist & Wiksell2008.
[21] F. Pascher, Systemic reactions to topically applied drugs, Int J Dermatol 17(10) (1978) 768-75.
[22] C. de la Fuente-Nunez, Antibiotic discovery with machine learning, Nature Biotechnology 40(6) (2022) 833-834.
[23] R. Rathinakumar, W.C. Wimley, High-throughput discovery of broad-spectrum peptide antibiotics, The FASEB Journal 24(9) (2010) 3232-3238.
[24] K.T. Savjani, A.K. Gajjar, J.K. Savjani, Drug solubility: importance and enhancement techniques, ISRN Pharmaceutics 2012 (2012) 195727.
[25] A. Francesko, P. Petkova, T. Tzanov, Hydrogel dressings for advanced wound management, Curr. Med. Chem. 25(41) (2019) 5782-5797.
[26] K. Yang, Q. Han, B. Chen, Y. Zheng, K. Zhang, Q. Li, J. Wang, Antimicrobial hydrogels: promising materials for medical application, Int J Nanomedicine 13 (2018) 2217-2263.
[27] J.J. Schmidt, J. Rowley, H.J. Kong, Hydrogels used for cell-based drug delivery, Journal of Biomedical Materials Research Part A 87A(4) (2008) 1113-1122.
[28] J. Li, D.J. Mooney, Designing hydrogels for controlled drug delivery, Nature Reviews Materials 1(12) (2016) 16071.

[29] Y.M. Kolambkar, K.M. Dupont, J.D. Boerckel, N. Huebsch, D.J. Mooney, D.W. Hutmacher, R.E. Guldberg, An alginate-based hybrid system for growth factor delivery in the functional repair of large bone defects, Biomaterials 32(1) (2011) 65-74.

[30] G.H. De Zoysa, K. Wang, J. Lu, Y. Hemar, V. Sarojini, Covalently Immobilized Battacin Lipopeptide Gels with Activity against Bacterial Biofilms, Molecules 25(24) (2020).

[31] S.C.T. Moorcroft, L. Roach, D.G. Jayne, Z.Y. Ong, S.D. Evans, Nanoparticle-Loaded Hydrogel for the Light-Activated Release and Photothermal Enhancement of Antimicrobial Peptides, ACS Applied Materials & Interfaces 12(22) (2020) 24544-24554.

[32] B. Kost, A. Kunicka-Styczyńska, A. Plucińska, K. Rajkowska, M. Basko, M. Brzeziński, Microfluidic preparation of antimicrobial microparticles composed of l-lactide/1,3-dioxolane (co)polymers loaded with quercetin, Food Chemistry 396 (2022) 133639.

[33] M. Shi, H. Zhang, T. Song, X. Liu, Y. Gao, J. Zhou, Y. Li, Sustainable Dual Release of Antibiotic and Growth Factor from pH-Responsive Uniform Alginate Composite Microparticles to Enhance Wound Healing, ACS Applied Materials & Interfaces 11(25) (2019) 22730-22744.

[34] H. Cheng, H. Liu, Z. Shi, Y. Xu, Q. Lian, Q. Zhong, Q. Liu, Y. Chen, X. Pan, R. Chen, P. Wang, J. Gao, C. Gao, Y. Zhang, K. Yue, J. Wang, Z. Shi, Long-term antibacterial and biofilm dispersion activity of an injectable in situ crosslinked co-delivery hydrogel/microgel for treatment of implant infection, Chemical Engineering Journal 433 (2022) 134451.

[35] B.C. Borro, R. Nordström, M. Malmsten, Microgels and hydrogels as delivery systems for antimicrobial peptides, Colloids Surf. B 187 (2020) 110835.

[36] J.L. Pugach, V. DiTizio, M.W. Mittelman, A.W. Bruce, F. DiCosmo, A.E. Khoury, ANTIBIOTIC HYDROGEL COATED FOLEY CATHETERS FOR PREVENTION OF URINARY TRACT INFECTION IN A RABBIT MODEL, The Journal of Urology 162(3, Part 1) (1999) 883-887.

[37] W. Gao, D. Vecchio, J. Li, J. Zhu, Q. Zhang, V. Fu, J. Li, S. Thamphiwatana, D. Lu, L. Zhang, Hydrogel Containing Nanoparticle-Stabilized Liposomes for Topical Antimicrobial Delivery, ACS Nano 8(3) (2014) 2900-2907.

[38] C. Hu, F. Zhang, L. Long, Q. Kong, R. Luo, Y. Wang, Dual-responsive injectable hydrogels encapsulating drug-loaded micelles for on-demand antimicrobial activity and accelerated wound healing, J Control Release 324 (2020) 204-217.

[39] L.E. Kass, J. Nguyen, Nanocarrier-hydrogel composite delivery systems for precision drug release, WIREs Nanomedicine and Nanobiotechnology 14(2) (2022) e1756.

[40] H. Deng, A. Dong, J. Song, X. Chen, Injectable thermosensitive hydrogel systems based on functional PEG/PCL block polymer for local drug delivery, Journal of Controlled Release 297 (2019) 60-70.

[41] H. Danafar, A. Sharafi, H. Kheiri Manjili, S. Andalib, Sulforaphane delivery using mPEG–PCL co-polymer nanoparticles to breast cancer cells, Pharmaceutical Development and Technology 22(5) (2017) 642-651.

[42] N.M.B. Smeets, E. Bakaic, M. Patenaude, T. Hoare, Injectable and tunable poly(ethylene glycol) analogue hydrogels based on poly(oligoethylene glycol methacrylate), ChemComm 50(25) (2014) 3306-3309.

[43] N.M. Smeets, E. Bakaic, M. Patenaude, T. Hoare, Injectable poly(oligoethylene glycol methacrylate)-based hydrogels with tunable phase transition behaviours: physicochemical and biological responses, Acta Biomater. 10(10) (2014) 4143-55.

[44] L.P. Sadowski, A. Singh, D.H. Luo, M.J. Majcher, I. Urosev, M. Rothenbroker, V. Kapishon, N.M.B. Smeets, T. Hoare, Functionalized poly(oligo(lactic acid) methacrylate)-block-poly(oligo(ethylene glycol) methacrylate) block copolymers: A synthetically tunable analogue to PLA-PEG for fabricating drug-loaded nanoparticles, European Polymer Journal 177 (2022) 111443.

[45] C.Y.J. Arcot Ravindran Chandrasekaran, Choong Sheau Theng, Teeba Muniandy, Selvadurai Muralidharan, Sokkalingam Arumugam Dhanaraj, In vitro studies and evaluation of metformin marketed tablets-Malaysia, J. Appl. Pharm. Sci. Volume : 1 (2011) 214-217.

[46] A. Sood, M.S. Granick, N.L. Tomaselli, Wound dressings and comparative effectiveness data, Adv Wound Care (New Rochelle) 3(8) (2014) 511-529.

[47] V. Brumberg, T. Astrelina, T. Malivanova, A. Samoilov, Modern Wound Dressings: Hydrogel Dressings, Biomedicines 9(9) (2021).

[48] H.J. Chung, T.G. Park, Self-assembled and nanostructured hydrogels for drug delivery and tissue engineering, Nano Today 4(5) (2009) 429-437.

[49] S. Park, J. Tao, L. Sun, C.-M. Fan, Y. Chen, An Economic, Modular, and Portable Skin Viscoelasticity Measurement Device for In Situ Longitudinal Studies, Molecules 24(5) (2019) 907.

[50] S. Dash, P.N. Murthy, L. Nath, P. Chowdhury, Kinetic modeling on drug release from controlled drug delivery systems, Acta Pol. Pharm. 67(3) (2010) 217-23.

[51] P. Fernandes, Fusidic Acid: A Bacterial Elongation Factor Inhibitor for the Oral Treatment of Acute and Chronic Staphylococcal Infections, Cold Spring Harb Perspect Med 6(1) (2016) a025437.

[52] A.B. Nair, S. Jacob, A simple practice guide for dose conversion between animals and human, J Basic Clin Pharm 7(2) (2016) 27-31.

2.7. Supporting Information

2.7.1. Mass spectrometry parameters

Electrospray ionization (ESI) in negative mode was used for quantification of fusidic acid (FA). Key FA-specific mass spectrometer settings used during analysis include a drying gas flow rate = 11 L/min, a drying gas temperature = 290°C, a nebulizer pressure = 30 psig, a sheath gas flow rate = 11 L/min, a sheath gas temperature = 300°C, a capillary voltage = 2000 V, a nozzle voltage = 1500 V, an acquisition rate = 1.23 cycles/s, and a retention time = 8.46 min. Deprotonated precursors (M-H)- were selected based on the intensity, and all analytes were further subjected to fragmentation. The same conditions were used for all injections, with the retention times confirmed to be consistent throughout each run and between batches. The transitions m/z 515.3 → 455.3 for FA and 521.4 → 461.3 for d6-FA spray ionization were monitored using multiple reaction monitoring (MRM).

Quantification of FA was based on the peak area measurement. Calibration curves were generated using an unweighted linear regression analysis of the standard, with the concentrations calculated from the calibration curve. Calibration standards were injected at the beginning and end of each analysis run and every 22 injections to ensure consistency. The average response of the bracketing calibration standards was used to develop the calibration curve that quantified that set of samples; three curves were generated per run, with a sample calibration curve included in Figure 2-6. Suitable sample dilutions were used to ensure the peak areas of samples were within the range of the calibration curve and the dilutions were accounted for in determining the amount of FA in the samples. The concentration in sample was calculated based on equation 2-5 in which x = the concentration (in ng/mL) of FA measured based on the calibration curve, SD is the sample dilution, and PD is the processing dilution. The average concentration between the n=2 injections is reported.

$$[\boldsymbol{fusidic}], \frac{\boldsymbol{ng}}{\boldsymbol{ml}} = \boldsymbol{x} \times \boldsymbol{SD} \times \boldsymbol{PD} \qquad \textbf{2-5)}$$

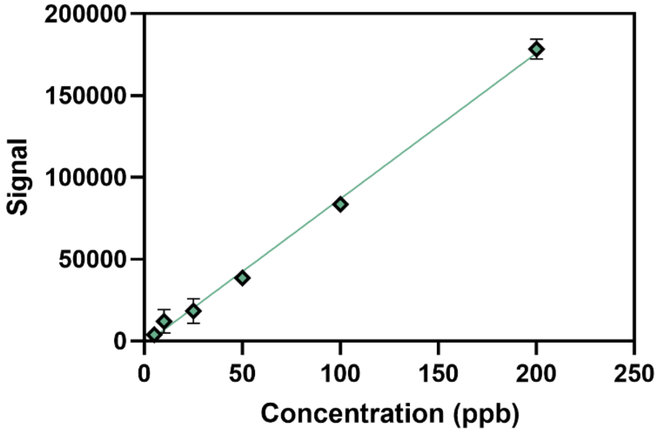

Figure 2-6-Calibration curve depicting LCMS signal vs. concentration (n=3, y=0.89x-191, R^2=0.98).

2.7.2. Drug release kinetics modeling

Zero Order Kinetics (C versus t linear)

$$\boldsymbol{Drug\ Released}\ (\%) = \boldsymbol{Slope} \times \boldsymbol{Time} + \boldsymbol{Y - intercept}$$

Best-fit values	
Slope	0.1870
Y-intercept	39.70
X-intercept	-212.3
1/slope	5.348
Std. Error	
Slope	0.04828
Y-intercept	2.738
95% Confidence Intervals	
Slope	0.08963 to 0.2843
Y-intercept	34.17 to 45.22
X-intercept	-488.9 to -124.0
Goodness of Fit	
R squared	**0.2587**

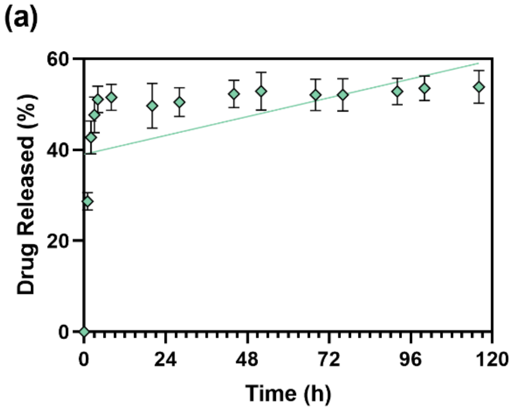

First Order Kinetics-Regression Output

$$\boldsymbol{Log\ Concentration}\ (\%) = \boldsymbol{Slope} \times \boldsymbol{Time} + \boldsymbol{Y - intercept}$$

Best-fit values	
Slope	0.001015
Y-intercept	1.655
X-intercept	-1630
1/slope	985.0
Std. Error	
Slope	0.0002535
Y-intercept	0.01488
95% Confidence Intervals	
Slope	0.0005028 to 0.001528
Y-intercept	1.625 to 1.685
X-intercept	-3337 to -1069
Goodness of Fit	
R squared	**0.2862**

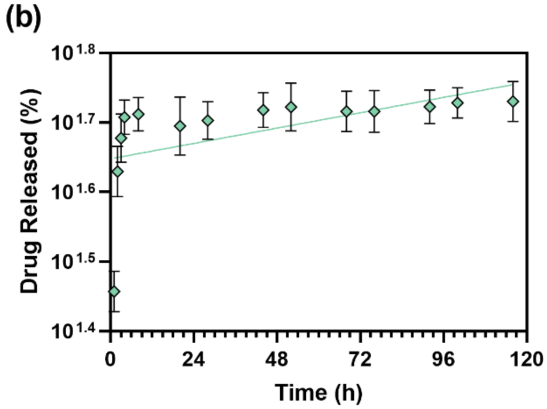

Korsmeyer-Peppas model (single diffusion coefficient regime)

$$\boldsymbol{Log\ (Concentration\ (\%)) = Slope \times Log\ (Time) + Y - intercept}$$

Best-fit values	
Slope	0.08192
Y-intercept	1.594
X-intercept	-19.45
1/slope	12.21
Std. Error	
Slope	0.01137
Y-intercept	0.01663
95% Confidence Intervals	
Slope	0.05893 to 0.1049
Y-intercept	1.560 to 1.627
X-intercept	-27.55 to -14.9
Goodness of Fit	
R squared	**0.5647**

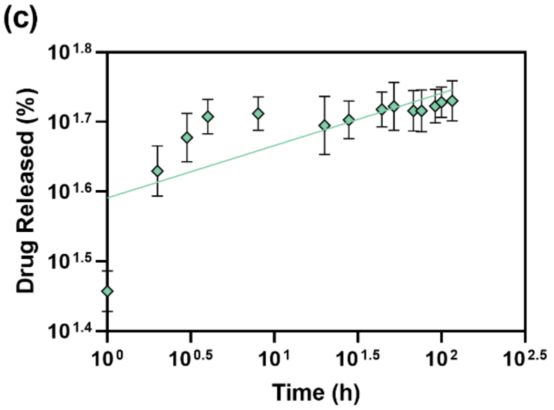

Korsmeyer-Peppas model (two diffusion coefficient regimes) – best fit model

$$\boldsymbol{Log\ (Time) \le 0.493 : Log\ (Drug\ Released\ (\%)) = slope1 \times Log\ (Time) + intercept\ 1}$$

$$\boldsymbol{Log\ (Time) > 0.493 : Log\ (Drug\ Released\ (\%)) = slope2 \times Log\ (Time) + Y_{log\ Time\ =0.493}}$$

Segmental linear regression	
Best-fit values	
intercept1	1.465
slope1	0.5697
X0	0.493
slope2	0.03108
95% CI (profile likelihood)	
intercept1	1.438 to 1.492
slope1	0.4431 to 0.6964
X0	0.3316 to 0.5119
slope2	0.01636 to 0.4580
Goodness of Fit	
Degrees of Freedom	38
R squared	**0.9122**

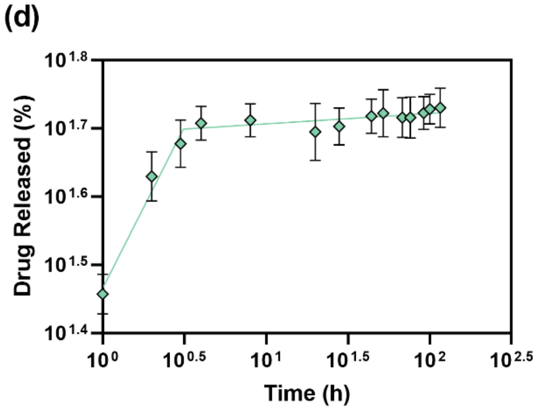

2.7.3. Animal equivalent dose calculations

FA oral administration for soft tissue infection for adults is 1500 mg administered over 3 doses daily). For 48 hour treatment (end point at 48 hours): 3000 mg would be needed for an adult (60 kg). Adult mouse weight was estimated as 0.020 kg or 20 g.

$$\boldsymbol{Animal\ Equivalent\ Dose\ (AED) = Human\ Equivalent\ Dose\ (HED)\ \times \frac{Animal\ Km}{Human\ Km}}$$

$$\boldsymbol{\frac{Mouse\ Km}{Human\ Km} = 12.3}$$

$$\mathbf{AED}\ = \boldsymbol{\frac{3000\ mg}{1\ kg}} \times \mathbf{12.3 = 36,900\ mg/kg}$$

$$\mathbf{36,900\frac{mg}{kg}\times\frac{1\ kg}{1000\ g}\times\frac{20\ g}{1\ mouse}\times\frac{1000\ \mu g}{1\ mg} = \ 738,000\ \mu g/mouse}$$

$$\boldsymbol{\frac{drug\ needed\ for\ oral\ treatement\ using\ FA\ \mu g}{drug\ loaded\ in\ each\ POEGMA - SAP\ Hydrogel\ \mu g} = \frac{738,000\ \mu g}{5.092\ \mu g} = \ 144,933}$$

$$\boldsymbol{\approx 100,000}$$

Chapter 3- Antibiotic-Loaded Crosslinked Sodium Alginate Fabricated via Pressurized Gas eXpanded Liquids Technology in Combination with Supercritical Adsorptive Precipitation as Wound Dressings for Treating Methicillin-Resistant *Staphylococcus aureus* Infections

Samaneh Toufanian[a,1], Jody Mohammed[b,1], Byron Yepez[c], Emily Y. Wong[c], Ricardo Couto[c], Bernhard Seifried[c], Paul Moquin[c], Brian K. Coombes[b], Todd Hoare[a,*],

[a] Department of Chemical Engineering, McMaster University, 1280 Main St. W., Hamilton, ON, Canada
[b] Department of Biochemistry and Biomedical Sciences, McMaster University, 1280 Main St. W. Hamilton, ON, Canada
[c] Ceapro, Inc., 7824–51 Avenue NW, Edmonton, AB, T6E6W2, Canada

[1] These authors contributed equally to this work.
[*] Corresponding author: hoaretr@mcmaster.ca

Abstract

Antibiotic resistance is a major healthcare challenge globally, and developing new antimicrobial therapies is challenging, expensive, and limited by the high hydrophobicity and low bioavailability of many newly identified antibiotic candidates. Herein, we describe the combination of Pressurized Gas eXpanded liquid technology (PGX) combined with supercritical adsorptive precipitation to load and subsequently deliver poorly water soluble antimicrobial compounds such as fusidic acid (FA) and tigecycline (TIG) directly to an infected wound. PGX-processed crosslinked sodium alginate compressed into disks exhibits an high specific surface area (~160 m^2/g) to enable drug impregnation and effective exudate absorption. FA-loaded disks successfully suppressed bacterial growth while TIG-loaded disks completely eliminated inoculum levels (10^6 CFU) of methicillin-resistant *Staphylococcus aureus* infections, even at extremely low overall drug doses relative to the conventionally-used therapeutic doses for intravenous (TIG) and oral (FA) administration. As such, the use of PGX technology combined with adsorptive precipitation offers potential to deliver bioactive compounds with low water solubility in a bioavailable format, offering potential to revive new classes of antimicrobial compounds that are excluded early in the discovery process due to low water solubility and concerns over effective administration.

Graphical Abstract

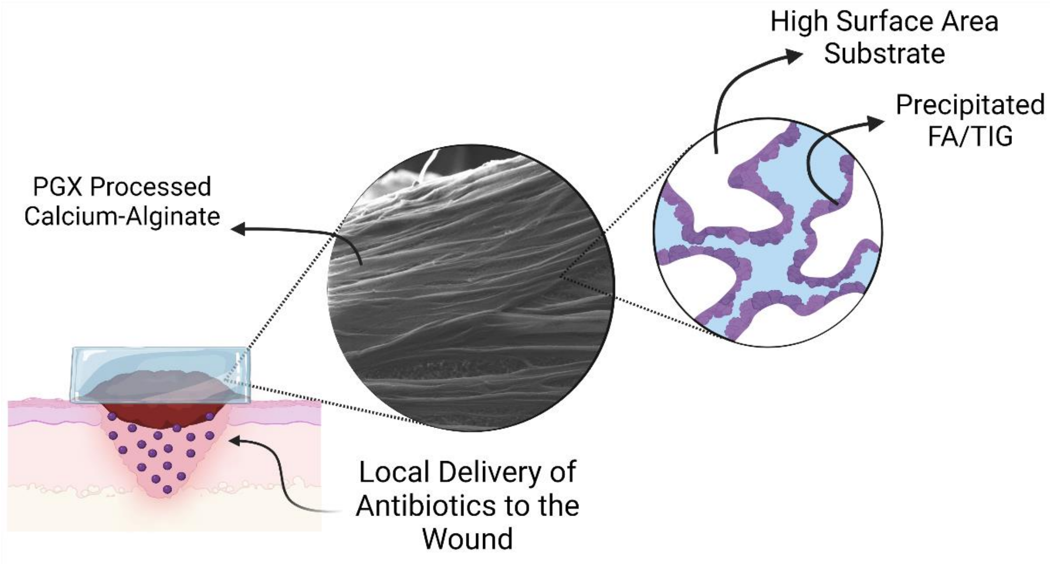

3.1. Introduction

More than 40% of hospital patients report wounds, over 7% of which involve an active infection [1]. Globally, patients in intensive care wards, irrespective of age, ethnicity, and socioeconomic background, are reported to experience higher rates of wound infections [2, 3]. Combined with pre-existing, immunocompromising conditions, these patients are at a higher risk of morbidity and/or mortality as a result of improperly treated wounds [3, 4]. As a result, the annual cost of wound care globally is expected to increase to 28 billion USD by 2029 from 17 billion USD in 2021[5].

In addition to the high global incidence of open wounds, the growing prevalence of antibiotic-resistant bacteria and multidrug-resistant strains has led to further challenges in treating infected wound sites. Identifying novel antimicrobial compounds has been one of the key methods explored in developing therapeutics in these cases. However, the therapeutic compound pipeline in the antibiotic space is notoriously challenging, resulting in very few antimicrobials being identified and subsequently brought to market each year [6]. Many potential compounds are dismissed due to failures in clinical trials, toxicity concerns, and other technical or administrative challenges. Among those challenges, low aqueous solubility is a key issue that limits the utility of many newly-discovered antimicrobials; indeed, over 40% of new chemical compounds developed by the pharmaceutical industry have low water solubility [7]. Different methods have been explored to overcome this issue. In some cases, the solubility of the compound itself can be modified by producing soluble salts of the target compounds [8], co-crystallizing the drug with water-dispersible components [4], altering the drug particle size [9, 10], and/or using additives such as water-soluble organic solvents, lipids, or non-ionic surfactants to increase water solubility [10, 11]. In other cases, the drug is either physically or chemically loaded into a delivery vehicle that facilitates water solubility or dispersibility of the drug; methods in this category include covalent tethering the drug to a water-soluble polymer [12] or encapsulating the drug in a delivery vehicle (e.g. microparticles [13], microgels [14], liposomes [15], micelles [16, 17], etc.). While these techniques can be effective in some therapeutic applications, they can also involve additives, surfactants or processes which can compromise the safety [18], efficacy [19], or stability [20] of the antimicrobial therapeutic.

An alternative approach to loading hydrophobic drugs is to utilize the high surface area of polymeric aerogels and other porous substrates to precipitate drug in a controlled manner on the porous interface. Adsorptive precipitation using supercritical carbon dioxide

($sc-CO_2$) offers a particularly attractive alternative in this context [21]. In an adsorptive precipitation process, the porous support is exposed to the drug solubilized in supercritical fluid for a certain period (adsorption) followed by rapid precipitation and subsequent surface deposition of drug at the pore interface (precipitation) under moderate temperatures (40-60 °C) and elevated pressures (200-300 bar) without requiring any organic solvents or additives [22, 23]. This method allows for loading of drugs in either amorphous or nanocrystalline form by controlling process parameters such as temperature, pressure, adsorption time, and pressurization/depressurization rates. [24, 25]. Compared to conventional diffusion-based loading techniques, the precipitated drug particles offer enhanced solubility and mass transfer kinetics due to their size and commonly targeted amorphous structure, an attribute noted to improve the bioavailability of drugs with low water solubility [21]. Furthermore, the mild processing conditions do not raise major concerns about the bioactivity and stability of the bioactive compound.

The success of a supercritical adsorptive precipitation process is tied to the chemistry and the specific surface area of the substrate used. Pressurized Gas eXpanded Liquids technology (PGX) provides a particularly attractive way to create highly porous substrates with high specific surface areas ($10 – 100\ m^2/g$) [26] that are ideal for adsorptive precipitation. The PGX process involves mixing aqueous polymer solution or slurry with the PGX liquid (a mixture of ethanol and $sc-CO_2$) in a coaxial nozzle. The low surface tension of the PGX liquid coupled with the rapid dehydration of the polymer leads to the formation of open-porous aerogels with high surface area while simultaneously removing impurities from the aerogels [27]. Compared to other supercritical fluid based-technologies that produce aerogels (e.g. emulsion templating, gas foaming, etc.[28]), PGX technology can directly process highly viscous aqueous polymers solutions into aerogels without requiring time-consuming solvent exchange steps. Furthermore, PGX technology improves process scalability by eliminating challenges associated with drop formation and jet break-up that pose challenges in other supercritical processing strategies [29].

Beyond the benefits associated with antibiotic loading, the highly porous PGX scaffolds offer additional potential benefits in terms of rapidly absorbing the often large amount of exudate released from wounds with severe infections [30]. However, currently reported PGX-based materials are not crosslinked, leading to potentially poor mechanical stability and/or dissolution upon exposure to exudate and thus requiring frequent dressing replacement [31]; this drawback is also relevant to many commercial wound dressings based on dried soluble polymers. As such, the development of crosslinked macroporous hydrogels based on supercritical processing strategies is important to both improving the mechanics of the dressings as well as enhancing the potential for exudate absorption. We have previously reported the preparation of macroporous hydrogel wound dressings based on PGX-processed sodium alginate that is drug loaded by supercritical adsorptive precipitation (ibuprofen) and then post-crosslinked in a calcium ion solution, with the resulting scaffold demonstrated to effectively accelerate wound healing [29]. However, the need for post-crosslinking in an aqueous solution can partially dissolves the PGX aerogel results in a significant decrease in the effective surface area (reducing the potential drug uptake if conducted prior to drug loading) and/or the potential loss of some of the loaded drug during the soaking-based crosslinking process (if conducted after drug loading). In addition, the scaffolds would need to be shipped either already in gel form or re-dried following processing, at which point the scaffold porosity and thus bioavailability of the drug is likely to be altered versus the (desirable) high surface area PGX material. To overcome these challenges, Ceapro Inc. has recently developed a method to simultaneously process and crosslink (via charge interactions with calcium ions) sodium alginate during the PGX process. This integrated process avoids a secondary crosslinking step (facilitating scale-up) while enabling full retention of the high aerogel porosity, to our knowledge the first such demonstration with a supercritical fluids-based processing strategy.

Herein, we report the evaluation of hydrogel-based scaffolds made from PGX calcium alginate, enabling the effective delivery of poorly water-soluble antibiotic agents for treating methicillin-resistant *S. aureus.* (MRSA) Specifically, the crosslinked PGX product was compressed into disks and impregnated with the poorly soluble antibiotics FA or TIG, both of which are considered primarily bacteriostatic but are commonly used to combat MRSA infections via oral or intravenous administration respectively (albeit requiring high drug doses) [32, 33]. The PGX-processed crosslinked alginate disks were stable and could effectively absorb model exudate without dissolving; furthermore, the drug-loaded dressings were able to effectively prevent bacterial expansion beyond inoculum levels in the wound when loaded with FA and completely eliminate the infective inoculum when loaded with TIG, even at extremely low overall drug doses. The combination of local delivery, significantly improved bioavailability, scalable fabrication, and easy handling enabled by this approach offers potential to treat drug-resistant infections otherwise challenging to resolve while also minimizing/avoiding excessive exposure to antibiotics that is linked to emergence of antibiotic-resistant bacterial strains [4, 34].

3.2. Materials and Methods

3.2.1. Materials

PGX calcium alginate (PGX-CA) disks (blank or impregnated with fusidic acid or tigecycline) and PGX sodium alginate (PGX-SA) disks or sheets were fabricated at Ceapro Inc. (Edmonton, AB, Canada) and were used as received. Ethylenediaminetetraacetic acid (EDTA), HEPES buffer (Bio-Rad, Mississauga, ON, Canada), 6 N hydrochloric acid (Fisher-Scientific Company, Saint-Laurent, QC, Canada), sodium chloride (NaCl, Sigma-Aldrich, Oakville, ON, Canada), calcium chloride ($CaCl_2$, Fisher-Scientific Company, Saint-Laurent, QC), sodium hydroxide (NaOH, Sigma-Aldrich, Oakville, ON), fusidic acid (FA, 97%, Ambeed, Arlington Heights, IL, USA), fusidic acid-d6 (≥99%, Cayman Chemical Company, E. Ellsworth; Ann Arbor, MI; USA), tigecycline (TIG, 98%, AK Scientific, Union City, CA, USA), and tigecycline-d9 (Cayman Chemical Company, E. Ellsworth; Ann Arbor, MI; USA) were used as received. Double distilled reverse osmosis (MilliQ) water was used for all experiments. The HEPES buffer used for most experiments was pH 7.4 HEPES buffer, 0.5 M, supplemented with 23.38 g/L NaCl and 2.23 g/L $CaCl_2$.

3.2.2. Fabrication of PGX polymer scaffolds

PGX calcium alginate (PGX-CA) and PGX sodium alginate (PGX-SA) were fabricated using a bench-size PGX system (10 L) located at Ceapro, Inc., employing the same protocol previously reported to dry sodium alginate [27] with some modifications to include the crosslinker agent ($CaCl_2$) for creating PGX-CA scaffolds [26]. The PGX products were then mechanically compressed at 20 MPa to form a thin (1.76 ± 0.07 mm),, porous film (0.16 g/inch^2), from which 3/16” diameter (~4.5 mg) disks were punched for the majority of the analysis; for mechanical testing only, larger disks (1” diameter) were punched.

3.2.3. Specific Surface Area Characterization

The specific surface area of both the PGX products as well as the compressed disks was measured using a gas sorption analyzer (NOVA 4200e, Quantachrome Instruments, Boynton Beach, FL, USA) based on nitrogen adsorption/desorption isotherms. Approximately 100 mg samples were outgassed under vacuum at room temperature (22°) for 24 hours. The samples were analyzed using multi-point the Brunauer-Emmett-Teller (BET) analysis using nitrogen as the adsorbent, with the data analyzed using the Quantachrome NovaWin software to calculate the specific surface area using the BET model.

3.2.4. Gravimetric Water Retention (Swelling)

PGX-CA disks (3/16” diameter, non-impregnated) were weighed individually and placed in cell strainers (0.2 µm mesh size, Corning). Following, the strainers were placed in 6 well plates filled with prewarmed HEPES buffer and incubated at 37 °C under gentle agitation (100 rpm) in triplicate. At each time point, samples were removed from the buffer, wicked dry to remove excess (surface) water, and weighed. The swelling ratio was calculated based on equation (3-1) in which W_t is the weight of the gel and strainer combined and W_s and W_0 are the weights of the strainer and the gel respectively at the beginning of the experiment.

$$\boldsymbol{swelling\ ratio} = \frac{\boldsymbol{W_t - W_s}}{\boldsymbol{W_0}} \tag{3-1}$$

3.2.5. Mechanical Testing

Uniaxial compressive testing was performed using the Mach-1 V500CST mechanical tester (Biomomentum Inc., Laval, QC). PGX-CA disks (1” diameter, non-impregnated) were incubated in prewarmed HEPES buffer and incubated at 37 °C with light agitation (100 rpm) overnight. Before being subject to mechanical testing, samples were removed from the buffer and wicked dry to remove non-absorbed water. Samples were then placed in a Petri dish (polystyrene, 3.5 cm diameter) lined with abrasive sandpaper (800 grit with adhesive backing, 3M) to immobilize the base of the sample during the mechanical test and avoid slipping artifacts. Samples were tested using a spherical indenter (1/4” diameter) in 6 different locations on the disk (5 locations at each corner of a pentagon with an inradius of ~¼” in addition to the pentagon center). The displacement was adjusted to the sample thickness in each location to ensure at least 50% compression was achieved in uniaxial compression at a 1% strain rate. The uniaxial compressive modulus was then calculated using the Mach-1-Analysis software. Dry disks were tested similarly with 10% compression.

3.2.6. Helium Ion Microscopy (HiM) Imaging

The morphology of PGX-CA and compressed disks formed from the PGX-processed samples was examined using a helium ion microscope (HiM ORION nanoFAB, Carl Zeiss Microscopy GmbH, Jena, Germany). Secondary electron images were collected using a 30 kV accelerating voltage and a 1.5 pA beam current. Positive charges on the surface of the samples were neutralized with an electron flood gun, allowing direct imaging of the insulating materials without requiring a conductive coating.

3.2.7. Supercritical Adsorptive Precipitation of Tigecycline and Fusidic Acid

PGX-CA disks were loaded with tigecycline and fusidic acid using a lab-scale supercritical adsorptive unit at Ceapro, Inc. comprised of a 24 mL high-pressure vessel and a gear pump to recirculate the CO_2 (Micropump, GAH-T23, Vancouver, WA, USA). To control the temperature, the unit was located inside an oven, and the system was pressurized using an air-driven CO_2 pump (Applied Separations, Inc., Model 7321, Allentown, PA, USA). To control the depressurization rate, the unit was equipped with a micrometering valve (Fitok, 15MSS-DFF2, Stafford, TX, USA) installed at the outlet.

In a loading experiment, 50 PGX-CA disks were loosely placed inside the high-pressure vessel together with a pouch made of filter paper containing ~10 mg of the drug of interest (FA or TIG). The high-pressure vessel was placed in the preheated oven to 40°C and pressurized with sc-CO_2 up to 20 MPa. The sc-CO_2 was then recirculated through the high-pressure vessel at a flowrate of 350 mL/min to solubilize the drug and allow it to be adsorbed into the PGX-CA disks. After 2 h of recirculation, the unit was depressurized to atmospheric pressure over a ~2 min period to drive the precipitation of the drug onto the exposed surface area of the PGX-CA disks.

3.2.8. Drug Loading Quantification

PGX-CA disks impregnated with FA were added to vials containing 6 mL of 0.2 M EDTA and 100 μL 0.1 M alginate lyase for 30 min at 37°C to de-crosslink the alginate gel. The hydrogel components were then extracted via precipitation by concentrated HCl and subsequent centrifugation (2000 × g, 5 min). The drug-containing supernatant was isolated, and drug was isolated using 3 × 1 mL dichloromethane extractions. The PGX-CA samples impregnated with TIG were not compatible with the FA procedure due to stronger TIG-Alginate interactions that resulted in insufficient extraction. Instead, TIG drug loading was indirectly quantified by soaking the TIG loaded disks in MilliQ water for 48 hours and incubated at 37 °C under light agitation (100 RPM) The supernatant was collected and tested to quantify the amount of released TIG.

3.2.9. Drug Release Kinetics

PGX-CA disks impregnated with FA were placed into 5 mL of prewarmed HEPES buffer and incubated in 37 °C with gentle agitation (100 rpm) protected from light. At each timepoint, 1 mL of the supernatant was collected and replaced with fresh drug-free buffer. Samples were stored at -10 °C until being characterized via LC/MS analysis (see section 3.2.10). Cumulative drug release was quantified based on equation (3-2) in which P_t is mass of drug released at time t and $P_{(t-1)}$ is amount released previous to time t [35].

$$\boldsymbol{Cumulative\ Drug\ Released} = \frac{\boldsymbol{Volume\ of\ sample\ withdrawn}}{\boldsymbol{Bath\ volume}} \times \boldsymbol{P_{(t-1)}} + \boldsymbol{P_t} \qquad \textbf{(3-2)}$$

Cumulative percentage release (%) was calculated based on total drug loading measured as described in section 3.2.8.

3.2.10. Drug Concentration Quantification via LC/MS

For FA quantification, a volume of 50 µL of each collected drug release sample was placed into a microcentrifuge tube to which 200 µL of ice-cold acetonitrile containing 0.1% formic acid and 56 ng/mL of fusidic acid-d6 (used as the internal standard). The tubes were vortexed for 1 minute and then centrifuged at 18,000 × g for 15 minutes to separate any solid precipitates. A volume of 100 µL was removed from the top and diluted 10-fold with acetonitrile containing 0.1% (v/v) formic acid and 45 ng/mL of fusidic acid-d6 to ensure the measured FA concentration falls within the established standard curve. A volume of 5 µL was injected into an Agilent 1290 Infinity II high performance liquid chromatograph equipped with an Agilent 6495C iFunnel QQQ mass spectrometer for detection (Agilent, Santa Clara, CA, USA). Each sample was prepared once and injected in duplicate. The autosampler was maintained at 10˚C throughout the analysis while the analytical column was maintained at 30 ˚C. Separation of the analytes was achieved on an Agilent RRHD Eclipse Plus C18 (100 mm × 2.1 mm, i.d., 1.8 µm) analytical column using mobile phases consisting of (A) 0.1% (v/v) formic acid in water and (B) 0.1% (v/v) formic acid in acetonitrile using a constant flow of 0.3 mL/min. Separation was achieved by a linear solvent gradient ramping from 5% B to 97% B over seven minutes, holding at 97% B for 30 s, ramping back down to 5% B over 30 s, and re-equilibrating the column at 97% B for an additional 2 minutes (10 minute total run time). Electrospray ionization (ESI) in negative mode was used for multiple reaction monitoring and quantification of analytes. Refer to the Supplementary Information for full details of the mass spectrometry measurement and data analysis.

To quantify samples containing TIG, 10 µL of each sample was diluted 10 times with acetonitrile containing 50 ng/mL of d9-tigecycline internal standard. The prepared samples (7 µL) were injected into an Agilent 1290 Infinity II HPLC with an Agilent 6495C iFunnel QQQ mass spectrometer (Agilent, Santa Clara, CA, USA) for detection. The separation of analytes and analysis was performed as described above for FA quantification.

3.2.11. In vitro Qualitative Bacterial Growth Inhibition Assays

An overnight culture of *Staphylococcus aureus* Rosenbach (USA 300) was grown in LB broth (37ºC, 230 rpm shaking). A sterile inoculum loop was used to transfer and spread ~10 μL of bacterial culture onto prepared LB agar plates. Treatment disks were immediately placed in triplicate on plates together with a control (non-impregnated PGX-CA) disk. Plates were inoculated at 37°C for 16 to 18 h. Zones of growth inhibition were then examined and measured with a ruler to 0.1 cm accuracy to assess the capacity of the disks to release bioactive antibiotics.

3.2.12. Full Thickness Murine Skin Wound Model

Animal experiments were conducted according to the guidelines set by the Canadian Council on Animal Care and the Province of Ontario, using protocols approved by the Animal Review Ethics Board and McMaster University under Animal Use Protocol #20-12-41. 6-8 week old female BALB/c mice (Charles River Laboratories) were anesthetized using inhalant isoflurane. Buprenorphine (0.1 mg/kg) was administered intraperitoneally, and eye gel was applied pre-procedure. A 2 cm^2 patch of hair was clipped on the dorsal surface, with the surface then sterilized using a povidone-iodine wash. A plastic washer (6 mm inner diameter) was sutured in place and furthered glued down using Vetbond for reinforcement. A 5 mm diameter full-thickness excisional wound was created using a biopsy punch. Wounds were immediately infected with a bacterial inoculum of ~5x10^6 CFU *Staphylococcus aureus* USA 300 suspended in PBS. The infection was left to establish for one hour prior to placement of treatment disk. Mice were monitored for wound bed humidity, weight change, and body condition scoring at the 24 h and 48 h marks and euthanized at an experimental endpoint of 48 h. Infected wound tissue and spleen samples were collected post-mortem and were briefly stored at 4ºC before being homogenized in phosphate buffered saline (Retsch Mixer Mill 400, 30/s, 10 min) and plated on LB plates supplemented with oxacillin to quantify bacterial loads.

3.3. Results and Discussion

3.3.1. PGX-CA Characterization

The addition to calcium chloride in the inlet stream of the PGX process facilitated simultaneous processing and crosslinking of alginate scaffolds with calcium chloride, avoiding the need for a secondary crosslinking step that is anticipated to improve maintenance of the highly porous microstructure in the crosslinked sample. HiM imaging was used to visualize the microstructure of PGX-CA (Figure 3-1 top row) and the compressed PGX-CA disks (Figure 3-1 bottom row). The raw PGX structure shows a textured enveloped structure (Figure 3-1-a, b) with a delicate fibrillar structure evident at higher magnifications (Figure 3-1-c). The compressed PGX-CA disks retain a highly textured structure internally (highlighted with the arrow in Figure 3-1-d) but a smoother interface in response to the compression step (Figure 3-1-e). As such, although reduced porosity is observed on the top and bottom of the PGX-CA disks following compression, the internal open-porous high surface area structure is maintained following bulk compression. The resulting compressed films were punched to form disks (Figure 3-1-f), with no significant flaking or crumbling observed upon the punching process.

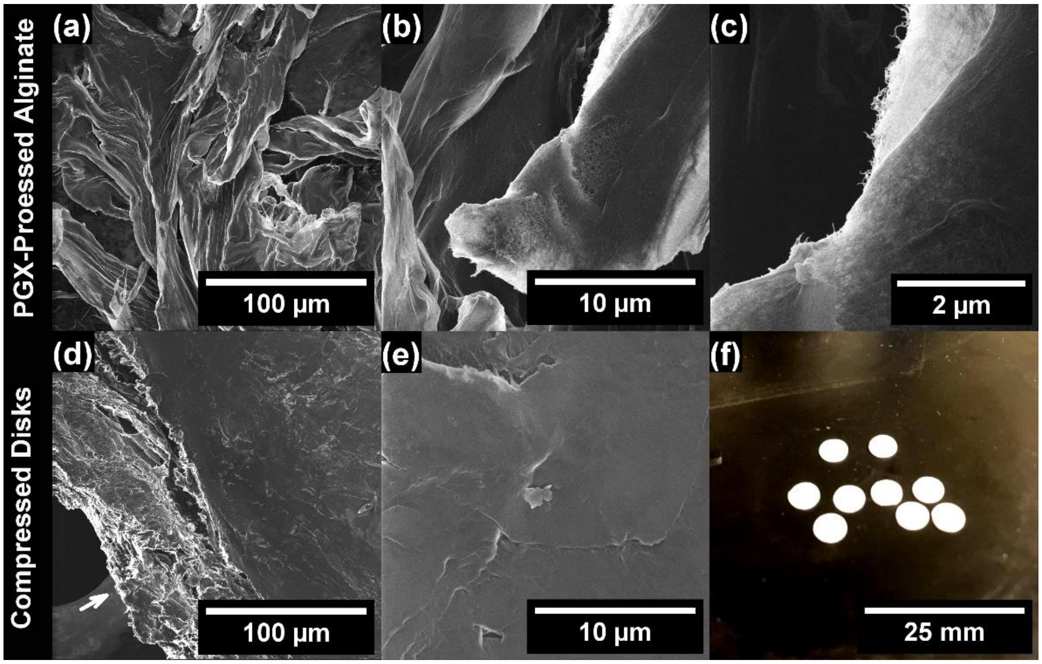

Figure 3-1- HiM images showing the microarchitecture of (A-C) PGX-CA prior to compression into disks (images on different length scales) and (D-E) compressed PGX-CA disks (images on different length scales); (F) macroscopic picture of the bulk compressed disks.

BET analysis is consistent with this interpretation, with the pre-compressed PGX-CA material and the compressed disks showing specific surface areas of 162 ± 10 and 143 ± 12 m^2/g respectively. As such, although the specific surface area of the material is very moderately reduced during the compression process, the resulting disks still have very high specific surface areas appropriate for supercritical adsorptive precipitation drug loading.

3.3.2. Swelling and Mechanics

Incubation of the PGX-CA disks in pH 7.4 calcium-supplemented HEPES buffer (Figure 3-2-a) indicated that the PGX-CA disks remained stable when hydrated, with no indication of dissolution, dissociation, or visible shedding over the five day duration of the swelling experiment (a timeframe within which a wound dressing is typically replaced at least once [36]). This result indicates that this dressing could be functionally utilized for wound healing applications when exudate is present [37, 38]. Relative to the uncrosslinked PGX-SA samples, the crosslinked PGX-CA samples swell in a significantly more controlled manner due to the presence of the calcium crosslinks; however, over extended incubation times, ion exchange with the buffer results in equally large equilibrium swelling ratios (12.3 ± 0.2) in both the PGX-SA and PGX-CA samples after ~72 hours. The swelling kinetics and capacities of the PGX-CA samples thus suggest the potential of the PGX-CA disks to effectively manage exudate, as is essential for effective wound care [39]. Compressive modulus in indentation results (Figure 3-2-b) show that the dry PGX-CA disks have a similar compressive modulus (584 ± 53 kPa) to that of skin (420-850 kPa depending on age and location, as indicated by the grey range in the figure [40]). Equilibrium swelling of the PGX-CA disks results in a decrease in the compressive modulus to 159 ± 22 kPa, a value that is still sufficiently strong to permit easy handling by healthcare professionals or patients during dressing changes as required.

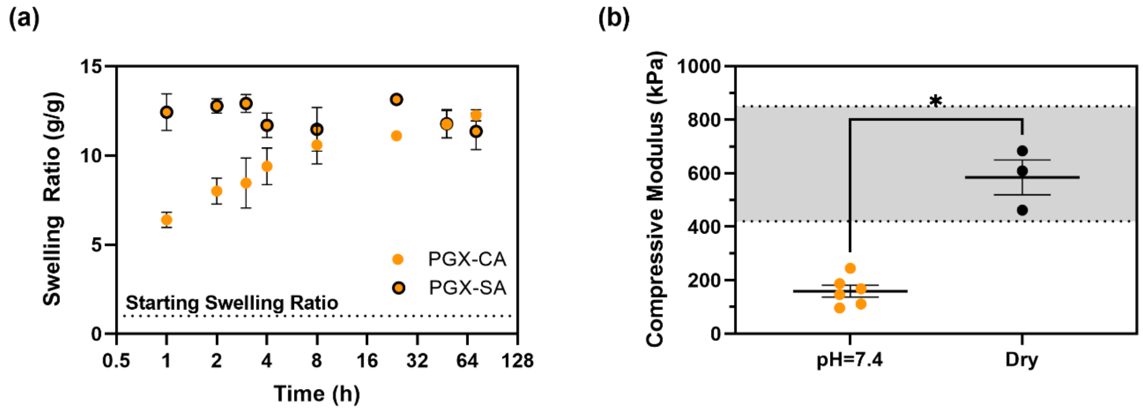

Figure 3-2- Physical characterization of PGX-CA disks: (a) Swelling kinetics of PGX-CA samples relative to non-crosslinked PGX-SA samples upon exposure to pH 7.4 calcium-supplemented HEPES buffer (n=3 replicates per sample); (b) Uniaxial compressive moduli of PGX-CA before and after incubation in buffer for 18 hours. Indentation experiments were performed in 6 locations, with outliers identified using ROUT test (Q = 1%); error bars show standard error (ns $p > 0.1$, * $p \leq 0.1$, ** $p \leq 0.01$, *** $p \leq 0.001$ as determined through one-way ANOVA followed by the Tukey test).

3.3.3. Drug Loading

To determine the amount of FA and TIG loaded into each disk, drug was either extracted from the disk using a 48 hour aqueous extraction process (TIG, exploiting the yellow color of TIG to confirm completion of the extraction) or isolated by de-crosslinking the PGX disk using a chelator and extracting the drug from the resulting solution (FA). LC/MS results indicating the success of the supercritical adsorptive precipitation-based loading process for each drug are summarized in Table 3-1. A total of 5.1 ± 0.3 µg of FA and 18.5 ± 1.4 µg of TIG was loaded in a single disk, corresponding to drug loading capacities of 0.12 wt% and 0.30 wt% drug respectively in the final scaffolds. As such, supercritical adsorptive precipitation can be used to impregnate each drug onto the highly porous PGX-CA scaffolds. Of note, relative to the typical oral dose of FA (36,900 mg/kg) or intravenous dose of TIG (3,075 mg/kg) currently used clinically, the total amount of drug that can be delivered by a single disk is orders of magnitude smaller. However, the potential of the PGX-CA scaffolds to both deliver the drug locally on the wound and deliver a more bioavailable dose (based on the likely amorphous nature of the drug precipitates) is hypothesized to still potentially result in effective therapy.

Table 3-1 Summary of LC/MS results of fusidic acid (FA) and tigecycline (TIG) drug loading into PGX-CA scaffolds via supercritical absorptive precipitation

Sample Description	Dry Mass (mg)	Loaded Drug (μg)	Drug Loading (wt%)
PGX-CA-FA	4.2 ± 0.1	5.1 ± 0.3	0.12 ± 0.01
PGX-CA-TIG	6.1 ± 0.6	18.5 ± 1.4	0.30 ± 0.01

3.3.4. Drug Release Kinetics

The release kinetics of FA loaded via supercritical adsorptive precipitation to the PGX-CA disks are shown in Figure 3-3-a. Fusidic acid was released relatively quickly from the scaffolds, with a plateau in release observed after ~8 hours. Of note, a slight initial delay was observed in the release kinetics which we attribute to the slow penetration of water to fully wet the highly porous PGX-CA scaffolds and thus solubilize surface-impregnated drug that is deposited throughout the scaffold; this induction period was omitted in the subsequent kinetic modeling to exclude the biasing of the model due to the wetting time which is not considered in the model assumptions. While this release is rapid, the purpose of the impregnation method chosen is primarily to increase the bioavailability of FA rather than design a long-term controlled release vehicle, with this more burst-like release suggesting rapid solubilization of the impregnated drug. In addition, while slow and sustained release is an effective approach to prevent wound infections [41], effective treatment of an established infection requires the antimicrobial compound to surpass the minimum inhibitory concentration (MIC) [42]; as such, the rapid large dose release followed by a sustaining dose is highly appropriate for practical infected wound treatment. We note that release is also likely to be slower in a real wound versus this model *in vitro* condition in which the disks were fully immersed in the release buffer rather than exposed on one side to a wound with varying amounts of exudate.

To assess the dominant mechanism of release kinetics, two mathematical models were evaluated: (1) A first-order kinetics model (often used to describe diffusion controlled kinetics) in which the dissolution rate is proportional to the difference between the concentration and the saturation solubility; this kinetic profile is represented by Equation (3-3) in which y is the percentage of drug released, t is time, A (plateau) is a constant value determined by the maximum drug released from the scaffold, and B is a constant value associated with the rate of drug release [43]. (2) A power law model (often describing dissolution-controlled release) in which the drug release kinetics are primarily determined by the amount of drug remaining in the drug release vehicle; this kinetic profile is represented by equation(3-4) in which t (time) is the base of the power. Least squares fitting of both models (supporting information Table 3-3) resulted in R^2 values of 0.80 for the first order model (equation (3-3)) and 0.96 for the power law model (equation (3-4)); the significantly higher R^2 value achieved with the power law suggests that drug release is primarily controlled by drug dissolution kinetics rather than diffusion kinetics. Note that none of the commonly used drug dissolution-based models [43-46] was suitable to explain the drug release kinetics directly given that the combination of the highly porous geometry of the PGX processed disks coupled with the surface-only deposition of FA via the absorptive precipitation process violate the key assumptions of those models.

$$y = A \times (1 - exp\,(-\mathrm{B}\,t)) \tag{3-3}$$

$$100 - y = Kt^{n} \tag{3-4}$$

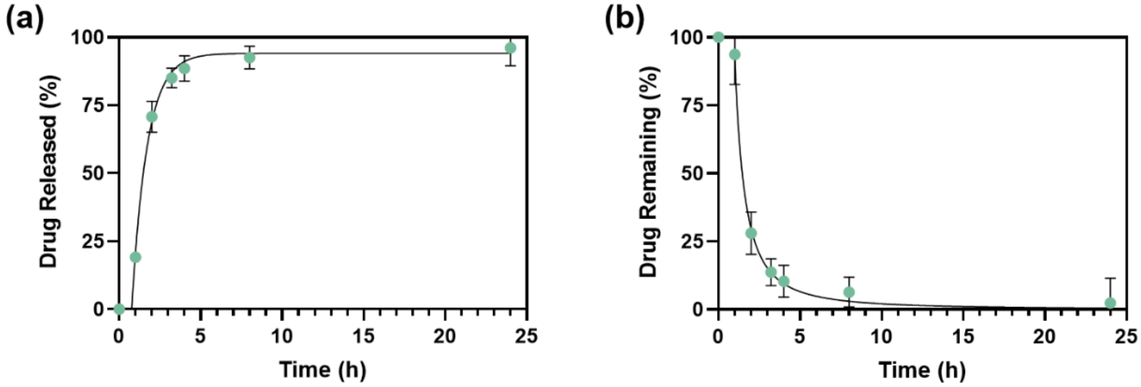

Figure 3-3- Drug release kinetics of FA-loaded PGX-CA compressed disks: (a) Cumulative release of FA versus time. The line indicates a first order kinetic model fit (diffusion-controlled release) based on eq. 3, excluding the initial point at (0,0) accounting for delays in wetting the porous PGX-CA matrix; (b) Percentage of drug remaining in PGX-CA compressed disks versus time. The line indicates a power law mathematical model (dissolution-controlled release) based on eq. 4, excluding the initial point at (0,100) accounting for delays in wetting the porous PGX-CA matrix. Error bars show standard error (n=3).

3.3.5. In vitro Antimicrobial Activity

Figure 3-4 shows the disk diffusion (Kirby-Bauer) assays used to qualitatively assess the capacity of the impregnated PGX-CA disks to kill MRSA over a 16-18 hr incubation time, with non-impregnated disks used as controls. Both drug-impregnated disks demonstrated full clearance of MRSA, with comparable large zones of inhibition observed for both FA-loaded PGX-CA disks and TIG-loaded PGX-CA disks; in contrast, the unloaded control disks resulted in no bacterial growth inhibition. As such, despite the low doses of drug loaded into the PGX-CA disks relative to the current clinical standard (Table 3-1), the disks retained a high capacity for bacterial growth inhibition.

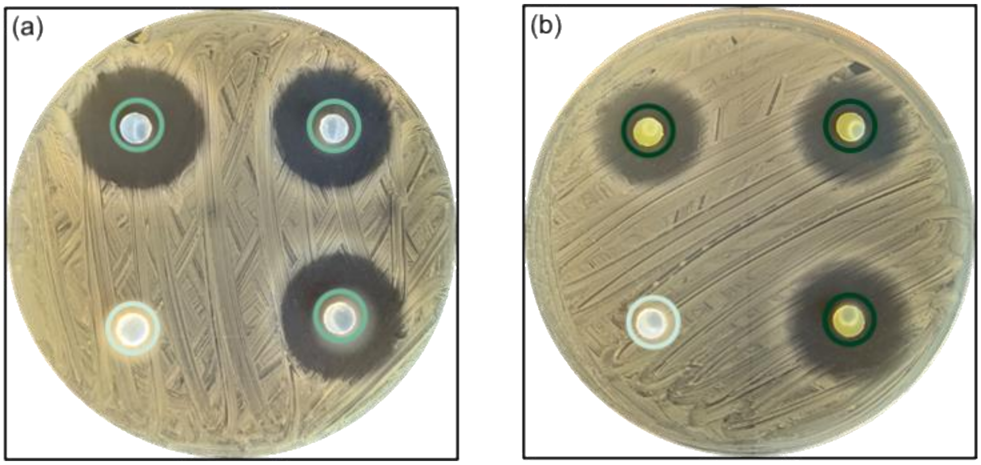

Figure 3-4-*In vitro* disk diffusion assays on LB agar against MSRA show clear zones of inhibition for (a) PGX-CA-FA and (b) PGX-CA-TIG disks but no zone of inhibition for blank disks (bottom left corner disks in each image).

3.3.6. In vivo Antimicrobial Activity

A full-thickness murine wound model was used to evaluate the potential of FA- and TIG loaded PGX-CA disks to treat MRSA-infected wounds *in vivo*. Treatment disks were placed in wound beds 1 hr post-infection (~5x10^6 CFU inoculum) and left to deposit drug for 48 hrs, consistent with a typical ~2-3 day interval for wound dressing changes. Figure 3-5-a shows the changes in bacterial load in the wound bead (indicative of local antibacterial activity) and in the spleen (indicative of the potential of the dressing to prevent systemic infection), while Figure 3-5-b shows the weight change in the mice over the 48 hour experiment timeframe. Animals receiving blank (no drug loaded) PGX-CA disks showed a slight reduction (~0.46 log) in bacterial CFU in wound tissue as compared to the untreated group. While this result is not statistically significant, it is possible that some of the inoculated bacteria are absorbed by the rapid swelling of the blank disk upon tissue contact during the infective period and are therefore removed from the wound bed. FA-loaded PGX-CA disk treated mice experienced no increase in bacterial CFU between the time of infection and the time of sacrifice, in comparison to untreated mice that experienced a 1-2 order of magnitude increase in bacterial CFU during the same timeframe (Figure 3-5-a). In parallel, 7/8 untreated mice showed significant spleen CFU counts after 48 hours while only 2/8 FA-loaded PGX-CA animals showed splenic infections, indicative of the potential of the drug-impregnated PGX dressings to reduce the probability of systemic infection. Mice treated with FA-loaded PGX-CA disks also lost minimal weight over the first 24 hrs (average <0.5% body weight), in contrast to control groups which experienced more significant weight loss (average 3-4% body weight); however, during the 24-48 hr period of the experiments, FA-loaded PGX-CA treated mice experienced a drop in weight (average 3% body weight). We speculate this is because the FA in the disks was depleted shortly after the 24 h mark and the remaining bacteria in the wound were able to proliferate and resume the infection progression in the mice. As such, we conclude that FA-loaded PGX-CA disks can effectively suppress growth of MRSA infections for at least 24 hrs.

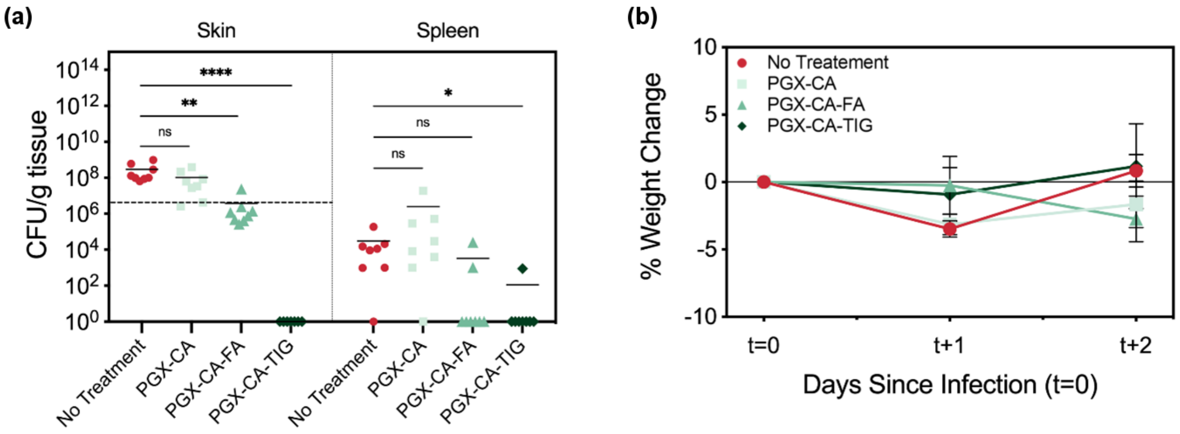

Figure 3-5- *In vivo* antimicrobial assay results from a full thickness MRSA-infected murine wound model: (a) Bacterial CFU counts at the wound site (local infection) and spleen (systemic infection) following treatment of full-thickness, excisional murine wounds infected topically with 5x10^6 CFU MRSA over a two-day treatment period. The dashed horizontal line represents the topical inoculum dose; (b) Average % body weight change over the two day observation period relative to initial weight of mice.

In contrast, TIG-loaded PGX-CA disks not only prevented expansion of bacteria in the wound but were also able to clear the infection in its entirety; no measurable bacterial CFU were present after 48 hrs in any of the treated animals while the control (untreated) mice again experienced a 1-2 orders of magnitude CFU increase relative to the inoculum level over the same timeframe (Figure 3-5-a). In parallel, 7/8 mice showed no CFU count in the spleen following treatment in the TIG-loaded PGX-CA treated group compared to just 1/8 of the untreated mice, showing the potential of TIG-loaded PGX-CA disks to prevent both local and systemic MRSA infection. Furthermore, minimal weight loss was observed in the treated animals over the first 24 h (average <1% body weight) while slight weight gain was observed over the full 48 hour observation period (average >1% body weight), a result that suggests that TIG-loaded PGX-CA disks deliver at least a maintenance level of antibiotic into the wound over the length of the infective period. This result is consistent with the higher deposited drug dose measured on the TIG-loaded PGX-CA disks relative to the FA-loaded PGX-CA disks (Table 3-1). Of note, by loading TIG by adsorptive precipitation and delivering it locally at the infected wound site, the typically bacteriostatic mode of action of TIG can be converted to a bactericidal mode of action despite the very low total drug dose that can be delivered by a single TIG-loaded disk (Table 3-1).

Together, these results suggest that combining PGX processing with supercritical adsorptive precipitation offers significant potential for fabricating antimicrobial wound dressings that can actively manage even antibiotic-resistant infections at drug doses significantly less than current oral or intravenous dose requirements. Indeed, based on estimated animal equivalent dose calculations (see Supplementary Information [44]) coupled with the LC/MS drug loading data (Table 3-1), the PGX-CA disks can reduce the required therapeutic dose by 10^5 for FA and 10^4 for TIG. Coupled with the ease of sterilization of the *in situ*-crosslinked aerogel scaffolds (inherent to the PGX process given the ethanol washes used [27]), the facile scalability of the PGX processing technique, and the suitable exudate absorption and mechanical properties of the compressed PGX disks for use as wound dressings, such a result offers potential not only for improving would treatment but also improving antibiotic stewardship in the treatment of already antibiotic-resistant bacterial infections by minimizing the dose of antibiotic required for effective therapy [45].

3.4. Conclusions

Treating antimicrobial resistant infections has major health and financial implications, and current approaches to treatment are either ineffective or could accelerate emergence of antibiotic resistance strains. Herein, we demonstrate that *in situ*-crosslinked PGX-processed calcium-alginate disks loaded with poorly water soluble antibiotics (here, fusidic acid and tigecycline) offer a potential alternative treatment for treating antibiotic-resistant infected wounds. The highly porous PGX-CA scaffolds can absorb exudate while maintaining sufficient mechanical properties to allow for handling. Furthermore, although relatively low drug doses can be delivered via a single treatment disk, effective antibacterial therapy can be achieved both *in vitro* and *in vivo*, including the complete eradication of local infection with TIG-loaded disks that would typically be expected to be bacteriostatic even using orders-of-magnitude lower drug doses than are required with conventional systemic therapies. These results suggest that PGX-CA disks loaded with FA or TIG represent a potential alternative to current therapeutic practice. Furthermore, the combination of *in situ*-gelling PGX processing and supercritical adsorptive precipitation described herein could in principle be applied to locally deliver other poorly water soluble therapeutics that are otherwise difficult to administer through conventional routes and/or have low bioavailability in their current dosage form.

3.5. Acknowledgements

This work was supported by a grant to B.K.C. and T.H. from the Collaborative Health Research Projects (CHRP) program from the Canadian Institutes of Health Research and the Natural Sciences Engineering Research Council of Canada.

3.6. References

[1] T. Hurd, J. Posnett, Point prevalence of wounds in a sample of acute hospitals in Canada, Int. Wound J. 6(4) (2009) 287-293.
[2] Z. Yao, J. Niu, B. Cheng, Prevalence of chronic skin wounds and their risk factors in an inpatient hospital setting in northern china, Adv Skin Wound Care 33(9) (2020) 1–10.
[3] R.T. Mayon-White, G. Ducel, T. Kereselidze, E. Tikomirov, An international survey of the prevalence of hospital-acquired infection, J. Hosp. Infect. 11 (1988) 43-48.
[4] H.D. Williams, N.L. Trevaskis, S.A. Charman, R.M. Shanker, W.N. Charman, C.W. Pouton, C.J.H. Porter, Strategies to address low drug solubility in discovery and development, Pharmacol. Rev. 65(1) (2013) 315-499.
[5] F.B. Insights, Wound care market to Hit USD 24.01 billion by 2028 with 6.1% CAGR | market size, share, growth, forecasts, & trends analysis report with COVID-19 impact by Fortune Business Insights™, 2021.
[6] M. Terreni, M. Taccani, M. Pregnolato, New antibiotics for multidrug-resistant bacterial strains: latest research developments and future perspectives, Molecules 26(9) (2021).
[7] K.T. Savjani, A.K. Gajjar, J.K. Savjani, Drug solubility: importance and enhancement techniques, ISRN Pharmaceutics 2012 (2012) 195727.
[8] L.-F. Huang, W.-Q. Tong, Impact of solid state properties on developability assessment of drug candidates, Adv. Drug Deliv. Rev. 56(3) (2004) 321-334.

[9] M. Vogt, K. Kunath, J.B. Dressman, Dissolution enhancement of fenofibrate by micronization, cogrinding and spray-drying: comparison with commercial preparations, Eur J Pharm Biopharm 68(2) (2008) 283-288.
[10] E. Merisko-Liversidge, G.G. Liversidge, Nanosizing for oral and parenteral drug delivery: a perspective on formulating poorly-water soluble compounds using wet media milling technology, Adv Drug Deliv Rev 63(6) (2011) 427-40.
[11] S.R. Bhatia, Surfactants and polymers in drug delivery. drugs and the Pharmaceutical Sciences. Volume 122 By Martin Malmsten (Royal Institute of Technology, Stockholm, Sweden). Marcel Dekker, Inc.: New York, Basel. 2002. x + 348 pp. $165.00. ISBN 0-8247-0804-0, J. Am. Chem. Soc. 125(11) (2003) 3400-3400.
[12] J. Li, D.J. Mooney, Designing hydrogels for controlled drug delivery, Nature Reviews Materials 1(12) (2016) 16071.
[13] M.-H. Xiong, Y. Bao, X.-Z. Yang, Y.-H. Zhu, J. Wang, Delivery of antibiotics with polymeric particles, Adv. Drug Deliv. Rev. 78 (2014) 63-76.
[14] B.C. Borro, R. Nordström, M. Malmsten, Microgels and hydrogels as delivery systems for antimicrobial peptides, Colloids Surf. B 187 (2020) 110835.
[15] H. Pinto-Alphandary, A. Andremont, P. Couvreur, Targeted delivery of antibiotics using liposomes and nanoparticles: research and applications, Int. J. Antimicrob. Agents 13(3) (2000) 155-168.
[16] C. Hu, F. Zhang, L. Long, Q. Kong, R. Luo, Y. Wang, Dual-responsive injectable hydrogels encapsulating drug-loaded micelles for on-demand antimicrobial activity and accelerated wound healing, J Control Release 324 (2020) 204-217.
[17] X. Yang, H. Ren, H. Zhang, G. Liu, Z. Jiang, Q. Qiu, C. Yu, N. Murthy, K. Zhao, J.F. Lovell, Y. Zhang, Antibiotic cross-linked micelles with reduced toxicity for multidrug-resistant bacterial sepsis treatment, ACS Appl. Mater. Interfaces 13(8) (2021) 9630-9642.
[18] I. Som, K. Bhatia, M. Yasir, Status of surfactants as penetration enhancers in transdermal drug delivery, J Pharm Bioallied Sci 4(1) (2012) 2-9.
[19] M. Bagheri, Cationic antimicrobial peptides (AMPs): thermodynamic characterization of peptide–lipid iInteractions and biological efficacy of surface-tethered peptides, ChemistryOpen 4(3) (2015) 389-393.
[20] K. Hadinoto, W.S. Cheow, Nano-antibiotics in chronic lung infection therapy against Pseudomonas aeruginosa, Colloids Surf. B 116 (2014) 772-785.
[21] P. Gurikov, I. Smirnova, Amorphization of drugs by adsorptive precipitation from supercritical solutions: A review, J Supercrit Fluids 132 (2018) 105-125.
[22] R. Yoganathan, R. Mammucari, N.R. Foster, Impregnation of ibuprofen into polycaprolactone using supercritical carbon dioxide, J. Phys. Conf. Ser. 215 (2010) 012087.
[23] S.J. Macnaughton, I. Kikic, N.R. Foster, P. Alessi, A. Cortesi, I. Colombo, Solubility of anti-inflammatory drugs in supercritical carbon dioxide, J. Chem. Eng. Data. 41(5) (1996) 1083-1086.
[24] J. Kerc, S. Srcic, Z. Knez, P. Sencar-Bozic, Micronization of drugs using supercritical carbon dioxide, Int J Pharm 182(1) (1999) 33-9.
[25] R. Couto, B. Seifried, B. Yépez, P. Moquin, F. Temelli, Adsorptive precipitation of co-enzyme Q10 on PGX-processed β-glucan powder, J Supercrit Fluids 141 (2018) 157-165.
[26] F. Temelli, B. Seifried, Supercritical fluid treatment of high molecular weight biopolymers, University of Alberta, 2016.
[27] Z. Liu, R. Couto, B. Seifried, B. Yépez, P. Moquin, F. Temelli, Drying of sodium alginate using Pressurized Gas eXpanded (PGX) liquid technology, J. CO2 Util. 61 (2022) 102006.
[28] K.J. De France, F. Xu, T. Hoare, Structured macroporous hydrogels: progress, challenges, and opportunities, Adv. Healthc. Mater. 7(1) (2018) 1700927.
[29] K.-a. Johnson, N. Muzzin, S. Toufanian, R.A. Slick, M.W. Lawlor, B. Seifried, P. Moquin, D. Latulippe, T. Hoare, Drug-impregnated, pressurized gas expanded liquid-processed alginate hydrogel scaffolds for accelerated burn wound healing, Acta Biomater. 112 (2020) 101-111.
[30] Wound exudate and the role of dressings. A consensus document, Int Wound J 5 Suppl 1(Suppl 1) (2008) iii-12.
[31] G. Dabiri, E. Damstetter, T. Phillips, Choosing a wound dressing based on common wound characteristics, Adv Wound Care (New Rochelle) 5(1) (2016) 32-41.
[32] N.D. Greer, Tigecycline (Tygacil): the first in the glycylcycline class of antibiotics, Proc (Bayl Univ Med Cent) 19(2) (2006) 155-61.
[33] E. Somekh, T. Golan, A. Tanay, F. Poch, M. Dan, Concentration and bactericidal activity of fusidic acid and cloxacillin in serum and synovial fluid, J. Antimicrob. Chemother. 43(4) (1999) 593-596.
[34] K.M.M. Pärnänen, C. Narciso-da-Rocha, D. Kneis, T.U. Berendonk, D. Cacace, T.T. Do, C. Elpers, D. Fatta-Kassinos, I. Henriques, T. Jaeger, A. Karkman, J.L. Martinez, S.G. Michael, I. Michael-Kordatou, K. O'Sullivan, S. Rodriguez-Mozaz, T. Schwartz, H. Sheng, H. Sørum, R.D. Stedtfeld, J.M. Tiedje, S.V.D. Giustina, F. Walsh, I. Vaz-Moreira, M. Virta, C.M. Manaia, Antibiotic resistance in European wastewater treatment plants mirrors the pattern of clinical antibiotic resistance prevalence, Sci. Adv. 5(3) (2019) eaau9124.

[35] C.Y.J. Arcot Ravindran Chandrasekaran, Choong Sheau Theng, Teeba Muniandy, Selvadurai Muralidharan, Sokkalingam Arumugam Dhanaraj, In vitro studies and evaluation of metformin marketed tablets-Malaysia, J. Appl. Pharm. Sci. Volume : 1 (2011) 214-217.
[36] A. Sood, M.S. Granick, N.L. Tomaselli, Wound dressings and comparative effectiveness data, Adv Wound Care (New Rochelle) 3(8) (2014) 511-529.
[37] S.H. Kuo, C.J. Shen, C.F. Shen, C.M. Cheng, Role of pH value in clinically relevant diagnosis, Diagnostics (Basel) 10(2) (2020).
[38] A.J. Bullock, M. Garcia, J. Shepherd, I. Rehman, M. Sheila, Bacteria induced pH changes in tissue-engineered human skin detected non-invasively using Raman confocal spectroscopy, Appl. Spectrosc. Rev. 55(2) (2020) 158-171.
[39] H.U. Zaman, J.M.M. Islam, M.A. Khan, R.A. Khan, Physico-mechanical properties of wound dressing material and its biomedical application, J Mech Behav Biomed Mater 4(7) (2011) 1369-1375.
[40] M. Pawlaczyk, M. Lelonkiewicz, M. Wieczorowski, Age-dependent biomechanical properties of the skin, Postepy Dermatol Alergol 30(5) (2013) 302-6.
[41] F.-L. Mi, Y.-B. Wu, S.-S. Shyu, J.-Y. Schoung, Y.-B. Huang, Y.-H. Tsai, J.-Y. Hao, Control of wound infections using a bilayer chitosan wound dressing with sustainable antibiotic delivery, J. Biomed. Mater. Res. 59(3) (2002) 438-449.
[42] B. Li, K.V. Brown, J.C. Wenke, S.A. Guelcher, Sustained release of vancomycin from polyurethane scaffolds inhibits infection of bone wounds in a rat femoral segmental defect model, J Control Release 145(3) (2010) 221-230.
[43] M.P. Paarakh, P.A. Jose, C. Setty, Release kinetics: concepts and applications, Int. J. Pharm. Res. Technol. (2019).
[44] A.B. Nair, S. Jacob, A simple practice guide for dose conversion between animals and human, J Basic Clin Pharm 7(2) (2016) 27-31.
[45] H.D. Marston, D.M. Dixon, J.M. Knisely, T.N. Palmore, A.S. Fauci, Antimicrobial resistance, JAMA 316(11) (2016) 1193-1204.

3.7. Supporting Information

3.7.1. Mass spectrometry parameters

Standards and Internal Standards

A certified standard and corresponding deuterated internal standard were used to quantify the amounts in the samples. The internal standard was added to all calibration standards and test samples. The internal standard was used to account for instrument variability, matrix effects, and sample recovery.

Quality Control (QC) Samples

QC samples were used to validate the extraction method and run alongside all test samples. To prepare these samples, the matrix was spiked with three different concentrations of FA standard (low, mid, and high) or TIG (low, mid, and high), spikes that were carried through the extraction procedure to assess % recoveries.

Calibration Standards Preparation

The QC samples were quantified using a FA and TIG standard curve in the presence of the matrix. FA working solutions (2, 5, 10, 25, 50, 100, and 200 ng/mL) were prepared from a 1 mg/mL FA stock through a series of dilutions. TIG working solutions (1, 2, 5, 10, 20, 50, 100, and 200 ng/mL) were prepared from 1 mg/mL TIG stock solution through a series of dilutions. All standards were made with 45 ng/mL d6-fusidic acid internal standard or 50 ng/mL d9-tigecycline internal standard depending on the drug being analyzed.

Mass Spectrometry Parameters

Electrospray ionization (ESI) in negative mode was used for multiple reaction monitoring and quantification of FA and TIG. The optimized mass spectrometer settings used during analysis are listed in Table 3-2. The retention times for FA and TIG are 8.5, and 1.2 minutes respectively.

Table 3-2 Mass spectrometer settings used for FA and TIG analysis

Testing Parameter	**FA**	**TIG**
Drying gas flow rate (L/min)	11	17
Drying gas temperature (°C)	290	150
Nebulizer pressure (psig)	30	35
Sheath gas flow rate (L/min)	11	11
Sheath gas temperature (°C)	300	250
Capillary voltage (V)	2000	4500
Nozzle voltage (V)	1500	500
Acquisition rate (cycles/s)	1.23	1.23

3.7.2. Kinetic Drug Release Profile Analysis

Table 3-3 shows more details on drug release kinetics modeling.

Table 3-3-Parameters calculated through non-linear regression to determine the mechanism and rate of drug release

Equation	Description	Mechanism	Parameter	Best-fit Value	95% CI	R^2
(3-3)	One-phase Association	Diffusion Controlled	A	94.1	90.5 to 100.7	0.80
			B	0.65	0.5 to 0.8	
(3-4)	Power Series	Dissolution Controlled	K	93.3	84.9 to 101.8	0.96
			N	-1.65	-2.0 to -1.4	

3.7.3. Equivalent Animal Dose Calculations

TIG IV administration for complicated skin infection in adults (initial dose of 100 mg in addition to 50 mg every 12 hours for 7-14 days)

For a 48 hour treatment (end point at 48 hours), a total of 250 mg of TIG would be needed for a human adult (HED). Adult human weight was estimated as 60 kg and adult mouse weight was estimated as 0.020 kg or 20 g.

$$\boldsymbol{Animal\ Equivalent\ Dose\ (AED) = Human\ Equivalent\ Dose\ (HED)\ \times \frac{Animal\ Km}{Human\ Km}}$$

$$\boldsymbol{\frac{Mouse\ Km}{Human\ Km} = 12.3}$$

$$\textbf{AED } = \frac{\boldsymbol{250\ mg}}{\boldsymbol{1\ kg}} \times \boldsymbol{12.3 = 3,750\ mg}/\textbf{kg}$$

$$\boldsymbol{3,750}\,\frac{\textbf{mg}}{\textbf{kg}} \times \frac{\textbf{1 kg}}{\textbf{1000 g}} \times \frac{\textbf{20 g}}{\textbf{1 mouse}} \times \frac{\textbf{1000 μg}}{\textbf{1 mg}} = \ \boldsymbol{61,500}\ \textbf{μg/mouse}$$

$$\boldsymbol{\frac{drug\ needed\ for\ oral\ treatement\ using\ FA\ \mu g}{drug\ loaded\ in\ each\ POEGMA - SAP\ Hydrogel\ \mu g} = \frac{61,500\ ug}{6.1\ ug} = \ 10,081 \approx \ 10^4}$$

FA oral administration for soft tissue infection for adults is 1500 mg administered over 3 doses daily). For 48 hour treatment (end point at 48 hours): 3000 mg would be needed for an adult (60 kg). Adult mouse weight was estimated as 0.020 kg or 20 g.

$$\boldsymbol{Animal\ Equivalent\ Dose\ (AED) = Human\ Equivalent\ Dose\ (HED)\ \times \frac{Animal\ Km}{Human\ Km}}$$

$$\boldsymbol{\frac{Mouse\ Km}{Human\ Km} = 12.3}$$

$$\textbf{AED } = \frac{\boldsymbol{3000\ mg}}{\boldsymbol{1\ kg}} \times \boldsymbol{12.3 = 36,900}\ \textbf{mg/kg}$$

$$\boldsymbol{36,900}\,\frac{\textbf{mg}}{\textbf{kg}} \times \frac{\textbf{1 kg}}{\textbf{1000 g}} \times \frac{\textbf{20 g}}{\textbf{1 mouse}} \times \frac{\textbf{1000 μg}}{\textbf{1 mg}} = \ \boldsymbol{738,000}\ \textbf{μg/mouse}$$

$$\boldsymbol{\frac{drug\ needed\ for\ oral\ treatement\ using\ FA\ \mu g}{drug\ loaded\ in\ each\ disk\ \mu g} = \frac{738,000\ \mu g}{4.2\ \mu g} = \ 175,714\ \approx 10^5}$$

Chapter 4- Injectable Macroporous Hydrogels by Combining the Rapid Evaporation of Perfluorocarbon Emulsions with Dynamic Covalent Crosslinking Chemistry

Samaneh Toufanian[1], Andrew Lofts[2], Seamus Adams[1], Meghan Kostashuk[1], Amanda M. Hopp[3], Michael W. Lawlor[3], and Todd Hoare[1,2]*

[1] Department of Chemical Engineering, McMaster University, 1280 Main St. W., Hamilton, Ontario, Canada, L8S 4L8
[2] School of Biomedical Engineering, McMaster University, 1280 Main St. W., Hamilton, Ontario, Canada, L8S 4L8
[3] Department of Pathology and Laboratory Medicine, Medical College of Wisconsin, Milwaukee, WI, USA, 53226
* To whom correspondence should be addressed: hoaretr@mcmaster.ca

Abstract

While injectable hydrogels are significantly less invasive than other available delivery vehicles for cell therapies, the lack of macroporosity in typical injectable hydrogels (and thus the limited free volume available for cell proliferation and nutrient/waste transport) limits the effectiveness of such therapies. Herein, non-cytotoxic and rapidly evaporating perfluorocarbon emulsions are combined with in situ-gelling dynamic covalently crosslinked hydrogels to create an injectable hydrogel in which macropore generation can occur simultaneous to gelation as the perfluorocarbon component evaporates upon heating to physiological temperature. Macropores can be generated at different densities dependent on the perfluorocarbon concentration both *in vitro* and *in vivo* without inducing any significant cytotoxicity or local or systemic inflammatory responses. The produced hydrogels are easy to handle, showing a compressive modulus of 27 ± 2 kPa. Furthermore, live/dead imaging showed 31% higher viability of encapsulated cells in porous hydrogels in comparison to non-porous controls, attributed to the improved mass transport achievable in the presence of macropores. The combination of controllable porosity, non-cytotoxicity, and ability to incorporate cells into the porous structure via a single injection offers a unique platform that could be adapted for use in cell therapy and/or tissue engineering applications.

Graphical Abstract

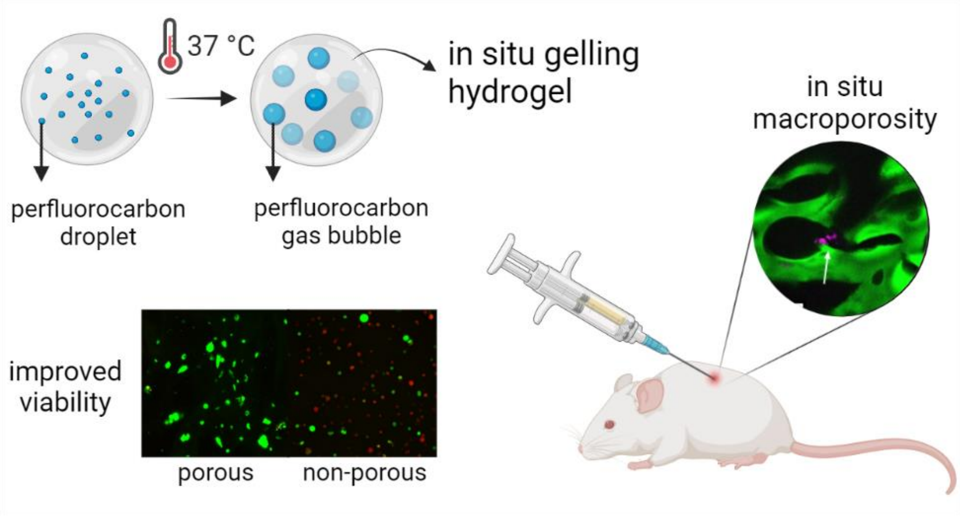

4.1. Introduction

Hydrogels have attracted significant interest in the context of tissue engineering given their ability to mimic the interfacial, mechanical, chemical, and biological functions of native extracellular matrix (ECM) [1, 2]. However, the minimally-invasive delivery of conventional hydrogels to tissue repair sites is a significant impediment to their effective use without surgical intervention. Due to the high yield stress of hydrogels, the injection of conventional pre-crosslinked hydrogels is only possible using materials that are sufficiently non-viscous/shear thinning (limiting the crosslink density and thus stiffness of the final hydrogel) and/or using large diameter needles [3], with both approaches typically exposing seeded cells to higher local stresses that can cause cell membranes to rupture [4].

In contrast, injectable hydrogels that can be delivered as low-viscosity precursor materials that gel *in situ* in the body can overcome this challenge to enable facile local delivery of regenerative hydrogels to target tissue sites [5], reducing patient recovery time and cost [1] as well as the shear experienced by cells co-injected with the precursor materials [6]. Injectable hydrogels can be made using physical approaches (e.g. hydrophobic interactions, charge interactions, supramolecular chemistry, or hydrogen bonding) [1, 7] or chemical methods, with a suite of click or click-like chemistries having been reported to tune the gelation time and degradation time of the resulting hydrogels [8, 9]. Our lab has extensively explored the use of hydrazone chemistry for designing dynamic covalent injectable hydrogels, with a specific emphasis on *in situ* gelation facilitated by mixing hydrazide and aldehyde-functionalized poly(oligoethylene glycol methacrylate) (POEGMA) precursor polymers [10]. The use of hydrazone crosslinking chemistry enables fast gelation and tunable hydrolytic degradation depending on the structure and reactive functional group density of the POEGMA precursor polymers [11]. The choice of POEGMA as the polymer backbone is motivated by its capacity to be polymerized by standard free radical methods, allowing for facile tuning of chemical functionalization [12], mechanics [13], and biological responses [11]; in addition, the number of ethylene glycol repeat units in the polymer side-chain (n) can be tuned to control the interfacial properties of the hydrogels, with longer side-chain length polymers (n>5-6 repeat units) yielding similar properties to poly(ethylene glycol) (e.g. hydrophilicity, non-cytotoxicity, and low protein adsorption [11]) while shorter side-chain length polymers can exhibit similar thermoresponsive properties to poly(N-isopropylacrylamide) [11].

However, the lack of macroporosity typically achievable with injectable hydrogels (including our previously reported POEGMA materials) represents a key bottleneck to the wide-spread use of such hydrogels in tissue engineering applications [14]. Macroporous pore structures are critical for successful tissue regeneration in terms of facilitating sufficient oxygen and nutrient transport as well as providing the physical space required for cell migration and proliferation [2, 14]. Macroporosity can be achieved in conventional hydrogels using a range of techniques including cryogelation, electrospinning, emulsion templating, salt/porogen templating, gas foaming, or 3D printing [2]. However, all these techniques require the use of non-tissue compatible additives (salt/porogen templating, gas forming, emulsion templating), non-physiological processing conditions (cryogelation), and/or external equipment that cannot be easily applied in a clinical setting (electrospinning, 3D printing) [14]. We have previously demonstrated the use of some of these techniques to create macrostructured hydrazone-crosslinked POEGMA hydrogels; for example, an all-aqueous reactive electrospinning process was developed to fabricate nanofibrous hydrogel networks with ultra-fast swelling responses [11], anisotropic hydrogels with direction-dependent structure and properties were fabricated using a freeze-casting technique aided by the incorporation of cellulose nanocrystals in the hydrogel to provide sufficient mechanical strength [15], and shape-tunable cellularized scaffolds were 3D printed using an embedded extrusion bioprinting technique [16]. However, in each case described above, the *in situ* gelation properties of the hydrogel were applied to enable precise control over the geometry of the resulting gelation reaction rather than facilitate practical *in vivo* injectability. While some recent efforts have demonstrated the potential of hand-held devices to perform *in situ* electrospinning [17] or 3D printing [18] to enable the generation of macroporous hydrogels in a surgical setting, in both situations the target tissue site needs to be openly accessible to the surgeon such that these delivery strategies would still require an invasive surgical procedure. As such, the development of a truly injectable macroporous hydrogel fabrication method would address an unmet need in the tissue regeneration space.

In this paper, we demonstrate the use of perfluorocarbons (PFCs) as tissue-compatible gas foaming agents to enable the safe, non-toxic production of injectable macroporous hydrogels. PFCs have previously been reported for use *in vivo* as oxygen gas carriers, typically using high boiling point PFCs such as perfluorodecalin (boiling point = 142°C) that remain liquid under typical *in vivo* conditions [19] for fabricating "poppable" PFC microbubbles or nanoemulsions suitable for ultrasound imaging and/or ultrasound-triggered drug delivery [20, 21]. Perfluorocarbon-based materials have also been utilized for photodynamic therapy in cancer treatment and bone fracture healing [22, 23] as well as to enhance oxygen transport and retention in tissue scaffolds and thus reduce cell mortality deeper into hydrogel structures, exploiting the high oxygen solubility of PFCs (~20 times greater than water [24]). Herein, we instead use a perfluorocarbon emulsion with a sub-physiological temperature boiling point (perfluoro-n-pentane or PFnP, boiling point = 29°C [25]) together with *in situ*-gelling hydrazide/aldehyde-functionalized POEGMA precursor polymers to form a macroporous injectable hydrogel (Figure 4-1). Upon heating the PFnP emulsion from room temperature (prior to injection) to physiological temperature (following *in vivo* injection), the emulsion droplets evaporate on the same time scale as gelation to create tunable densities of (semi-continuous) macropores while preserving hydrogel injectability through a single syringe (Figure 4-1). We demonstrate the fabrication of such networks both *in vitro* and *in vivo*, with macroporosity shown to be enabled while maintaining high cell and tissue compatibility.

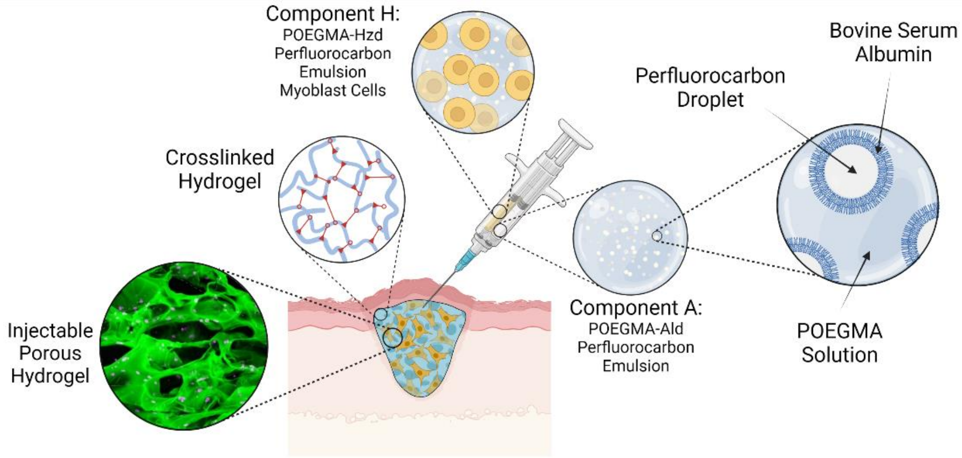

Figure 4-1- Schematic showing subcutaneous injection of hydrogel in which *in situ* gelation of hydrazide/aldehyde-functionalized POEGMA precursor polymers and evaporation of a perfluorocarbon-based emulsion occur simultaneously to create a macroporous hydrogel.

4.2. Materials and Methods

4.2.1. Materials

Poly(ethylene glycol) methyl ether methacrylate (average M_n ~ 500 Da, containing 200 ppm butylated hydroxytoluene and 100 ppm mequinol as inhibitors, Millipore Sigma, Oakville, ON) and di(ethylene glycol) methyl ether methacrylate (95%, Millipore Sigma, Oakville, ON) were used after purification using basic alumina (60-325 mesh, Fisher Scientific, Burlington, ON). 1,4-dioxane (Caledon Laboratories, Georgetown, ON), the initiator 2,2'-azobis(2-methylpropionate) (AIBME, 98.5%, Wako Chemicals, Shanghai, China), thioglycolic acid (98%, Millipore Sigma, Oakville, ON), acrylic acid (AA anhydrous, containing 200 ppm of mequinol as inhibitor, 99%, Millipore Sigma, Oakville, ON), adipic dihydrazide (Fisher Scientific, Burlington, ON) and N′-ethyl-N-(3-

dimethylaminopropyl)-carbodiimide (EDC, 98%, TCI America, Tokyo, Japan), and chloroform-d (99.8 atom %, Millipore Sigma, Oakville, ON) Blocker™ BSA (10X) in PBS (ThermoFisher Scientific, Burlington, ON), perfluoro-n-pentane (Fluoromed, Round Rock, TX), anhydrous ethanol (Commercial Alcohols, Brampton, ON), fetal bovine serum (Wisent Inc., Saint-Jean-Baptiste, QC), Dulbecco's Modified Eagle Medium (DMEM, Wisent Inc., Saint-Jean-Baptiste, QC), phosphate buffered saline (PBS, Wisent Inc., Saint-Jean-Baptiste, QC), agar (Bio-Rad Laboratories Ltd, Mississauga, ON), penicillin streptomycin (Wisent Inc., Saint-Jean-Baptiste, QC), formalin solution (10% PBS buffered, Millipore Sigma, Oakville, ON) were all used as received. N-(2,2-dimethoxyethyl) methacrylamide (DMAEMA) was synthesized in-house based on previously reported protocols [26]. MilliQ-grade distilled deionized water (DIW) was used for all experiments.

4.2.2. Synthesis of polymer precursors

Hydrazide-functionalized POEGMA precursor polymer (POEGMA-Hzd) was synthesized according to previously established protocols [13]. Briefly, oligo(ethylene glycol) methyl ether methacrylate (1.80 g), di(ethylene glycol) methyl ether methacrylate (6.20 g), AA (1.10 g), TGA (0.02 g), AIBME (0.074 g) and 1,4-dioxane (40 mL) were added to a 500 mL round bottom flask and stirred at 250 rpm using an magnetic stir bar. After 30 minutes of purging with nitrogen, the flask was placed in an 85 °C oil bath and allowed to react for 4 hours. To ensure termination of the reaction, the reaction was purged with air for 30 minutes prior to removing the 1,4-dioxane using rotary evaporation (37 °C, 30 min, maximum vacuum). To functionalize the acrylic acid residues with hydrazide groups, the remaining polymer (~9.2 g) was dissolved in 300 mL of Milli-Q water, ADH (6.27 g) and EDC (2.79 g) were added, and the solution pH was adjusted to pH 4.7. The pH of the solution was subsequently maintained between 4.6-4.8 using 0.1 M HCl over at least 4 hours to facilitate the conjugation reaction, after which the reaction was stirred under ambient condition overnight.

Aldehyde-functionalized POEGMA precursor polymers (POEGMA-Ald) were synthesized via a similar approach, dissolving oligo(ethylene glycol) methyl ether methacrylate (1.80 g), di(ethylene glycol) methyl ether methacrylate (6.20 g), DMAEMA (2.60 g), TGA (0.02 g), and AIBME (0.100 g) in 1,4-dioxane (40 mL) and following the same polymerization procedure outlined above. To subsequently deprotect the acetal group on the DMEAMA monomer to generate aldehyde groups, the product polymer (~9.3 g) was dissolved in 100 mL of deionized water and 100 mL of 1 M HCl and stirred overnight at room temperature.

Both polymer precursor solutions were then dialysed separately against 5 L of Milli-Q water for 6 cycles of at least 6 hours (SnakeSkin™ dialysis tubing, 3.5 kDa molecular weight cut-off, 3.5 mm diameter, ThermoFisher Scientific). Each resulting polymer solution was then filtered through a 0.2 µm polyethersulfone (PES) filter inside a biosafety cabinet, with the filtrate contained in a sterile glass jar and subsequently freeze dried under aseptic conditions using a Teflon valve to connect a sterile bell jar into which a secondary glass jar containing sterile frozen polymer solution was inserted to a lyophilizer. Finally, the resulting polymers were dissolved in sterile phosphate buffered saline to obtain 40 wt% polymer solutions that were subsequently stored at 4°C.

To enable the visualization of the hydrogel structures using fluorescence microscopy, fluorescein isothiocyanate (35 mg) was added to a diluted POEGMA-Hzd solution (5.76 g in PBS, 2.5 wt% concentration) and stirred overnight in the dark at room temperature to fluorescently label the POEGMA-Hzd polymer (target label density = 1 mol% of hydrazide functional groups). The solution was then dialysed (SnakeSkin™ dialysis tubing, 3.5 kDa molecular weight cut-of, 3.5 mm diameter, ThermoFisher Scientific) against MilliQ water for at least 6 cycles of at least 6 hours each. The sterile 40 wt% POEGMA-Hzd-FITC polymer solution in PBS was prepared as described for the non-labeled polymers and subsequently stored protected from light at 4 °C.

4.2.3. Polymer precursor characterization

Gel permeation chromatography (GPC, Agilent Technologies, Santa Clara, California, USA) was performed on both POEGMA precursor polymers in phosphate buffered saline (1 mg/mL) to determine the average molecular weight and polydispersity of the two polymer precursors. The detector temperature was set to 30 °C using Superose 6 Increase 10/300 GL column (Cytiva, Toronto, ON). PBS with 0.05 wt% sodium azide was used as the solvent, and the solvent flow rate was set to 0.5 mL/min. Nuclear magnetic resonance (^{1}H NMR, Bruker AV 600, Bruker Corporation, Billerica, Massachusetts, USA) was performed on both POEGMA-Hzd and POEGMA-Ald polymer precursors in chloroform-d (5 mg/mL) to quantify copolymer content and aldehyde monomer incorporation. To determine the POEGMA-Hzd functionalization, conductometric titration (base-into-acid using 0.1 M sodium hydroxide as the titrant, ManTech Inc., Guelph, ON) by comparing the carboxylic acid content of the polymer before and after the carbodiimide-mediated hydrazide functionalization step.

4.2.4. Preparation of perfluorocarbon emulsion

Bovine serum albumin solution (5% in PBS) was prepared by diluting Blocker™ BSA solution with an equal volume of sterile PBS. Perfluoro-n-pentane (5 mL) was added to 40 mL of the prepared 5 wt% BSA solution and sonicated using a probe sonicator (amplitude 80%, duration 1.5 minutes, 2 seconds on, 30 seconds off, Q700-Q-Sonica, Newtown, CT, USA) while chilled on ice. The temperature was maintained below 12 °C over the duration of sonication. The perfluorocarbon emulsion was stored on ice and used as soon as possible but in all cases within 3-4 hours, after which a fresh emulsion would be prepared to ensure sample-to-sample consistency in the starting materials.

4.2.5. Characterization of perfluorocarbon emulsion

The diameter of the perfluorocarbon droplets was measured by diluting the perfluorocarbon emulsion produced in section 4.2.4 in chilled PBS at 1 vol% and measuring particle size via dynamic light scattering (DLS) using a Brookhaven NanoBrook 90Plus Particle Size Analyser and the accompanying BIC Particle Solutions Software (Version 2.6, Brookhaven Instruments Corporation, Holtsville, NY). Electrophoretic mobility was measured using a ZetaPlus zeta potential analyzer (Brookhaven Instruments Corporation) operating in phase analysis light scattering (PALS) mode. For this experiment, the perfluorocarbon emulsion was diluted at a concentration of 1 vol% into 8.6 mM sodium chloride solution in MilliQ water, resulting in a final sodium chloride concentration of 10 mM. In both cases, measurements were collected at temperatures between 17 to 37 °C, with a fresh sample used for each temperature measured.

4.2.6. Preparation of hydrogels

Polymer precursor solutions (40 wt%) were diluted with PBS (non-porous control) or the perfluorocarbon emulsion (to make macroporous hydrogels) at a volume ratio of 1:3 polymer solution:PBS. Three different pore-forming agents (PFAs) were then prepared containing 100 vol %, 10 vol %, and 1 vol % of the initial perfluorocarbon emulsion stock solution, with the remainder of the volume made up with PBS. Representative preparation volumes specific to the mechanics measurements are shown in Table 4-1 for each of the four key hydrogels prepared in this work; Supporting information Table 4-4Table 4-2 shows how these volumes were scaled (in the same ratios) to fabricate different sizes of samples for different types of analyses. The sample codes refer to the percentage of stock perfluorocarbon emulsion in the PFA that was mixed with the POEGMA polymer precursor solutions (POEGMA-Ald or POEGMA-Hzd) prior to injection.

For *in vivo* experiments, the precursor solutions (0.3 mL of each precursor polymer leading to a total gel volume of 0.6 mL) were co-injected subcutaneously using a double barrel syringe (MedMix, ZUG, Switzerland) using a 5/8 inch long 25 G needle. Accounting for the dead volume in the static mixer, each animal received a 0.4 mL dose of hydrogel. For *in vitro* biological assays and swelling and degradation assays, the precursor solutions (1 mL, corresponding to a 0.8 mL total gel volume accounting for the static mixer dead volume) were injected into a 50 mL conical centrifuge tube and immediately placed into a 37°C preheated water bath for 15 minutes. Swelling and degradation samples were maintained at 37°C in a shaking incubator over the duration of the study. For cell studies, gels were removed from the bottom of the conical tubes, placed in a 6 well plate, and incubated in 5 mL of DMEM (5% CO_2, 37 °C) before further analysis or staining. For mechanical studies, the precursor solutions (3 mL total volume) were injected into 35 mm diameter Petri dishes and allowed to gel in a preheated water bath for 15 minutes, resulting in gels with a thickness between 1.4-3 mm depending on the degree of gel expansion observed during pore formation.

Table 4-1- Hydrogel formulations used to prepare macroporous hydrogels and non-porous control hydrogels by varying the amount of perfluorocarbon emulsion added

	Component H (hydrazide)			Component A (aldehyde)		
	PFA		40 wt% POEGMA-Hzd (µL)	PFA		40 wt% POEGMA-Ald (µL)
	Perfluorocarbon Emulsion (µL)	PBS (µL)		Perfluorocarbon Emulsion (µL)	PBS (µL)	
POEGMA-PFA-0	0	2250	750	0	2250	750
POEGMA-PFA-1	23	2227	750	23	2227	750
POEGMA-PFA-10	225	2025	750	225	2025	750
POEGMA-PFA-100	2250	0	750	2250	0	750

4.2.7. Hydrogel structure visualization

Fluorescent hydrogels were prepared as described in section 4.2.6 by replacing 25% of the volume of the POEGMA-Hzd solution with a POEGMA-Hzd-FITC solution prepared at the same precursor polymer concentration. The pore structure was visualized using laser scanning confocal microscopy (CLSM, A1R HD25, Nikon, pinhole 1, optimal step size) using z-stack imaging and an excitation wavelength of 488 nm and an emission range of 500-542 nm. Alternately, using the same ratio of POEGMA-Hzd-FITC:POEGMA-Hzd in the precursor polymer solution, the kinetics of pore generation were tracked for materials prepared by mixing undiluted (100%) perfluorocarbon emulsion (to create a porous hydrogel, POEGMA-PFA-100) or PBS (to create a non-porous control hydrogel, POEGMA-PFA-0) by co-injecting the precursor materials using a double barrel syringe into a polystyrene Petri dish (35 mm in diameter) inside a preheated chamber (37 °C) mounted on an optical microscope. A series of images was collected at equally spaced time intervals to track the kinetics of pore generation in the hydrogels.

4.2.8. Hydrogel mechanics

The Mach-1 V500CST mechanical tester (Biomomentum Inc.) was used to evaluate the mechanical properties of the porous and non-porous POEGMA gels. Uniaxial compressive moduli were measured via indentation using a spherical indenter (1/4" diameter) by compressing the gels by 25% of their original thickness and tracking the normal force during the compression. The strain rate was set to 0.01 1/s for all compression tests. The compressive modulus was calculated using the Mach-1-Analysis software. All experiments were performed at 6 different locations in the hydrogel, with any outlying measurement identified using Grubb's test ($p<0.05$). The resulting reported modulus values represent the average of the non-outlier measurements, with the error bar corresponding to the standard deviation (minimum n=5 repeat measurements per sample).

4.2.9. Hydrogel swelling and degradation

Gels were prepared as discussed in section 4.2.6, weighed after being removed from conical tubes, and placed in nylon mesh cell strainers (mesh size 40 µm). Cells were then incubated in 15 mL of the test solution. For swelling studies, a standard PBS solution was used; for the degradation studies, 0.1 N HCl solution was used to accelerate hydrazone bond hydrolysis and expedite the degradation process on a more measurable timescale to enable comparisons of degradation times between different sample recipes. At pre-defined time points, the samples were removed from the swelling or degradation media, wicked dry to remove non-bound water using a Kimwipe, and weighed. The swelling ratio was calculated by dividing the measured mass of the gel at each time point by the original (unswollen) mass of the gel (n=3 repeat measurements per sample).

4.2.10. Cell culture

C2C12 mouse myoblasts (ATCC©, CRL-1772) were cultured in cell culture flasks in DMEM media containing 10% FBS and 1% penicillin streptomycin and incubated in 37 °C in a 5% CO_2 atmosphere. Cell confluence was maintained below 75%. To harvest cells from T175 tissue culture flasks, cell culture media was removed, 20 mL of prewarmed PBS was used to rinse the cells, and 5 mL of 25% w/v trypsin-EDTA was added to each flask and incubated at 37°C for ~5 minutes to detach the majority of adhered cells from the flasks (as confirmed using light microscopy). 20 mL of prewarmed DMEM cell culture media (10% FBS, 1% penicillin streptomycin) was then added to each flask to neutralize trypsin-EDTA, after which the cell population in the resulting cell suspension was determined using a hemocytometer. For each gel, 4 million cells were added to a 15 mL conical tube, pelletized (250 RCF, 5 min), resuspended in either 375 µL PBS or the perfluorocarbon emulsion prepared as described in section 4.2.4, and mixed with 125 µL of 40 wt% hydrazide functionalized POEGMA solution. No cells were added to the aldehyde-functionalized precursor polymer solution. The precursor materials were loaded into sterilized double barrel syringes with a 16 G needle and extruded through a 25G needle to obtain gels as described in section 4.2.6. Cell culture media was changed every 2-3 days.

4.2.11. Cytocompatibility and metabolic activity assays

The cytocompatibility of hydrogel precursor solutions was measured against C2C12 mouse myoblasts using a CellTiter 96® AQueous One Solution Cell Proliferation (MTS) Assay. C2C12 mouse myoblasts were plated in a 96-well black well plates with a clear bottom at a cell density of 4000 cells/well. Each well plate was incubated for 24 hours to ensure cell adhesion prior to exposing cells to the test solutions. Cytocompatibility was tested against polymer precursor solutions prepared by diluting polymer precursor solutions in media, perfluorocarbon emulsions diluted to multiple concentrations in a mixture of media, and BSA solutions prepared at the same BSA concentration used to fabricate the perfluorocarbon emulsions (the latter of the two being tested as controls). Gel leachates were also tested to evaluate whether any of the degradation/leachate products released as the gel degrades induced cytotoxicity. Gel leachates were collected by incubating pre-formed hydrogels (prepared as described as in section 4.2.6 for biological experiments with no encapsulated cells) in 5 mL of DMEM. At pre-defined time points, the media was collected, filtered through a 0.2 µm PES syringe filter to ensure no transfer of any gel fraction in the sample, and replaced with fresh media. The process was repeated at days 1, and 3 after gel preparation, with the collected leachate stored at -20°C prior to testing. Each test solution was incubated with the cells for 24 hours, after which the supernatant was removed, each well was thoroughly washed with PBS and fresh media (100 µL), and MTS assay ragent (20 µL) was added to each well. Plates were incubated in a humidified environment at 37°C (5% CO2) for ~4 hours, after which the absorbance was measured in each well at a wavelength of 490 nm. Cell viability (metabolic activity) was calculated by subtracting the average background (cell culture media and MTS reagent without cells) from each well and dividing the resulting absorbance value by the absorbance of the negative control wells (i.e. cells treated with standard cell culture media and MTS reagent). This assay was performed with n=8 replicates, with the standard error reported as the error bar.

4.2.12. Live/Dead imaging

A LIVE/DEAD™ Cell Imaging Kit (Invitrogen) was used to determine cell membrane integrity at different timepoints (days 1, 7, and 14). Samples containing cells were prepared as described in section 4.2.6. At each timepoint, media was removed from the well plates and replaced with the staining solution prepared according to the manufacturer’s recommended protocol. After 15 minutes of staining at room temperature, the samples were washed once with PBS and moved to a 3.5 mm Petri dish with a 1 N glass slide viewing chamber. All samples were imaged using laser scanning confocal microscopy (LSCM) at various magnifications. Z-stack images (20x magnification, pinhole = 1, optimal step = 0.25 µm) were then acquired using laser scanning confocal microscopy operating in resonant mode with averaging set to 16 using the optimal slice thickness recommended by Nikon imaging software (Figure 4-2). To image live cells, the FITC channel with excitation of 488 nm and emission range of 500-542 nm was used; for dead cells, the TRITC channel with excitation wavelength of 561 nm and an emission range of 578-623 nm was used.

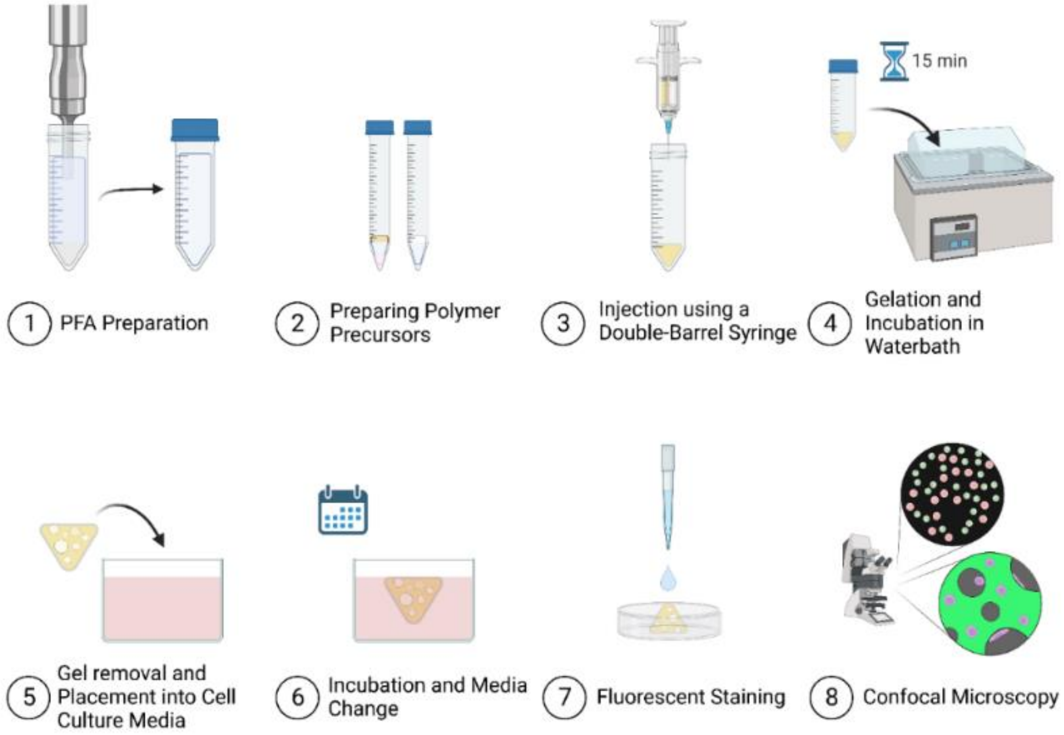

Figure 4-2- *In vitro* sample preparation, staining, and imaging workflow for fabricating cell-loaded macroporous hydrogels.

To use the images to calculate cell viability, images from different samples were normalized based on the total thickness of the imaged block and the intensity of each image in the stacks was adjusted to 0.1. Following, maximum intensity projections were created and analyzed using an image processing macro developed by the Centre for Advanced Light Microscopy at McMaster University. Cell viability was calculated based on the total number of live (green) and red (dead) cells imaged according to (4-1)**.** For each timepoint, at least 2-3 images were used to determine the standard deviation.

$$\frac{\boldsymbol{Live}}{\boldsymbol{Live} + \boldsymbol{Dead}} = \%\,\boldsymbol{viability} \qquad \textbf{(4-1)}$$

4.2.13. 3D cell-scaffold imaging

To highlight the interactions between cells and the hydrogel scaffold, C2C12 mouse myoblast cells were stained 16-24 hours prior to gel preparation using Vibrant FarRed CellTrace (Invitrogen) according to the manufacturer's recommended protocol. To obtain fluorescent hydrogel, 25% of the POEGMA-Hzd solution volume used to make the hydrogel was replaced with POEGMA-Hzd-FITC prepared at the same precursor polymer concentration, with gels prepared based on procedures described in sections 4.2.6 and 4.2.12. Samples were fixed in phosphate buffered formalin solution for 30 minutes at room temperature prior to imaging using confocal microscopy as described in section 4.2.12 using excitation wavelengths of 488 nm and 640 nm and detection ranges of 500-542 nm and 624-680 nm for POEGMA-Hzd-FITC and FarRed labeled cells respectively.

4.2.14. In vivo tissue compatibility and pore generation

All animal procedures were performed in accordance with protocols approved by the Animal Research Ethics Board of McMaster University, the Animals for Research Act of Province of Ontario, and the guidelines of the Canadian Council on Animal Care. Male BALB/c mice (Charles River Laboratories, Wilmington, MA, 21.2-24.7 g weight) were exposed to a 12 h light/dark cycle with access food and water as desired. To assess the tolerability of the injectable macroporous hydrogels *in vivo,* mice were randomly assigned to groups of 4 with each group receiving 0.4 mL subcutaneous injections of: (1) a POEGMA-perfluorocarbon emulsion prepared using an undiluted perfluorocarbon emulsion (POEGMA-PFA-100, macroporous hydrogel); (2) a POEGMA-only hydrogel prepared by mixing 10 wt% aldehyde or hydrazide-functionalized POEGMA precursor polymer solutions to match the final polymer concentrations in the macroporous hydrogel precursor solutions (POEGMA-PFA-0, non-porous hydrogel); or (3) saline (negative control); see Table 4-2 for the full precursor polymer preparation recipes corresponding to the fabrication of the tested hydrogels.

Table 4-2- Hydrogel compositions for *in vivo* tolerability and inflammation studies

	Component H (hydrazide)			Component A (aldehyde)		
	PFA		40 wt% POEGMA-Hzd (μL)	PFA		40 wt% POEGMA-ALD (μL)
	Perfluorocarbon Emulsion (μL)	PBS (μL)		Perfluorocarbon Emulsion (μL)	PBS (μL)	
Saline Control	N/A					
POEGMA-PFA-0	0	300	100	0	300	100
POEGMA-PFA-100	300	0	100	300	0	100

Mice were monitored daily for the first 48 hours and weighed twice per week to ensure they did not reach any endpoint with regards to excessive weight gain/loss. At pre-determined time points (day 3 for acute and day 28 for chronic), mice were sacrificed using a combination of isoflurane and carbon dioxide followed by cervical dislocation as a secondary measure. After the skin above the injection site was shaved, skin and muscle tissue surrounding the injection site was collected in addition to vital organs including the spleen, kidneys, liver, heart, and lungs. Collected tissue samples were rinsed in PBS and fixed in formalin solution (neutral buffered, 10%, Sigma-Aldrich, Oakville, ON) for 18-24 hours. Tissue samples were then dehydrated via exposure to 50%, 60% and 70% ethanol solutions for 4 hours each, with samples stored in 70% ethanol until they were embedded in paraffin. Histological sections were then prepared and stained using a standard H&E staining protocol to assess the degree of inflammation in each collected tissue. Histological analysis of the stained tissue sections was performed by a blinded observer using a numerical scale where 0 = no inflammation, 1 = focal or few foci of inflammation, 2 = mild or moderate inflammation (more than a few foci or higher inflammation compared to samples rated as with minimal inflammation), and 3 = severe inflammation.

In a separate experiment to directly assess the porosity generated in the hydrogels upon *in vivo* administration, a second set of BALB/c mice was randomly assigned to 4 groups of n=3 mice and injected subcutaneously with 0.4 mL of the precursor polymer suspension. The precursor polymers were prepared by replacing 25% of the POEGMA-Hzd fraction with POEGMA-Hzd-FITC (to enable fluorescence imaging of the resulting hydrogel) and mixing with one of four dilutions of the perfluorocarbon emulsion: (1) 100% (undiluted) perfluorocarbon emulsion matching the tissue compatibility test concentration (POEGMA-PFA-100); (2) 10% perfluorocarbon emulsion diluted in PBS (POEGMA-PFA-10); (3) 1% perfluorocarbon emulsion diluted in PBS (POEGMA-PFA-1); or (4) a PBS-only control (POEGMA-PFA-0). After 24 hours, animals were sacrificed as described above and the fluorescent hydrogels were explanted and fixed in formalin solution for at least 18 hours. Imaging was performed using laser scanning confocal microscopy operating at an excitation wavelength of 488 nm and an emission range of 500-542 nm. Samples were imaged within 48 hours after sacrifice and explantation of the fluorescent hydrogels.

4.3. Results and Discussion

4.3.1. Polymer characterization

Table 4-3 summarizes the key physical and chemical properties of the hydrazide and aldehyde-functionalized precursor polymers used to form the hydrogels. Over multiple (n=3) batches, the number average molecular weights were consistently <10 kDa with dispersity (Đ) values <2.5; given that the precursor polymers are regenerated as the degradation products following hydrazone bond hydrolysis [13], this molecular weight range suggests the potential for renal clearance of the hydrogel following degradation [26]. The degree of functionalization achieved over multiple batches also matched the target 30 mol% aldehyde/hydrazide functionalization. As such, the polymers could be synthesized reproducibly with properties consistent with rapid *in situ* gelation and ultimate clearance of the hydrogel over time.

Table 4-3- Characterization of POEGMA precursor polymers

	M_n (kDa)	Dispersity *Đ*	Target Degree of Functionalization	Actual Degree of Functionalization
POEGMA-Hzd	9.8 ± 1.5	2.6 ± 0.1	30%	29 ± 2 %
POEGMA-Ald	7.8 ± 1.4	2.4 ± 0.2	30%	29 ± 1 %

4.3.2. Perfluorocarbon emulsion characterization

Perfluorocarbon emulsions were fabricated by sonicating a 1:8 volume ratio of perfluoro-n-pentane:PBS (including albumin as the interfacial stabilizer) on ice to minimize perfluorocarbon evaporation during emulsification. Figure 4-3 shows the evolution of the droplet size (Figure 4-3-a) and the electrophoretic mobility (Figure 4-3-b) of the resulting emulsions as a function of temperature. Discontinuous changes in emulsion properties were observed when the temperature was increased above the boiling point of perfluoro-n-pentane (~29 °C); specifically, the droplet size significantly increases while the count rate significantly decreases around the perfluorocarbon boiling point (Figure 4-3-a), both of which are consistent with the onset of evaporation of the perfluorocarbon. The emulsion remains stable on ice (~10% change in droplet size) over the maximum four hour storage time allowed before a fresh emulsion was used for macroporous hydrogel fabrication, ensuring good sample-to-sample reproducibility. Concurrently, the absolute electrophoretic mobility of the emulsion droplets decreases around the perfluorocarbon boiling point (Figure 4-3-b), consistent with the same amount of stabilizing albumin now being distributed over a larger overall surface area as the droplet expands.

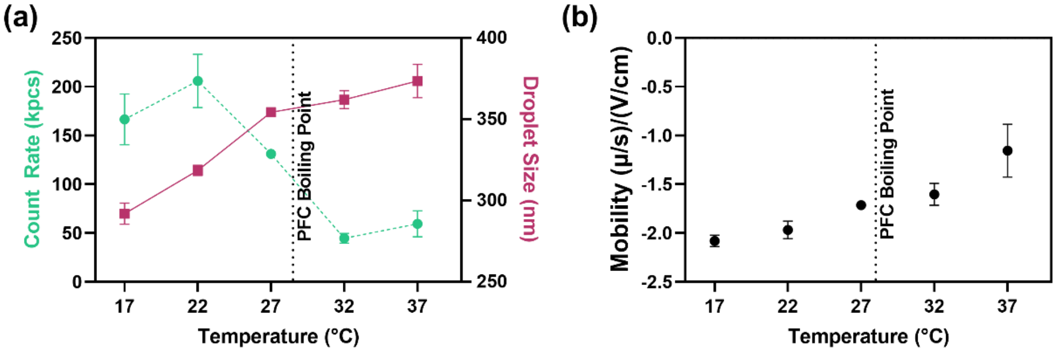

Figure 4-3- Droplet size (a, right axis), light scattering count rate (a, left axis), and electrophoretic mobility (b) of the prepared perfluorocarbon/PBS/albumin emulsions as a function of temperature. The dotted vertical line in each figure represents the boiling point of perfluoro-n-pentane (29 °C).

4.3.3. Hydrogel fabrication and pore generation

Hydrogels were next formed by mixing the perfluorocarbon emulsion (either undiluted or diluted 10-fold or 100-fold with PBS to reduce the total perfluorocarbon content in the resulting gels) with 40 wt% precursor polymer solutions in a 1:3 volume ratio, resulting in a final POEGMA precursor polymer concentration of 10 wt%. This fabrication approach was chosen to maximize the amount of perfluorocarbon incorporated into the gels, as 40 wt% is the maximum concentration at which the POEGMA precursor polymers are freely soluble in PBS. The gelation time was <10 s with or without the added perfluorocarbon emulsion as estimated by a vial inversion test, enabling rapid entrapment of the perfluorocarbon emulsion within the gel phase to prevent creaming or, as the perfluorocarbon evaporates, surface-only foaming that would lead to inhomogeneous pore generation.

To confirm that *in situ* pore generation could be driven by the incorporation of the perfluorocarbon emulsion, samples with and without perfluorocarbon were injected onto a prewarmed polystyrene petri dish placed in a preheated chamber and imaged in real time to track pore generation (Figure 4-4). In the sample containing perfluorocarbon, both an increasing number of pores and larger pores (including the merging of neighbouring pores) are observed over time as the perfluorocarbon evaporates upon exposure to the 37°C incubation condition; in contrast, in the sample with no perfluorocarbon added, no pores are observed to be generated. As such, perfluorocarbon is confirmed to effectively drive *in situ* pore generation and air bubbles that may arise from mixing the precursor polymers are not the principal driver of the pore structure generated.

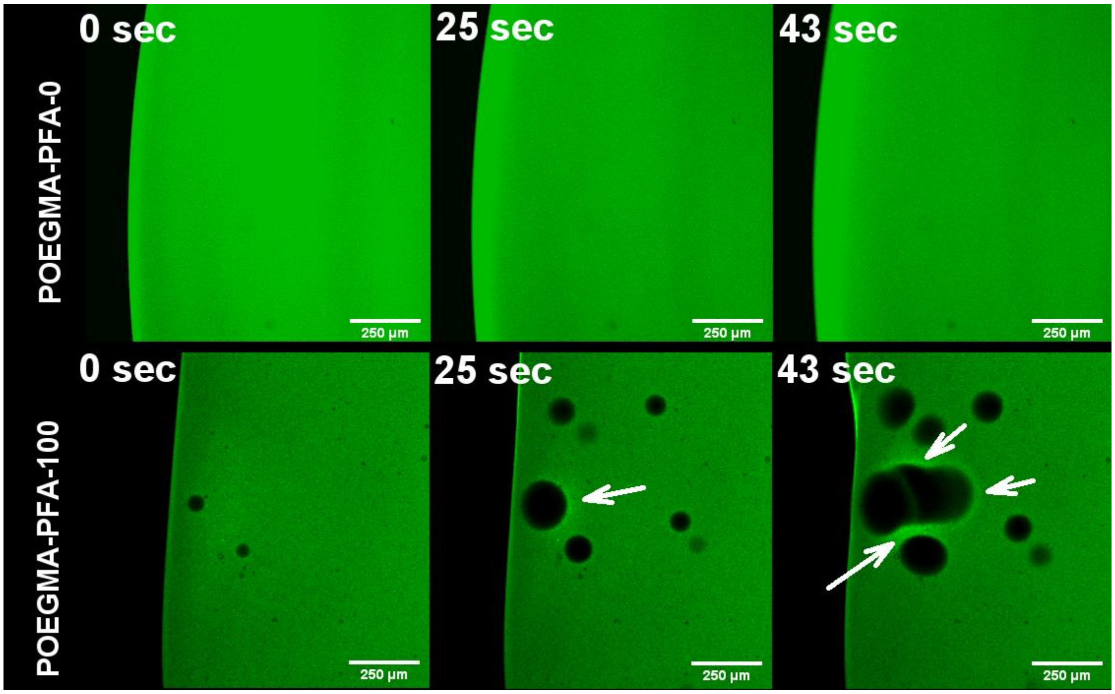

Figure 4-4- Screenshots of the real-time pore generation in a perfluorocarbon-free POEGMA-PFA-0 hydrogel (top) relative to the nucleation and expansion of pores in a perfluorocarbon-containing POEGMA-PFA-100 hydrogel (bottom) as a function of time. Arrows highlight increases in the local fluorescence signal that support local dewatering of the hydrogel around the pores during pore formation (see section 4.3.5).

4.3.4. Pore structure control

Figure 4-5 shows 3D reconstructions of the macroporous hydrogel structures generated in vitro (using the protocol in section 4.2.6) and in vivo (using the protocol in section 4.2.6) using different perfluorocarbon emulsion concentrations. In the absence of perfluorocarbon, no macropores are observed; as more perfluorocarbon is added, more pores and more interconnected pores are generated and maintained within the gel. We hypothesize this pore generation and entrapment within the gel is a direct result of the balance between the heat transfer kinetics (i.e. heating from room temperature at the point of injection to physiological temperature) and the gelation kinetics, such that pores are made on the timescale of gelation and thus can be trapped within the forming gel network instead of being fully dissipated through the precursor polymer solution prior to gelation. Perfluorocarbon emulsion diluted 10:1 versus the stock solution (POEGMA-PFA-10) still facilitates significant porosity in the constructs, with the non-diluted (POEGMA-PFA-100) emulsion yielding the highest pore interconnectivity consistent with the increased volume and frequency of gas generation achieved during the evaporation process. Interestingly, very similar pore structures were generated *in vitro* as well as *in vivo* at the same perfluorocarbon concentrations in terms of both total porosity and the degree of pore interconnectivity, suggesting relatively good control over the pore structure formation provided the heat transfer occurring *in vivo* is correctly mimicked *in vitro.*

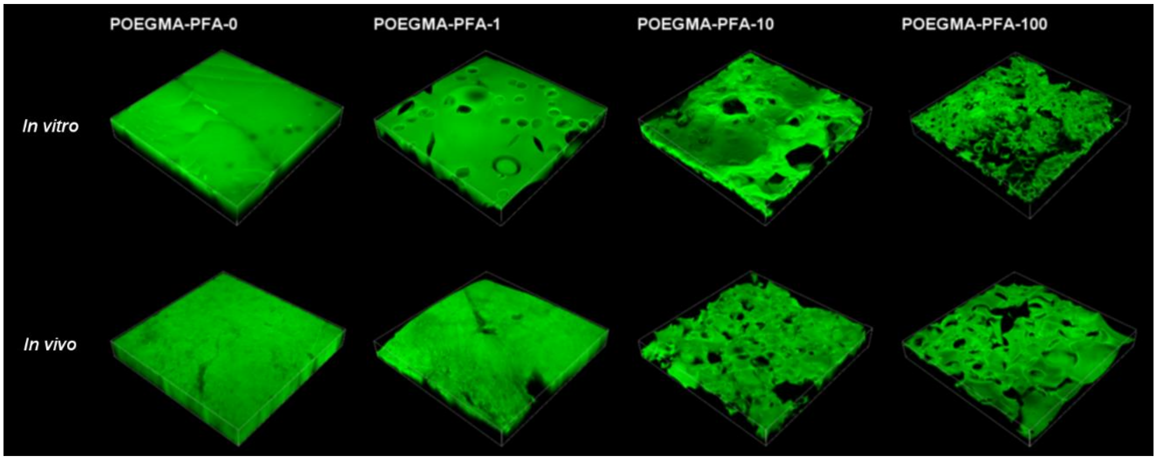

Figure 4-5- Images of 3D confocal fluorescence microscopy reconstructions of fluorescent hydrogel structures prepared *in vitro* (top row) or following subcutaneous injection *in vivo* in BALB/c mice (bottom row) of POEGMA-perfluorocarbon emulsion precursor materials containing (column 1) no perfluorocarbon (POEGMA-PFA-0), (column 2) a 100-fold diluted stock perfluorocarbon emulsion (POEGMA-PFA-1), (column 3) a 10-fold diluted stock perfluorocarbon emulsion (POEGMA-PFA-10), or (column 4) an undiluted stock perfluorocarbon emulsion (POEGMA-PFA-100). All imaged blocks are approximately 1768 µm x 1768 µm in dimensions.

4.3.5. Physical Hydrogel Properties

Uniaxial compression experiments (Figure 4-6-a) show that samples containing different amounts of perfluorocarbon can maintain the relevant mechanical properties of the non-porous hydrogels for use as tissue scaffolds despite the significant different bulk porosities of the different hydrogels. A one-way ANOVA analysis followed by a Tukey's pairwise comparisons indicated no significant difference between the measured compressive modulus values for POEGMA-PFA-0, POEGMA-PFA-1, and POEGMA-PFA-10 samples ($p<0.05$, $n=5$ or 6); however, the POEGMA-PFA-100 sample shows a significantly higher compressive modulus in comparison to the other samples (adjusted p values < 0.05). While this result is somewhat counterintuitive in light of the significantly higher degree of macroporosity observed in the POEGMA-PFA-100 hydrogel (Figure 4-5), we hypothesize that the internal pressure resulting from the perfluorocarbon evaporating result in dewatering of the aqueous polymer phase and thus leads to higher effective polymer concentrations in the aqueous phase of the POEGMA-PFA-100 gels that result in higher local crosslink densities within the gel phase. This hypothesis is consistent with the significant bulk syneresis observed during the gelation of the POEGMA-PFA-100 sample, in which a layer of surface water was expelled from the gel during the incubation period after injection. Localized increases in the relative fluorescence signal around the generating pores observed during the *in situ* LSCM of hydrogels during the pore formation (as depicted in Figure 4-4) also support this de-watering hypothesis; note that this phenomenon was not observed with any of the other hydrogels (Figure 4-6-d). However, overall, the modulus values for all the hydrogels were maintained in the 15-25 kPa range relevant to modeling soft tissues such as skeletal muscle tissue (25 ± 4 kPa) [27], and spleen (24 ± 6 kPa) [28].

Incubation of the macroporous hydrogels in PBS showed relatively flat swelling profiles over time across all hydrogels tested (Figure 4-6-b), with all hydrogels maintaining swelling ratios as measured relative to the gel mass extracted from the mold between 0.75 and 1.1 over the full 27 day incubation period tested. Of particular note, the POEGMA-PFA-10 hydrogel de-swells significant more than the other tested hydrogels, an observation related to the lower critical solution temperature properties of the POEGMA polymers used in this work [13] as well as the higher macroporosity that assists in driving larger total volume transitions with similar intermolecular polymer interactions. Conversely, the observed syneresis of POEGMA-PFA-100 during the gelation process and the resulting the higher polymer concentration (and thus higher crosslink density, Figure 4-6-d) in the gel phase results in a minimal swelling response over time for POEGMA-PFA-100 despite its higher internal porosity. Corresponding degradation experiments in which the hydrogels were incubated in 0.1 M HCl instead of PBS showed that each hydrogel underwent significant mass loss over the 16 day observation period consistent with bulk hydrogel degradation driven by acid-catalyzed hydrolysis of the hydrazone crosslinks (Figure 4-6-c). Interestingly, the degradation profile of POEGMA-PFA-1 shows a plateau persisting at minimal weight loss for an extended period prior to the onset of bulk degradation that is inconsistent with the other hydrogels tested (including the pore-free control). We hypothesize that the local dewatering observed upon gelation (observed on the bulk scale with the POEGMA-PFA-100 hydrogel, Figure 4-6-d) condenses the hydrogel phase to make the in-diffusion of HCl through the gel phase slower. In the POEGMA-PFA-10 and POEGMA-PFA-100 hydrogels, the introduction of (connected) macropores offsets this increased gel phase crosslink density to maintain the overall kinetics of HCl transport into the gel and thus a similar degradation rate; in contrast, for the POEGMA-PFA-1 hydrogel, the lower overall macroporosity and significantly lower degree of connected macroporosity relative to the hydrogels prepared at higher perfluorocarbon concentrations cannot counteract the higher gel-phase crosslink density, resulting in slower HCl transport into the gel and thus slower bulk hydrogel degradation. This hypothesis is also consistent with the observation that the macroporous structures collapse at different timepoints during the degradation process, with earlier collapse observed in gels prepared with higher ratios of perfluorocarbon (i.e. higher internal porosities and thus higher overall surface areas in contact with the acid degrading medium).

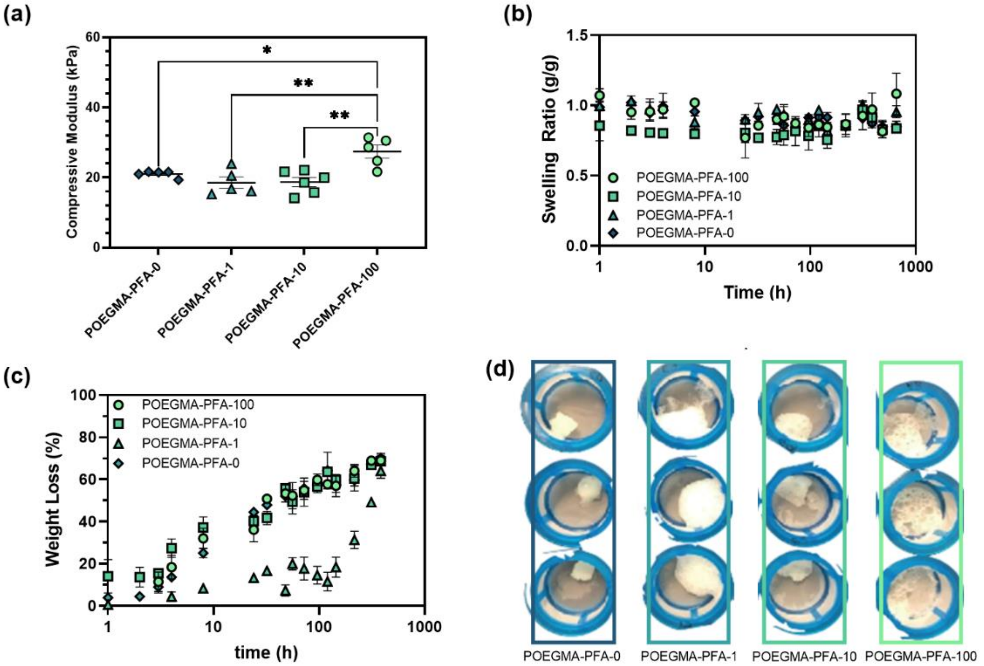

Figure 4-6- Physical properties of POEGMA-PFA hydrogels: (a) Uniaxial compressive modulus of POEGMA-PFA hydrogels prepared with different dilutions of the stock perfluorocarbon emulsion; (b) swelling kinetics profile of POEGMA-PFA hydrogels prepared with different dilutions of the stock perfluorocarbon emulsion incubated in PBS; (c) degradation kinetics profile of POEGMA-PFA hydrogels prepared with different dilutions of the stock perfluorocarbon emulsion incubated in 0.1 M HCl; (d) Images of hydrogels prepared with different amounts of perfluorocarbon emulsion incorporated into the hydrogel formulation after exposure to 0.1 M HCl for 48 hours.

4.3.6. Cell compatibility

The cytocompatibility of the precursor polymers/perfluorocarbon emulsion as well as the leachates from the hydrogels over time was assessed using the MTS assay on C2C12 mouse myoblasts cells (Figure 4-7). Exposure of cells to the precursor polymer solutions, the perfluorocarbon emulsion, and hydrogel leachates was demonstrated to maintain cell metabolic activity above the typical cytotoxicity standard of >70% metabolic activity relative to the cell-only control as represented by the dashed horizontal lines (Figure 4-7 a-c), indicating that none of the precursor materials or leachate products have significant cytotoxicity. Of particular note, there was no significant difference between the cytotoxicity of POEGMA-PFA-100 and POEGMA-PFA-0 samples at each leachate collection day tested as assessed via a one-way ANOVA followed by a Tukey test with p value of 0.05 chosen as a threshold for significance, suggesting that the presence of the perfluorocarbon has no significant negative effect on cytotoxicity.

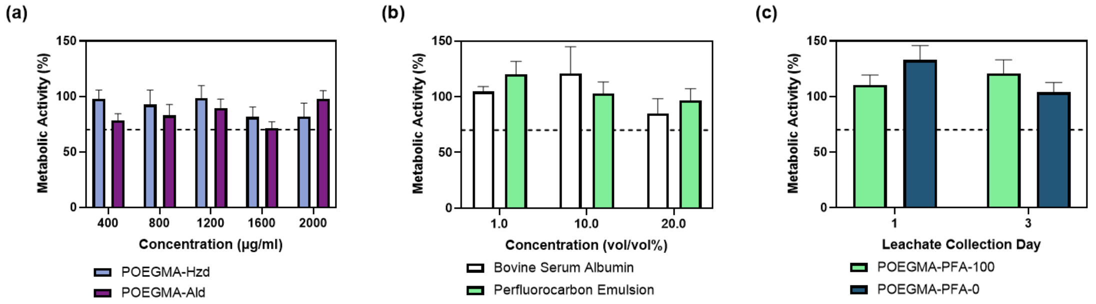

Figure 4-7- Cytotoxicity of precursor and leachate materials used for hydrogel fabrication (4000 C2C12 mouse myoblast cells per well) using the MTS assay: (a) exposure to polymer precursors and various concentrations (n=8); (b) exposure to the perfluorocarbon emulsion components at the same concentrations as used for pore forming agent preparation (bovine serum albumin and perfluoro-n-pentane) (n=8); (c) exposure to leachates collected from POEGMA-PFA-100 and POEGMA-PFA-0 gels after 1 day or 3 days (n=8). In all cases error bars depict standard error. All results were reported from 8 replicates and analyzed using two-way ANOVA followed by a Tukey test ($p<0.05$).

4.3.7. 3D cell encapsulation and cell viability

To assess the compatibility of the hydrogels toward encapsulated cells, 4 million cells at a density of 4 million cells/mL of hydrogel (total of component-A and component-H) were prepared. This was achieved through suspending 4 million cells in perfluorocarbon for the porous POEGMA-PFA-100 gels and PBS for the non-porous POEGMA-PFA-0 gels to which hydrazide-functionalized polymer precursor (POEGMA-Hzd) solution was added. Component A was similarly prepared with no cells and POEGMA-Ald instead of POEGMA-Hzd. Components A and H were co-extruded together during the formation of the hydrogel and immediately placed in a pre-warmed water bath (37 °C) to enable perfluorocarbon evaporation and macropore generation. Figure 4-8-a shows the resulting Live/Dead images for cells encapsulated in a perfluorocarbon-containing POEGMA-PFA-100 hydrogel (top row) relative to a perfluorocarbon-free POEGMA-PFA-0 hydrogel (bottom row), with the % live cells in each image at each time point quantified in Figure 4-8-b. Note that while the cell concentration in the polymer solutions is equivalent in both samples, the porosity of the POEGMA-PFA-100 hydrogel results in a much smaller apparent cell density in the 2D images given the significant percentage of the cross-sectional area now representing a pore, particularly at the earlier observation times prior to any cell proliferation occurring.

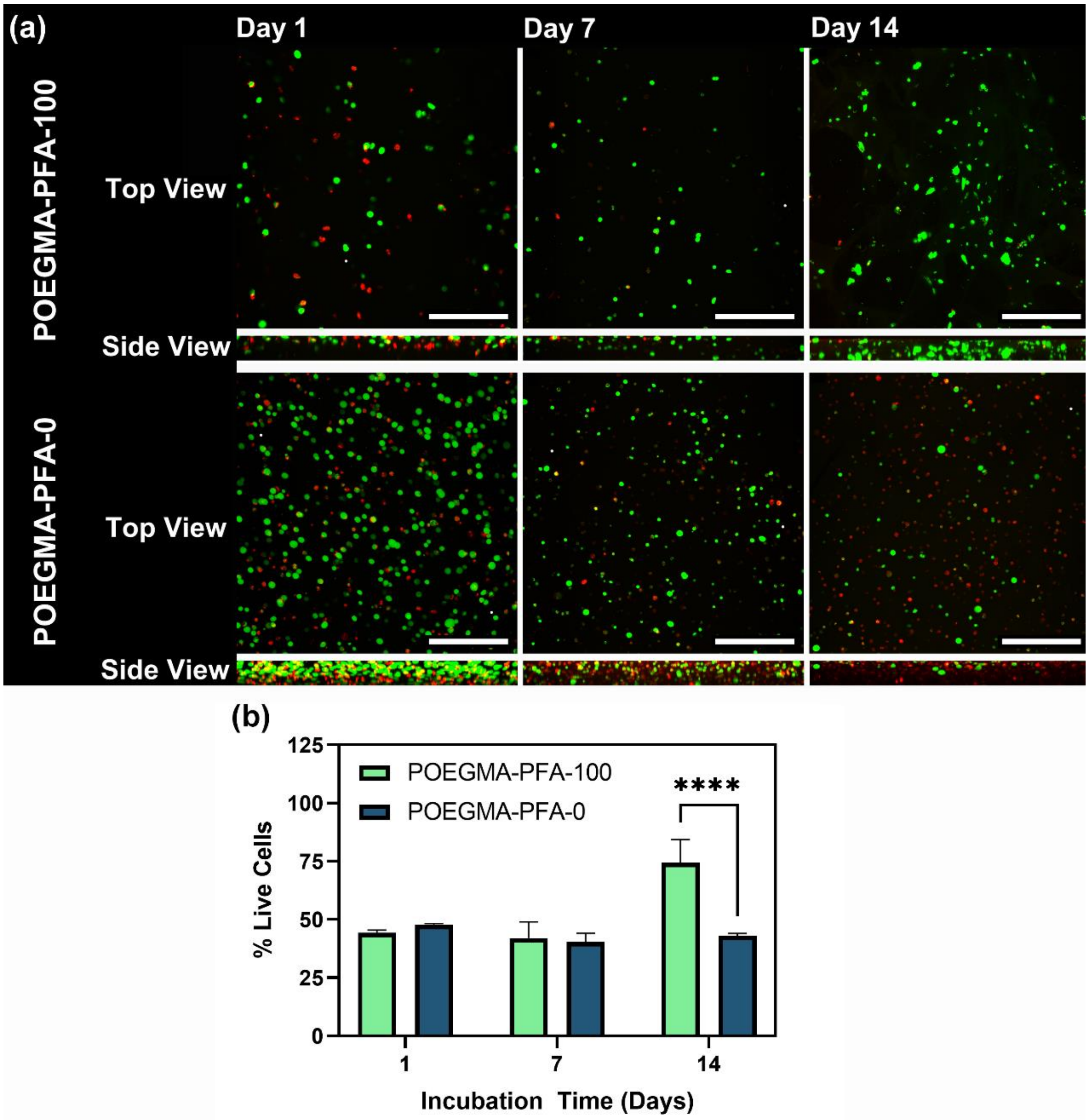

Figure 4-8- Viability of encapsulated C2C12 mouse myoblast cells within POEGMA-PFA hydrogels: (a) Live (green)/Dead (red) images for C2C12 cells encapsulated in perfluorocarbon-containing POEGMA-PFA-100 hydrogels (top row) or control POEGMA-PFA-0 hydrogels (bottom row) over a 14 day incubation period (scale bar = 250 µm; (b) calculated percentage of live cells inside hydrogels prepared without (POEGMA-PFA-0) and with (POEGMA-PFA-100) perfluorocarbon as measured from the images in (a) using a customized macro (n = 3). Results are reported in at least triplicate, with error bars representing the standard deviation. Two-way ANOVA followed by Sidal's multiple comparisons tests showed significant differences at day 14 ($p<0.05$); the number of asterisks indicates number of digits after the decimal point in the adjusted p value.

While both hydrogels show similar % live cells at the shorter time points (particularly at Day 1), significantly higher cell viability is maintained in the macroporous

POEGMA-PFA-100 hydrogel at the 14 day timepoint. We hypothesize this much higher live cell fraction can be attributed to the improved mass transport of nutrients/wastes in and out of the scaffold coupled with the increased physical space available for cell proliferation in the macroporous perfluorocarbon-containing hydrogel, the benefits of which become apparent over longer incubation/proliferation times. Enhanced cell proliferation (which is also an anticipated benefit of the enhanced macroporosity) is also apparent in the majority of the images, although quantifying such proliferation by counting the total number cells per gel volume in the macroporous hydrogels is challenging based on differences in the local porosities in different locations in the images at each timepoint.

4.3.8. Cell-scaffold interactions

To assess the distribution of the co-extruded cells within the hydrogel matrix, laser scanning confocal imaging of FarRed-labeled cells encapsulated in FITC-labeled fluorescent hydrogels was conducted (Figure 4-9). In presence of perfluorocarbon, confocal images provide evidence for cells proliferating out of the pore wall (struts) into the pores (Figure 4-9-a), cells spreading along the interface of the internal pores (Figure 4-9-b), and cells proliferating from one pore into the adjacent pore in cases in which the pores are interconnected (Figure 4-9-c and 9-d). As such, cells in the macroporous hydrogels showed significantly more mobility to an (internal or external) hydrogel interface, consistent with the improved encapsulated cell viability observed at longer time points and supportive of the improved potential proliferative capacity of the macroporous hydrogels. In contrast, in the absence of the pore-forming perfluorocarbon emulsion, no significant macropores were observed and cells were observed to be fully embedded inside the hydrogels with minimal surrounding free volume (Figure 4-9-e and 9-f).

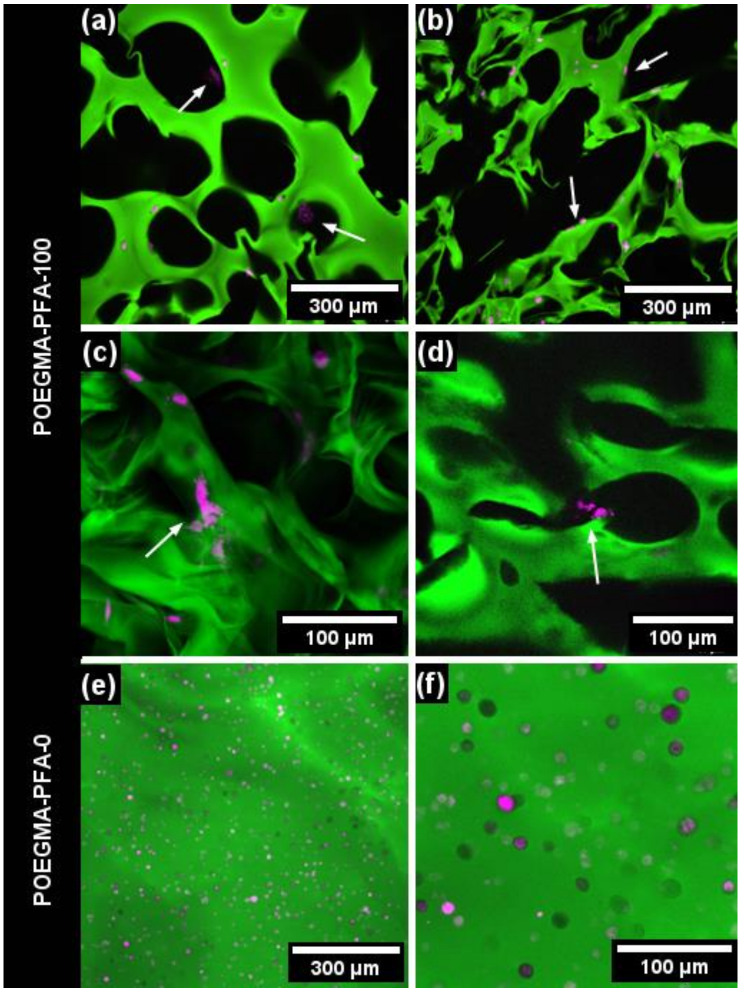

Figure 4-9- Laser scanning confocal microscopy images of FarRed pre-stained C2C12 cells (magenta) encapsulated in a hydrogel containing POEGMA-H30-FITC (green) prepared (a-d) with added perfluorocarbon emulsion (POEGMA-PFA-100) and (e-f) without added perfluorocarbon emulsion (POEGMA-PFA-0) after 7 days of incubation.

4.3.9. In vivo Tolerability

To assess the interfacial and systemic tissue compatibility of the injectable perfluorocarbon-containing hydrogels *in vivo*, tissues both local to the subcutaneous hydrogel injection site as well as organs elsewhere in the body that often experience biomaterials-related toxicity were harvested following acute (3 days) and chronic (28 days) exposure in a mouse model. Scored histology assessments of the resulting responses of lung, heart, kidney, spleen, liver, and skin tissue (the latter taken directly beside the subcutaneously injected hydrogel) showed no significant inflammatory response in the lung, heart, kidney, or spleen at any tested formulation for any tested timepoint (Figure 4-10-a). Minimal liver inflammation was also observed in some treatment groups (see Figure 4-10-b-c for representative histological images); however, given that the affected groups included the chronic saline control group, it is likely that this inflammation is not a direct result of the material itself. Moderate inflammation was observed in the skin at the acute timepoint but was largely resolved at the chronic timepoint despite the persistence of the material over the full 28-day monitoring period (see Figure 4-10-d-f for representative histological images related to the range of scores observed); as such, we attribute the moderate acute inflammatory response to the short-term retention of the evaporated perfluorocarbon under the skin at the acute timepoint which separates the skin from the underlying tissue. No clear evidence of fibrous capsule formation was observed in any of the groups, even in chronic samples in which the majority of the original mass of the hydrogel is still present. In addition, none of the treatment groups was terminated due to reaching endpoints related to animal discomfort, mobility, or weight gain/loss. Collectively, these results suggest that the POEGMA-PFA hydrogels were well-tolerated *in vivo* in addition to being capable of creating tunable macroporous structures following a minimally invasive injection *in vivo* (Figure 4-5), in contrast with previous studies which involve either non-cytocompatible reagents or create potentially toxic by-products [29].

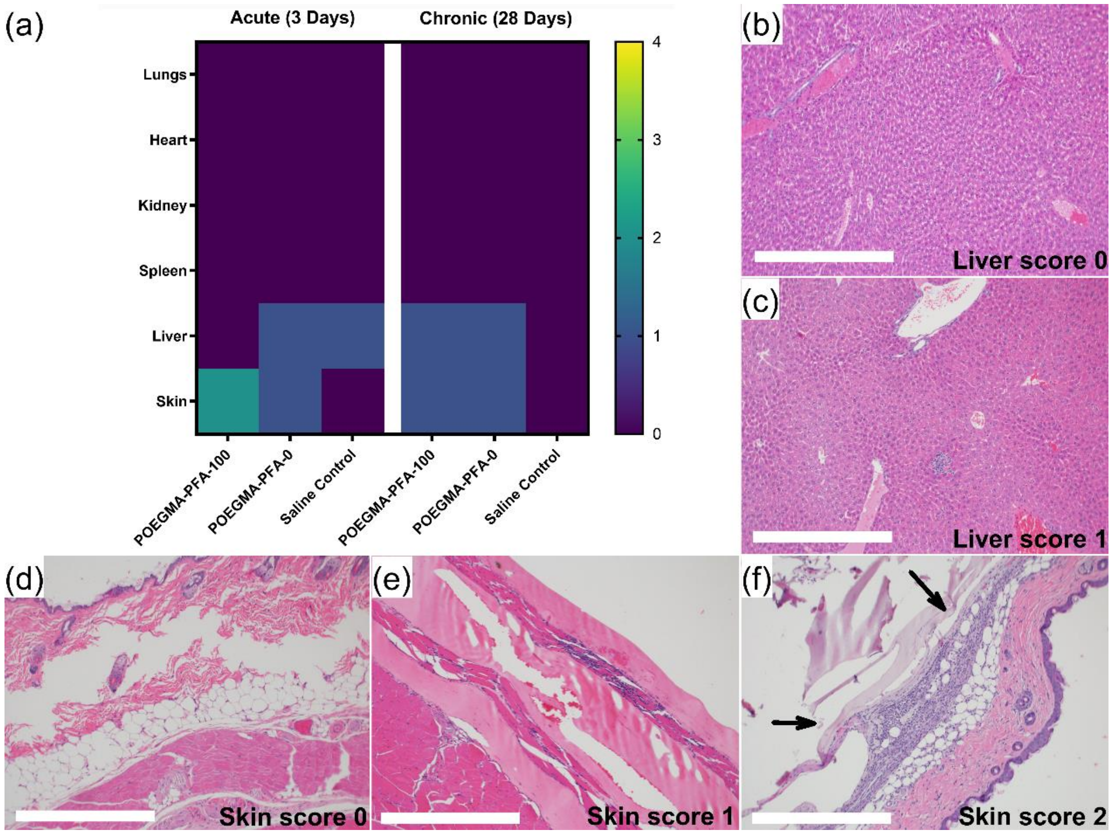

Figure 4-10- Tissue responses to subcutaneously injected hydrogels: (a) summary of average inflammation scoring showing low levels of inflammation in different tissues at both acute and chronic endpoints (see experimental section for an explanation of the scoring system used); (b-c) representative histological images of liver samples with scores of 0 (b) and 1 (c), respectively. (d, e, and f) representative histological images of skin samples with scores of 0 (d), 1 (e), and 2 (f) respectively. Arrows in (f) highlight the hydrogel-skin interface. Scale bars = 500 µm in all images.

4.3.10. Discussion

The combination of an *in situ*-gelling hydrogel with a tunable gelation time (hydrazone-crosslinked POEGMA) with a perfluorocarbon emulsion with a boiling point between room temperature and physiological temperature (perfluoro-n-pentane) enables the generation of tissue-compatible macroporous hydrogels in a single injection step. The amount of perfluorocarbon added to the precursor polymer solutions can be adjusted to determine not only the size but also the interconnectivity of the pores generated in the resulting hydrogel without raising any apparent safety, cytocompatibility or toxicity concerns. The low viscosity of the components prior to injection allows for cells to be incorporated into the hydrogel without excessive shear forces being applied during the injection; at the same time, the porosity generated by evaporation of the perfluorocarbon emulsion (and the interconnection of the pores achievable at higher perfluorocarbon contents) allows for improved transport of nutrients, waste, and oxygen while providing internal surface area for cells to spread and sufficient free volume for cells to proliferate through the hydrogel. Of note, while cell adhesion to this same hydrogel in 2D is relatively weak [30], the porosity generated by the perfluorocarbon provides an effective 3D environment with significantly higher internal interfacial area that enables cells to adhere and migrate despite the lack of defined cell adhesion sites as would be present on natural polymer-based scaffolds based on native ECM components (e.g. collagen). This result is also consistent with our previous work on elecrospun hydrogel nanofibers [31]. Although surgical implantation of the electrospun scaffolds would be considered invasive, while the in situ fabrication of the perfluorocarbon-based macroporous hydrogels would enable minimally invasive injection.

The incorporation of perfluorocarbon emulsion in injectable hydrogels combined with cell delivery could be used in any application in which the viability of transplanted cells (either autograft or allograft) over long periods of time is otherwise limited and/or the proliferation/migration of cells is critical for effective treatment. Based on the mechanical properties of the hydrogel used in this study, the use of the hydrogel for soft tissue targets such as skeletal muscle and spleen could be relevant. However, other applications such as beta cell therapies might also benefit from this platform, as the *in situ*-generated macroporosity may pose a solution to the lack of long-term viability achieved with most transplanted cells that has been linked to limitations on the transport of nutrients, oxygen, and secreted biomolecules in and out of conventional injectable hydrogels - a challenge directly addressed by the incorporation of the tissue-compatible perfluorocarbon emulsion.

4.4. Conclusions

A macroporous hydrogel can be formed following a minimally invasive injection by co-injecting a perfluorocarbon emulsion with a dynamic covalent crosslinking hydrogel. Highly interconnected pore structures can be generated both *in vitro* and *in vivo* (following subcutaneous injection) that can be tuned by incorporating different amounts of the perfluorocarbon emulsion in the two co-injected hydrogel precursor polymer solutions. The viability of co-injected myoblasts in the macroporous hydrogels was significantly higher over extended incubation times relative to non-porous control hydrogels, while no significant acute or chronic inflammatory response was observed in response to the hydrogels when injected *in vivo*. In this context, we believe this platform can be adapted for numerous cell therapy applications such as muscle regeneration or beta cell transplantation in which supporting cell adhesion/proliferation and/or promoting more effective material transport is of particular importance and the invasiveness of administration must be minimized.

4.5. Acknowledgements

The Natural Sciences and Engineering Research Council of Canada (Discovery Grant RGPIN-2017-06455) is gratefully acknowledged for funding. Special thanks to João

Pedro Bronze de Firmino at McMaster Center for Advanced Light Microscopy for his support in developing the image analysis software macro used in this study. We would also like to thank the McMaster Immunology Research Center Core Facility for preparing the H&E slides.

4.6. Disclosures

Michael W. Lawlor (MWL) is the founder, CEO, and owner of Diverge Translational Science Laboratory. MWL is or has recently been a member of advisory boards for Solid Biosciences, Taysha Gene Therapies, Vial, Astellas Gene Therapies (formerly Audentes Therapeutics), and Ichorion Therapeutics. MWL is also a consultant for Astellas Gene Therapies (formerly Audentes Therapeutics), Encoded Therapeutics, Modis Therapeutics, Lacerta Therapeutics, Dynacure, AGADA Biosciences, Affinia Therapeutics, Biomarin, Locanabio, Vertex Pharmaceuticals, Voyager Therapeutics, and Entrada Therapeutics. MWL receives research support from Astellas Gene Therapies, Solid Biosciences, Kate Therapeutics, Prothelia, Cure Rare Disease, Rocket Pharma, Ultragenyx, and Carbon Biosciences.

4.7. References

[1] A. Sivashanmugam, R. Arun Kumar, M. Vishnu Priya, S.V. Nair, R. Jayakumar, An Overview of Injectable Polymeric Hydrogels for Tissue Engineering, Eur. Polym. J. 72 (2015) 543-565.
[2] K.J. De France, F. Xu, T. Hoare, Structured macroporous hydrogels: progress, challenges, and opportunities, Adv. Healthc. Mater. 7(1) (2018) 1700927.
[3] S.A. Bencherif, R.W. Sands, D. Bhatta, P. Arany, C.S. Verbeke, D.A. Edwards, D.J. Mooney, Injectable Preformed Scaffolds with Shape-Memory Properties, PNAS 109(48) (2012) 19590-19595.
[4] B.D. Olsen, J.A. Kornfield, D.A. Tirrell, Yielding Behavior in Injectable Hydrogels from Telechelic Proteins, Macromolecules 43(21) (2010) 9094-9099.
[5] S. Mansoor, P.P.D. Kondiah, Y.E. Choonara, Advanced Hydrogels for the Controlled Delivery of Insulin, Pharmaceutics 13(12) (2021).
[6] H. Tan, K.G. Marra, Injectable, Biodegradable Hydrogels for Tissue Engineering Applications, Materials (Basel) 3(3) (2010) 1746-67.
[7] L. Cai, R.E. Dewi, S.C. Heilshorn, Injectable Hydrogels with In Situ Double Network Formation Enhance Retention of Transplanted Stem Cells, Adv Funct Mater 25(9) (2015) 1344-1351.
[8] T.E. Creighton, Disulfide Bond Formation in Proteins, Methods in Enzymology, Academic Press1984, pp. 305-329.
[9] E. Mueller, I. Poulin, W.J. Bodnaryk, T. Hoare, Click Chemistry Hydrogels for Extrusion Bioprinting: Progress, Challenges, and Opportunities, Biomacromolecules 23(3) (2022) 619-640.
[10] K.J. De France, K.J.W. Chan, E.D. Cranston, T. Hoare, Enhanced Mechanical Properties in Cellulose Nanocrystal–Poly(oligoethylene glycol methacrylate) Injectable Nanocomposite Hydrogels through Control of Physical and Chemical Cross-Linking, Biomacromolecules 17(2) (2016) 649-660.
[11] F. Xu, H. Sheardown, T. Hoare, Reactive electrospinning of degradable poly(oligoethylene glycol methacrylate)-based nanofibrous hydrogel networks, ChemComm 52(7) (2016) 1451-1454.
[12] E. Bakaic, N.M.B. Smeets, M. Badv, M. Dodd, O. Barrigar, E. Siebers, M. Lawlor, H. Sheardown, T. Hoare, Injectable and degradable poly(Oligoethylene glycol methacrylate) hydrogels with tunable charge densities as adhesive peptide-free cell scaffolds, ACS Biomater. Sci. Eng. 4(11) (2018) 3713-3725.
[13] N.M. Smeets, E. Bakaic, M. Patenaude, T. Hoare, Injectable poly(oligoethylene glycol methacrylate)-based hydrogels with tunable phase transition behaviours: physicochemical and biological responses, Acta Biomater. 10(10) (2014) 4143-55.
[14] X. Tong, F. Yang, Recent Progress in Developing Injectable Matrices for Enhancing Cell Delivery and Tissue Regeneration, Adv Healthc Mater 7(7) (2018) e1701065.
[15] M. Chau, K.J. De France, B. Kopera, V.R. Machado, S. Rosenfeldt, L. Reyes, K.J.W. Chan, S. Förster, E.D. Cranston, T. Hoare, E. Kumacheva, Composite Hydrogels with Tunable Anisotropic Morphologies and Mechanical Properties, Chem. Mater. 28(10) (2016) 3406-3415.
[16] E. Mueller, F. Xu, T. Hoare, FRESH Bioprinting of Dynamic Hydrazone-Cross-Linked Synthetic Hydrogels, Biomacromolecules 23 (2022).
[17] F. Xu, I. Gough, J. Dorogin, H. Sheardown, T. Hoare, Nanostructured Degradable Macroporous Hydrogel Scaffolds with Controllable Internal Morphologies via Reactive Electrospinning, Acta Biomater 104 (2020) 135-146.
[18] M. Whitely, S. Cereceres, P. Dhavalikar, K. Salhadar, T. Wilems, B. Smith, A. Mikos, E. Cosgriff-Hernandez, Improved in situ Seeding of 3D Printed Scaffolds using Cell-releasing Hydrogels, Biomaterials 185 (2018) 194-204.
[19] A. Wrobeln, J. Laudien, C. Groß-Heitfeld, J. Linders, C. Mayer, B. Wilde, T. Knoll, D. Naglav, M. Kirsch, K.B. Ferenz, Albumin-derived Perfluorocarbon-based Artificial Oxygen carriers: A Physico-chemical Characterization and First in vivo Evaluation of Biocompatibility, Eur J Pharm Biopharm 115 (2017) 52-64.
[20] J. Chen, H. Pan, G.M. Lanza, S.A. Wickline, Perfluorocarbon Nanoparticles for Physiological and Molecular Imaging and Therapy, Adv Chronic Kidney Dis. 20(6) (2013) 466-478.
[21] P.S. Sheeran, S.H. Luois, L.B. Mullin, T.O. Matsunaga, P.A. Dayton, Design of Ultrasonically-Activatable NanoparticlesUsing Low Boiling Point Perfluorocarbons, Biomaterials 33(11) (2012) 3262-9.
[22] Y. Cheng, H. Cheng, C. Jiang, X. Qiu, K. Wang, W. Huan, A. Yuan, J. Wu, Y. Hu, Perfluorocarbon Nanoparticles Enhance Reactive Oxygen Levels and Tumour Growth Inhibition in Photodynamic Therapy, Nat Commun 6 (2015) 8785.
[23] S. Wang, J. Qiu, A. Guo, R. Ren, W. He, S. Liu, Y. Liu, Nanoscale Perfluorocarbon Expediates bone Fracture Healing through Selectively Activating Osteoblastic Differentiation and Functions, J. Nanobiotechnology. 18(1) (2020) 84.
[24] H. Niu, C. Li, Y. Guan, Y. Dang, X. Li, Z. Fan, J. Shen, L. Ma, J. Guan, High Oxygen Preservation Hydrogels to Augment Cell Survival Under Hypoxic Condition, Acta Biomater. 105 (2020) 56-67.
[25] M.A. Kandadai, P. Mohan, G. Lin, A. Butterfield, M. Skliar, J.J. Magda, Comparison of Surfactants Used to Prepare Aqueous Perfluoropentane Emulsions for Pharmaceutical Applications, Langmuir 26(7) (2010) 4655-60.

[26] N.M.B. Smeets, E. Bakaic, M. Patenaude, T. Hoare, Injectable and tunable poly(ethylene glycol) analogue hydrogels based on poly(oligoethylene glycol methacrylate), ChemComm 50(25) (2014) 3306-3309.
[27] A.B. Mathur, A.M. Collinsworth, W.M. Reichert, W.E. Kraus, G.A. Truskey, Endothelial, Cardiac Muscle and Skeletal Muscle Exhibit Different Viscous and Elastic Properties as Determined by Atomic Force Microscopy, J. Biomech. 34(12) (2001) 1545-1553.
[28] G. Singh, A. Chanda, Mechanical Properties of Whole-body Soft Human Tissues: a Review, Biomed Mater 16(6) (2021).
[29] L. Wang, S. Dong, Y. Liu, Y. Ma, J. Zhang, Z. Yang, W. Jiang, Y. Yuan, Fabrication of Injectable, Porous Hyaluronic Acid Hydrogel Based on an In-Situ Bubble-Forming Hydrogel Entrapment Process, Polymers (Basel) 12(5) (2020).
[30] E. Bakaic, N.M.B. Smeets, H. Dorrington, T. Hoare, "Off-the-shelf" Thermoresponsive Hydrogel Fesign: Tuning Hydrogel Properties by Mixing Precursor Polymers with Different Lower-Critical Solution Temperatures, RSC Adv. 5(42) (2015) 33364-33376.
[31] F. Xu, A. Lam, Z. Pan, G. Randhawa, M. Lamb, H. Sheardown, T. Hoare, Fast Thermoresponsive Poly(oligoethylene glycol methacrylate) (POEGMA)-Based Nanostructured Hydrogels for Reversible Tuning of Cell Interactions, ACS Biomaterials Science & Engineering 7(9) (2021) 4258-4268.

4.8. Supporting Information

Recipes for different hydrogel formulations and relevant volumes of each component used to prepare hydrogels for each reported characterization technique is included in Table 4-4.

Table 4-4 Recipes for different hydrogel formulations and relevant volumes of each component used to prepare hydrogels for each reported characterization technique

		Component H (hydrazide)					Component A (aldehyde)		
		PFA		40 wt% POEGMA-Hzd (µL)	40 wt% POEGMA-Hzd-FITC (µL)	Cells (million)	PFA		40 wt% POEGMA-Ald (µL)
		Perfluorocarbon Emulsion (µL)	PBS (µL)				Perfluorocarbon Emulsion (µL)	PBS (µL)	
Mechanics	POEGMA-PFA-0	0	2250	750	-	-	0	2250	750
	POEGMA-PFA-1	23	2227	750	-	-	23	2227	750
	POEGMA-PFA-10	225	2025	750	-	-	225	2025	750
	POEGMA-PFA-100	2250	0	750	-	-	2250	0	750
Swelling/ Degradation	POEGMA-PFA-0	0	375	125	-	-	0	375	125
	POEGMA-PFA-1	4	371	125	-	-	4	371	125
	POEGMA-PFA-10	38	337	125	-	-	38	337	125
	POEGMA-PFA-100	375	0	125	-	-	375	0	125
Porosity Experiments (*In vitro*)	POEGMA-PFA-0	0	375	94	31	-	0	375	125
	POEGMA-PFA-1	4	375	94	31	-	4	371	125
	POEGMA-PFA-10	38	337	94	31	-	38	337	125
	POEGMA-PFA-100	375	0	94	31	-	375	0	125
Porosity Experiments (*In vivo*)	POEGMA-PFA-0	0	400	75	50	-	0	400	100
	POEGMA-PFA-1	3	397	75	50	-	3	397	100
	POEGMA-PFA-10	30	370	75	50	-	30	370	100
	POEGMA-PFA-100	300	100	75	50	-	300	100	100
Tolerability and Inflammation (*In vivo*)	Saline	-							
	POEGMA-PFA-0	0	300	100		-	0	300	100
	POEGMA-PFA-100	300	0	100			300	0	100
Live/Dead Imaging	POEGMA-PFA-0	0	375	125	0	4	0	375	125
	POEGMA-PFA-100	375	0	125	0	4	375	0	125
Cell-Scaffold Interactions Imaging	POEGMA-PFA-0	0	375	94	31	4 (pre-stained)	0	375	125
	POEGMA-PFA-100	375	0	94	31	4 (pre-stained)	375	0	125

Chapter 5- Electrospun "Hard-Soft" Interpenetrating Nanofibrous Tissue Scaffolds Facilitating Improved Cell Proliferation Soft-Hard Electrospun

Samaneh Toufanian[a], Evelyn Cudmore[a], Christina McCabe[a], Mya Sharma[a], Alex Caschera[a], Todd Hoare[a]*

[a] Department of Chemical Engineering, McMaster University, 1280 Main St. W., Hamilton, ON, Canada
* To whom correspondence should be addressed: hoaretr@mcmaster.ca

Abstract

"Soft" electrospun hydrogel scaffolds have been widely used in tissue engineering and drug delivery applications due to their hydrated interfaces and macroporous structures but have drawbacks related to their weak mechanics and often weak adhesion to cells; in contrast, "hard" poly(caprolactone) (PCL) electrospun fibrous networks have desirable mechanical strength and ductility but offer minimal interfacial hydration and thus limited potential for cell proliferation. Herein, we demonstrate the potential to create interpenetrating nanofibrous networks based on co-electrospun PCL and (oligoethylene glycol methacrylate) (POEGMA) nanofibers that can mitigate these challenges. The electrospun scaffolds exhibit minimal internal phase separation that results in anisotropic but strong mechanical properties, with the ultimate tensile strengths of the swollen scaffolds measured as 429 ± 39 kPa in the direction of fiber alignment (longitudinal) and 86 ± 25 kPa perpendicular to fiber alignment (cross-longitudinal) typical to PCL-based scaffolds. However, contact angle measurements in the pre-hydrated and dry state indicate the presence of hydrogel-like interfacial properties due to the presence of the interpenetrating POEGMA network. Bacterial adhesion was shown to be delayed by PCL-POEGMA scaffolds compared to PCL-only scaffolds, while C2C12 myoblast proliferation in the PCL-POEGMA scaffolds was roughly four-fold higher relative to PCL-only scaffolds due to the higher interfacial hydrophilicity promoted by the interpenetrating POEGMA nanofiber phase. These properties, combined with the single-step fabrication method used to create the interpenetrating scaffolds, offers potential to fabricate strong macroporous but still interfacially hydrophilic scaffolds for tissue engineering applications.

5.1. Introduction

Hydrogels have been widely studied in medicine, with their controllable porosity and high water retention capability being leveraged in a variety of biomedical applications including drug delivery, cancer treatment, regenerative medicine, and medical device design. [1]. Macroporous hydrogels that offer porosity on both the microscale (controlled by the fabrication technique) and the nanoscale (controlled by the hydrogel crosslinking density) have attracted particular attention for tissue engineering-related applications given that macroporous structures can provide both more physical space for cell proliferation [2] and improved diffusion properties for nutrient/waste transport [3].

Among the multiple methods used to fabricate macroporous hydrogels [4, 5], electrospinning is among the most widely used for regenerative medicine applications. Electrospinning involves generating thin polymer nanofibers from a droplet through continuous pulling of charged polymer solutions (or emulsion) in a strong electric field. The morphology of the produced fibers can be controlled through modifying processing parameters including the flow rate [6], the electric field strength (e.g. the overall electric potential and/or the distance between the dispensing needle and the collector) [7], the solution properties (e.g. viscosity, polymer concentration, or polymer molecular weight) [6, 8], the dispensing needle gauge [9], and/or the environmental conditions around the collector [10], making electrospinning among the more adaptable available methods for nanofibrous material fabrication. Specific to tissue engineering applications, electrospun scaffolds are highly porous [11] and can directly create nanofibrous materials that mimic the dimension and morphology of natural extracellular matrix, offering potential to promote cell adhesion and proliferation due to the high surface area:volume ratio of the fabricated scaffolds [12]. The potential to align the fibers by proper choice of collector [13] offer further benefits in terms of mimicking the directional properties of natural extracellular matrix in many types of aligned/directional tissues (e.g. muscles or nerves), resulting in improved orientation and phenotypic expression of the cultured cells [14, 15].

Electrospinning has widely been reported to facilitate the fabrication of tissue engineering scaffolds based on “hard” water-insoluble polymers, with degradable polyesters such as polylactic acid (PLA) [16], poly D,L-lactic-co-glycolic acid (PLGA) [17] and poly(ε-caprolactone) (PCL) [18] being most commonly used. More recently, hydrogel electrospinning strategies in which water soluble polymers are electrospun and then post-crosslinked through chemical [19], ionic [19], and/or light-induced [20] mechanisms have been reported to facilitate the fabrication of gel-based nanofibers. We have recently reported a reactive electrospinning strategy in which hydrazide and aldehyde-functionalized poly(oligoethylene glycol methacrylate) (POEGMA) nanofibers can be fabricated via simultaneous electrospinning and hydrazone crosslinking, eliminating the need for UV crosslinking or any post-electrospinning gelation step [21, 22].

However, the low mechanical strength of hydrogels generally coupled with the macroporosity of electrospun hydrogel fibers (which further weakens the bulk mechanics of the resulting scaffolds) significantly limits the practical applications of such scaffolds in tissue engineering [23, 24]. While many methods to enhance hydrogel mechanics including the formation of double-network (DN) hydrogels [25, 26], the use of slide-ring crosslinkers [27, 28], and the use of nanoparticles as reinforcement agents [24] have been reported, all these techniques have drawbacks in the context of gel electrospinning. Double network formation requires the implementation of two simultaneous crosslinking reactions in parallel to or subsequent to an electrospinning step, introducing operational complexity into the system, while slide ring crosslinkers significant limit the scope of potential scaffold materials that can be used. Nanoparticle fillers are the most adaptable to an broad electrospinning context but can have biological drawbacks, with nanoparticle aspect ratio and size [29] and surface chemistry [30] having potential to significantly impact nanoparticle cytotoxicity and *in vivo* pathogenicity. For example, while graphene oxide is an excellent reinforcing filler from a mechanical perspective [31], it also has a tendency to accumulate in different organs (in most cases the liver and spleen [32], although lung accumulation has also been reported [33]). Particle agglomeration, which can be promoted by the use of an electric field and rapid matrix drying observed in electrospinning, represents another key challenge given that nanoparticle agglomerates can act as stress concentration points that functionally reduce the effective matrix mechanics rather than reinforce them [34]. Furthermore, for nanoparticle modifiers to improve hydrogel mechanics, strong interactions between the hydrogel matrix and the nanoparticle modifiers need to be present [35], often requiring complex and time consuming multi-step surface functionalization of nanoparticles [36].

As an alternative to fabricate stiffer scaffolds with hydrogel-like interfacial properties, blend electrospinning in which a hydrogel component and a strong polyester are co-electrospun into a single scaffold has attracted recent interest. Relative to “hard” polymer (e.g. degradable polyester) scaffolds, the increase hydrophilicity of blend scaffolds has been demonstrated to significantly improve cell proliferation [22, 37]; for example, the combination of a hydrogel component with PCL (an easy-to-electrospin polymer with low hydrophilicity) has been specifically shown to improve the regenerative capacity of PCL-based scaffolds due improved interfacial hydration around the PCL fibers [38]. Relative to hydrogel-only scaffolds, blend scaffolds offer significantly improved mechanics as well as improved cell adhesion properties. While this approach is simple and economical, significant challenges persist around maintaining sufficient stability in each phase while minimizing phase separation between the “hard” hydrophobic phase and the “soft” hydrogel phase, both of which can lead to heterogeneous cell responses and sub-optimal mechanical strength [39]. For example, Manotoya et al. co-electrospun PCL and bovine gelatin to leverage the desirable mechanical properties of PCL and adhesion-promoting peptides present in gelatin but reported rapid degradation of the gelatin phase, making the improved cell proliferation more closely correlated with the increased pore size of the gelatin-PCL scaffolds instead of the presence of the supporting gelatin phase [40]. Wu et al. prepared co-electrospun scaffolds using PLGA and chitosan but observed significant decreases in ductility of the resulting scaffold despite improvements in cell adhesion and proliferation [41]. Thus, developing blend electrospun scaffolds in which both nanofiber phases are intimately mixed and stable over the required timescales is expected to facilitate both improved scaffold mechanics and improved cell responses.

Herein, we demonstrate an effective “hard-soft” co-electrospinning technique that combines the mechanical strength of PCL and hydrophilicity the POEGMA into a single interpenetrating nanofibrous scaffold. PCL was chosen as the “hard” phase due to its desirable mechanical properties, ease of electrospinning, tissue compatibility and biodegradability [42]; POEGMA was chosen as the “soft” hydrogel phase due to its high interfacial hydrophilicity and water binding capacity coupled with its demonstrated efficacy in reactive electrospinning via simultaneous fiber generation and hydrazide-aldehyde crosslinking [21]. By co-collecting the POEGMA and PCL fibers on a rotating collector, we can successfully produce a tubular scaffold with optionally anisotropic mechanical properties with ultimate tensile strengths as high as 0.5 MPa; at the same time, contact angle measurements demonstrate the preserved interfacial hydrophilicity of the scaffold. The resulting "hard-soft" scaffolds are shown to delay bacterial adhesion and promote significantly higher C2C12 cell proliferation compared to PCL-only scaffolds, offering a potential solution to create stiff but still interfacially gel-like macroporous scaffolds for tissue engineering applications.

5.2. Materials and Methods

5.2.1. Materials

Oligo(ethylene glycol) methyl ether methacrylate with a number average molecular weight of 475 g/mol (Sigma-Aldrich, 95%) was purified using a basic aluminum-packed column to remove the inhibitors methyl ether hydroquinone and butylated hydroxytoluene prior to use. Thioglycolic acid (TGA Sigma-Aldrich, 95%), 2,2'-azobis(2-methylpropionate) (AIBME, 98.5%, Wako Chemicals, Shanghai, China), acrylic acid (AA, 99% Sigma-Aldrich), 1,4-dioxane (anhydrous, Caledon Laboratory Chemicals), adipic acid dihydrazide (ADH, Alfa Aesar, 98%), N′-ethyl-N-(3-(dimethylamino)propyl)-carbodiimide (EDC, Carbosynth, Compton CA, commercial grade), poly (lactic-co-glycolic acid) conjugated with Rhodamine B (PLGA-Rb 50:50 LA/GA, 20 kDa, Nanosoft Polymers, USA), poly (lactic-co-glycolic acid) conjugated with Cyanine 5 (PLGA-Cy5 50:50 LA/GA, 20 kDa, Nanosoft Polymers, USA), poly(caprolactone) (PCL, M_n = 80 kDa, Sigma-Aldrich), FITC-conjugated albumin from bovine serum (BSA-FIT-C, Invitrogen, Waltham, MA, USA), FITC-conjugated fibrinogen from human serum (fibrinogen-FIT-C, Invitrogen, Waltham, MA, USA), fetal bovine serum (Wisent Inc., Saint-Jean-Baptiste, QC), Dulbecco's Modified Eagle Medium (DMEM, Wisent Inc., Saint-Jean-Baptiste, QC), phosphate buffered saline (PBS, Wisent Inc., Saint-Jean-Baptiste, QC), penicillin streptomycin (Wisent Inc., Saint-Jean-Baptiste, QC), agar (Bio-Rad Laboratories Ltd, Mississauga, ON), Luria-Bertani (LB) broth (Sigma-Aldrich), sodium chloride (NaCl, Sigma-Aldrich), and formalin solution (10%, PBS buffered, Sigma-Aldrich) were all used as received. N,N-dimethylaminoethyl methacrylate (DMAEMA) was synthesized in-house as reported previously [36]. Double distilled reverse osmosis water (MilliQ grade) was used for all experiments. The fluorescent stains/assays SYTO 9, CyQuant Proliferation Assay, CellTrace™ FarRed Cell Proliferation Kit, and mounting media Prolong Diamond Antifade (all from Invitrogen) were used as recommended by the manufacturer.

5.2.2. Polymer synthesis

Hydrazide functionalized POEGMA (POEGMA-Hzd) was synthesized according to a previously reported method [43]. Oligo(ethylene glycol) methyl ether methacrylate (8 g), AA (0.6) g, TGA (0.002 g dissolved in 40 mL of 1,4-dioxane), and AIBME (0.074 g) were added to a 500 mL round bottom flask and subsequently purged with nitrogen for at least 30 minutes while being stirred at room temperature (250 rpm). The flask was then placed in a preheated oil bath (85°C) to initiate the reaction. The synthesis was continued for 4 hours under nitrogen, after which the reaction was terminated by removing the flask from the heated oil bath and purging with air for at least 30 minutes. The solvent (1,4-dioxane) was then removed through rotary evaporation (30 minutes, 37 °C, maximum vacuum). A 50 mg sample was reserved for further analysis (titration) while the remaining polymer (~8.7 g) was dissolved in 300 mL of MilliQ water and ADH (6.94 g) and EDC (4.58 g) were added. The pH of the reaction was maintained between 4.6-4.8 for at least 4 hours using 1 M HCl and stirred at room temperature overnight. The polymer solution was then purified through 6 cycles of dialysis against 5 L of MilliQ water (cellulose acetate membrane, 12.5 kDa molecular weight cut-off), with each cycle lasting at least 6 hours. After purification, the solution was filtered using a 0.2 μm PES filter, freeze dried, and dissolved to obtain a 15 wt% polymer solution in PBS to be stored at 4 °C until use.

Aldehyde-functionalized POEGMA (POEGMA-Ald) was synthesized by dissolving Oligo(ethylene glycol) methyl ether methacrylate (8 g), DMAEMA (0.6 g), TGA (0.002 g pre-dissolved in dioxane 10 wt%), and AIBME (0.074 g) in 1,4-dioxane (40 mL) in a 500 mL round bottom flask. The mixture was purged with nitrogen for at least 30 minutes while being stirred at room temperature (250 rpm), after which the flask was placed in a preheated oil bath (85 °C) and allowed to react for 4 hours. The reaction was then terminated by removing the round bottom flask from the oil bath and purging the reaction with air for at least 30 minutes. A rotary evaporator (30 minutes, 37 °C) was used to remove the solvent, after which the resulting viscous polymer solution (~9.4 g) was dissolved in 100 mL of MilliQ water to which 100 mL of 1 M HCl was added. The mixture was then stirred overnight to hydrolyze the acetal groups on the DMAEMA monomer to aldehyde groups. The resulting aldehyde-functionalized polymer solution was dialyzed against 5 L of MilliQ water for 6 cycles of at least 6 hours (cellulose acetate membrane, 12.5 kDa molecular weight cut-off), filtered using a 0.2 μm PES filter, and freeze dried. Finally, a 15 wt% polymer solution in PBS was prepared and stored at 4 °C until use.

The degree of functionalization of POEGMA-Hzd was determined using base-into-acid titration using 0.1 M NaOH as the titrant to measure the difference in titrated -COOH content before and after ADH/EDC conjugation. Nuclear magnetic resonance (^{1}H NMR) in d6-choroform (solvent) was used to confirm the POEGMA-Ald degree of functionalization.

POEGMA-Hzd-FIT-C was synthesized by adding fluorescein isothiocyanate (35 mg) to a dilute solution of POEGMA-Hzd in PBS (5.76 g, 2.5 wt%). The mixture was stirred overnight protected from light at room temperature. After 6 cycles of dialysis (cycles of >6 hours, SnakeSkin™ dialysis tubing, 3.5 kDa molecular weight cut-off, ThermoFisher Scientific) against MilliQ water, the resulting polymer solution was lyophilized, dissolved at 15 wt% in PBS, and stored at 4°C protected from light until use.

5.2.3. Electrospinning

POEGMA hydrogel precursor solutions were prepared by mixing 15 wt% solutions of each polymer precursor (POEGMA-Hzd or POEGMA-Ald) with a 5 wt% solution of PEO pre-dissolved in PBS in two separate 15 mL conical tubes. The resulting POEGMA-Hzd-PEO and POEGMA-Ald-PEO solutions were loaded into a double barrel syringe (MedMix, ZUG, Switzerland), and a 16 G blunt needle was attached to the mixer to direct the POEGMA stream on the grounded rotating rod collector (¼ inch diameter, 3000 rpm).

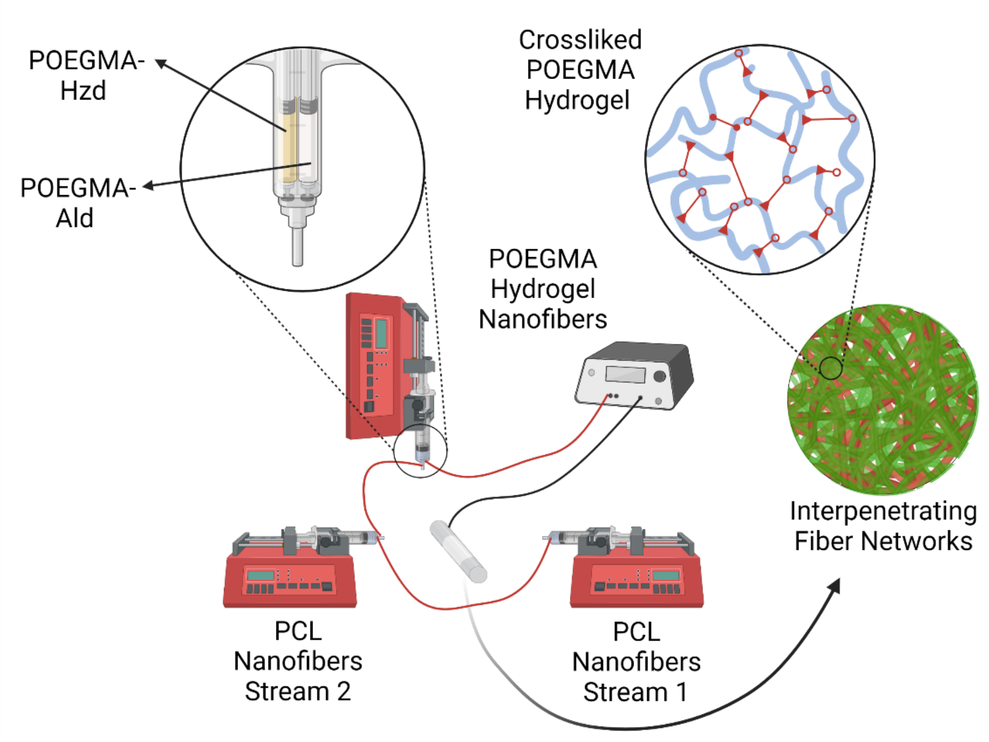

Figure 5-1- Schematic diagram showing the aluminum collector rod and the three electrospinning polymer stream orientation used to fabricate PCL-POEGMA hard-soft scaffolds

The PCL nanofiber stream 1 (12.5 wt% PCL solution) was prepared by dissolving 0.65 g of PCL in 4.5 mL of dichloromethane and magnetically stirring until fully dissolved. Subsequently, 1.5 mL of ethanol was added to the solution and stirred until a clear solution was obtained. The PCL nanofibers stream 2 (10 wt% PCL solution) was prepared similarly using 0.5 g of PCL and identical amounts of dichloromethane and ethanol. PCL-POEGMA electrospun samples were obtained by simultaneously co-electrospinning both PCL nanofiber streams and the POEGMA stream from three separate needles connected in a parallel circuit to maintain the electric field required for electrospinning (Figure 1). A ¼ inch diameter grounded aluminum rod was used as the conductive (grounded) collector. A rotation speed of 3000 rpm was maintained throughout the electrospinning process using an electric motor/stand developed in-house. PCL-only electrospun samples were obtained by co-electrospinning the two PCL nanofiber streams without the POEGMA stream using the same electrospinning parameters. Each sample was electrospun for 45 minutes using the electrospinning parameters summarized in Table 5-1. In case of PCL nanofiber stream 2, a dual dispensing blunt needle was used to maximize fiber deposition without impacting fiber diameter.

Table 5-1- Electrospinning parameters used for each syringe for PCL-POEGMA scaffold electrospinning

Stream	Flowrate (µL/h)	Distance (cm)	Syringe Diameter (mm)	Voltage (kV)	Needle Gauge	Needle Type
POEGMA	1400	9.0	8.2 (each barrel)	9.0	16	Standard Blunt
PCL nanofiber stream 1	2000	6.5	12.0	9.0	16	Standard Blunt
PCL nanofiber stream 2	1200	8.0	12.0	9.0	20	Dual Dispensing-Blunt

5.2.4. Laser scanning confocal microscopy (LSCM)

To visualize the fiber structure created using laser scanning confocal microscopy, 25% of the POEMGA-Hzd polymer was replaced with POEGMA-Hzd-FIT-C while PLGA-RhB (PLGA-RhB:PCL 0.05 wt%) was added to the PCL nanofiber stream 2 and PCL nanofiber stream 1 streams; note that PLGA-RhB and PLGA-Cy5 were chosen as the PCL phase fluorophore given that it is a commercially available PCL-miscible polymer fluorescent dye with distinct excitation/emission to POEGMA-Hzd-FIT-C. Following electrospinning using the fluorescently-labeled polymers, the electrospun scaffolds were cut, rehydrated in PBS, mounted onto glass slides using ProLong™ Diamond Antifade Mountant (Invitrogen), and covered with 1 N cover slip. After curing at room temperature (24 hours), samples were imaged using laser scanning confocal microscopy (LSCM, A1R HD25, Nikon) operating in Galvano acquisition mode. An excitation wavelength of 488 nm and detection range of 500-542 nm was used for imaging POEGMA-Hzd-FITC (POEGMA phase), while the TRITC channel with an excitation wavelength of 561 nm and an emission range of 578-623 nm was used to image the PLGA-RhB distribution (PCL phase). PLGA-Cy5 distribution (PCL phase) was visualized using 640 nm excitation wavelength and emission range of 624-680 nm.

5.2.5. Equilibrium water retention

Electrospun scaffolds were cut into 4 equal strips (4 mm × 25 mm), weighed using a microbalance, and then incubated in PBS. At each pre-determined timepoint, samples were removed, wicked dry, and weighed, with the swelling ratio calculated using equation (5-1). Experiments were performed in triplicate, with error bars representing the standard error.

$$\boldsymbol{swelling\,ratio} = \frac{\boldsymbol{W_t - W_s}}{\boldsymbol{W_0}} \tag{5-1}$$

5.2.6. Contact angle measurements

Electrospun scaffolds were removed from the collector after a lengthwise cut and directly tested using a Krüss Drop Shape Analyzer DSA 10 (USA) equipped with an analysis system (version 1.80.0.2), and a gauge 26S needle. To perform the test, a 5 μL droplet of ultrapure water was dropped on the sample surface and the resulting dry contact angle was measured immediately. Subsequently, the samples were submerged into phosphate buffered saline (PBS) for 45 minutes, wicked dry using a Kimwipe to remove excess water, and the contact angle was re-measured to obtain the wet contact angle. Measurements for both dried and wet samples were obtained in two directions: (1) the direction in which the spreading of the droplet would be perpendicular to the fiber alignment (cross-longitudinal); and (2) the direction in which the spreading of the droplet would be parallel to the direction of the fiber alignment (longitudinal). At least 5 replicates were performed per sample, with the error bar representing the standard deviation of the measured angles.

5.2.7. Mechanical testing

Sample mechanics were tested using the Mach-1 micromechanical analyzer (Biomomentum, Montreal, PQ). Samples were pre-swollen to equilibrium swelling (as described in section5.2.5) and then tested in 3 different orientations: longitudinal (with displacement parallel to the intended fiber alignment, tested using a C-shaped grip), cross-longitudinal (with displacement perpendicular in the intended fiber alignment, tested using a C-shaped grip), and circumferential (ring, tested with a T-shaped fixture). All tensile testing was performed using a 0.01 1/s strain rate continued until failure. The raw displacement versus force data were then converted to stress/strain curves based on the measured dimensions of each sample prior to mechanical testing.

5.2.8. Protein uptake

Electrospun samples were cut into equally sized 4 mm × 4 mm squares using a cutting die consisting of 6 parallel blades with equal gaps and placed into separate wells of a low protein binding 96 well plate. BSA-FIT-C and fibrinogen-FIT-C solutions were prepared at concentrations of 0.25 mg/mL and 1 mg/mL and then incubated in 100 µL aliquots with the cut electrospun samples for 4 hours at 37 °C in the dark under gentle agitation (100 rpm) [44]. 2× serial dilutions were prepared using 50 µL of the supernatant to measure the concentration of protein in the supernatant. The amount of protein uptake was calculated by comparing the concentration of protein in the supernatant relative to the original concentration of protein in the incubation solutions.

5.2.9. Bacterial adhesion

Pseudomonas aeruginosa (ATCC© 15442) bacteria were cultured at 37°C for 24 h in 10 mL sterilized Luria-Bertani (LB) broth (25 g/L) under mild agitation (250 RPM). 1 mL of the bacterial suspension was added to a 1.5 mL microtube and centrifuged at 9000 × g for 4 minutes. The supernatant was then removed, replaced with saline solution (0.9 wt%), re-centrifuged, resuspended in saline, and diluted 1000× in physiological saline to obtain the bacterial inoculum. Sub-dilutions (non-diluted, 10×, 100×, or 1000× dilutions) of the inoculum were prepared and incubated on LB agar plates (24 hours, 37 °C) to quantify the CFU of the inoculum (determined to be 3.4×10^7 CFU/mL). To assess bacterial adhesion to the electrospun samples, samples were cut into 5 mm × 5 mm squares, placed in separate wells of a low binding 96 well plate, and exposed to a 100 µL aliquot of the *P. aeruginosa* inoculum. After 25 or 45 minutes of inoculation time, 80 µL of the exposed inoculum was collected and transferred to a black walled/clear bottom well plate, after which 20 µL of a 250 mM solution of SYTO 9 was added to each well. The plates were incubated at room temperature for 15 minutes, after which the fluorescence intensity was quantified using the Tecan Infinite M200 plate reader (excitation wavelength = 470 nm, emission wavelength = 515 nm, gain = 80). The bacterial load of the collected inoculum was then quantified using a calibration curve (Supporting Information Figure 5-9).

5.2.10. Mammalian cell proliferation and directionality

C2C12 mouse myoblasts were cultured in cell culture flasks using DMEM media supplemented with 10% FBS and 1% PS inside an incubator set at 37°C and 5% CO_2. To harvest the cells, cell culture media was removed, the cells were rinsed with 10 mL of prewarmed PBS, 25% w/v trypsin-EDTA (3 mL) was added and incubated at 37 °C for ~5 min to delaminate the cells from the flask, and prewarmed cell culture media (10 mL) was added to neutralize the trypsin-EDTA. The density of the resulting cell suspension was determined using a hemocytometer.

For proliferation assays, C2C12 mouse myoblasts were pre-stained using CellTrace™ FarRed Cell Proliferation Kit as per the manufacturer's protocol for adherent cells and subsequently trypsinized and prepared into a 7,000 cells/mL suspension as described earlier. Electrospun scaffolds were punched into 5/8" diameter patches using a hammer-driven punch. After UV sterilization (2 cycles × 30 minutes per side) samples were secured to the bottom of a 24 well plate using silicone washers with inner and outer diameters of 15/32" and 5/8" respectively. Subsequently, 1 mL of pre-stained cell suspension was added to each sample, with standard treated polystyrene well plates used as controls. At day 3 and day 5 post- seeding, samples were fixed using 10% formalin (PBS buffered) for at least 30 minutes, after which the scaffolds were mounted on 1 N glass slides. Stained cells within the scaffold were then visualized using laser scanning confocal microscopy using the Cy5 channel (excitation 640 nm, detection 624-680 nm) following protocols described in section 5.2.4. Proliferation was quantified by processing z-stack projection images using ImageJ software, with the percentage of the imaged area covered with cells at each timepoint quantified using a binary mask. Two images obtained from two different locations were analysed for each timepoint and substrate, with the standard error of the resulting cell density measurements reported. To determine cell directionality, images were analysed using Fiji Directionality Analysis.

5.3. Results and Discussion

5.3.1. Polymer characterization

The key physical and chemical properties of the POEGMA-Hzd and POEGMA-Ald precursor polymers used to form the electrospun hydrogel component are summarized in Table 5-2. The number average molecular weights of both precursor polymers (M_n <13 kDa) are below the renal cut-off, suggesting the potential for kidney clearance following degradation [45]. The experimental degree of functionalization was also directly correlated with the target degree of functionalization for both hydrazide and aldehyde groups.

Table 5-2- Molecular weight and degree of functionalization of the precursor POEGMA polymers.

	M_n (kDa)	Dispersity *Đ*	Target Degree of Functionalization	Actual Degree of Functionalization
POEGMA-Hzd	10.0	4.3	30%	34%^{a}
POEGMA-Ald	12.6	4.5	30%	32%^{b}

[a] from conductometric titration and [b] from ^{1}H nuclear magnetic resonance

5.3.2. Scaffold fabrication and morphology

PCL-POEGMA hard-soft scaffolds were fabricated by simultaneously electrospinning the contents of up to three syringes (two containing PCL and one double barrel syringe containing the hydrazide and aldehyde-functionalized POEGMA precursor polymers in separate barrels) on a spinning cylindrical collector. Laser scanning confocal microscopy was used to visualize the electrospun fiber morphology by separately visualizing POEGMA-Hzd-FIT-C (identifying the POEGMA hydrogel phase, visualized in green) and PLGA-RhB (identifying the PCL phase, visualized in red). Figure 5-2-a depicts co-electrospun PCL nanofiber stream 1 and POEGMA fibers while Figure 5-2-b was obtained following co-electrospinning of PCL nanofiber stream 2 and POEGMA fibers. The lower concentration PCL nanofiber stream 2 precursor solution leads to significantly smaller diameter fibers that appear to be encased within a POEGMA hydrogel nanofiber mat; in contrast, the higher concentration PCL nanofiber stream 1 precursor solution leads to thicker PCL fibers that appear to induce wrapping of the co-electrospun POEGMA nanofibers around the PCL fibers. Co-electrospinning of all three streams Figure 5-2-c results in an intermediate morphology consisting of multi-scale PCL fibers intermixed with POEGMA nanofibers, with no clear evidence of phase separation observed aside from wrapping of some of the POEGMA nanofibers around the larger PCL fibers. As such, depending on the electrospinning parameters used (in this case, the “hard” network precursor polymer concentration), diverse scaffold microstructures can be obtained. However, in any case, a fully interpenetrated network of the “hard” PCL phase and the “soft” POEGMA phase can be achieved by the simultaneous electrospinning process without large-scale phase separation being observed.

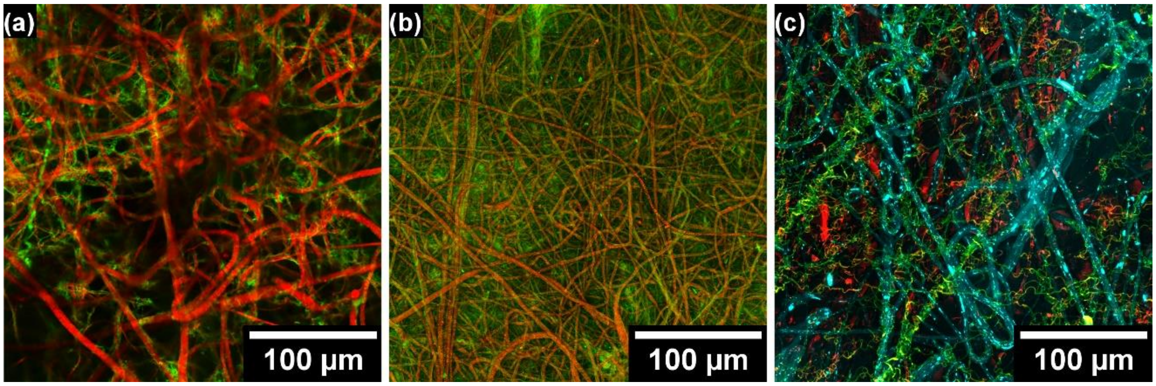

Figure 5-2- POEGMA fibers (green) and PCL (red and blue) co-electrospun hard-soft scaffolds visualized using laser scanning confocal microscopy: (a) Scaffold fabricated by co-electrospinning the higher concentration PCL nanofiber stream 1 (red) with POEGMA (green); (b) Scaffold fabricated by co-electrospinning the lower concentration PCL nanofiber stream 2 (red) with POEGMA (green); (c) Scaffold fabricated by co-electrospinning thin PCL nanofiber stream 1 (cyan), the thick PCL nanofiber stream 2 (red) and POEGMA (green).

5.3.3. Swelling

The gravimetric swelling profiles of the co-electrospun PCL-POEGMA scaffolds relative to PCL-only scaffolds prepared using the same method but excluding the POEGMA stream during fabrication are shown in Figure 5-3. The full swelling profile (Figure 5-3-a) shows a small increase in the swelling ratio within the first 12-24 hours for both scaffolds, reaching an equilibrium degree of swelling of ~30% within 30 hours. Comparing the equilibrium swelling ratios observed for two samples (averaged values between 48-72 hours at the plateau region, Figure 5-3-b), an unpaired t-test showed no significant difference in the equilibrium water retention between PCL-POEGMA and PCL samples. Given that PCL itself does not typically swell (equilibrium swelling ratio of bulk

PCL≈0.02 in PBS after 8 weeks [46]), the primary driver for swelling is hypothesized to be water absorption into the porous polar PCL scaffold, although an increase in the porosity of the scaffold as the PCL fibers harden upon exposure to water (an anti-solvent) may also contribute to promoting water influx. Although the POEGMA nanofiber phase will swell upon water exposure (as we have demonstrated in previous work [21]), the interpenetrating nature of the PCL-POEGMA scaffolds limits the degree of water uptake facilitated by the POEGMA nanofibers as well as the capacity of POEGMA swelling to alter the dimensions of the hard-soft scaffolds. Thus, the inclusion of the POEGMA interpenetrating network does not significantly influence the bulk swelling properties of the electrospun scaffolds.

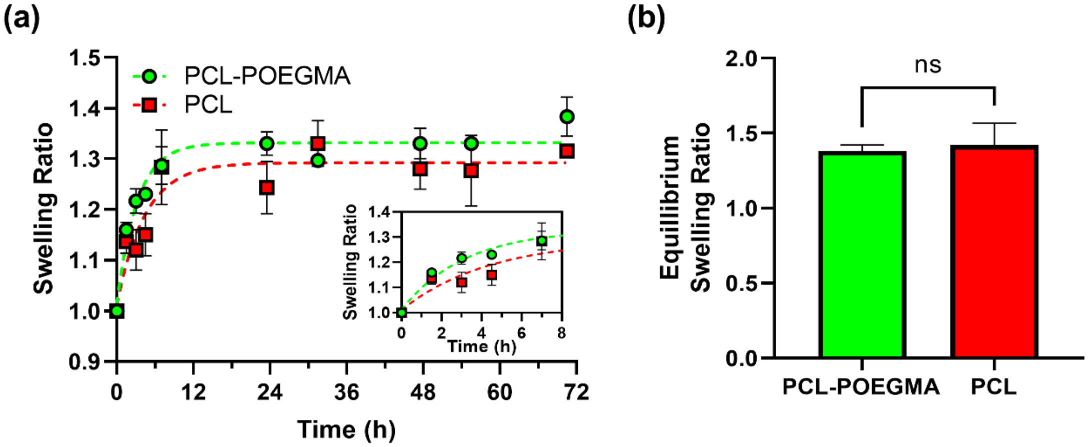

Figure 5-3- Swelling properties of hard-soft electrospun scaffolds: (a) Gravimetric swelling profile of electrospun PCL-POEMGA (green) and PCL-only (red) scaffolds in PBS (dashed lines are a guide to the eye); (b) Equilibrium (48-72 h average) swelling ratio of PCL-POEGMA scaffolds compared to PCL-only scaffolds (n=3, p>0.05 in unpaired two tailed t-test).

5.3.4. Contact angle

Contact angle measurements were obtained to elucidate the impact of fiber alignment and POEGMA-driven hydration on the interfacial properties of the electrospun scaffolds. Figure 5-4-a depicts a schematic of the incision was made to removed samples from the collector and the fiber orientation. The contact angle was measured in both the longitudinal and cross-longitudinal directions similar to the mechanical measurements, as depicted schematically in Figure 5-4-a. Analysis of the results (summarized in Figure 4-b) using a three-way matched ANOVA followed by a Tukey test ($p<0.05$ for significance) indicated that the contact angle is influenced by a combination of the direction of alignment and the hydration of the scaffold. This result is consistent with previous observations made around the wetting behavior of electrospun scaffolds [47], in which interfacial interactions with the nanofiber material, the effect of nano/microfiber curvature, and bulk water transport through the pores in the scaffold can all confound a direct interpretation of contact angle measurements. In PCL-POEGMA scaffolds, the swelling of the POEGMA hydrogel network adds an additional variable that may modify the contact angle. Figure 5-4-c depicts a schematic of droplet spreading on the electrospun scaffolds tested based on the results obtained in Figure 5-4-b. In the PCL-only scaffolds, no significant difference is noted in the contact angles in the longitudinal direction between hydrated and dry samples while a significant decrease in the contact angle was observed upon hydration in the cross-longitudinal direction. We attribute this result to the entrapment of water between the PCL fibers, leading to enhanced water droplet spreading perpendicular to the fibers as opposed to along the fibers given their relative hydrophobicity. In contrast, for the PCL-POEGMA scaffolds, the opposite trend was observed. The swelling of the POEGMA fibers upon hydration leads to an increase in fiber diameter (and thus interfacial roughness) as well as an increase in the interfacial hydrophilicity of the POEGMA nanofiber phase. In the cross-longitudinal direction, the combination of these effects results in a net zero impact on the contact angle measured; in the longitudinal direction, the presence of swollen POEGMA fibers promotes directional wetting along the (hydrophilic) fiber direction to promote directional droplet spreading and thus a more significant decrease in contact angle than observed with the PCL fibers. As such, the inclusion of a swellable interpenetrating nanofiber phase in the PCL-POEGMA hard/soft scaffolds can significantly alter interfacial scaffold wettability.

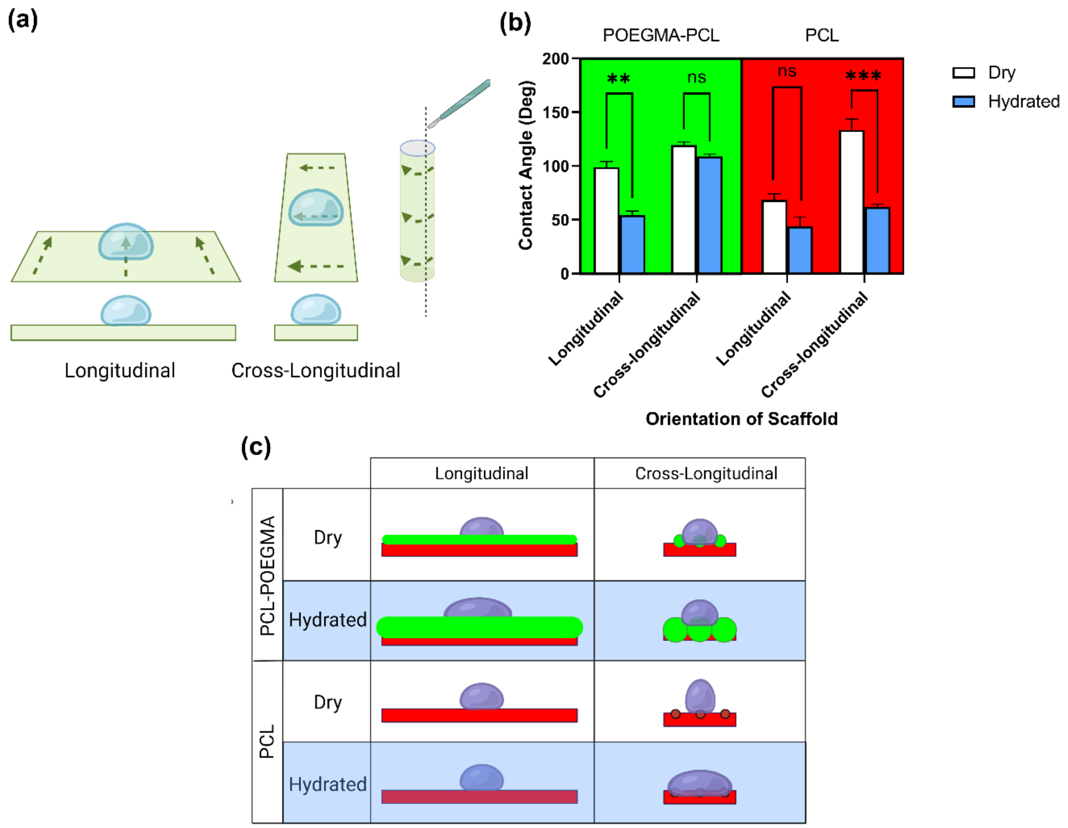

Figure 5-4- Contact angle characterization of hard/soft PCL-POEGMA co-electrospun scaffolds relative to PCL-only electrospun scaffolds: (a) Schematic depicting fiber orientation on the aluminum rod used as a grounded collector, how the samples were removed from the collector, and the location of incision; (b) Summary of contact angle measurements in both the longitudinal (parallel to fibers) and cross-longitudinal (perpendicular to fibers) directions on both PCL-POEGMA and POEGMA-only scaffolds (error bars represent the standard error from n=5 independent measurements, ns = not significant p=0.1, *=p<0.1, ** = p<0.01, *** = p<0.001; (c) Schematic of the hypothesized impact of POEGMA fiber hydration and both PCL and POEGMA directionality on the contact angle results. POEGMA fibers are depicted in green while PCL fibers are depicted in red (schematics not to scale).

5.3.5. Mechanical Properties

To assess the effect of the interpenetrating hard and soft nanofibrous networks on the swollen scaffold mechanics, uniaxial tensile testing was performed in three different orientations: (1) with the force applied parallel to the expected fiber direction on samples cut into strips (labeled as longitudinal); (2) with the force applied perpendicular to the expected fiber direction on samples cut into strips (labeled as cross-longitudinal); and (3) with the force applied on samples cut into rings and mounted on two T-shaped sample holders (labeled as circumferential) (Figure 5-5-a). The stress-strain curves (Figure 5-5-b) show large differences in the mechanical properties depending on the direction of the applied force. In the longitudinal direction (Figure 5-5-c), in which the fiber strength is the main contributor to the scaffold mechanical properties, the ultimate tensile strength, the elongation at break, and Young's modulus (429 ± 39 kPa, 1.34 mm/mm, and Young's modulus of 1114 ± 130 kPa) are much higher than those observed in the cross-longitudinal (Figure 5-5-d) direction (86 ± 25 kPa, 0.58 mm/mm, and Young's modulus of 184 ± 54 kPa). Meanwhile, in the circumferential (ring) direction (Figure 5-5-e) the samples show the highest elongation at break matching ultimate tensile strength value measured in the longitudinal direction (413 ± 71 kPa, 3.56 mm/mm, and Young's modulus of 1700 ± 81 kPa). In contrast, POEGMA-only samples could not be removed from the collector either in the dry or the hydrated state due to their fragile mechanics, with even bulk POEGMA hydrogels prepared with polymers at the same concentration and with the same degree of aldehyde/hydrazide functionalization showing a compressive modulus over two orders of magnitude lower (1.6 ± 0.4 kPa) [45]; even dry POEGMA-only electrospun scaffolds have lower moduli (~100 kPa) [48]. As such, the dual hard/soft electrospinning strategy can create tissue scaffolds with anisotropic mechanics with high tensile strength in hydrated state without sacrificing the presence of a hydrogel domain within the scaffold.

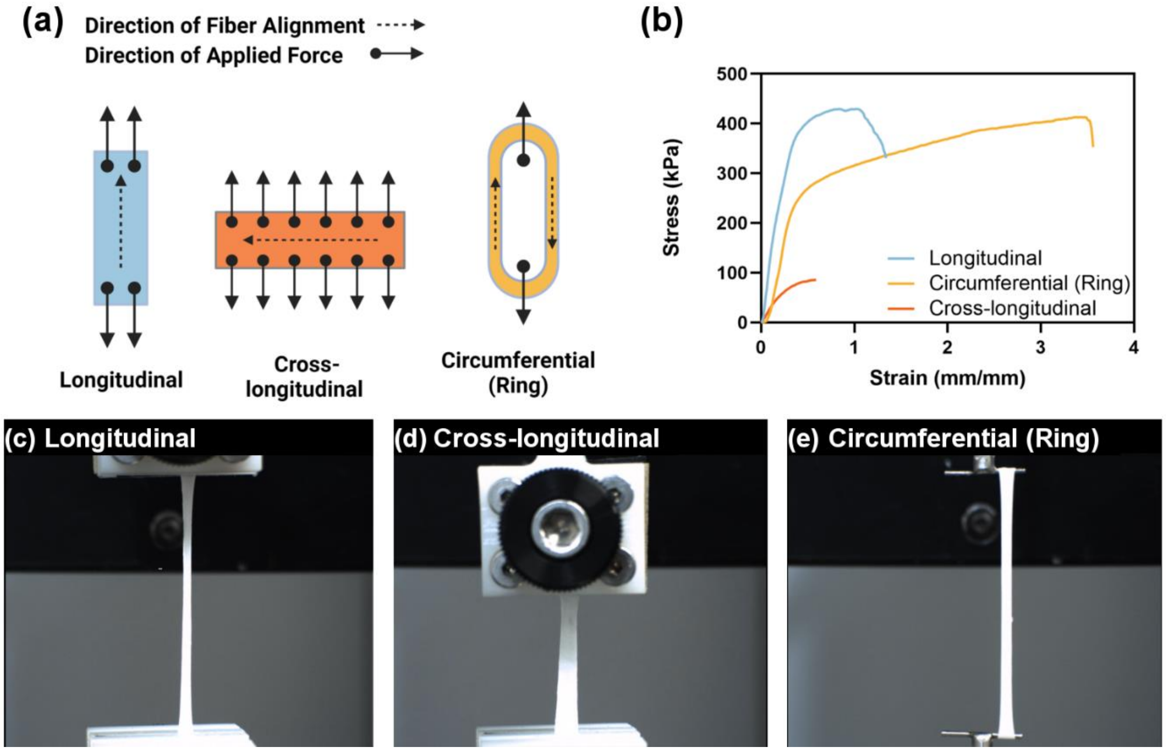

Figure 5-5- Mechanical testing of hard-soft electrospun scaffolds: (a) Schematic depicting the direction of mechanical testing and the corresponding fiber alignment; (b) Stress-strain curve depicting results from uniaxial tensile testing in 3 different orientations; (c) Longitudinal (parallel to fiber orientation), (d) cross-longitudinal (perpendicular to the fiber orientation) and (e) circumferential (ring) testing geometries.

5.3.6. Protein Uptake

The total uptake (combined adsorption/absorption) of bovine serum albumin and fibrinogen to the PCL-POEGMA scaffolds relative to the PCL-only scaffolds and a low protein binding multiwell plate control is shown in Figure 5-6. Two-way ANOVA followed by a Tukey pairwise comparison indicated that the PCL-POEGMA scaffold facilitates a significant reduction in BSA uptake at higher BSA concentrations compared to a low protein-binding plate control (Figure 5-6-a), consistent with previous observations around the high protein repellency of POEGMA-based hydrogels [49, 50]. In contrast, at the same protein concentration, the PCL-POEGMA scaffolds show increased fibrinogen uptake in comparison to both the PCL-only scaffolds and the low protein binding plate control. Fibrinogen uptake is generally significantly higher than BSA uptake due to the much higher molecular mass of fibrinogen [51]. In this case, the much higher binding affinity of fibrinogen to PCL-POEGMA scaffolds results from the combination of the fiber diameter/curvature, the hydrophilicity of the POEGMA interpenetrating fibers, and the higher overall surface area, the latter a result of the introduction of the POEGMA nanofiber phase as well as the small diameter and thus high surface area-to-volume ratio of those fibers. Fibrinogen has been reported to show higher affinity than BSA on hydrophilic surfaces with curvatures similar to the POEGMA fibers while BSA shows higher binding affinity on hydrophobic surfaces of similar curvature [52]. As such, by introducing the POEGMA phase, the balance of enhanced hydrophilicity and higher interfacial surface area results in differential protein uptake.

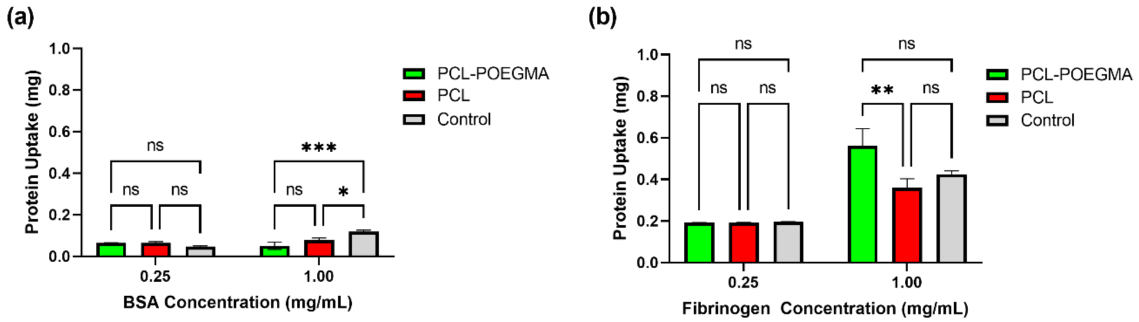

Figure 5-6- Protein uptake of (a) bovine serum albumin and (b) fibrinogen to PCL-POEGMA hard/soft scaffolds relative to PCL-only scaffolds and a low protein-binding multiwell plate surface; n=4 *p*=0.1, *=*p*<0.1, ** = *p*<0.01, *** = *p*<0.001.

5.3.7. Bacterial Adhesion

To assess the potential of the hard/soft PCL-POEGMA scaffolds interaction with bacteria the adhesion *P. aeruginosa* to scaffolds prepared with or without the POEGMA nanofibers was assessed. Figure 5-7 illustrates the results from the bacterial adhesion test, expressed in terms of the percentage of the added bacteria binding to the surfaces following different incubation times. The PCL-POEGMA scaffold adhered significantly less bacteria (i.e. more bacteria remained in the supernatant) relative to the PCL-only scaffold as well as the low protein-binding multiwell plate control after 25 minutes of incubation, although this beneficial property was lost after 45 minutes of incubation. We attribute this delay in the establishment of adhered bacteria to the hydrophilicity introduced by the POEGMA interpenetrating nanofibrous network, reducing the affinity between the bacteria and the surface and functionally delaying the establishment of infection upon bacteria exposure. Note that the concentration of bacteria used in this test is very high (>10^7 CFU/mL) such that this represents a very strong challenge to the materials' potential to suppress bacterial adhesion; as such, the observation that a delay in bacterial adhesion can be achieved is potentially significant in a clinical context in which bacterial loads are typically much lower [53]. This result suggests the potential application of these scaffolds in biomedical applications in which bacterial adhesion and ultimate biofilm formation must be suppressed.

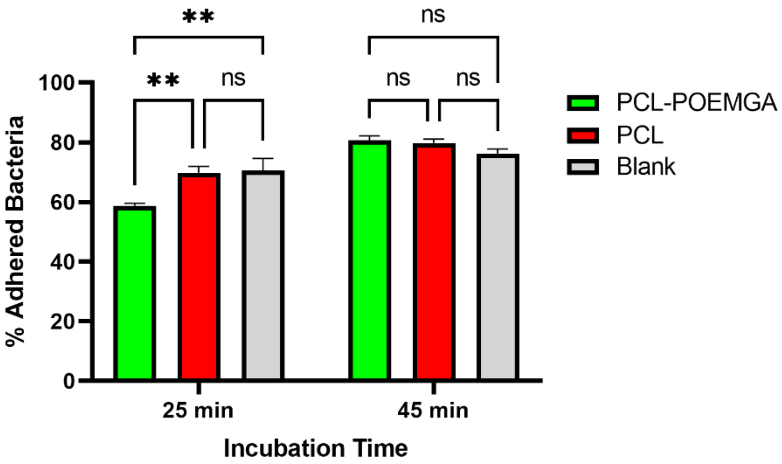

Figure 5-7- Bacterial adhesion of *P. aeruginosa* to hard/soft PCL-POEGMA co-electrospun scaffolds relative to PCL-only electrospun scaffolds and a non-binding multiwell plate surface (inoculum load = 3.4×10^7 CFU/mL); n=4, *p*=0.1, *=p<0.1, ** = *p*<0.01, *** = *p*<0.001, **** = *p*<0.0001.

5.3.8. Cell Alignment and Proliferation

To assess the capacity of the scaffolds to facilitate mammalian cell proliferation, C2C12 myoblasts were pre-stained with CellTrace™ FarRed, seeded on the scaffolds, and tracked using confocal microscopy (Figure 5-8-a). Both cell morphology and cell proliferation were significantly different between the PCL-POEGMA and PCL-only scaffolds. At day 3, significantly higher cell directionality was observed in the PCL-only scaffolds, with the presence of the hydrated POEGMA nanofiber network significantly altering the impact of the PCL alignment cues on cell orientation. However, image analysis of the directionality of cells adhered to each type of scaffold still indicates significant directionality of the cells seeded on the PCL-POEGMA scaffolds (See Supplementary Information Figure 5-10). This was determined by the dispersion value reported by the FIJI Directionality Analysis function, suggesting that while the POEGMA phase dilutes the directionality cues of the PCL fibers such cues are not entirely scrambled. This result is consistent with previous studies on multi-scale structuring of composite hydrogel sheets in which cell alignment was affected by smaller randomly oriented fibers present on highly directional substrates [54].

By day 5, large patches of proliferating cells were observed on the PCL-POEGMA scaffolds (similar to the polystyrene control at day 3) while the PCL scaffolds maintained more isolated cells tightly associated with the PCL fibers. Quantitative image analysis to track the percentage of image area covered by C2C12 cells showed that cells covered a ~4× larger area in the PCL-POEGMA scaffolds compared to the PCL-only scaffolds (

Figure 5-8-b), indicating the significantly enhanced potential of the hard/soft PCL-POEGMA scaffold for promoting cell proliferation.

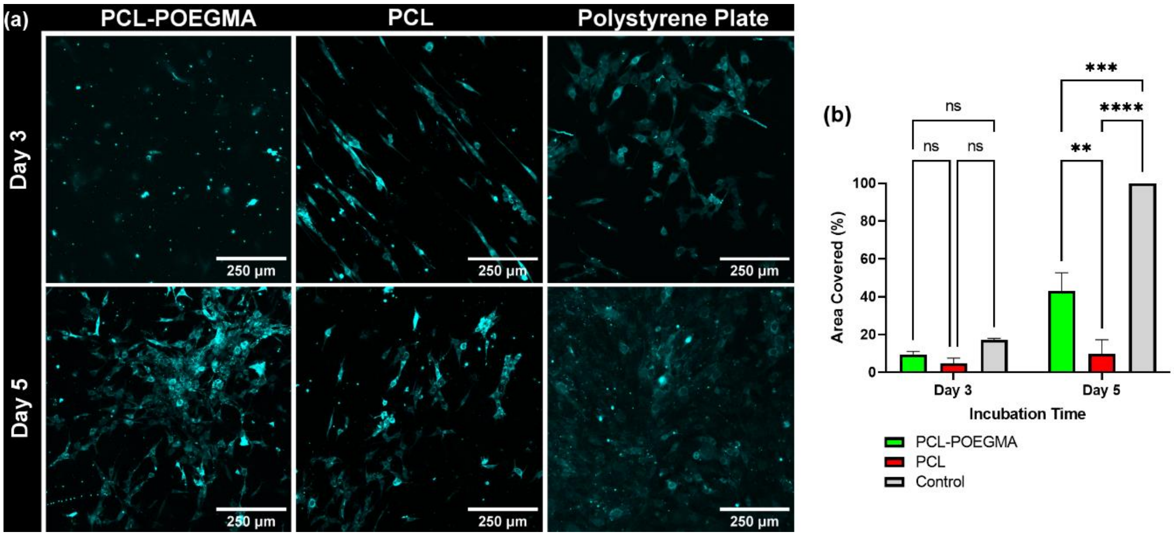

Figure 5-8- Cell proliferation on hard/soft PCL-POEGMA co-electrospun scaffolds relative to PCL-only electrospun scaffolds and a non-binding multiwell plate surface: (a) Laser scanning confocal microscopy images depicting cell morphology and proliferation; (b) Image analysis results of the area covered by cells after 3 and 5 days of incubation (ns = not significant at p=0.1, *=p<0.1, ** = p<0.01, *** = p<0.001, **** = p<0.0001).

The application of PCL electrospun scaffolds in tissue regeneration has previously been limited by the high interfacial hydrophobicity (i.e. low surface hydration) of such scaffolds, inhibiting the capacity of cells to proliferate on the scaffold [39]. The interpenetrating network of PCL and POEGMA nanofibers developed herein can address this challenge by facilitating high cell proliferation without compromising the favorable mechanics of PCL-based scaffolds (Figure 5-5-b), which together with relatively weak cell adhesion observed represents the key drawback of POEGMA-only scaffolds [45]. The mechanics of the scaffold can be maintained without requiring the use of nanoparticle fillers (which can introduce both processing and biological clearance challenges [55]), the use of complex hydrogel chemistries such as double network hydrogels that are challenging to implement in an electrospinning context [25], or any post-processing or crosslinking step that could result in loss of the desirable nanofibrous morphology [39]. Furthermore, relative to previous co-electrospinning strategies, the lack of large-scale phase separation observed in the PCL-POEGMA system (Figure 5-3) results in more homogeneous scaffolds without mechanical weak points that can limit the ultimate tensile strength or burst pressure of the scaffold in load or pressure-bearing applications.

5.4. Conclusion

An interpenetrating fiber network of “hard” PCL fibers and “soft” POEGMA nanofibers has been developed using a single-step co-electrospinning strategy. Relatively homogeneous interpenetrating fibrous networks can be fabricated that offer the desirable interfacial hydration of POEGMA-based scaffolds combined with the favorable (anisotropic) mechanical properties of PCL-based scaffolds, resulting in delayed bacterial adhesion but significantly enhanced cell proliferation relative to PCL-only scaffolds. The combination of interfacial “soft” hydrogel-like properties and bulk “hard” scaffold mechanics achieved with PCL-POEGMA electrospun scaffolds suggests the potential of PCL-POEGMA electrospun scaffolds for applications in tissue engineering and regenerative medicine.

5.5. Acknowledgements

This work was supported by The Natural Sciences and Engineering Research Council of Canada (Discovery Grant RGPIN-2017-06455).

5.6. References

[1] A. Jayakumar, V.K. Jose, J.-M. Lee, Hydrogels for medical and environmental applications, Small Methods 4(3) (2020) 1900735.
[2] A.S. Hoffman, Hydrogels for biomedical applications, Adv. Drug Deliv. Rev. 64 (2012) 18-23.
[3] J. Xue, T. Wu, Y. Dai, Y. Xia, Electrospinning and electrospun nanofibers: methods, materials, and applications, Chem. Rev. 119(8) (2019) 5298-5415.
[4] K.J. De France, F. Xu, T. Hoare, Structured macroporous hydrogels: progress, challenges, and opportunities, Adv. Healthc. Mater. 7(1) (2018) 1700927.
[5] F. Xu, C. Dawson, M. Lamb, E. Mueller, E. Stefanek, M. Akbari, T. Hoare, Hydrogels for tissue engineering: addressing key design needs toward clinical translation, Front Bioeng Biotechnol 10 (2022) 849831.
[6] V. Beachley, X. Wen, Effect of electrospinning parameters on the nanofiber diameter and length, Mater. Sci. Eng. C 29(3) (2009) 663-668.
[7] Y. Shin, M. Hohman, M. Brenner, G. Rutledge, Experimental characterization of electrospinning: the electrically forced jet and instabilities, Polymer 42(25) (2001) 09955-09967.
[8] P. Gupta, C. Elkins, T.E. Long, G.L. Wilkes, Electrospinning of linear homopolymers of poly (methyl methacrylate): exploring relationships between fiber formation, viscosity, molecular weight and concentration in a good solvent, Polymer 46(13) (2005) 4799-4810.
[9] J. Macossay, A. Marruffo, R. Rincon, T. Eubanks, A. Kuang, Effect of needle diameter on nanofiber diameter and thermal properties of electrospun poly (methyl methacrylate), Polym Adv Technol 18(3) (2007) 180-183.
[10] S. De Vrieze, T. Van Camp, A. Nelvig, B. Hagström, P. Westbroek, K. De Clerck, The effect of temperature and humidity on electrospinning, J. Mater. Sci. 44 (2009) 1357-1362.
[11] H.S. Yoo, T.G. Kim, T.G. Park, Surface-functionalized electrospun nanofibers for tissue engineering and drug delivery, Adv. Drug Deliv. Rev. 61(12) (2009) 1033-1042.
[12] D. Liang, B.S. Hsiao, B. Chu, Functional electrospun nanofibrous scaffolds for biomedical applications, Adv. Drug Deliv. Rev. 59(14) (2007) 1392-1412.
[13] R. Tonndorf, D. Aibibu, C. Cherif, Isotropic and anisotropic scaffolds for tissue engineering: collagen, conventional, and textile fabrication technologies and properties, Int J Mol Sci 22(17) (2021).
[14] B. Yi, Y. Shen, H. Tang, X. Wang, B. Li, Y. Zhang, Stiffness of aligned fibers regulates the phenotypic expression of vascular smooth muscle cells, ACS Appl. Mater. Interfaces 11(7) (2019) 6867-6880.
[15] J. Xie, H. Shen, G. Yuan, K. Lin, J. Su, The effects of alignment and diameter of electrospun fibers on the cellular behaviors and osteogenesis of BMSCs, Mater. Sci. Eng. C 120 (2021) 111787.
[16] T.A.M. Valente, D.M. Silva, P.S. Gomes, M.H. Fernandes, J.D. Santos, V. Sencadas, Effect of sterilization methods on electrospun poly(lactic acid) (PLA) fiber alignment for biomedical applications, ACS Appl. Mater. Interfaces 8(5) (2016) 3241-3249.
[17] W. Zhao, J. Li, K. Jin, W. Liu, X. Qiu, C. Li, Fabrication of functional PLGA-based electrospun scaffolds and their applications in biomedical engineering, Mater. Sci. Eng. C 59 (2016) 1181-1194.
[18] G.H. Kim, Electrospun PCL nanofibers with anisotropic mechanical properties as a biomedical scaffold, Biomed Mater 3(2) (2008) 025010.
[19] Z. Cui, Z. Zheng, L. Lin, J. Si, Q. Wang, X. Peng, W. Chen, Electrospinning and crosslinking of polyvinyl alcohol/chitosan composite nanofiber for transdermal drug delivery, Adv. Polym. Technol. 37(6) (2018) 1917-1928.
[20] Y. Li, M. Vergaelen, E. Schoolaert, R. Hoogenboom, K. De Clerck, Effect of crosslinking stage on photocrosslinking of benzophenone functionalized poly(2-ethyl-2-oxazoline) nanofibers obtained by aqueous electrospinning, Eur. Polym. J. 112 (2019) 24-30.
[21] F. Xu, H. Sheardown, T. Hoare, Reactive electrospinning of degradable poly(oligoethylene glycol methacrylate)-based nanofibrous hydrogel networks, ChemComm 52(7) (2016) 1451-1454.
[22] L. Daelemans, I. Steyaert, E. Schoolaert, C. Goudenhooft, H. Rahier, K. De Clerck, Nanostructured hydrogels by blend electrospinning of polycaprolactone/gelatin nanofibers, Nanomaterials 8(7) (2018).
[23] S. Xu, L. Deng, J. Zhang, L. Yin, A. Dong, Composites of electrospun-fibers and hydrogels: A potential solution to current challenges in biological and biomedical field, J. Biomed. Mater. Res.:B Appl. 104(3) (2016) 640-656.
[24] K. Haraguchi, T. Takehisa, Nanocomposite hydrogels: A unique organic–inorganic network structure with extraordinary mechanical, optical, and swelling/de-swelling properties, Adv Mater 14(16) (2002) 1120-1124.
[25] J.P. Gong, Y. Katsuyama, T. Kurokawa, Y. Osada, Double-network hydrogels with extremely high mechanical strength, Adv Mater 15(14) (2003) 1155-1158.
[26] W. Xing, Y. Tang, On mechanical properties of nanocomposite hydrogels: Searching for superior properties, Nano Mater. Sci. 4(2) (2022) 83-96.

[27] A. Bin Imran, K. Esaki, H. Gotoh, T. Seki, K. Ito, Y. Sakai, Y. Takeoka, Extremely stretchable thermosensitive hydrogels by introducing slide-ring polyrotaxane cross-linkers and ionic groups into the polymer network, Nature Comm 5(1) (2014) 5124.

[28] Y. Okumura, K. Ito, The polyrotaxane gel: a topological gel by figure-of-eight cross-links, Adv Mater 13(7) (2001) 485-487.

[29] C. Bussy, H. Ali-Boucetta, K. Kostarelos, Safety considerations for graphene:lessons learnt from carbon nanotubes, Acc. Chem. Res. 46(3) (2013) 692-701.

[30] H. Gao, Q. He, The interaction of nanoparticles with plasma proteins and the consequent influence on nanoparticles behavior, Expert Opin Drug Deliv 11(3) (2014) 409-420.

[31] S. Kashyap, S.K. Pratihar, S.K. Behera, Strong and ductile graphene oxide reinforced PVA nanocomposites, J. Alloys Compd. 684 (2016) 254-260.

[32] J.-Y. Lin, P.-X. Lai, Y.-C. Sun, C.-C. Huang, C.-K. Su, Biodistribution of graphene oxide determined through postadministration labeling with DNA-conjugated gold nanoparticles and ICPMS, Anal. Chem. 92(20) (2020) 13997-14005.

[33] L. Zhang, S. Ouyang, H. Zhang, M. Qiu, Y. Dai, S. Wang, Y. Wang, J. Ou, Graphene oxide induces dose-dependent lung injury in rats by regulating autophagy, Exp Ther Med 21(5) (2021) 462.

[34] J. Yang, J.-J. Zhao, C.-R. Han, J.-F. Duan, Keys to enhancing mechanical properties of silica nanoparticle composites hydrogels: The role of network structure and interfacial interactions, Compos. Sci. Technol. 95 (2014) 1-7.

[35] Z. Emami, M. Ehsani, M. Zandi, H. Daemi, M.-H. Ghanian, R. Foudazi, Modified hydroxyapatite nanoparticles reinforced nanocomposite hydrogels based on gelatin/oxidized alginate via schiff base reaction, Carbohydr. Polym. Technol. and Appl. 2 (2021) 100056.

[36] D. Yang, X. Peng, L. Zhong, X. Cao, W. Chen, S. Wang, C. Liu, R. Sun, Fabrication of a highly elastic nanocomposite hydrogel by surface modification of cellulose nanocrystals, RSC Adv. 5(18) (2015) 13878-13885.

[37] I. Tiyek, A. Gunduz, F. Yalcinkaya, J. Chaloupek, Influence of electrospinning parameters on the hydrophilicity of electrospun polycaprolactone nanofibres, J Nanosci Nanotechnol 19(11) (2019) 7251-7260.

[38] Â. Semitela, A.F. Girão, C. Fernandes, G. Ramalho, I. Bdikin, A. Completo, P.A.A.P. Marques, Electrospinning of bioactive polycaprolactone-gelatin nanofibres with increased pore size for cartilage tissue engineering applications, J. Biomater. Appl. 35(4-5) (2020) 471-484.

[39] A.O. Lobo, S. Afewerki, M.M.M. de Paula, P. Ghannadian, F.R. Marciano, Y.S. Zhang, T.J. Webster, A. Khademhosseini, Electrospun nanofiber blend with improved mechanical and biological performance, Int J Nanomedicine 13 (2018) 7891-7903.

[40] Y. Montoya, J. Cardenas, J. Bustamante, R. Valencia, Effect of sequential electrospinning and co-electrospinning on morphological and fluid mechanical wall properties of polycaprolactone and bovine gelatin scaffolds, for potential use in small diameter vascular grafts, Biomater. Res. 25(1) (2021) 38.

[41] L. Wu, H. Li, S. Li, X. Li, X. Yuan, X. Li, Y. Zhang, Composite fibrous membranes of PLGA and chitosan prepared by coelectrospinning and coaxial electrospinning, J Biomed Mater Res A 92A(2) (2010) 563-574.

[42] F. Croisier, A.S. Duwez, C. Jérôme, A.F. Léonard, K.O. van der Werf, P.J. Dijkstra, M.L. Bennink, Mechanical testing of electrospun PCL fibers, Acta Biomater. 8(1) (2012) 218-224.

[43] N.M. Smeets, E. Bakaic, M. Patenaude, T. Hoare, Injectable poly(oligoethylene glycol methacrylate)-based hydrogels with tunable phase transition behaviours: physicochemical and biological responses, Acta Biomater. 10(10) (2014) 4143-55.

[44] I. Urosev, H. Dorrington, N. Muzzin, R. Alsop, E. Bakaic, T. Gilbert, M. Rheinstädter, T. Hoare, Injectable poly(oligoethylene glycol methacrylate)-based hydrogels fabricated from highly branched precursor polymers: controlling gel properties by precursor polymer morphology, ACS Appl. Polym. Mater. 1(3) (2019) 369-380.

[45] N.M.B. Smeets, E. Bakaic, M. Patenaude, T. Hoare, Injectable and tunable poly(ethylene glycol) analogue hydrogels based on poly(oligoethylene glycol methacrylate), ChemComm 50(25) (2014) 3306-3309.

[46] D. Łysik, J. Mystkowska, G. Markiewicz, P. Deptuła, R. Bucki, The Influence of mucin-based artificial saliva on properties of oolycaprolactone and polylactide, Polymers, 2019.

[47] P.K. Szewczyk, D.P. Ura, S. Metwally, J. Knapczyk-Korczak, M. Gajek, M.M. Marzec, A. Bernasik, U. Stachewicz, Roughness and fiber fraction dominated wetting of electrospun fiber-based porous meshes, Polymers 11(1) (2019).

[48] F. Xu, M. Dodd, H. Sheardown, T. Hoare, Single-step reactive electrospinning of cell-loaded nanofibrous scaffolds as ready-to-use tissue patches, Biomacromolecules 19(11) (2018) 4182-4192.

[49] K.J. De France, M. Badv, J. Dorogin, E. Siebers, V. Panchal, M. Babi, J. Moran-Mirabal, M. Lawlor, E.D. Cranston, T. Hoare, Tissue response and biodistribution of injectable cellulose nanocrystal composite hydrogels, ACS Biomater. Sci. Eng. 5(5) (2019) 2235-2246.

[50] A. Hucknall, S. Rangarajan, A. Chilkoti, In pursuit of zero: polymer brushes that resist the adsorption of proteins, Adv Mater 21(23) (2009) 2441-2446.

[51] R. Kargl, M. Bračič, M. Resnik, M. Mozetič, W. Bauer, K. Stana Kleinschek, T. Mohan, Affinity of serum albumin and fibrinogen to Cellulose, its hydrophobic derivatives and blends, Front. Chem. 7 (2019).

[52] P. Roach, D. Farrar, C.C. Perry, Surface tailoring for controlled protein adsorption: effect of topography at the nanometer scale and chemistry, J. Am. Chem. Soc. 128(12) (2006) 3939-3945.
[53] S. Zheng, M. Bawazir, A. Dhall, H.E. Kim, L. He, J. Heo, G. Hwang, Implication of surface properties, bacterial motility, and hydrodynamic conditions on bacterial surface sensing and their Initial adhesion, Front Bioeng Biotechnol 9 (2021) 643722.
[54] K.J. De France, F. Xu, S. Toufanian, K.J.W. Chan, S. Said, T.C. Stimpson, E. González-Martínez, J.M. Moran-Mirabal, E.D. Cranston, T. Hoare, Multi-scale structuring of cell-instructive cellulose nanocrystal composite hydrogel sheets via sequential electrospinning and thermal wrinkling, Acta Biomater. 128 (2021) 250-261.
[55] V. Sinha, S. Chakma, Advances in the preparation of hydrogel for wastewater treatment: A concise review, J. Environ. Chem. Eng. 7(5) (2019) 103295.

5.7. Supporting Information

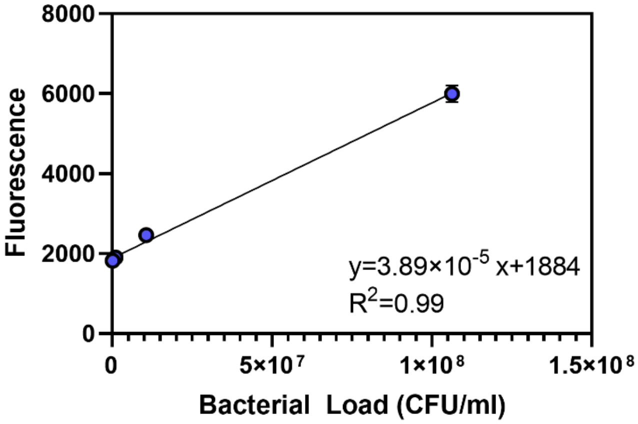

Figure 5-9-Calibration curve used in bacterial adhesion assay depicting fluorescence vs. bacterial load.

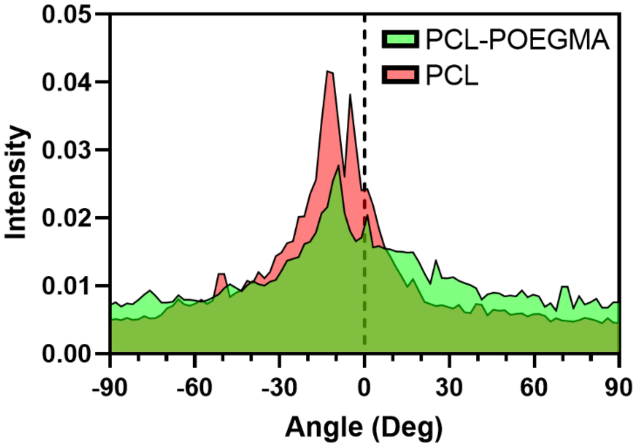

Figure 5-10-Histogram output reported by FIJI Directionality Analysis function highlighting cell alignment in both PCL-POEGMA and PCL scaffolds with the reduced cell alignment in PCL-POEGMA scaffolds compared to PCL scaffolds

.

Chapter 6- Conclusions and Future Direction

6.1. Summary and Conclusion

The overall goal of this Ph.D. thesis is to identify and address some of the limitations in designing hydrogel scaffolds for tissue engineering and wound dressings by addressing specific gaps and challenges in design and application of macroporous hydrogel scaffolds as identified in the review of available literature.

In chapter 1, an overview of the current applications of macroporous hydrogels and common methods used to produce macroporous hydrogels including gas-in-liquid foam templating, gas foaming using effervescent salts, technologies based on supercritical fluids, 3D printing, electrospinning, emulsion templating, salt leaching, inverse opal templating, microgel assembly, cryogenic techniques and combination techniques were described and assessed in terms of their advantages and disadvantages. Subsequently, the importance of pore architecture in regulating the biological responses to tissue engineering scaffolds was expanded on to highlight both the key benefits of macroporous hydrogels in tissue engineering and wound care as well as the design needs for controlling porosity in macroporous hydrogels suitable for a given application.

In chapter 2, the encapsulation of antimicrobial compounds in a hydrogel scaffold for the treatment of methicillin-resistant *Staphylococcus aureus* (MRSA) was described. Fusidic acid was encapsulated in poly(lactic acid)-*block*-poly(oligoethylene glycol methacrylate) (PLA-POEGMA) self-assembled nanoparticles and subsequently physically encapsulated in a dynamically-crosslinked POEGMA hydrogel matrix. In the treatment of established MRSA infected wounds in mice. FA-loaded hydrogels facilitated 1-2 order of magnitude reductions in the bacterial load of the wound, significantly reducing the risk of systemic infection and sepsis. The PLA-POEGMA self-assembled nanoparticle used in this chapter could be applied to encapsulate other hydrophobic antimicrobial compounds, offering potential to simply mix self-assembled nanoparticles loaded with different antimicrobial compounds to create customized combination therapies in which multiple antimicrobial compounds are used to reduce the risk of antibiotic resistance.

In chapter 3, a combination of two supercritical fluids technologies (Pressurized Gas eXpanded liquids, PGX, and supercritical adsorptive precipitation) were used to produce *in situ*-crosslinked alginate scaffolds in a single processing step and subsequently leverage the high porosity of the resulting scaffold for supercritical carbon dioxide-assisted solubilization and precipitation of poorly soluble drugs inside the scaffold. This platform provides a scalable technique to deliver hydrophobic compounds directly to the wound, with fusidic acid and tigecycline-loaded PGX disks resulting in a significant reduction or complete clearance of bacterial load respectively after 48 hours of treatment. The complete killing achieved with the tigecycline-loaded disks was particularly notable given the typically bacteriostatic mode of action of tigecycline and the very low drug dose required relative to conventional (intravenous) therapy needs. The broad utility of this method to load poorly water-soluble drugs in a much more bioavailable format offers potential to rescue other potential antibiotics that have not found clinical use due to low bioavailability while also minimizing overall antibiotic use toward improving antibiotic stewardship.

In chapter 4, a new type of injectable macroporous hydrogel was formulated by combining *in situ*-gelling dynamic covalent crosslinked hydrogels with a perfluorocarbon emulsion that evaporates at physiological temperature on the same time scale as gelation. The formulation presented does not contain any toxic compounds or harmful surfactants, unlike other potential injectable hydrogel options to create macroporosity. The injectable porous hydrogels are well tolerated *in vivo* and do not cause significant inflammation. Furthermore, this platform supports simultaneously encapsulated cells *in vitro*, with a significantly larger percentage of cells surviving a 14-day incubation period in the injectable macroporous hydrogels compared to non-porous controls. Future anticipated uses of this injectable macroporous hydrogel could lie in cell transplantation for musculoskeletal or hepatic tissue regeneration, taking advantage of the improved capacity for native tissue in-growth into the macroporous hydrogels relative to conventional, only inherently porous injectable hydrogels.

In chapter 5, the challenge of weak mechanics of macroporous hydrogels was addressed by co-electrospinning polycaprolactone (PCL, hard) and poly(oligoethylene glycol methacrylate) (POEGMA, soft) nanofibers into a single scaffold without requiring any type of post-processing. The resulting interpenetrated PCL-POEGMA electrospun fibers showed strong anisotropic mechanical properties coupled with more hydrophilic gel-like interfacial properties, with minimal macroscopic phase separation observed between the hard and soft nanofiber phases. The presence of POEGMA in these scaffolds led to a delay in bacterial adhesion while at the same time facilitating a significant improvement in cell proliferation relative to the hydrophobic PCL scaffolds, addressing challenges with using either material on its own as a tissue scaffold. The combination of properties offered suggests promise to apply PCL-POEGMA soft-hard electrospun scaffolds as cellularized tissue patches and grafts (e.g.) as skin grafts, vascular grafts, or cardiac patches in which significant mechanical strength is required of the scaffold immediately upon implantation.

6.2. Future Directions

The encapsulation of antimicrobial compounds in PLA-POEGMA self-assembled nanoparticles as explored in chapter 2 can be adapted to a wide array of hydrophobic antimicrobial compounds. One of the advantages of the hydrogel preparation technique described in chapter 2 is its adaptability in terms of combining multiple bioactive compounds for combination therapy. Research has shown that combination drug therapy can be highly beneficial in treating complex infections, enabling exploitation of the synergistic effects of multiple antibiotics to more effectively de-escalate high-risk infection cases. Combination therapy has been shown to be effective for two main reasons: 1) it is more difficult for bacteria to adapt and survive when two killing pathways are simultaneously targeted, and 2) it is statistically less likely for bacteria to be resistant to two different classes of antibiotics. The design of the hydrogels in chapter 2 facilitates the use of such combination therapies by having different batches of self-assembled nanoparticles encapsulated with different antimicrobial compounds that can be mixed with the (water-like) gel polymer precursors in any desired ratio to produce antimicrobial hydrogels containing different combinations of antibiotics. This platform could be used to assist with high-throughput screening of potential antibiotics of interest or to evaluate synergistic drug effects, even when drug solubility in water is low. Alternately, this platform could be used in the context of personalized medicine to produce antimicrobial hydrogels with a suitable antibiotic mix to treat a specific patient following culture of the patient's specific infection and evaluation of that infection's drug susceptibility. In this example, the healthcare staff could produce the right dose of hydrogel in an in-patient setting and apply it directly to the wound using an applicator or a double barrel dispenser in the correct dose.

While combination therapy is an attractive approach to treating infections using already established antibiotics, there are still numerous antimicrobial compounds that are excluded from clinical use during the early stages of drug discovery due to their low water solubility and challenges associated with administrating these compounds. Supercritical absorptive precipitation, as described in chapter 3, offers potential to revive these compounds and bring new classes of antimicrobials to use. The demonstrated efficacy of the method to precipitate two poorly water-soluble drugs is anticipated to be applicable to assisting other poorly soluble drugs in achieving therapeutic relevance, particularly emerging antimicrobial small molecules/peptides now being identified via machine learning and artificial intelligence approaches that can predict hydrophobicity and thus potential suitability for loading via supercritical adsorptive precipitation.

While chapter 4 shows significant improvement in cell viability over a 14-day incubation time using the perfluorocarbon-induced macroporous hydrogel scaffolds, the scaffolds still did not support significant cell proliferation. We suspect that this is mainly due to the slow degradation of the POEGMA scaffold used in this study which limits cells from reaching the internal surface of pores and access empty volumes into which they can proliferate. If cell proliferation is not desired, this platform would already be effective in maintaining cell viability in medical devices in which live cells secrete a desired protein or biomarkers (e.g. islet transplantation devices), with the macroporous structure addressing the significant mass transport limitations of such systems that can lead to cell death over extended implantation times. However, to unlock the potential for true tissue regeneration, degradation must be accelerated and the affinity of the scaffold for cell adhesion must be enhanced. This can likely be achieved by replacing hydrozone chemistry with imine crosslinking that can exhibit faster degradation. Cell adhesion and proliferation may be encouraged by incorporating adhesion promoting peptides such as arginine-glycine-aspartate (RGD) in the formulation by covalently tethering the amine terminus of the peptide to aldehyde or ketone-functionalized POEGMA.

Finally, from chapter 5, the interpenetrating network of PCL-POEGMA electrospun scaffolds offers promising preliminary results for supporting cell proliferation but needs to be further studied to evaluate its potential as a tissue patch. Since PCL and hydrazone-crosslinked POEGMA are both biodegradable, it would be valuable to prepare tissue patches following longer-term culture of cells on the scaffolds (i.e. >14 days) and study the performance of the tissue patches. Furthermore, for practical use of the scaffolds as regenerative scaffolds, suture retention and permeability must be confirmed and a wider variety of cells must be tested to identify a suitable target tissue for this platform; skin, cardiac muscle, and vascular tissues seem to be suitable candidates for such studies based on the mechanics and interfacial properties of the scaffolds reported herein.